Technische Universität München
TUM School of Life Sciences

Exploring “Click” chemistry for *in vivo* detoxification of Amanitin-based Antibody-Drug Conjugates

Alessandra Totti

Vollständiger Abdruck der von der TUM School of Life Sciences der Technischen Universität München zur Erlangung des akademischen Grades einer

Doktorin der Naturwissenschaften (Dr. rer. nat.)

genehmigten Dissertation.

Vorsitz: Prof. Dr. Dietmar Zehn

Prüfende der Dissertation:

1. Prof. Dr. Arne Skerra
2. Prof. Dr. Andreas Pahl

Die Dissertation wurde am 29.08.2024 bei der Technischen Universität München eingereicht und durch die TUM School of Life Sciences am 11.02.2025 angenommen.

Acknowledgments

As I conclude this chapter of my life, I would like to extend my heartfelt gratitude to those who have guided and accompanied me on this journey.

First and foremost, a huge thank you to my supervisor, Dr. Torsten Hechler. I couldn't have asked for a more supportive mentor. Your invaluable insights into my project and our scientific discussions have helped me grow both as a researcher and as a person. Thank you for always listening and supporting me through both the good and the challenging times. I am immensely grateful, and I will carry your teachings with me throughout my career.

I also want to express my deep appreciation to Prof. Dr. Andreas Pahl for giving me the opportunity to conduct this research at Heidelberg Pharma and for guiding me throughout this journey. Your mentorship has taught me to approach scientific projects from multiple angles, fostering a broader perspective. Thank you for your invaluable feedback and for always maintaining a positive outlook on science.

My gratitude extends to Prof. Dr. Arne Skerra for allowing me to learn new techniques and conduct new scientific research within his group. Thank you for the valuable feedback on my project and for challenging my critical thinking and ideas on different scientific topics. I am also grateful to your lab group for welcoming me and engaging in scientific discussions and idea-sharing during my visit at TUM.

I would also like to thank Dorothée Fraleux and Dr. Guilhem Chaubet for their coordination, organization, and support within the TACT European consortium. Furthermore, I am grateful to the European Commission for funding this project and enabling its successful realization.

Additionally, I want to thank the Biochemistry Department at Heidelberg Pharma for their support and assistance in designing laboratory experiments. A special thank you to Dr. Andreas Pelz for your witty and positive humor, which always helped me see the bright side of every situation. Thank you for our scientific discussions, the ideas we shared, and for encouraging me to think outside the box. Thank you for your daily support during these challenging years.

My gratitude also goes to the Chemistry Department at Heidelberg Pharma, which adopted and guided me during my synthesis work. A special thank you to Francesca Gallo for your support, for helping me understand how to perform chemical reactions, for clarifying my doubts, and for being my office friend. Thank you for the knowledge and insights you shared with me. Grazie per avermi supportato e sopportato in questi anni e per aver condiviso con me gioie, paure e tristezze tutti i giorni in ufficio e fuori. Mi mancherai.

I would also like to extend a huge thank you to the *in vivo* department and especially to Dr. Hélène Willer for guiding and supporting me in the design of the *in vivo* experiments and for always being so helpful.

I want to express my immense gratitude to my lab pals, Elena, Daniela, and Pablo. You have been my work family, providing support, sharing laughs, tears, chats, and even the occasional disagreements. Thank you for enriching this experience and sharing this adventure with me!

I also want to thank the wonderful people I met in Heidelberg who have become valuable friends: Caterina, Georgia, Federica, and Giulia. Your friendship has meant so much to me.

Thanks to all the fellow students in the network with whom I shared meaningful experiences and from whom I learned and expanded my scientific knowledge. Special thanks to Ana, Rania, Yağmur, Lorenzo, Bianka, Ilias, Thomas, Léa, Irene, and Loïc.

To Elena, Luca, Bianca, Andrea, Gianluca, Varvara, Giulia, Giorgia, Viviana, Davide, Silvia, and Matteo: thank you for your support, your friendship, and for being there for me, even from afar. Thank you for always believing in me!

To my family and especially to my parents, Mauro and Roberta, for the love and the support they always showed me, for believing in me, for teaching me the values of perseverance and to never give up. Grazie per avermi sempre sostenuto, per avermi insegnato quali valori sono importanti, per avere sempre creduto in me e per tutte le volte che non vedevo la via d'uscita e mi avete aiutato a trovare la strada.

Table of Contents

1 INTRODUCTION 1

1.1 Cancer: Traditional and Emerging Therapies 1

1.1.1 Traditional Cancer Therapies 1

1.1.2 Emerging Cancer Therapies 2

1.2 Antibody Drug Conjugates (ADCs) 3

1.2.1 ADC therapies on the market 5

1.2.2 Mechanisms of ADC toxicities 7

1.2.3 Target antigen 10

1.2.4 Antibody 11

1.2.5 Linker 12

1.2.6 Conjugation 13

1.2.7 Payload 16

1.3 Amanitin and Amatoxin-based ADCs (ATAC®s) 18

1.4 Bioorthogonal „Click“ Chemistry 20

2 AIM OF THE STUDY 24

3 MATERIAL AND METHODS 25

3.1 Material 25

3.1.1 Laboratory equipment 25

3.1.2 Consumables 26

3.1.3 Chemicals and solutions 27

3.1.4 Kits 29

3.1.5 Buffers 29

3.1.6 Cell culture media 30

3.1.7 Bacterial culture media 30

3.1.8 Enzymes 30

3.1.9 RT-PCR Primers 30

3.1.10 Antibodies and protein conjugates 30

3.1.11 Cell lines 31

3.1.12 Amanitin derivatives 32

3.1.13 Neutralizing compounds 34

3.1.14 Mouse strains 35
3.1.15 Software 35

3.2 Methods 36
3.2.1 Chemical synthesis of amanitin clicked compounds 36
3.2.2 RNA polymerase II Inhibition assay 42
3.2.3 Cell Culture 44
3.2.4 Cytotoxicity assay 45
3.2.5 Antibody cloning and expression 46
3.2.6 SEC-HPLC 48
3.2.7 Endotoxin assay 48
3.2.8 Antibody conjugation 49
3.2.9 SDS-PAGE 50
3.2.10 Western Blot 50
3.2.11 Free-amanitin competitive ELISA 50
3.2.12 *In vivo* studies 51
3.2.13 Cell line-derived xenograft (CDX) mice models 52
3.2.14 Determination of the maximum tolerated dose 52
3.2.15 Co-administration studies with the ADC and the neutralizing agents 53
3.2.16 Efficacy studies in CDX mice 53
3.2.17 Histopathological and Biodistribution studies 53
3.2.18 Organs and tumor preparation for the ELISA assays 54
3.2.19 Azido-ADC ELISA 54
3.2.20 Total ADC ELISA 55
3.2.21 Statistical analysis 56

4 RESULTS 58

4.1 Generation of neutralized amanitin compounds and their *in vitro* bioactivity 58
4.1.1 Generation of neutralized amanitin compounds 58
4.1.2 Cytotoxicity of the neutralized compounds on HEK293-OATP1B3 cells 60
4.1.3 Impact of the neutralizing reaction on RNA polymerase II activity 65

4.2 Generation of new azido-amanitin ADCs and *in vitro* evaluation 68
4.2.1 Thiol-bromoacetamide conjugation to a Trastuzumab-based THIOMAB™ 69
4.2.2 Cytotoxicity of N-azido-ADC and W-azido-ADC on HER2-positive and HER2-negative cell lines 73

4.3 *In vitro* evaluation of the neutralization strategy for the azido-ADC treatment ……76

4.3.1 Impact of BCN-PEG_6-OH (6) and DBCO-PEG_4-COOH (7) on N-azido-ADC treatment of JIMT-1 HER2-positive cells 76

4.4 Development of an N-azido-ADC ELISA to detect N-azido-ADC in tissue 79

4.4.1 Establishment of a new azido-ADC ELISA 79

4.5 The neutralizing effect of BCN-PEG_6-OH (6) and DBCO-PEG_4-COOH (7) on the tolerability of N-azido-ADC *in vivo* 83

4.5.1 Analysis of the maximum tolerated dose of N-azido-ADC 83

4.5.2 Tolerability of N-azido-ADC after administration of the neutralizing compounds ……84

4.5.3 Evaluation of N-azido-ADC in plasma and comparison of Strain-promoted azido-alkyne Cycloaddition (SPAAC) efficiency with BCN-PEG_6-OH (6) or DBCO-PEG_4-COOH (7) 85

4.6 The influence of DBCO-PEG_4-COOH (7) administration at different timepoints on N-azido-ADC tolerability 87

4.6.1 Effects of administration of DBCO-PEG_4-COOH (7) at different timepoints on the tolerability of a lethal dose of N-azido-ADC 88

4.7 Histopathological analysis of liver and kidney tissues following N-azido-ADC treatment and administration of DBCO-PEG_4-COOH (7) 90

4.7.1 The Impact of DBCO-PEG_4-COOH (7) administration following N-azido-ADC treatment on liver and kidneys 91

4.7.2 Histopathological findings in liver tissue 92

4.7.3 Histopathological findings in kidney tissues 94

4.8 The impact of DBCO-PEG_4-COOH (7) administration on N-azido-ADC tumor efficacy 96

4.8.1 N-azido-ADC efficacy in JIMT-1 CDX model 97

4.8.2 Impact of DBCO-PEG_4-COOH (7) administration on the tumor efficacy of N-azido-ADC in JIMT-1 CDX model 98

4.8.3 Biodistribution of N-azido-ADC and total ADC in JIMT-1 CDX female NMRI nude mice ……..101

4.9 Application of the neutralization strategy in a difficult-to-treat prostatic tumor model ……..105

4.9.1 Generation and characterization of PSMA-azido-ADC and PSMA-ADC 106

4.9.2 Cytotoxicity of PSMA-azido-ADC and PSMA-ADC on PSMA-positive and -negative cell lines 108
4.9.3 Maximum Tolerated Dose (MTD) of PSMA-azido-ADC and PSMA-ADC in tumor-bearing mice 110
4.9.4 Lethal doses of PSMA-azido-ADC and additional DBCO-PEG$_4$-COOH (7) treatment in 22RV1 CDX in male NMRI nude mice 110
4.9.5 Efficacy study of PSMA-azido-ADC with additional DBCO-PEG$_4$-COOH (7) treatment in 22RV1 CDX male NMRI nude mice 113

5 DISCUSSION 116

5.1 *In vitro* activity of the azido-amanitin compounds after SPAAC reaction with the neutralizing agents 118

***5.2* *In vitro* characterization of Azido-amanitin ADCs on target-positive cell lines 121**

5.3 Impact of the neutralization on ADC tolerability 123

5.4 Preserving tumor efficacy while enhancing tolerability through the neutralization strategy 127

5.5 Future directions 130

6 ABSTRACT 133

7 ZUSAMMENFASSUNG 135

8 ABBREVIATIONS 137

9 BIBLIOGRAPHY 140

1 Introduction

1.1 Cancer: Traditional and Emerging Therapies

Cancer is a major global cause of death (Bray et al. 2021). In 2022, the Global Cancer Observatory (GCO) recorded 9,7 million deaths attributed to cancer and 20 million new cases reported worldwide. The prevalent cancers in men include lung cancer (15.2%), prostate cancer (14.2%), and colorectal cancer (10.4%). Whereas, for women, breast cancer (23.8%), lung cancer (9.4%), and colorectal cancer (8.9%) exhibit the highest incidence rates (Bray et al. 2022).

Cancer is a complex and diverse condition characterized by many genomic and molecular changes that trigger uncontrollable cell growth and proliferation, rapidly accumulating tissue mass in affected body areas. In contrast to the normal process where cells receive signals to undergo programmed cell death and be replaced by healthier counterparts, cancer cells utilize the body's oxygen and nutrients, disrupting the regular supply to surrounding cells and impeding normal growth processes. Additionally, these cancerous cells can manipulate their microenvironment, evade the body's immune system, and exploit neighboring cells' physiology to meet their nutritional and growth requirements (Hanahan and Weinberg 2000; Costa et al. 2014; Laplagne et al. 2019). The intricate diversity and complexity of cancer, coupled with the identification of distinct pathways within each tumor, necessitates the advancement of more potent and precise therapies capable of surpassing the limitations of traditional cancer treatments.

1.1.1 Traditional Cancer Therapies

Traditional cancer therapies include chemotherapy, surgery, and radiotherapy, often combined to reduce recurrence risks. The term "chemotherapy" traces back to Paul Ehrlich, who coined it in the early 20th century, defining it as a chemical treatment approach to fight diseases (DeVita and Chu 2008). The first chemotherapeutic agents, derived from mustard gas, displayed benefits in treating lymphoma patients in the 1940s, leading to the synthesis of new agents like cisplatin and doxorubicin, hindering DNA double-strand generation and cell division. Alkylating agents, including cisplatin, are widely used across cancer types due to their effectiveness in inhibiting cancer growth (Kondo et al. 2010). Along with chemotherapy, radiation therapy pioneered by Röntgen and Curie in the 19th century, has been used for more than 100 years in cancer therapy and evolved with modern techniques like four-dimensional conformal radiotherapy and radiogenic

therapy (Arruebo et al. 2011). While chemotherapy and radiotherapy have shown initial efficacy in treating cancer, they are not capable of only targeting cancer cells but reach tissues of the whole body, leading to off-target toxicity and severe side effects. These side effects may include fatigue, depression, hair loss, toxicity in vital organs, and cognitive impairment. Additionally, the rapid development of tumor heterogeneity and adaptation to these therapies can result in drug resistance and accelerated drug metabolism (Luqmani 2005; Bower 2014; Altun and Sonkaya 2018). Given the challenges in tumor treatment, personalized targeted therapies are experiencing significant growth as alternatives to traditional treatments.

1.1.2 Emerging Cancer Therapies

The understanding of different cancer pathways, the identification of specific markers, and the improvement of diagnostic procedures for early-stage cancer detection have paved the way for developing more personalized and targeted cancer therapies. These new therapies include gene therapies, photodynamic therapies, nanocarrier therapy, stem cell therapy, targeted therapy, and immunotherapy. Among these therapies, cancer immunotherapies have obtained promising results in treating and even curing specific types of cancers. Immunotherapies activate or amplify the immune system's natural mechanisms to target and attack cancer cells, addressing evasion tactics employed by cancer during disease progression. Part of this category are cytokine treatments applied directly within the tumor mass, monoclonal antibodies (mAbs) that target immune checkpoint inhibitors (PD-1 and CTL4), cancer vaccines and CAR-T therapies (Riley et al. 2019). CAR-T cells, a groundbreaking immunotherapy, have gained attention for their clinical successes and accelerated Food and Drug Administration (FDA) approvals. In this approach, patient T cells are genetically engineered to express Chimeric Antigen Receptors (CARs) specific to tumor antigens, offering a one-time therapy with prolonged activity (Lim and June 2017). Another way to promote T cell activity against tumors is with the use of bispecific antibodies that target an antigen on the tumor surface and at the same time engage specific receptors on T cells (Klein et al. 2024). Other therapies that involve the use of antibodies include treatments with mAbs, e.g. Trastuzumab or Cetuximab, which bind to growth factor receptor signaling, blocking their activation, and causing tumor cell death (Zahavi and Weiner 2020). Furthermore, mAbs can also be used as targeted therapy conjugated to chemotherapeutic agents, generating the so-called Antibody Drug Conjugates (ADCs). ADCs can specifically deliver the toxin to tumor cells, sparing healthy tissues (Hafeez et al. 2020).

1.2 Antibody Drug Conjugates (ADCs)

In 1907, Paul Ehrlich coined the term “magic bullet”, referring to the need of a “*chemotherapia specifica*”, a specific chemical therapy that could target and kill certain parasites, sparing healthy tissues from damages (Ehrlich 1907). From the work of Paul Ehrlich and the development of a hybridoma technology for the production of monoclonal antibodies (mAbs), the research on the generation of new targeted therapies such as Antibody drug conjugates (ADCs) started to grow (Strebhardt and Ullrich 2008). ADCs represent the bridging gap between mAbs and chemotherapy, fusing the specificity of a targeted therapy to the potency of a chemotherapeutic drug.

The primary advantage of using targeted therapies like ADCs is their ability to enhance the therapeutic index of a treatment compared to conventional small-molecule drug. The therapeutic index (TI) is a parameter used to assess the safety of a drug. It is calculated as the ratio of the maximum tolerated dose (MTD) and the minimum effective dose (MED) of a specific treatment. The MTD and MED also define the therapeutic window, which is the dosage range or concentration of a drug within a bodily system that ensures both safety and effectiveness in therapy. The larger the TI, the safer the drug. Small molecule chemotherapies typically exhibit high efficacy but possess a low TI (TI=1) and a narrow therapeutic window. Conversely, with ADCs, the TI increases (TI>1), resulting in a wider therapeutic window (**Figure 1**) (Tamargo et al. 2015; Tarcsa et al. 2020).

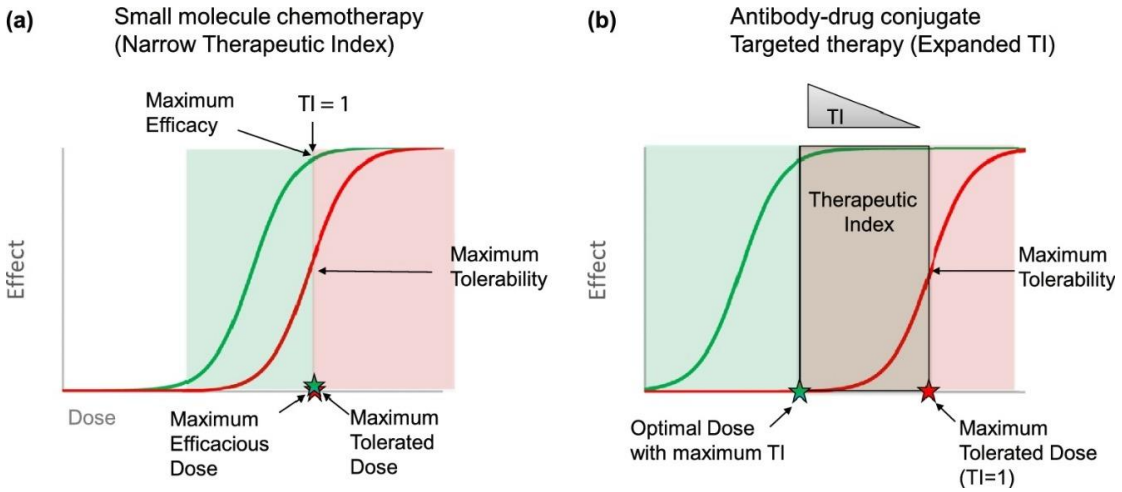

Figure 1: Schematic representation of proposed improvement in therapeutic window by targeted therapies, like ADCs*. (A) small molecule chemotherapy TI. (B) Antibody-drug conjugates TI. Reproduced from Edit Tarcsa, Magali R. Guffroy, Hadi Falahatpisheh, Colin Phipps, John C. Kalvass, Antibody-drug conjugates as targeted therapies: Are we there yet? A critical review of the current clinical landscape, Drug Discov. Today: Technol., 37, 13-22 (2020). Reproduced with permission from Springer Nature.*

ADCs consist of an antibody, that recognizes the target antigen expressed on cancer cells, and a cytotoxic payload, e.g. a chemotherapeutic drug, conjugated via a chemical linker to the antibody (**Figure 2**). The antibody usually comprises a fragment crystallizable (Fc) region, where normally the payload is conjugated and a Fragment antigen-binding (Fab) region which recognizes the antigen expressed on tumor cells (Hafeez et al. 2020).

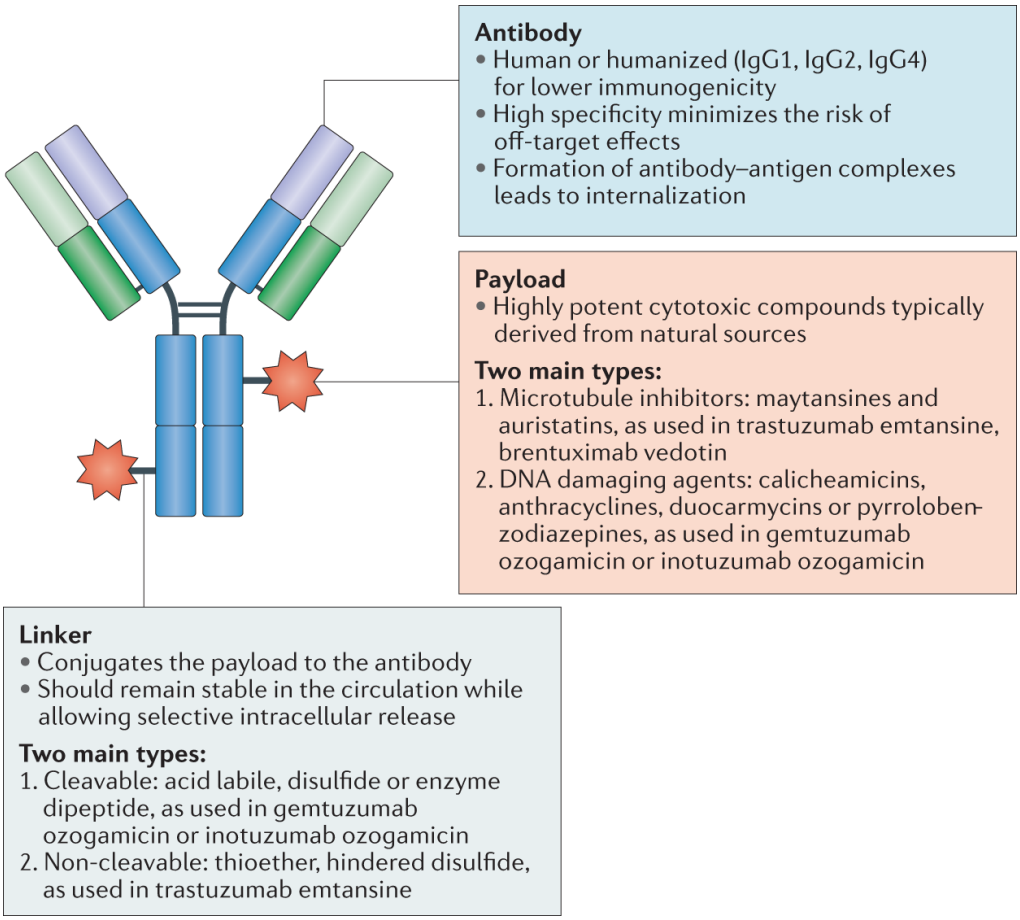

Figure 2: Antibody-drug conjugate constructs. *Reproduced from Jabbour, E., Paul, S. & Kantarjian, H. The clinical development of antibody–drug conjugates — lessons from leukaemia. Nat Rev Clin Oncol 18, 418–433 (2021). Reproduced with permission from Springer Nature.*

ADCs exhibit a synergistic mechanism by precisely targeting cancer cells and efficiently inducing cell death, while minimizing off-target side effects. The primary mechanism of action of the ADC starts with the binding of the Fab region of the antibody to the antigen target expressed on cancer cells. After that, the ADC is internalized/endocytosed in an early endosome by the cells. The early endosome matures into a late endosome, which is then fused with lysosomes, resulting in cell apoptosis/death caused by the activity of the cytotoxic payload (Fu et al. 2022). If the payload is hydrophobic and cell membrane permeable, it can also induce a diffusion-driven bystander effect and kill nearby non-targeted tumor cells, increasing the efficacy of the ADC therapy (Staudacher and Brown

2017). Moreover, certain ADCs have the potential to indirectly stimulate components of the host immune system by engaging the Fc region, which binds to specific Fc receptors (FcR) on the surface of effector cells like macrophages and Natural Killer (NK) cells. This so-called effector function, results in complement-dependent cytotoxicity (CDC), antibody-dependent cellular phagocytosis (ADCP), and antibody-dependent cellular cytotoxicity (ADCC), amplifying the killing effect on tumor cells (**Figure 3**) (Zahavi and Weiner 2020).

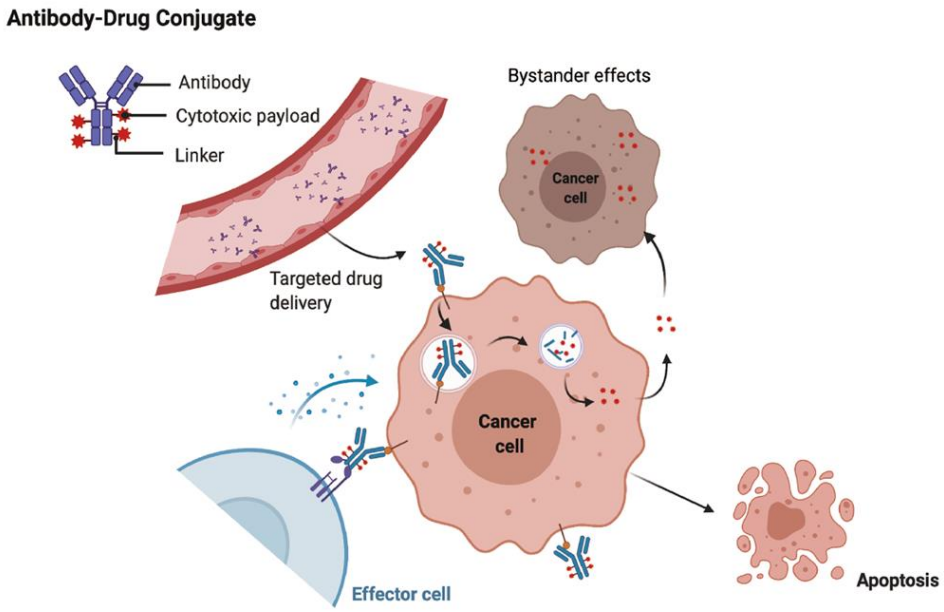

***Figure 3: Mechanisms of action of an ADC**. Adapted from Z. Fu, S. Li, S. Han, C. Shi, and Y. Zhang, "Antibody drug conjugate: the 'biological missile' for targeted cancer therapy," Signal Transduction and Targeted Therapy 2022 7:1, vol. 7, no. 1, pp. 1–25, 2022, open access article distributed under the terms of Creative Commons CC BY*

1.2.1 ADC therapies on the market

The first ADC on the market was Mylotarg®, approved in 2000 by the US Food and Drug Administration (FDA) for the treatment of acute myeloid leukemia (AML). In the 24 years since then, 260 ADCs have entered clinical trials, but only 14 new ADCs have been approved (**Table 1**) (Maecker et al. 2023).

Although ADC therapy showed promising results in patients, their clinical development has encountered a substantial rate of failure, primarily due to the persisting challenge of off-site toxicity in healthy organs. The risk of off-site toxicity and side effects restricts the tolerable ADC doses to levels below those necessary for significant anti-cancer efficacy (Donaghy 2016).

***Table 1**: ADCs approved by the FDA as of October 2023.* *(Maecker et al. 2023)*

Drug	Trade name	Manufacturer	Target	Payload	Indication	Approval Year
Gemtuzumab ozogamicin	Mylotarg	Pfizer/Wyeth	CD33	Calicheamicins	relapsed acute myelogenous leukemia (AML)	2000, 2017
Brentuximab vedotin	Adcetris	Seattle Genetics, Millennium/Takeda	CD30	Monomethyl auristatin E (MMAE)	relapsed HL and relapsed sALCL	2011
Trastuzumab emtansine	Kadcyla	Genentech, Roche	HER2	Maytansinoid (DM1)	HER2-positive metastatic breast cancer (mBC)	2013
Inotuzumab ozogamicin	Besponsa	Pfizer/Wyeth	CD22	Calicheamicins	CD22-positive B-cell precursor acute lymphoblastic leukemia	2017
Moxetumomab pasudotox	Lumoxiti	Astrazeneca	CD22	Pseudomonas exotoxin (PE38)	hairy cell leukemia (HCL)	2018
Polatuzumab vedotin	Polivy	Genentech, Roche	CD79	MMAE	diffuse large B-cell lymphoma (DLBCL)	2019
Enfortumab vedotin	Padcev	Astellas/Seattle Genetics	Nectin 4	MMAE	urothelial cancer	2019
Trastuzumab deruxtecan	Enhertu	AstraZeneca/Daiichi Sankyo	HER2	Deruxtecan	HER2-positive breast cancer	2019
Sacituzumab govitecan	Trodelvy	Immunomedics	TROP2	SN-38	triple-negative breast cancer (mTNBC)	2020
Belantamab mafodotin	Blenrep	Glaxo Smith Kline (GSK)	BCMA	Maleimidocaproyl monomethyl auristatin F (mcMMAF)	multiple myeloma	2020 Discontinued in 2022
Cetuximab saratolacan	Akalux	Rakuten Medical	EGFR	IRDye700DX (Photosensitizer)	Head and neck cancer	2020
Loncastuximab tesirine-lpyl	Zynlonta	ADC Therapeutics	CD19	Pyrrolobenzodiazepine (PBD) dimer	Large B-cell lymphoma	2021
Disitamab vedotin	Aidixi	RemeGen	HER2	MMAE	HER2+ gastric carcinoma	2021
Tistotumab vedotin-tftv	Tivdak	Seagen	TF	MMAE	Cervical cancer	2021
Mirvetuximab soravtansine-gyxn	ELAHERE	ImmunoGen, Inc.	FRα	Maytansinoid (DM4)	Ovarian Cancer	2022

Common ADC-specific toxicities that have been documented in clinical trials involve hepatotoxicity, neutropenia (low levels of neutrophils in the blood), thrombocytopenia (low levels of platelets in the blood), bleeding, ocular toxicity, peripheral neuropathies, fatigue,

gastrointestinal symptoms, and cardiotoxicity. Moreover, treatment-related deaths during clinical trials were registered for Gemtuzumab Ozogamicin (17.1 % patients), Brentuximab Vedotin (1%), Inotuzumab Ozogamicin (2.9%), Loncastuzumab Tesirine (1.4%) and Polatuzumab Vedotin (3%). The majority of adverse events and death-derived toxicities were caused by the intrinsic toxicity of the payload and the poor stability of the chemical linker that connects the payload to the antibody (Johns and Campbell 2022). At present, a significant proportion of ADC treated patients necessitate supportive interventions to mitigate the severity of ADC-associated toxicities of the approved ADCs. Additionally, a considerable number of patients require dose reduction, encounter treatment delays, or face treatment discontinuation (Wolska-Washer and Robak 2019). Therefore, the analysis of ADC-related toxic mechanisms can help in the development of improved ADCs with reduced side effects and increased therapeutic index.

1.2.2 Mechanisms of ADC toxicities

It is estimated that only approximately 0.1% of the injected dose of an ADC reaches the targeted diseased cell population, while the majority of the administered dose is metabolized "off-site" within non-targeted healthy cells, potentially resulting in undesired toxicities. Current findings from Zhu et al. indicate that the majority of ADC toxicity stems from the delivery of the cytotoxic payload to unintended sites (Zhu et al. 2023). Such off-site ADC toxicity can be classified as "on-target", when the ADC binds to the targeted cell surface protein on healthy cells, or "off-target", when the antigen-ADC binding is not directly involved. The extent of ADC-induced toxicities may be influenced by each component of the ADC, including the antibody, linker, and payload (Nguyen 2023).

The payload delivery to healthy cells significantly influences the tolerability of ADCs and determines the recommended doses for patients (Zhu et al. 2023). **Figure 4** shows an example of the principal mechanisms of ADC toxicities. Unwanted toxicity in healthy cells can be caused by the premature release of the payload in systemic circulation, due to poor linker stability. This happens most frequently with the use of cleavable linkers, which incorporate chemical or enzymatic functionalities designed to exploit specific conditions unique to the intracellular or extracellular tumor environments (Lu et al. 2016). Factors that influence linker stability include sensitivity to serum proteases, instability at neutral pH and transfer to serum proteins, such as the retro-Michael maleimide transfer to thiols of plasma proteins (Alley et al. 2008; Dokter et al. 2014; Lu et al. 2016). Most payloads in marketed ADCs are lipophilic and produce a diffusion-driven bystander effect when they are released in tumor cells by permeating the cell membrane and enhancing anti-tumor efficacy against tumor cells that do not express the target. Premature release of such

payloads may lead to passive diffusion through the membranes of healthy cells, potentially resulting in off-target toxicity (Staudacher and Brown 2017).

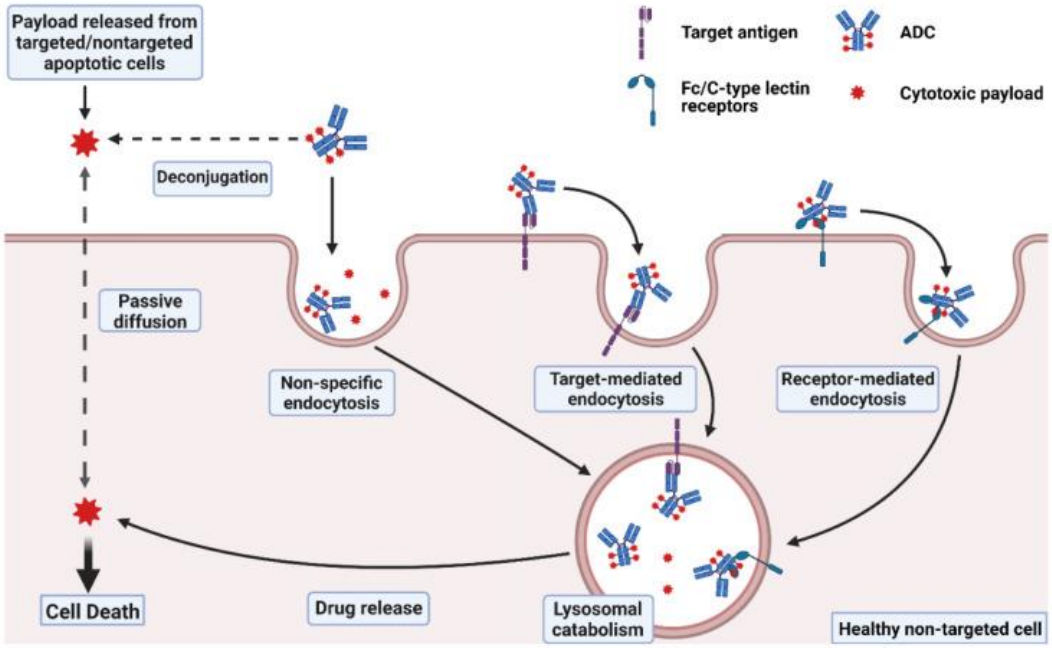

Figure 4: Mechanisms of ADC toxicity. *Image adapted from Nguyen TD, Bordeau BM, Balthasar JP. Mechanisms of ADC Toxicity and Strategies to Increase ADC Tolerability. Cancers (Basel). 2023 Jan 24;15(3):713. open access article distributed under the terms of Creative Commons CC BY.*

Moreover, off-target delivery of payload may also occur through nonspecific endocytosis of intact ADCs. This process can be influenced by the physicochemical properties of ADCs, such as hydrophobicity and charge. Given that the drug-linker compositions commonly used in ADC technology are typically highly lipophilic, the hydrophobicity of ADCs often correlates with the drug loading (i.e., drug-to-antibody ratio, DAR). It has been shown that ADCs with a high DAR and hydrophobic payloads have generally lower tolerability and are prone to aggregation and accelerated clearance (Lyon et al. 2015). Furthermore, it has been demonstrated that monoclonal antibodies and ADCs with a positive charge show heightened uptake in the liver, undergoing increased charge-mediated endocytic uptake (Zhao et al. 2018; Liu et al. 2021). Target-independent uptake can also be mediated by several receptors, e.g. Fc gamma receptors (FcγRs) or C-type lectine receptors (CLRs) that recognize the Fc region of the antibody. FcγRs are some of the most extensively studied endocytic cell surface receptors and play a crucial role not only in mediating the effector functions of IgG antibodies but also in facilitating the internalization and clearance of IgG-opsonized antigens from the systemic circulation (Zhu et al. 2016b). As FcγRs are expressed on megakaryocytes, platelets, and hematopoietic

stem cells, the non-specific uptake of ADCs mediated by this receptor can lead to hematotoxicities, such as thrombocytopenia (Uppal et al. 2015).

Off-target toxicity can also result from binding of the N-linked glycosylation sites of the Fc region of the antibody to the CLRs. N-glycosylation is a post-translational modification that involves the Asn297 residue on the Fc region of the antibody. This modification is important to retain binding to FcγR and activate the effector function of the ADCs. Modification of the glycosylation profile of the antibody can affect the structure and binding to the CLRs affecting pharmacokinetic and tolerability of the ADC (Boune et al. 2020). Specifically, the uptake of ADCs by Mannose receptors (MR), a subtype of CLRs, in the liver may contribute to hepatotoxicity (Gorovits and Krinos-Fiorotti 2013).

Fc neonatal receptors (FcRn) are other types of receptors recognizing the Fc region of the antibody. They play a critical for the recycling of the antibodies after internalization back to the extracellular space, protecting them from lysosomal degradation and extending their half-life in circulation. FcRn is expressed on the epithelial cells of several tissues, e.g. liver, kidney, skin and on hematopoietic cells such as dendritic cells, macrophages, monocytes, differentiating hematopoietic cells as well as on endothelial cells of the vascular tissues (Akilesh et al. 2007; Latvala et al. 2017). ADCs are internalized in acidic early endosomes by cells expressing FcRn. Subsequently, FcRn-ADC complexes are directed into recycling endosomes to avoid lysosomal degradation and are recycled back to the cell surface. This process allows the release of ADCs at neutral pH into the extracellular space or systemic circulation. If the ADC loses its binding to FcRn, it is directed to lysosomes for degradation, potentially releasing the payload in healthy tissues (Akilesh et al. 2007). Hence, modifying FcRn binding of ADCs could be a promising strategy to mitigate undesired toxicity or adverse events in normal cells with significant FcRn expression.

While evidence indicates that off-target mechanisms are the primary drivers of ADC toxicities, the binding of ADCs to target antigens expressed in healthy tissues also contributes to significant toxicities. On-target toxicity can be predicted to a certain degree if information about the expression of the target in healthy tissues is available. However, this proved to be challenging as several parameters can influence the translation of target expression to a dose-limiting toxicity, including the biodistribution of the ADC and its exposure in different tissues, the specific linker and drug of the ADC, and the particular cell types expressing the target (Damelin et al. 2015).

To reduce off-target and on-target toxicities and enhance the tolerability and efficacy of ADC therapies, careful selection of tumor target antigens and optimization of the three key components of an ADC - antibody, linker, and payload - are essential.

1.2.3 Target antigen

The target antigen is the extracellular structure on the membrane of tumor cells recognized by the antibody part of an ADC that mediates its internalization. Ideally, the target antigen should be expressed exclusively on the cell surface of tumor cells, grant endocytosis of the ADC, and should not be secreted in circulation (Fu et al. 2022). The current ADCs on the market target specific proteins that are overexpressed in cancer cells. These include HER2, Trop-2, Nectin-4, and EGFR on solid tumors,, and CD19, CD22, CD33, CD30, BCMA, and CD79b in hematological malignancies (Beck et al. 2017). However, expression of some of these targets has been found also on healthy tissues, causing on-target toxicities. In clinical trials, Enfortumab Vedotin, an anti-Nectin-4 ADC approved for the treatment of metastatic urothelial cancer, induced altered taste perception (dysgeusia) in 40% of patients and skin rash in 22% of patients. These effects were attributed to the expression of the target Nectin-4 on skin cells and salivary gland cells (Alt et al. 2020). Trastuzumab-based ADCs exhibited cardiotoxicity attributed to the expression of HER2 in cardiomyocytes (McKeage and Perry 2002; Sysa-Shah et al. 2012; Johns and Campbell 2022).

A principal aspect to consider in the selection of an antigen target is, therefore, the level of expression in cancer cells compared to healthy tissues, which can impact not only the safety of the therapy but also biodistribution and efficacy. This is particularly crucial in the context of solid tumors. For hematological malignancies, target overexpression may not be as critical to achieve a therapeutic window with the ADC, likely due to the continuous turnover of the normal hematological compartment. Even if normal blood cells are depleted, they are consistently replenished by hematopoietic stem cells (HSCs). However, evaluating antigen expression on HSCs is vital, especially if the drug affects non-proliferative cells (Damelin et al. 2015).

A tool to analyze target expression in the different tissues can be the comparison of mRNA expression from different databases that offer data form RNA sequencing such as The Cancer Genome Atlas (TCGA) and the Gene-Tissue expression (GTEx) (Lonsdale et al. 2013; Weinstein et al. 2013). These data can be complemented to Mass spectrometry based-proteomic approaches, which can provide information on abundance and copy number of a protein and alternative splicing, post-transcriptional regulation, post-translational modification and regulation of trafficking to the cell surface (Damelin et al. 2015). Using these tools and learning from past clinical trials can help to predict side-effects and to regulate dose-administration accordingly.

1.2.4 Antibody

The antibody moiety plays a critical role in facilitating specific binding between the target antigens and the ADC. An ideal antibody moiety should possess a specific high binding affinity to the target, promote efficient internalization, exhibit low immunogenicity, and maintain a long plasma half-life (Fu et al. 2022). Antibodies utilized in ADC drugs primarily belong to the immunoglobulin G (IgG) class, the predominant component of immunoglobulins in serum encompassing four subtypes: IgG1, IgG2, IgG3, and IgG4. Among these, IgG1 is the most commonly used subtype for ADCs due to its ability to elicit potent effector functions, CDC, ADCP and ADCC, through high binding affinity to Fc receptors (Natsume et al. 2009). However, the effector function is not always desirable in an ADC therapy. For example, Trastuzumab is a monoclonal antibody belonging to the IgG1 subclass that targets HER2 and inhibits the activation of HER2 signaling pathway, while also engaging in the ADCC function, which enhances the anti-tumoral efficacy of Trastuzumab treatment. However, treatment with Trastuzumab emtansine, a Trastuzumab-based ADC bearing the microtubule inhibitor DM1, resulted in drug-driven thrombocytopenia in patients during clinical trials. This thrombocytopenia occurred due to binding of the antibody to FcγRIIa on megakaryocyte progenitors, affecting platelet production (Uppal et al. 2015). To avoid such kind of off-target toxicity, the effector function of IgG1 can be silenced via mutation in different sites of the Fc region of IgG1 like E233P, L234V and/or L235A (McDonagh et al. 2008). The anti-HER2 ADC MEDI4276, now in a Phase I clinical trial has three mutations on the Fc region that reduce binding to FcγR (E234F, S239C and S442C) to diminish thrombocytopenia (Pegram et al. 2021).

Another way to eliminate the ADCC effect is to use different IgG isotypes like IgG2 and IgG4 which are limited by nature in their effector function (McDonagh et al. 2008). IgG4 has been used for Gemtuzumab ozogamicin, Inotuzumab ozogamicin and Indatuximab ravtansine, while IgG2 was used for glembatumumab vedotin and ASG-5ME (Beck et al. 2017).

The Fc region of the antibody also plays an important role in the half-life of the ADC. The half-life of ADCs exhibits significant variation and is influenced by the recycling pathway mediated by the FcRn. While a longer half-life allows the ADC to accumulate in the tumor and increase tumor efficacy, the prolonged circulation heightens also the risk of ADC uptake in healthy tissues, potentially causing off-target toxicity (Hedrich et al. 2018; López de Sá et al. 2023).

1.2.5 Linker

The linker in ADCs serves to connect the antibody with the cytotoxic drug, playing a crucial role in maintaining the stability of the ADC and regulating payload release. It significantly influences the therapeutic index of ADCs by regulating payload stability in circulation and payload release exclusively within target cells. An ideal linker should prevent ADC aggregation, minimize premature payload release in plasma, and facilitate active drug release at targeted sites. ADC drugs utilize two types of linkers—cleavable and non-cleavable—depending on their metabolic fate within cells (Fu et al. 2022). Acid labile linkers exploit the acidic environment in the endosome (pH 5.5-6.2) and in the lysosome (pH 4.5-5.0) to release the payload. An example of acid labile linker is the hydrazone linker used in gemtuzumab ozogamicin (Mylotarg®) and inotuzumab ozogamicin (Besponsa®) (Bargh et al. 2019). However, studies revealed that the hydrazone linker lacks stability in plasma at pH 7.4 and can hydrolyze, potentially causing off-target toxicity. Consequently, this type of linker has been discontinued from use (van der Velden et al. 2001).

The disulfide bond-based linker is another chemically sensitive cleavable linker, susceptible to reductive glutathione (GSH). GSH is vital for cell survival, proliferation, and maintaining intracellular redox balance. While blood GSH concentration is relatively low, cancer cells exhibit elevated GSH levels. Consequently, this linker type remains stable in the bloodstream but selectively releases active payloads in cancer cells with heightened GSH levels (Estrela et al. 2006; Bargh et al. 2019). This type of linker has also been employed for maytansinoid-derived ADCs like huC242-SPDB-DM4 (Sheyi et al. 2022).

Peptide-cleavable linkers have been used in most of the ADCs that reached clinical trials. These linkers are designed to be sensitive to intracellular proteases, such as Cathepsin B, which recognize specific dipeptide motifs, ultimately facilitating payload release. An example of dipeptides recognized by Cathepsin B are valine–citrulline (Val–Cit) and phenylalanine–lysine (Phe–Lys) (Gondi and Rao 2013). Most of the monomethyl auristatin E (MMAE) conjugated ADCs use the Val-Cit linker. However, the Val-Cit linker showed instability in plasma and premature payload release led to specific toxin-derived toxicities such as neutropenia, thrombocytopenia, and peripheral neuropathy (Donaghy 2016). To improve the linker stability in plasma, the Val-Ala linker was generated, a less hydrophobic linker with higher plasma stability using an alanine residue instead of the citrulline (Sheyi et al. 2022).

Alternatively, a distinct enzyme-sensitive linker has been engineered to respond to the lysosomal enzyme β-glucuronidase. This β-glucuronidase-cleavable linker allowed the generation of highly loaded ADCs with a DAR of 8, displaying reduced aggregation, thanks

to the hydrophilicity of the β-glucuronic acid component within the linker (Bargh et al. 2019).

To prevent toxicity resulting from premature payload release in circulation, non-cleavable linkers have been developed, demonstrating superior tolerability compared to cleavable linkers in *in vivo* studies. Non-cleavable linkers can be divided in two groups, the thioether and maleimidocaproyl (MC) linkers. Both require the degradation of the antibody in the lysosome to release the payload. An advantage of non-cleavable linkers is their stability in circulation. One example of a marketed ADC with non-cleavable linker is Trastuzumab emtansine (Kadcyla®), where the DM1 payload is conjugated via an SMCC (N-succinimidyl-4-(maleimidomethyl) cyclohexane-1-carboxylate) linker to lysines (Sheyi et al. 2022). Belantamab mafodotin-blmf (Blenrep®) is alongside Kadcyla® the only approved ADC with a non-clevable linker, bearing a MMAF payload conjugated via a maleimidocaproyl non-clevable linker. Unfortunately Blenrep® was withdrawn from the market on 2022 due to low effectiveness in relapsed/recurrent multiple myeloma patients (Morè et al. 2023).

While non-cleavable linkers have improved payload stability in circulation, patients still experience adverse effects due to off-target toxicity such as thrombocytopenia and ocular toxicity (Donaghy 2016).

1.2.6 Conjugation

The conjugation strategy along with the choice of linker plays an important role in ADC development and can impact the efficacy as well as pharmacokinetic and tolerability. ADCs under development on the market exploit the presence of lysine (Lys) and cysteine residues to conjugate the linker using N-hydroxysuccinimide (NHS) and maleimide as moiety. The primary amine in Lysine readily reacts with NHS esters incorporated into the drug-linker, resulting in the formation of a stable amide bond. Since in an IgG1 approximately around 30 Lys can be modified, 1 to 30 payloads can be conjugated to the antibody (Ducry and Stump 2010). As an example, Kadcyla® has an average drug-to-antibody ratio (DAR) of 3.5, however the DAR species span from DAR 0 to DAR 8 (Chen et al. 2016). The Drug-to-Antibody Ratio (DAR) plays a pivotal role in determining the tolerability, efficacy, and pharmacokinetics of an ADC. ADCs with heterogeneous DAR are usually composed by unconjugated antibodies and multiple DAR species with high and low DAR. High DAR ADCs demonstrated heightened tumor efficacy, yet they are prone to increased aggregation causing lower tolerability and quicker clearance *in vivo* (Hamblett et al. 2004; Sun et al. 2017). In fact, high DAR species have also been found in high concentrations in the liver, probably because of unspecific uptake by Kupffer cells,

potentially causing higher liver toxicity (Mahalingaiah et al. 2019). Conversely, unconjugated antibodies compete for the target antigen alongside the ADC, thereby diminishing ADC activity. In contrast, ADCs with homogeneous DAR offer distinct advantages. They showcase enhanced efficacy and tolerability while providing a more predictable pharmacokinetic profile. This predictability arises from their composition, consisting solely of a single ADC species (Jackson 2016; Anami et al. 2022). Therefore, developing a strategy to produce ADCs with a homogeneous DAR is preferable.

IgG1 comprises thirty-two cysteine residues, forming sixteen disulfide bonds. Twelve are intrachain disulfide bonds linking the two layers of antiparallel β-sheets within each domain, while four are interchain disulfide bonds connecting the light and heavy chains (Chumsae et al. 2009). The disulfide bonds that connect the heavy and light chain of the antibody can be reduced, allowing the free thiol groups to be conjugated via thiol-maleimide conjugation and form a thiosuccinimide bond with the maleimide moiety on the linker (Lu et al. 2016). This type of conjugation is also called “interchain” conjugation and was applied for example in Trastuzumab Deruxtecan, generating an ADC with a DAR of 8 (Azar et al. 2021). Thanks to the limited number of interchain cysteines in the antibody, DAR heterogeneity is reduced and the optimization of the reduction step can produce ADCs with DAR of 2, 4, 6, and 8 with better homogeneity compared to products from lysine coupling (Nadkarni 2020). However, cysteine conjugation can undergo the retro-Micheal exchange reaction where the maleimide payload deconjugates from the antibody to re-conjugate to the free thiol of plasma proteins, e.g. albumin. To avoid this side reaction, thiol-maleimide conjugates can undergo stabilization through the opening of the maleimide ring following the formation of the thiosuccinimide bond under alkaline conditions. This process yields two isomeric succinamic acid thioethers, enhancing the stability of the conjugates (Fontaine et al. 2015). Another approach that leads to the generation of a stable thioether bond relies on the use of α-halocarbonyl electrophiles, e.g. iodoacetamides (Koniev and Wagner 2015). Interchain conjugation can compromise the stability of the antibody by opening of the interchain disulfide bond during the conjugation (Shen et al. 2012; Levengood et al. 2017). Therefore, to improve ADC stability and DAR homogeneity, site-specific conjugation to engineered cysteine was developed. The site-specific substitution of cysteine residues to different sites of the antibody was first applied by Jununtula et al. and patented by Genentech (THIOMAB™). The advantages of this conjugation method include the creation of ADCs with a uniform DAR, enhancing tolerability (Junutula et al. 2008b; Bhakta et al. 2016).

Other types of conjugation methods involve the use of unnatural amino acids, remodeling of glycans and enzyme-assisted ligation (Fu et al. 2022). The introduction of unnatural amino acids through engineered tRNA synthetase can provide new functional groups, e.g.

N-acetyl-L-phenylalanine, azido methyl-L-phenylalanine and azido lysine that enable site-specific conjugation. In particular, the azide moiety can be reacted using copper-free click chemistry to the linker via a dibenzocyclooctyne (DBCO) handle. This type of conjugation proved to generate homogeneous ADCs with high efficacy and good stability, however the risk of immunogenicity and aggregation due to increased hydrophobicity of the unnatural amino acid can pose a problem (Hallam et al. 2015).

In enzyme-assisted ligation, targeted amino acid sequences are deliberately incorporated into the antibody. These sequences serve as recognition sites for specific enzymes to modify the corresponding amino acids, facilitating precise conjugation. Now, formyl glycine-generating enzymes, transglutaminase, and Sortase represent the most used enzymes for this type of conjugation. Even in this scenario, a risk of immunogenicity associated with the modification of specific antibody amino acids remains (Rao et al. 2015).

Glycan remodeling and glycoconjugation is based on specific modifications of the native N-glycosylated asparagine residue, Asn297 (according to EU numbering). The EU numbering system is based on the amino acid sequence of the human Eu myeloma protein, a human IgG1 antibody, whose first complete sequence analysis was described by Edelman et al. (1969). This numbering scheme is primarily used when working with the constant region of human IgG1 and can be used to compare different constant heavy chain engineered variants of IgG1 (Lefranc et al. 2022). Comparing the variable regions or constant regions of other human IgGs subclasses and animal immunoglobulins requires the use of alternative numbering schemes, for example the Kabat numbering, which also is widely used for annotating antibody residues (Kabat et al. 1979, Dodelinger et al. 2018).

Several strategies for targeting the N-glycan for bioconjugation have been devised, such as metabolic engineering, chemical oxidation, and enzymatic and chemo-enzymatic modifications (Wang et al. 2019). GlycoConnect™ is an example of technology that introduces an azidosugar in the glycan and relies on metal-free click chemistry to conjugate the payload. Glycan remodeling provides a precise method for conjugating payloads to antibodies, yielding stable ADCs with homogeneous DAR without the need for changing their ammino acids sequence. Furthermore, altering the glycan pattern can attenuate binding to the Fcγ receptor, thereby inhibiting the effector function and increasing tolerability (Wijdeven et al. 2022).

1.2.7 Payload

The crucial key component of an ADC is the cytotoxic payload, which is also the main driver of off-target toxicity. Many payloads exhibit cytotoxicity ranging from nanomolar to picomolar concentrations, as measured by their half-maximal inhibitory concentration (IC_{50}) values, which is the concentration of a drug needed to inhibit 50% of cell viability (Fu et al. 2022). Since only 0.1 % of the ADC reaches tumor cells high potency of the payload is required to obtain tumor efficacy (Beck et al. 2017). The initial wave of ADCs employed chemotherapeutic agents like doxorubicin and vinblastine. However, these early immunoconjugates fell short of demonstrating adequate tumor efficacy, resulting in the failure of all clinical trials. The second generation of ADCs used more potent payloads with IC_{50} in the nanomolar range: tubulin and microtubule inhibitors (Wang et al. 2023). Microtubule inhibitors include auristatines, such as MMAE and its derivative MMAF, and maytansinoids, such as DM1 and DM4. These drugs inhibit microtubule growth and polymerization, thus preventing mitosis. Hence, tumor cells, being characterized by a higher rate of division, exhibit greater sensitivity to tubulin inhibitors in contrast to normal cells (Oroudjev et al. 2010; Akaiwa et al. 2020). Most of the ADCs currently approved on the market use MMAE as the payload, paired with a cleavable linker. This design facilitates the bystander effect, allowing the drug to target tumor cells even if they lack antigen expression. These ADCs are Brentuximab vedotin, Enfortumab vedotin, Polatuzumab vedotin, Disitamab vedotin, and Tisotumab vedotin (Wang et al. 2023). Besides their efficient anti-cancer activity, MMAE conjugates have been associated with peripheral neuropathy and neutropenia in patients treated with Brentuximab vedotin, Polatuzumab vedotin, and Enfortumab vedotin. These adverse effects were found to be consistent with payload toxicity caused by the instability of the cleavable linker and premature release of the drug (Alt et al. 2020; Powles et al. 2021). Regarding maytansinoid conjugates such as Trastuzumab emtansine, thrombocytopenia was one of the main adverse effects caused by the drug DM1 (Uppal et al. 2015).

Although tubulin inhibitors demonstrate high efficacy against actively dividing tumor cells, their effectiveness diminishes significantly against quiescent cancer cells. To potentially address this limitation, DNA damaging agents, capable of targeting the entire cell cycle, were chosen as the cytotoxic payloads for the majority of third-generation ADCs. DNA damaging agents exert their cytotoxic effects on tumor cells by disrupting DNA structures through mechanisms such as double-strand breaking, alkylation, intercalation, and cross-linking. Notable examples of DNA damaging payloads include enediynes, Calicheamicins, topoisomerase I inhibitors, and pyrrolobenzodiazepines (PBD) (Wang et al. 2023). Compared to microtubule inhibitors, which typically exhibit IC_{50} values in the nanomolar

range, DNA damaging agents can achieve IC_{50} values in the picomolar range.(Cheung-Ong et al. 2013).

The DNA damaging mechanism of anti-tumor antibiotic, Calicheamicins function by binding to the minor groove of DNA, inducing generation of free radicals ultimately leading to DNA strand breaks. Calicheamicins were initially utilized with a hydrazone cleavable linker in Inotuzumab ozogamicin and Gemtuzumab ozogamicin. Unfortunately, treatment with calicheamicin conjugates has been associated with Veno-occlusive disease in patients, marked by damage and obstruction of liver sinusoidal endothelial cells, resulting in hepatic dysfunction (Ellestad and Ding 1994; McDonald et al. 2019).

Another type of DNA-damaging agents are Duocarmycin, a potent class of antitumor antibiotics, which binds to the minor groove of DNA and alkylates the nucleobase adenine (Takahashi et al. 1988).

Camptothecin derived DNA topoisomerase I inhibitors, such as SN-38 (7-ethyl-10-hydroxycamptothecin) and deruxtecan (exatecan derivative) have been used as warheads for Sacituzumab govitecan and Trastuzumab deruxtecan, respectively (Beck et al. 2017).

PBDs are antitumor antibiotics that function as a dimer to bind to the DNA minor groove. Upon binding, it facilitates amino cross-linking with guanine at the N_2 position of DNA, preventing DNA from combining with transcription factors. This halts cell proliferation, leading to cell death. The mechanism of action of PBDs is distinct from other chemotherapeutic agents in that it does not depend on a specific cell replication cycle. Additionally, the DNA damage it induces is difficult to repair, leading to potent cytotoxicity (Gregson et al. 2017). Currently, Loncastuximab tesirine is the sole ADC in clinical use employing PBD as payload (Lee 2021). Other PBD-based ADCs failed in clinical trials due to severe cytopenia, in particular neutropenia (Nguyen 2023).

Most of the payloads in marketed ADCs exhibit high hydrophobicity, which can be advantageous for diffusion driven bystander effect activity. However, it also poses risks such as increased ADC aggregation, fast clearance, and reduced tolerability due to passive diffusion in the cell membranes of healthy tissues (Nguyen 2023). Moreover, many of these hydrophobic drugs were found to be substrate of different multidrug resistance proteins (MRP) that are expressed on tumor cells rendering them resistant to several anticancer drugs (Sodani et al. 2012). Hence, current research efforts are directed towards discovering and developing new hydrophilic payloads that exhibit reduced drug aggregation and lower rates of drug resistance (Johnson and Chen 2017; Satomaa et al. 2018).

1.3 Amanitin and Amatoxin-based ADCs (ATAC®s)

Amatoxins are a group of nine different toxins naturally found in the Basidiomycota mushroom family *Amanita*. Among this group, *Amanita Phalloides* (Death Cap) is responsible of most deaths upon mushroom ingestion worldwide (Vo et al. 2017; Pahl et al. 2019). In 1940, Rudolf Hallermayer and Nobel laureate Heinrich Wieland successfully extracted and crystallized one of these amatoxins from the mushroom toadstool, naming it “amanitin.” In 1949, Theodor Wieland succeeded in isolating a new acidic amanitin, named β-amanitin, distinct from its neutral counterpart, later termed α-amanitin. Subsequent years saw further characterization of amanitin's structure and molecular activity conducted by Heinz Faulstich, Luigi Fiume and other prominent researchers, ultimately leading to the discovery of its molecular mechanism and toxicokinetics (Wieland 1986). Nowadays amanitin is rarely extracted and purified from the *A.phalloides* toadstool, instead methods have been developed for total synthesis (Lutz et al. 2020). Amanitin is a bicyclic octapeptide with molecular weight of ~900 g/mol composed of eight L-amino acids, featuring three uncommon amino acids: 4-hydroxyproline, dihydroxy-isoleucine, and 6-hydroxy-tryptophan. In particular, the 6-hydroxy-tryptophan forms a "triptathionine" bond with the thiol group of a cysteine (**Figure 5**) (Wieland 1983; Vetter 2023). The presence of hydroxyl groups on the side chains of the ammino acids, makes amanitin more hydrophilic compared to current in-use payloads. As a result, amanitin is water-soluble and less prone to passive diffusion through cell membrane and tissues (Pahl et al. 2019; Vetter 2023).

In fact, the cytotoxicity of free amanitin is in the micromolar range with an IC_{50} of ~ 10^{-6}M, and thus three orders of magnitude higher than the IC_{50} of microtubule inhibitors (Oroudjev et al. 2010). Moreover, amanitin demonstrates plasma stability and rapid renal clearance, reducing the chances of tissue accumulation. Additionally, amanitin is resistant to heat, acidic and enzymatic degradation (Pahl et al. 2019).

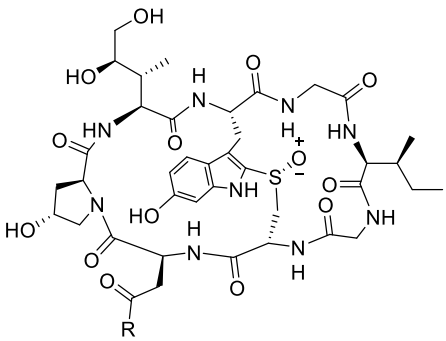

Figure 5: Structure of α-amanitin and β-amanitin.

Fiume and Stirpe initially proposed the molecular toxic mechanism of amanitin when they observed a rapid 45% reduction in RNA content in liver nuclei of mice within just 30 minutes post-injection with amanitin (Stirpe and Fiume 1967). This discovery led to the characterization of its mode of action as an RNA polymerase II inhibitor. Amanitin non-covalently binds beneath the “bridge helix” between the two largest subunits, Rpb1 and Rpb2, of the enzyme in a 1:1 binding stoichiometry. The binding of amanitin inhibits conformational changes that are essential for the RNA elongation process. This mechanism leads to the disruption of RNA transcription, 1000-fold decline in mRNA levels and protein synthesis, which ultimately results in cell death. Moreover, it seems that upon binding to amanitin the Rpb1 subunit of the RNA polymerase II enzyme is degraded, resulting in irreversible inhibition (Garcia et al. 2015). By inhibiting cell transcription, amanitin possesses the capability to kill both actively dividing and non-dividing dormant tumor cells. This is because RNA polymerase II, a critical enzyme in cellular transcription, operates independently of the cell cycle and cell division (Pahl et al. 2019).

Toxicokinetic studies of amanitin revealed the liver as the primary organ affected by amatoxin poisoning. This was attributed to the uptake of amanitin by an organic anion transport polypeptide (OATP), specifically OATP1B3, expressed on the sinusoidal membrane of hepatocytes. Uptake of amanitin by the OATP1B3 transporter results in acute hepatic toxicities which can ultimately lead to liver failure and death (Letschert et al. 2006; Garcia et al. 2015).

To take advantage of the unique mechanism of amanitin and avoid liver complications caused by free toxin, amanitin was conjugated to antibodies by Heidelberg Pharma, generating amatoxin-based ADCs (ATAC®s). Amanitin is conjugated via maleimide chemistry using a cleavable or non-cleavable linker attached to the hydroxyl group of the 6-hydroxy-tryptophan or the carboxyl group of aspartic acid (beta-amanitin). The conjugation approach utilizes site-specific THIOMAB™ conjugation to engineered cysteine residues in the heavy chain of humanized IgG1. The engineered cysteines are introduced through site-directed mutagenesis within the heavy chain sequence of the antibody. Specifically, the aspartate 265 residue (EU numbering) is mutated to cysteine, generating two engineered cysteines in the Fc portion of the antibody (Edelman et al. 1969). This approach ensures a consistent DAR of 2, resulting in a homogeneous ADC to broaden the therapeutic index. Conjugated amanitin delivered to target positive tumor cells showed improved cytotoxicity compared to the free toxin, with IC_{50} values of 10^{-11}-10^{-12} M. Studies have also shown that due to its hydrophilicity, amanitin is a poor substrate for Multidrug Resistant ProteMultidrug-Resistantnting drug resistance issues. Furthermore, to prevent binding to the Fcγ receptor, which could activate the effector function of the IgG1 antibody,

leading to off-target uptake and toxicity, the Fcγ binding recognition site was silenced (Pahl et al. 2019). The leucine residues in the 234 and 235 position (EU numbering) were mutated to alanine residues (LALA mutation), eliminating complement binding, Fcγ-dependent and antibody-dependent cell-mediated cytotoxicity (Edelman et al. 1969; Lo et al. 2017). This procedure, known as Fc silencing, enhanced the *in vivo* tolerability of ATAC and further improved the therapeutic index.

ATAC®s offer another advantage over other ADCs due to the increased sensitivity of tumor cells bearing the 17p deletion to amanitin. The gene for RNA polymerase II, POLR2A, resides on chromosome 17, close to the tumor suppressor gene TP53. In many types of tumors, a huge part of one arm of chromosome 17 is often deleted (hemizygous deletion), resulting in the simultaneous loss of one allele of the tumor suppressor gene TP53 and one allele of the POLR2A gene. This hemizygous deletion renders tumor cells highly aggressive on one hand and more susceptible to amanitin on the other hand (Liu et al. 2015; Pahl et al. 2019).

The most advanced ATAC® is HDP-101, which targets the B-cell maturation antigen BCMA (CD269), expressed on plasma cells in multiple myeloma patients. Preclinical data demonstrated that HDP-101 exhibited robust *in vitro* and *in vivo* anti-tumor activity with complete tumor remission in multiple myeloma mouse models. Furthermore, safety studies conducted in mice and monkeys revealed a highly favorable therapeutic window (Pahl et al. 2019). HDP-101 is now in clinical trial Phase I/IIa showing promising results of partial tumor remission on multiple myeloma patients (Heidelberg Pharma AG 2024).

Given the potent nature of amanitin and the potential risk of off-target toxicity, particularly affecting the liver, strategies to further improve the tolerability of ATAC®s and to prevent adverse events are in high demand. One such strategy may involve direct *in vivo* modification of the payload activity using biologically safe chemical reactions.

1.4 Bioorthogonal „Click“ Chemistry

In 2022, Barry Sharpless, Morten Meldal and Carolyn Bertozzi won the Nobel Prize in Chemistry for “the development of click chemistry and bioorthogonal chemistry” (Bertozzi et al. 2022). The term “click chemistry” was first coined by Sharpless in 2000 and was based on the use of small units that would join together to generate substances with heteroatom links (C-X-C). The reaction had to be “modular, wide in scope, give very high yields, generate only inoffensive byproducts (..) and be stereospecific” (Kolb et al. 2001). Meldal and Sharpless developed the first click reaction; the copper(I)-catalyzed cycloaddition (CuAAC) of terminal alkynes to azides, leading to the generation of 1,2,3-

triazoles (Rostovtsev et al. 2002; Tornøe et al. 2002). In the same period, Bertozzi was investigating the application of bioorthogonal chemistry to study cellular glycosylation metabolism and its influence on multiple diseases. Bertozzi et al. employed the bioorthogonal Staudinger reaction (Staudinger ligation), a click chemistry method involving a phosphine and an azide, to label phosphine probes onto azidoglycans (glycans engineered with an azide moiety) on the cell surface (Saxon and Bertozzi 2001; Hang et al. 2003). The term bioorthogonal chemistry was then employed to refer to an orthogonal reaction, a selective chemical reaction with no cross-reactivity, which could proceed in living systems without interfering with biological processes and biomolecules (Shahrokhinia et al. 2021; Mitry et al. 2023). Later on, Bertozzi et. al improved the slow kinetic of the Staudinger ligation ($k=7.7x10^{-3}$ $M^{-1}s^{-1}$), developing a new biorthogonal reaction, the Strain-Promoted Azido-Alkyne Cycloaddition (SPAAC), inspired by the copper(I)-catalyzed cycloaddition previously described by Sharpless and Meldal. Instead of relying on copper as a catalyst, since it is toxic in mammalian cells, a cyclooctyne derivative (strained alkyne) was used in the reaction with the azide.(Wittig and Krebs 1961; Agard et al. 2004) SPAAC reaction kinetic ($k= 2.4x10^{-3}$ $M^{-1}s^{-1}$) did not show much of an improvement compared to the Staudinger ligation kinetic, but in recent years, novel strained alkyne derivatives with enhanced reaction kinetics for strain-promoted azide-alkyne cycloaddition (SPAAC) have been synthesized: bicyclo[6.1.0]non-4-yne (BCN), dibenzoazacyclooctyne (DBCO) and dibenzocyclooctyne (DIBO) (Dommerholt et al. 2016).

Recently, another bioorthogonal reaction has been developed by Blackman and Devaraj, the inverse Electron Demand Diels-Alder (IEDDA) reaction. The IEDDA is based on the cycloaddition reaction between tetrazines and dienophiles, e.g. cyclooctene and transcyclooctene (TCO) and outperforms the kinetic of SPAAC reaction, with reaction rates between 10^2 and 10^6 M^{-1} s^{-1} (Kenry and Liu 2019). The aforementioned click chemistry reactions are illustrated in **Figure 6**.

Currently, bioorthogonal click reactions find application across a diverse array of fields. SPAAC and IEDDA have been extensively employed in biomaterial science to create biocompatible, cross-linked materials suitable for use as cellular scaffolds (Battigelli et al. 2022). They have also found application in antibody conjugation for attaching payloads and in the creation of novel complex bispecific constructs (Chio and Bane 2020; Szijj et al. 2023). However, the most intriguing application of bioorthogonal click reactions is their utilization within living systems, such as cells or animals. They have been used in metabolic labeling and to track biomolecular processes.

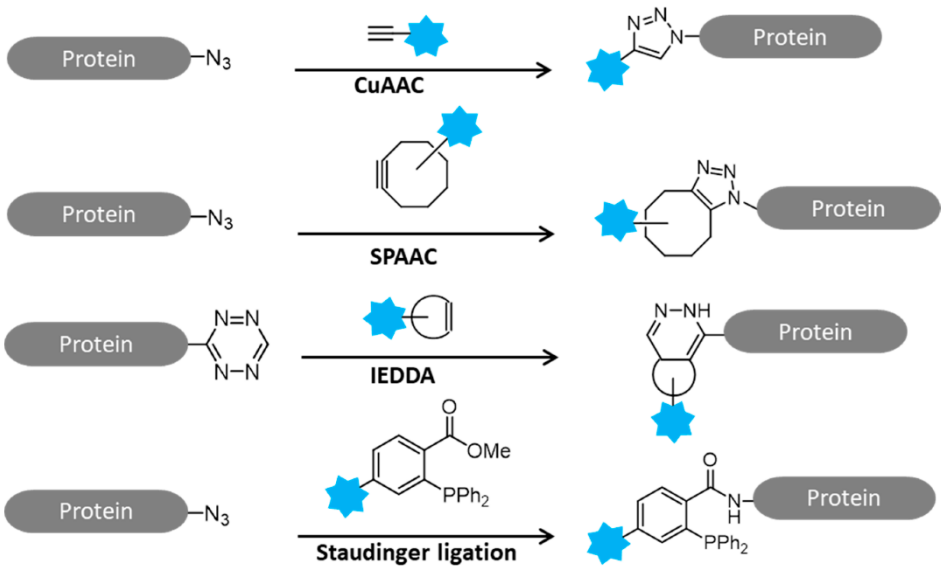

Figure 6: Schematic representation of click chemistry reactions. *Image adapted from Yao T, Xu X, Huang R. Recent Advances about the Applications of Click Reaction in Chemical Proteomics. Molecules. 2021; 26(17):5368. Open access article distributed under the terms of Creative Commons CC BY.*

An example is metabolic glycoengineering, which is used to detect spatiotemporal glycan changes in the embryonic development of C. elegans and zebrafish. Embryos were cultured with N-azidoacetylgalactosamine (GalNAz), which was integrated into metabolic processes. *In vivo* imaging was then conducted using a SPAAC reaction with DIFO-Alexa Fluor conjugates (Sletten and Bertozzi 2011). Metabolic glycoengineering coupled with SPAAC reaction has also found application in visualizing the fate of therapeutic cells, thereby enhancing cell-based therapeutic strategies (Kenry and Liu 2019). Bioorthogonal chemistry finds another valuable application in tumor radioimaging and radiotherapy. Rossin et. al developed a TCO-conjugated mAb for tumor pretargeting that was later reacted via IEDDA with a ^{177}Lu-labeled DOTA-tetrazine probe for imaging and radiotherapy. The results showed specific accumulation of the radiolabel in the tumor sparing healthy tissues. Furthermore, to prevent an off-site reaction between the Lu-labeled DOTA-tetrazine probe and the circulating TCO-conjugated mAb, the TCO-conjugated mAb was selectively cleared from circulation using "clearing agents." These agents facilitate the binding of the mAb to specific receptors, directing its accumulation in metabolizing organs such as the liver and spleen. These clearing agents consisted of albumin conjugated with a galactose handle, facilitating active liver uptake, and tetrazine for the IEDDA reaction with the TCO-mAb (Rossin et al. 2013).

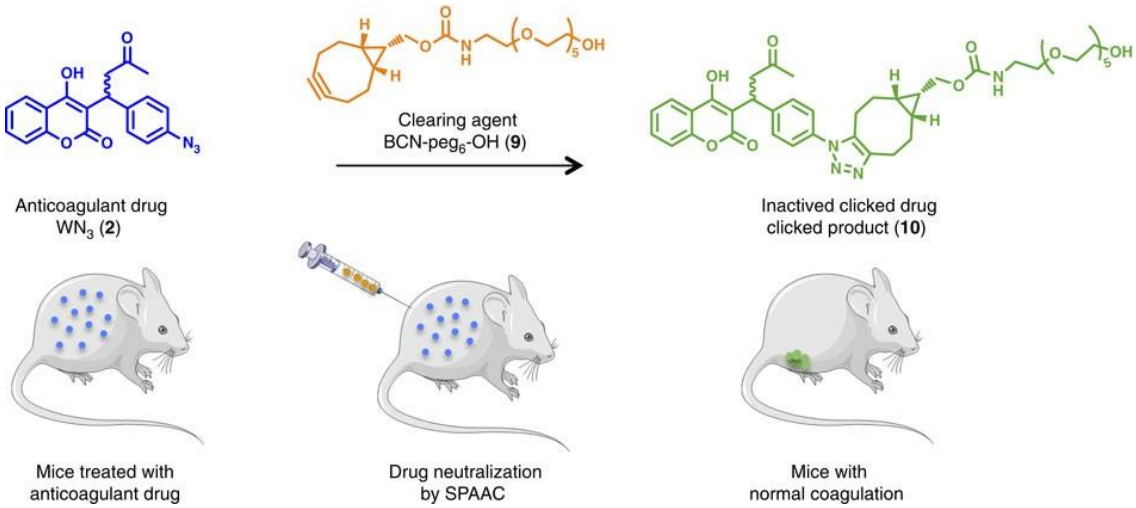

Figure 7: Illustration of the neutralization strategy applied by Ursuegui et. al. *Image adapted from Ursuegui, S., Recher, M., Krężel, W. et al. An in vivo strategy to counteract post-administration anticoagulant activity of azido-Warfarin. Nat Commun 8, 15242 (2017). Open access article distributed under the terms of Creative Commons CC BY.*

Similar to the “clearing agent” approach of Rossin et al., Ursuegui et. al used the SPAAC reaction *in vivo* to neutralize the anticoagulant activity of warfarin, a famous anticoagulant drug, post-administration. Mice were initially administered with azidowarfarin (WN_3), a form of warfarin containing an azide moiety. Just 5 minutes later, they were given a "clearing agent" to undergo SPAAC reaction, resulting in the formation of an inactivated clicked product (**Figure 7**). The “clearing agent” used in this case was BCN-PEG_6-OH, a BCN conjugated with Polyethylene glycol (PEG) chains to improve plasma solubility. They demonstrated that the reaction between BCN-PEG_6-OH and WN_3 produced a non-active compound within 10 minutes post BCN-PEG_6-OH administration. Furthermore, this inactive compound displayed no anticoagulant activity and was rapidly cleared within 1 hour (Ursuegui et al. 2017). This neutralization strategy, aimed at neutralizing treatment activity *in vivo*, holds significant promise for the development of drugs with switchable biophysical properties. It also has the potential to alleviate the adverse toxic effects commonly associated with many anticancer drugs.

2 Aim of the study

Amatoxin-based antibody-drug conjugates (ATAC®s) are a promising approach for targeted cancer therapy developed by Heidelberg Pharma. ATAC®s are using amanitin as a toxic payload; a toxin that efficiently inhibits cellular transcription by binding to RNA pol II. ATAC®s demonstrated promising results in both *in vitro* and *in vivo* studies. While ADCs have been designed to target specifically tumor tissue, there is still a risk of reaching healthy tissues. Such off-tumor toxicity poses a substantial obstacle in ADC treatment, and thorough research has revealed that the target-independent uptake of the ADC or of the free payload by healthy cells contributes to this challenge. A recent study by Ursuegui et al. implemented a new way to control and modulate post-treatment off-target drug effects using Strain-Promoted Azide-Alkyne Cycloaddition (SPAAC) reaction directly *in vivo*.

This thesis aimed to employ SPAAC reaction in a neutralization strategy, which switches off the activity of Amatoxin-based ADCs post *in vivo* administration, thus improving their tolerability and enhancing their therapeutic index.

Generating a proof-of-concept for the neutralization of ATAC®s involves multiple steps, which is why certain milestones were planned for the project:

1. *In vitro* evaluation of different strained alkynes (neutralizing agents) to reduce the activity of new azido-amanitin payloads—amanitin derivatives with an azide moiety—using the SPAAC reaction. Additionally, application of the same technique using azido-amanitin-based ADCs and evaluating their efficacy across different cell lines, either with or without performing the neutralization strategy.
2. Evaluation of *in vivo* tolerability enhancement. Treatment of both tumor-free and tumor-bearing mice with azido-amanitin ADCs along with neutralizing agents under different time regimens. Additional, histopathological analyses of liver and kidney tissues post-ADC administration to ascertain whether the neutralization strategy can prevent the formation of toxic lesions caused by amanitin.
3. *In vivo* efficacy studies in tumor-bearing mice to determine the influence of the SPAAC reaction on tumor response and treatment tolerability.

3 Material and Methods

3.1 Material

3.1.1 Laboratory equipment

***Table 2**: Laboratory equipment*

Device	Manufacturer
Äkta pure 25 L, FPLC	Cytiva
Äkta start	Cytiva
Analytical balance	Kern AEJ
Azure C300 Imaging system	Azure Biosystems
Biological Safety Cabinet	Thermo Fisher Scientific
Bio-Rad C1000 Touch, Thermocycler	BioRad
BioRad CFX Connect, Real-Time PCR	BioRad
BMG CLARIOstar, Microplate Reader	BMG Labtech
Centrifuge Multifuge X3R	Thermo Fischer Scientific
CO_2 Incubator	Thermo Forma
Cytiva ÄKTA start, FPLC-System	Cytivia
Cytosmart	Corning
Double Neubauer Chamber	Optik Labor
Downflow Cabinet	Bioair
Filtration Pump	KNF
ForteBio Octet K2	Fortebio
Heat Block	Techne
HiLoad 16/600 Superdex 200 pg column	Cytiva
HiLoad 26/600 Superdex 200 pg column	Cytiva
HPLC, 1260 Infinity II	Agilent
HPLC, Hitachi Chromaster	Hitachi Hightech
Hydrospeed ELISA Washer	Tecan
Laboratory balance	Kern
Laboratory freeze-dryer	Christ
Magnetic stirrer M5	CAT
Microplate Reader BMG CLARIOstar	BMG Labtech
Microscope	Zeiss

Minicentrifuge	SunLab
NanoDrop Onec Spectrophotometer	Thermo Fisher Scientific
Orbital shaker	neoLab
PCR Plate Spinner	VWR
pH Meter	Sartorius
Power Supply	Consort
Prep HPLC, 1260 Infinity preparative LC System	Agilent
Rocking plate shaker	neoLab
Rotation-Vacuum-Concentrator	Christ
Tabletop Centrifuge	Heraeus Fresco
Technical balance	Sartorius
Thermomixer	neoLab
Tissue homogenizer	Bertin Instruments
Tosoh UP SW 3000 4.6mm x 15cm, 2µm gel filtration column	Tosoh Bioscience
TOYOSCREEN® AF-rProtein A HC-650F 5ml	Tosoh Bioscience
Trans-Blot Turbo	BioRad
Vortexer	Scientific Industries
Water bath	Thermo Fisher Scientific
Western Blot electrophoresis chamber	BioRad

3.1.2 Consumables

***Table 3**: Consumables*

Consumables	**Manufacturer**
Adhesive clear qPCR seal	Biozym
Amicon Ultra Centrifugal Filters 50,000 MWCO	Millipore
Cell culture flasks T25, T75, T175	Greiner Bio-One
Cell culture microplate 96-well, U-bottom	Greiner Bio-One
Cell culture microplate 96-well, V-bottom	Greiner Bio-One
Cell culture multiwell plate, 24-well	Greiner Bio-One
Cell culture multiwell plate, 6-well	Greiner Bio-One
Cell culture plate Cell Carrier-96 Black, optically clear bottom	Perkin Elmer
Centrifuge tubes 500 mL	Corning
Combitips advanced 5mL, 10mL	Eppendorf
Deep Well MegaBlock® 96 wells	Sarsted
DNA-Exitus Plus (IF)	Applichem

Erlenmeyer flasks 2L	Corning
Filter units 0.22µM	Millipore
Membrane filter	Millipore
Nunc-Immuno 96-well plates	Thermo Scientific
Omnifix ® syringe	Braun
PCR 96-well plates	Brand
PD MiniTrap G-25	Cytiva
PD-10 Columns	Cytiva
Phusion® High-Fidelity PCR Master Mix with HF Buffer	NEB
Pierce Streptavidin High Binding Capacity Coated Plates	Life Technologies
Precellys lysing kit	Bertin Technologies
Reaction tubes 15mL, 50 mL	Greiner Bio-One
Round-bottom flask	Witeg
Sartoclear Dynamics® Lab V, 500ml, 20g	Sartorius
Slide-A-Lyzer Cassette 20000 MWCO	Thermo Fischer Scientific

3.1.3 Chemicals and solutions

***Table 4**: Chemicals and solutions*

Chemicals and solutions	Manufacturer
30% H_2O_2	Fluka
3,3´, 5,5´ Tetramethylbenzidine (TMB)	Sigma-Aldrich
Acetic acid	Carl Roth
Acetonitrile	Carl Roth
Ampicillin (100 mg/mL in H_2O)	Serva
Blasticidin 10 mg/mL	Invitrogen
Boric acid	Carl Roth
Bovine serum albumin (BSA)	Carl Roth
Bromophenol blue	SERVA
Clarity Western ECL Substrate	BioRad
Dehydroascorbic acid	Sigma-Aldrich
Dimethyl sulfoxide (DMSO)	Sigma-Aldrich
Dimethylformamide (DMF)	Sigma-Aldrich
Di-sodium hydrogen phosphate	Carl Roth
DPBS	PAN Biotech
Ethanol	Carl Roth

Ethylenediaminetetraacetic acid (EDTA)	Sigma-Aldrich
Fetal Bovine Serum Advanced	Capricorn Scientific
Glycerol	Carl Roth
Glycin	Carl Roth
Hydrochloric acid (HCl)	Carl Roth
L-glutamine	Sigma-Aldrich
LB Agar	Carl Roth
Methanol	Carl Roth
Milk powder	Carl Roth
Mouse serum	Neo Biotech
N-acetyl-L-cysteine	Sigma-Aldrich
N-ethylmaleimide	Sigma-Aldrich
Page Ruler plus prestained protein marker	Thermo Fischer Scientific
Penicillin 10 000 U/mL Streptomycin 10 mg/mL	Sigma-Aldrich
Polyethylenimine 2mg/mL	Polysciences
Poly-D-Lysin	Sigma-Aldrich
Potassium chloride (KCl)	Carl Roth
Potassium dihydrogen phosphate (KH_2PO_4)	Carl Roth
Precision Plus Protein Unstained Standard	BioRad
Propanol-2	Carl Roth
Roti-Load 4x	Carl Roth
Sample Buffer	Candor Bioscience
SDS pellets	Carl Roth
Smart Block TM	Candor Bioscience
Sodium Acetate (NaOAc)	Sigma-Aldrich
Sodium azide (NaN_3)	Carl Roth
Sodium chloride (NaCl)	Carl Roth
Sodium hydroxide (NaOH)	Carl Roth
Sodium phosphate dibasic dihydrate (Na_2HPO_4 $2H_2O$)	Carl Roth
Sodium sulfate (Na_2SO_4)	Carl Roth
Sterile filter Millex-GV	Millipore
Trifluoroacetic acid (TFA)	Carl Roth
Tris	Carl Roth
Tris (2-carboxyethyl) phosphine (TCEP)	Sigma-Aldrich

Tris -HCl	Carl Roth
Trypan blue solution	Sigma-Aldrich
Trypsin/EDTA	Sigma-Aldrich
Tween 20	Sigma-Aldrich

3.1.4 Kits

***Table 5**: Kits*

Kits	Manufacturer
Cell proliferation ELISA, BrdU chemiluminescent	Sigma-Aldrich
Endofree Plasmid Mega Kit	Qiagen
Endozyme® II Endotoxin Detection Assays	Biomerieux
Nuclear extract kit (HeLa Scribe)	Promega
QIAprep Spin Miniprep Kit	Qiagen
QIAquick PCR purification Kit	Qiagen
QuantiNova Probe RT-PCR Kit	Qiagen
Rneasy 96 Kit	Qiagen

3.1.5 Buffers

***Table 6**: Buffers*

Buffers	Composition
1x Tris, glycine, SDS gel running buffer	25 mM Tris, 192 mM glycine, 0.1% SDS
4 x Laemlii reducing sample buffer	250 mM Tris-HCl pH = 6.8, SDS 8%, Glycerol 40 %, 2-Mercaptoethanol 8%, Bromophenol Blue 0.02%
ELISA blocking buffer	3%BSA in PBS
ELISA sample buffer	1% BSA in PBS + 20% ethanol
ELISA washing buffer	PBS + 0.05% Tween 20
Luminol solution	Clarity Western ECL Substrate, 1:1 of each solution
PBS	137 mM NaCl, 2.7 mM KCl, 10 mM $Na_2HPO_4x2H_2O$, 2 mM KH_2PO_4
SEC-HPLC running buffer	0.05%NaN_3 + 0.1mol/l Na_2SO_4 in 0.1 mol/l Na-PO_4 pH 6.7
TBST buffer	50 mM Tris, 150 mM NaCl, 0,1%, Tween 20
TMB working solution	10% TMB (1mg/ml), 0.02% of 30% H_2O_2 in 0.1 M Na-Acetate, pH 6.0
Western blot blocking buffer	5% skimmed milk in TBST buffer

3.1.6 Cell culture media

***Table 7**: Cell culture media*

Cell culture media	Manufacturer
DMEM	PAN Biotech
DMEM/F12	PAN Biotech
Expi293 Expression Medium	Life Technologies
Ham´s F12/ RPMI 1:1	PAN Biotech
McCoy's 5A	Gibco
OptiMEM	Life Technologies
RPMI	PAN Biotech

3.1.7 Bacterial culture media

***Table 8**: Bacterial culture media*

Bacterial culture media	Manufacturer
SOC outgrowth medium	NEB
Terrific Broth	Gibco

3.1.8 Enzymes

***Table 9**: Enzymes*

Enzymes	Manufacturer
DpnI	NEB
RNAse-free DNase set	Qiagen

3.1.9 RT-PCR Primers

***Table 10**: Primers*

Primers	Sequence (5´-3´)
CB_HN_Scribe_fwd_3	AATGCGCTCATCGTCATCCT
CB_HN_Scribe_probe_3	CGGCACCGTCACCCTGGATGC (5'Fam - 3'Tamra)
CB_HN_Scribe_rev_3	GGCAGTACCGGCATAACCAA

3.1.10 Antibodies and protein conjugates

***Table 11**: Antibodies and protein conjugates used in detection assays*

Antibodies and protein conjugates	Manufacturer
anti-amanitin polyclonal antibody (rabbit)	Heidelberg Pharma Research GmbH
anti-amanitin Serum (rabbit)	Biogenes
anti-Human-IgG-HRP, H&L, pre-adsorbed (goat)	Abcam

Anti-rabbit IgG HRP-linked (goat)	Cell Signaling
Streptavidin HRP conjugate	Sigma
α-amanitin- biotin conjugate	Heidelberg Pharma Research GmbH
Dibenzocyclooctyne-PEG_4-biotin conjugate	Sigma-Aldrich

3.1.11 Cell lines

***Table 12**: Cell lines*

Cell lines	Source	Medium composition
22RV1	DSMZ	RPMI + 10%FBS + 2mM L-Glutamine + 1% Pen/Strep
HEK 293-OATP1B3 Clone E2	HDPR	DMEM/F12 + 10%FBS (Charcoal stripped) + 2mM L-Glutamine + 4µg/mL Blasticidin
HEK 293-wt	CLS	DMEM/F12 + 10%FBS + 2mM L-Glutamine + 1% Pen/Strep
JIMT-1	DSMZ	DMEM + 10%FBS + 2mM L-Glutamine + 1% Pen/Strep
LNCap	Uni Freiburg	RPMI + 10%FBS + 2mM L-Glutamine + 1% Pen/Strep
MDA-MB-231	DSMZ	RPMI + 10%FBS + 2mM L-Glutamine + 1% Pen/Strep
PC3	DSMZ	Ham´s F12/RPMI 1:1 + 10%FBS + 2mM L-Glutamine + 1% Pen/Strep
SKBR-3	ATCC	McCoy´s 5A Gibco Advanced + 10% FBS + 1% Pen/Strep

3.1.12 Amanitin derivatives

***Table 13**: Amanitin-derived compounds. Compounds were synthesized by the chemistry department of Heidelberg Pharma.*

Name	Structure
α-amanitin (Ama)(1)	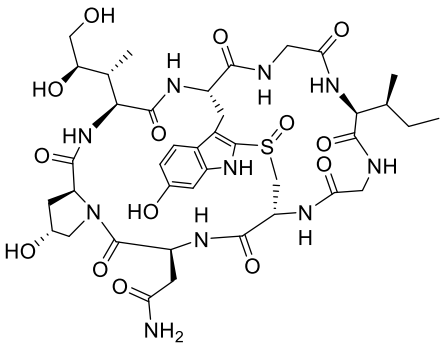 Chemical Formula: $C_{39}H_{54}N_{10}O_{14}S$ Molecular Weight: 918.98
Ama-N-azido (2)	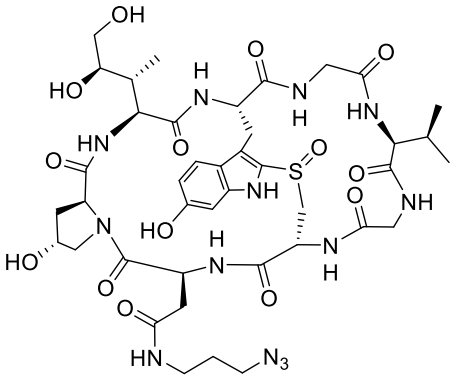 Chemical Formula: $C_{42}H_{59}N_{13}O_{14}S$ Molecular Weight: 1002.07
Ama-W-azido (3)	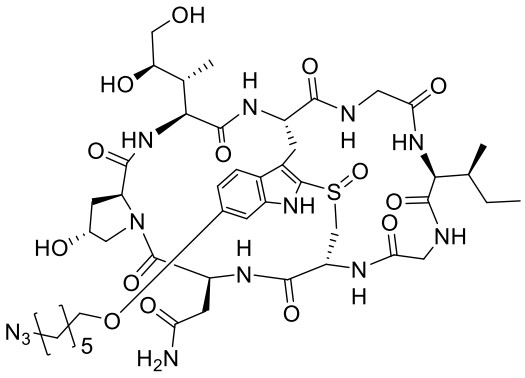 Chemical Formula: $C_{45}H_{65}N_{13}O_{14}S$ Molecular Weight: 1044.15

Ama-N-azido-Bromoacetamide (16)	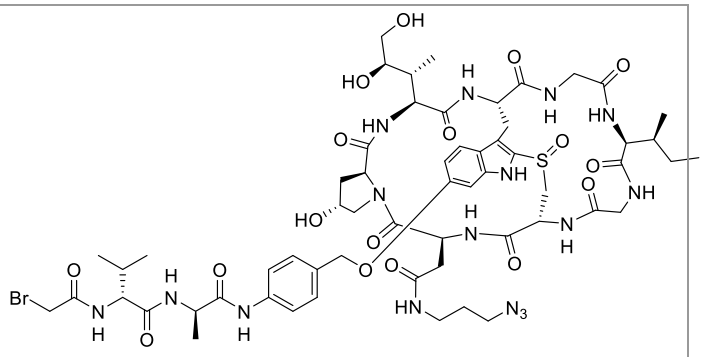 Chemical Formula: $C_{59}H_{81}BrN_{16}O_{17}S$ Molecular Weight: 1398.36
Ama-W-azido-Bromoacetamide (17)	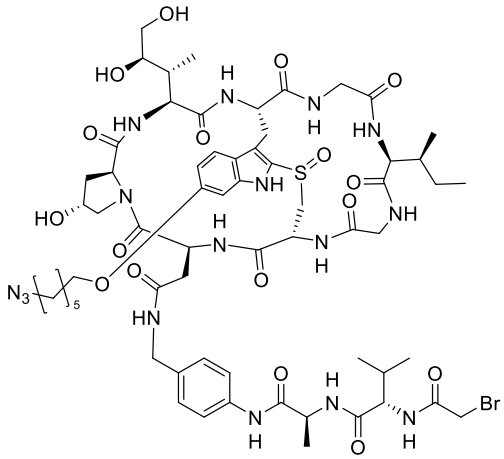 Chemical Formula: $C_{62}H_{87}BrN_{16}O_{17}S$ Molecular Weight: 1440.44
Ama-N-ctrl (18)	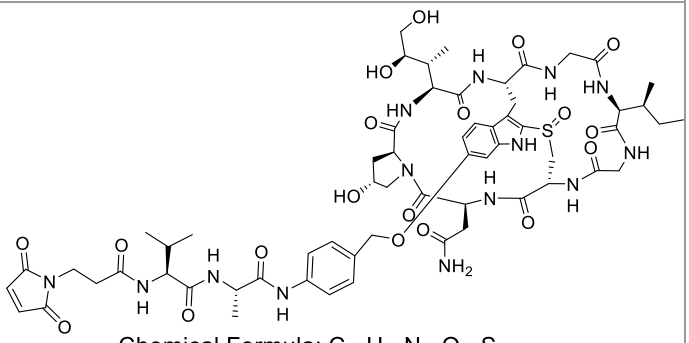 Chemical Formula: $C_{61}H_{80}N_{14}O_{19}S$ Molecular Weight: 1345.45

Ama-W-ctrl (19)	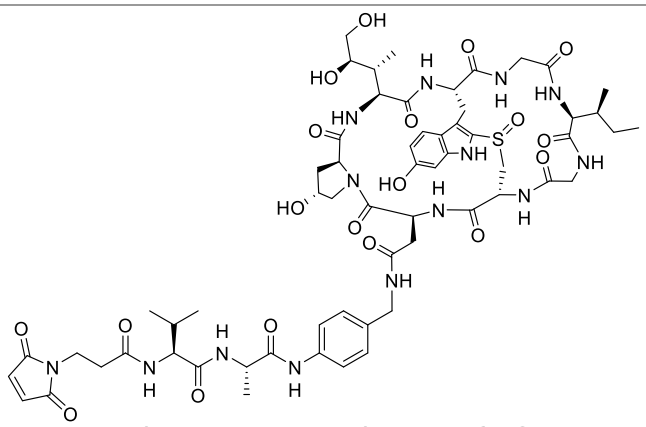 Chemical Formula: $C_{61}H_{80}N_{14}O_{19}S$ Molecular Weight: 1345.45

3.1.13 Neutralizing compounds

***Table 14**: Bicyclononynes (BCN) derivatives. The derivatives were provided by Prof. Wagner´s group at the University of Strasbourg.*

Name	Structure
BCN-OH (4)	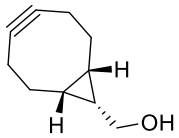 Chemical Formula: $C_{10}H_{14}O$ Molecular Weight: 150.22
BCN-PEG$_6$-OH (6)	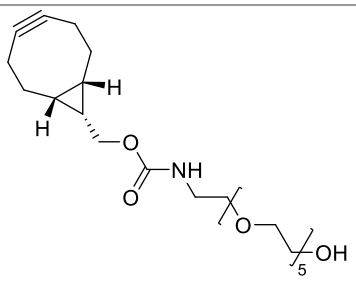 Chemical Formula: $C_{23}H_{39}NO_8$ Molecular Weight: 457.56

***Table 15**: Dibenzocyclooctyne derivatives purchased at Sigma-Aldrich.*

Name	Structure
DBCO-COOH (5)	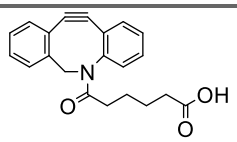 Chemical Formula: $C_{21}H_{19}NO_3$ Molecular Weight: 333.39

DBCO-PEG$_4$-COOH (7)	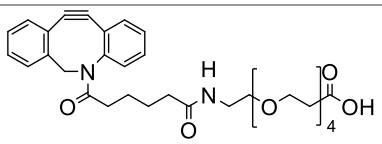 Chemical Formula: $C_{32}H_{40}N_2O_8$ Molecular Weight: 580.68

3.1.14 Mouse strains

***Table 16**: Mouse strains*

Mouse strains	Genetic background	Supplier
NMRI nude-female	Rj: NMRI-Foxn1$^{nu/nu}$, homozygous, T cell-deficient	Janvier, Le Genest Saint Isle, (FR)
NMRI nude-male	Rj: NMRI-Foxn1$^{nu/nu}$, homozygous, T cell-deficient	Janvier, Le Genest Saint Isle, (FR)

3.1.15 Software

***Table 17**: Softwares*

Software	Supplier
GraphPad Prism 9	Dotmatics Software
CFX Maestro Software	Biorad
Lab Advisor Software	Agilent
Mars Data Analysis	BGM Labtech
MS Office Suite	Microsoft
OpenLab	Agilent
SnapGene	Dotmatics Software
UNICORN™ 7	Cytiva
UNICORN™ start	Cytiva

3.2 Methods

3.2.1 Chemical synthesis of amanitin clicked compounds

Ama-N-BCN-OH (8)

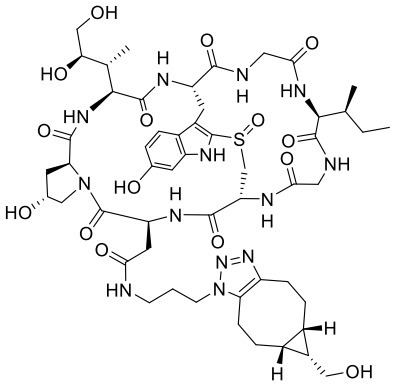

Chemical Formula:
$C_{52}H_{73}N_{13}O_{15}S$
Molecular Weight: 1152,29

Ama-N-azido (**2**) (4.48 mg, 4.48 µmol) was dissolved in 150 µL DMF. **BCN-OH** (**4**) (2.02 mg, 13.43 µmol) was dissolved in 50 µL DMF and added to the compound **2** solution. The reaction was stirred at room temperature for 3 h and then purified in RP-HPLC under the following conditions: λ= 305 nm; gradient: 0 min 5% B; 0-20 min 46% B; 20-20.5 min 100% B; 20.5-22 min 100% B; 22.5-25 min 5% B; A= water with 0.05% TFA; B=ACN. The product was isolated and lyophilized overnight.

Ama-N-BCN-OH (8): colorless powder (4.93 mg, yield 96%). MS(ESI+) *m/z*: $[MH]^+$ calcd. for $C_{52}H_{73}N_{13}O_{15}S^+$: 1152.58, found: 1152.51; $[M+Na]^+$ calcd. for $C_{52}H_{74}N_{13}NaO_{15}S^+$: 1174.67, found: 1174.50

Ama-N-DBCO-COOH-a, -b (9a, 9b)

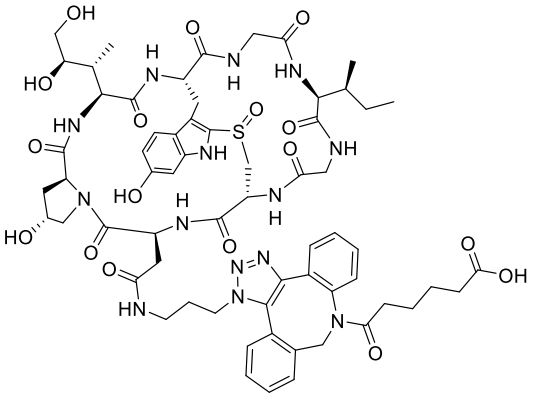

Chemical Formula: $C_{63}H_{78}N_{14}O_{17}S$
Molecular Weight: 1335,46

Ama-N-azido (**2**) (3.53 mg, 3.52 µmol) was dissolved in 150 µL DMF. **DBCO-COOH** (**5**) (3.32 mg, 11.22 µmol) was dissolved in 50 µL DMF and added to the compound **2** solution. The reaction was stirred at room temperature for 4h and then purified in RP-HPLC under the following conditions: λ= 305 nm; gradient: 0 min 5% B; 0-20 min 46% B; 20-20.5 min 100% B; 20.5-22 min 100% B; 22.5-25 min 5% B; A= water with 0.05% TFA; B=ACN. The two isomeric products were isolated and lyophilized overnight.

Ama-N-DBCO-COOH-a (9a): colorless powder (1.25 mg, yield 30%). MS(ESI+) *m/z*: $[MH]^+$ calcd. for $C_{63}H_{79}N_{14}O_{17}S^+$: 1335.54, found: 1335.75; $[M+Na]^+$ calcd. for $C_{63}H_{78}N_{14}NaO_{17}S^+$: 1357.52, found: 1357.75; $[M+2H]^{2+}$: calcd. for $C_{63}H_{80}N_{14}O_{17}S^{2+}$: 668.27, found: 668.50

Ama-N-DBCO-COOH-b (9b): colorless powder (1.30 mg, yield 30%). MS(ESI+) *m/z*: $[MH]^+$ calcd. for $C_{63}H_{79}N_{14}O_{17}S^+$: 1335.54, found: 1335.75; $[M+Na]^+$ calcd. for $C_{63}H_{78}N_{14}NaO_{17}S^+$: 1357.52, found: 1357.75; $[M+2NH_4]^{2+}$ calcd. for $C_{63}H_{86}N_{16}O_{17}S^{2+}$: 685.30, found: 687.50.

Ama-N-BCN-PEG$_6$-OH (10)

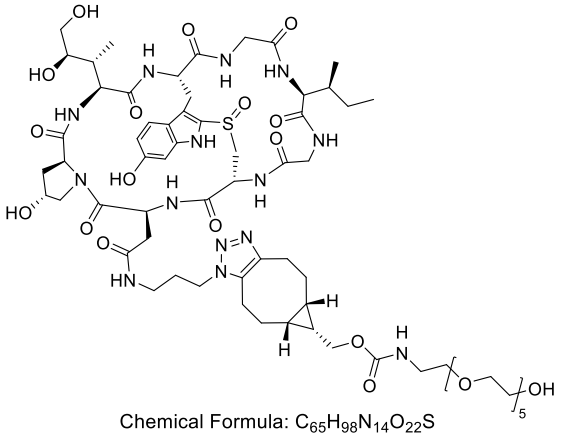

Chemical Formula: $C_{65}H_{98}N_{14}O_{22}S$
Molecular Weight: 1459,63

Ama-N-azido (**2**) (3.58 mg, 3.57 µmol) was dissolved in 150 µL DMF. **BCN-PEG$_6$-OH** (**6**) (4.90 mg, 10.71 µmol) was dissolved in 50 µL DMF and added to the compound **2** solution. The reaction was stirred at room temperature for 3h and then purified in RP-HPLC under the following conditions: λ= 305 nm; gradient: 0 min 5% B; 0-20 min 46% B; 20-20.5 min 100% B; 20.5-22 min 100% B; 22.5-25 min 5% B; A= water with 0.05% TFA; B=ACN. The product was isolated and lyophilized overnight.

Ama-N-BCN-PEG$_6$-OH (10): colorless powder (5.21 mg, yield 90%). MS(ESI+) *m/z*: $[MH]^+$ calcd. for $C_{65}H_{98}N_{14}O_{22}S^+$: 1459.63, found: 1459.83; $[M+Na]^+$ calcd. for $C_{65}H_{99}N_{14}NaO_{22}S^+$: 1481.65, found: 1481.83

Ama-N-DBCO-PEG$_4$-COOH-a, -b (11a, 11b)

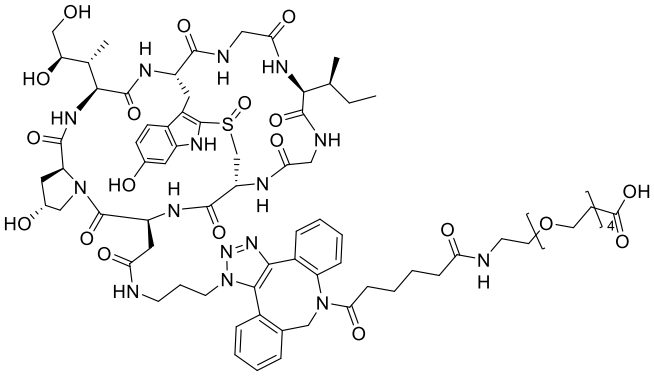

Chemical Formula: $C_{74}H_{99}N_{15}O_{22}S$
Molecular Weight: 1582,75

Ama-N-azido (**2**) (3.35 mg, 3.34 µmol) was dissolved in 150 µL DMF. **DBCO-PEG$_4$-COOH** (**7**) (5.57 mg, 9.88 µmol) was dissolved in 50 µL DMF and added to the compound **2** solution. The reaction was stirred at room temperature for 2h and then purified in RP-

HPLC under the following conditions: λ= 305 nm; gradient: 0 min 5% B; 0-20 min 46% B; 20-20.5 min 100% B; 20.5-22 min 100% B; 22.5-25 min 5% B; A= water with 0.05% TFA; B=ACN. The two isomeric products were isolated and lyophilized overnight.

Ama-N-DBCO-PEG$_4$-COOH-a (11a): colorless powder (1.8 mg, yield 34%). MS(ESI+) *m/z*: $[MH]^+$ calcd. for $C_{74}H_{100}N_{15}O_{22}S^+$: 1582.68, found: 1582.67; $[M+Na]^+$ calcd. for $C_{74}H_{99}N_{15}NaO_{22}S^+$: 1604.67, found: 1604.58; $[M+K]^+$ calcd. for $C_{74}KH_{99}N_{15}O_{22}S^+$: 1620.64, found: 1620.67

Ama-N-DBCO-PEG$_4$-COOH-b (11b): colorless powder (2 mg, yield 37%). MS(ESI+) *m/z*: $[MH]^+$ calcd. for $C_{74}H_{100}N_{15}O_{22}S^+$: 1582.68, found: 1583.67; $[M+Na]^+$ calcd. for $C_{74}H_{99}N_{15}NaO_{22}S^+$: 1604.67, found: 1604.67; $[M+K]^+$ calcd. for $C_{74}KH_{99}N_{15}O_{22}S^+$: 1620.64, found: 1620.58

Ama-W-BCN-OH (12)

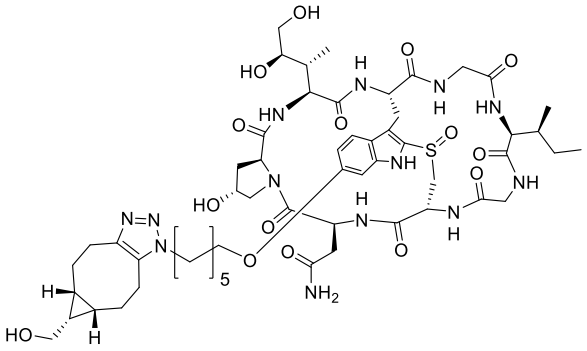

Chemical Formula: $C_{55}H_{79}N_{13}O_{15}S$
Molecular Weight: 1194,37

Ama-W-azido (**3**) (2.95 mg, 2.83 µmol) was dissolved in 150 µL DMF. **BCN-OH** (**4**) (3 mg, 20 µmol) was dissolved in 50 µL DMF and added to the compound **3** solution. The reaction was stirred at room temperature for 4.5h and then purified in RP-HPLC under the following conditions: λ= 305 nm; gradient: 0 min 5% B; 0-14.8 min 46% B; 14.8-15 min 100% B; 15-18 min 100% B; 18.5-22 min 5% B; A= water with 0.05% TFA; B=ACN. The product was isolated and lyophilized overnight.

Ama-W-BCN-OH (12): colorless powder (2.75 mg, yield 81%). MS(ESI+) *m/z*: $[MH]^+$ calcd. for $C_{55}H_{80}N_{13}O_{15}S^+$: 1194.56, found: 1194.75; $[M+Na]^+$ calcd. for $C_{55}H_{79}N_{13}NaO_{15}S^+$: 1216.54, found: 1216.67; $[M+2H]^{2+}$ calcd. for $C_{55}H_{81}N_{13}O_{15}S^{2+}$: 597.78, found: 597.92

Ama-W-DBCO-COOH (13)

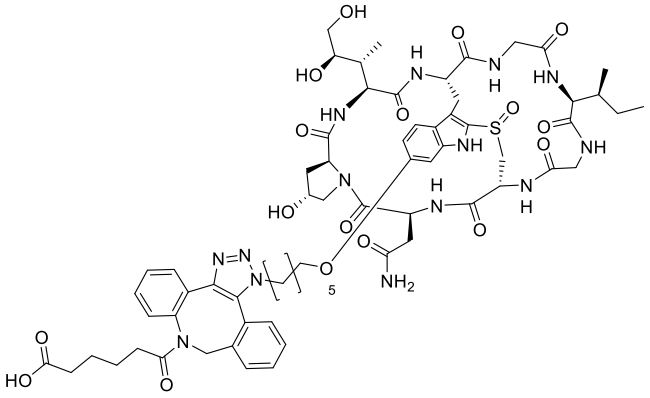

Chemical Formula: $C_{66}H_{84}N_{14}O_{17}S$
Molecular Weight: 1377,54

Ama-W-azido (**3**) (3.79 mg, 3.63 µmol) was dissolved in 150 µL DMF. **DBCO-COOH** (**5**) (1.81 mg, 5.43 µmol) was dissolved in 50 µL DMF and added to the compound **3** solution. The reaction was stirred at room temperature for 4h and then purified in RP-HPLC under the following conditions: λ= 305 nm; gradient: 0 min 5% B; 0-20 min 46% B; 20-20.5 min 100% B; 20.5-22 min 100% B; 22.5-25 min 5% B; A= water with 0.05% TFA; B=ACN. The two isomeric products were isolated and lyophilized overnight.

Ama-W-DBCO-COOH (13): colorless powder (2.76 mg, yield 56%). MS(ESI+) *m/z*: $[MH]^+$ calcd. for $C_{66}H_{85}N_{14}O_{17}S^+$: 1377.59, found: 1377.79; $[M+Na]^+$ calcd. for $C_{66}H_{84}N_{14}NaO_{17}S^+$: 1399.57, found: 1399.75; $[M+2H]^{2+}$: calcd. for $C_{66}H_{86}N_{14}O_{17}S^{2+}$: 689.30, found: 689.50.

Ama-W-BCN-PEG$_6$-OH (14)

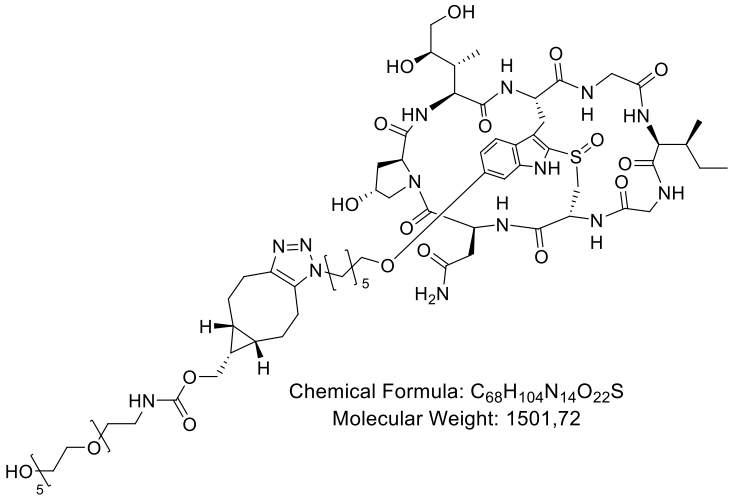

Chemical Formula: $C_{68}H_{104}N_{14}O_{22}S$
Molecular Weight: 1501,72

Ama-W-azido (**3**) (3.30 mg, 3.16 µmol) was dissolved in 150 µL DMF. **BCN-PEG$_6$-OH** (**6**) (4.35 mg, 9.50 µmol) was dissolved in 50 µL DMF and added to the compound **3** solution. The reaction was stirred at room temperature for 3h and then purified in RP-HPLC under the following conditions: λ= 305 nm; gradient: 0 min 5% B; 0-20 min 46% B; 20-20.5 min 100% B; 20.5-22 min 100% B; 22.5-25 min 5% B; A= water with 0.05% TFA; B=ACN. The product was isolated and lyophilized overnight.

Ama-W-BCN-PEG$_6$-OH (14): colorless powder (3.90 mg, yield 82%). MS(ESI+) *m/z*: $[MH]^+$ calcd. for $C_{68}H_{105}N_{14}O_{22}S^+$: 1501.72, found: 1502.83; $[M+Na]^+$ calcd. for $C_{68}H_{104}N_{14}NaO_{22}S^+$: 1523.70, found: 1523.92; $[M+2H]^{2+}$ calcd. for $C_{68}H_{106}N_{14}O_{22}S^+$: 751.37, found: 751.58

Ama-W-DBCO-PEG$_4$-COOH (15)

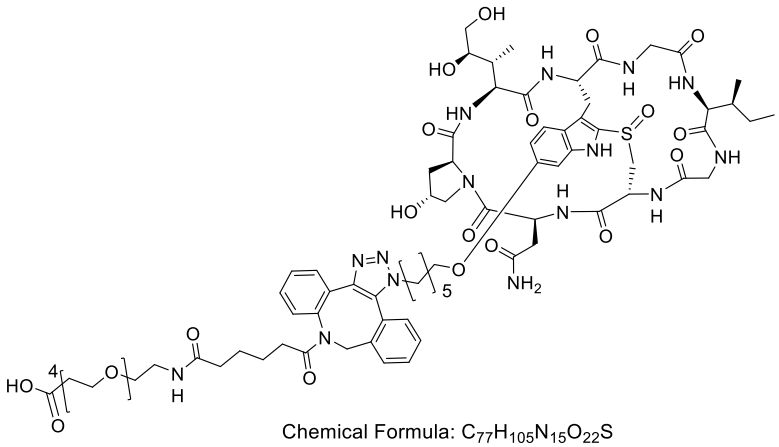

Ama-W-azido (**3**) (3.32 mg, 3.17 µmol) was dissolved in 150 µL DMF. **DBCO-PEG$_4$-COOH** (**7**) (5.13 mg, 8.83 µmol) was dissolved in 50 µL DMF and added to the compound **3** solution. The reaction was stirred at room temperature for 3h and then purified in RP-HPLC under the following conditions: λ= 305 nm; gradient: 0 min 5% B; 0-20 min 46% B; 20-20.5 min 100% B; 20.5-22 min 100% B; 22.5-25 min 5% B; A= water with 0.05% TFA; B=ACN. The product was isolated and lyophilized overnight.

Ama-W-DBCO-PEG$_4$-COOH (15): colorless powder (3.40 mg, yield 63%). MS(ESI+) *m/z*: $[MH]^+$ calcd. for $C_{77}H_{106}N_{15}O_{22}S^+$: 1624.73, found: 1624.75; $[M+Na]^+$ calcd. for $C_{77}H_{105}N_{15}NaO_{22}S^+$: 1646.71, found: 1646.75.

3.2.2 RNA polymerase II Inhibition assay

In vitro RNA transcription assay

The assay was performed in a 96-well plate. In each well, the following components from the Nuclear extract kit (HeLa Scribe) from Promega were added as shown in **Table 18**:

***Table 18**: Hela Scribe Master mix components.*

HelaScribe master mix	Concentration (1xwell)
Hela Nuclear Extract Transcription Buffer	1x
50 mM $MgCl_2$	3 mM
Hela Scribe nuclear extract	8 units
CMV DNA (1 ng/µL)	1 ng
H_2O	Up to 21.5 µL

Starting from a concentration of $1x10^{-5}$M, amanitin and amanitin-derived compounds were serially diluted 1:5 in H_2O, to obtain a range of seven different concentrations. Then, each dilution was added to the nuclear extract mix in the respective wells in triplicates to obtain the concentrations shown in **Table 19**.

***Table 19**: RNA transcription assay plate setup*

	1	2	3	4	5	6	7	8	9	10	11	12
A	Untreated	Untreated	Untreated	Neg ctrl w/o NTPs	Neg ctrl w/o NTPs							
B	$1x10^{-6}$ M Amanitin	$1x10^{-6}$ M Amanitin	$1x10^{-6}$ M Amanitin	$1x10^{-6}$ M Toxin 1	$1x10^{-6}$ M Toxin 1	$1x10^{-6}$ M Toxin 1	$1x10^{-6}$ M Toxin 2	$1x10^{-6}$ M Toxin 2	$1x10^{-6}$ M Toxin 2	$1x10^{-6}$ M Toxin 3	$1x10^{-6}$ M Toxin 3	$1x10^{-6}$ M Toxin 3
C	$2x10^{-7}$ M Amanitin	$2x10^{-7}$ M Amanitin	$2x10^{-7}$ M Amanitin	$2x10^{-7}$ M Toxin 1	$2x10^{-7}$ M Toxin 1	$2x10^{-7}$ M Toxin 1	$2x10^{-7}$ M Toxin 2	$2x10^{-7}$ M Toxin 2	$2x10^{-7}$ M Toxin 2	$2x10^{-7}$ M Toxin 3	$2x10^{-7}$ M Toxin 3	$2x10^{-7}$ M Toxin 3
D	$4x10^{-8}$ M Amanitin	$4x10^{-8}$ M Amanitin	$4x10^{-8}$ M Amanitin	$4x10^{-8}$ M Toxin 1	$4x10^{-8}$ M Toxin 1	$4x10^{-8}$ M Toxin 1	$4x10^{-8}$ M Toxin 2	$4x10^{-8}$ M Toxin 2	$4x10^{-8}$ M Toxin 2	$4x10^{-8}$ M Toxin 3	$4x10^{-8}$ M Toxin 3	$4x10^{-8}$ M Toxin 3
E	$8x10^{-9}$ M Amanitin	$8x10^{-9}$ M Amanitin	$8x10^{-9}$ M Amanitin	$8x10^{-9}$ M Toxin 1	$8x10^{-9}$ M Toxin 1	$8x10^{-9}$ M Toxin 1	$8x10^{-9}$ M Toxin 2	$8x10^{-9}$ M Toxin 2	$8x10^{-9}$ M Toxin 2	$8x10^{-9}$ M Toxin 3	$8x10^{-9}$ M Toxin 3	$8x10^{-9}$ M Toxin 3
F	$1.6x10^{-9}$ M Amanitin	$1.6x10^{-9}$ M Amanitin	$1.6x10^{-9}$ M Amanitin	$1.6x10^{-9}$ M Toxin 1	$1.6x10^{-9}$ M Toxin 1	$1.6x10^{-9}$ M Toxin 1	$1.6x10^{-9}$ M Toxin 2	$1.6x10^{-9}$ M Toxin 2	$1.6x10^{-9}$ M Toxin 2	$1.6x10^{-9}$ M Toxin 3	$1.6x10^{-9}$ M Toxin 3	$1.6x10^{-9}$ M Toxin 3
G	$3.2x10^{-10}$ M Amanitin	$3.2x10^{-10}$ M Amanitin	$3.2x10^{-10}$ M Amanitin	$3.2x10^{-10}$ M Toxin 1	$3.2x10^{-10}$ M Toxin 1	$3.2x10^{-10}$ M Toxin 1	$3.2x10^{-10}$ M Toxin 2	$3.2x10^{-10}$ M Toxin 2	$3.2x10^{-10}$ M Toxin 2	$3.2x10^{-10}$ M Toxin 3	$3.2x10^{-10}$ M Toxin 3	$3.2x10^{-10}$ M Toxin 3
H	$6.4x10^{-11}$ M Amanitin	$6.4x10^{-11}$ M Amanitin	$6.4x10^{-11}$ M Amanitin	$6.4x10^{-11}$ M Toxin 1	$6.4x10^{-11}$ M Toxin 1	$6.4x10^{-11}$ M Toxin 1	$6.4x10^{-11}$ M Toxin 2	$6.4x10^{-11}$ M Toxin 2	$6.4x10^{-11}$ M Toxin 2	$6.4x10^{-11}$ M Toxin 3	$6.4x10^{-11}$ M Toxin 3	$6.4x10^{-11}$ M Toxin 3

For the “Untreated” and “Neg ctrl” wells, H_2O was added instead. The plate was then incubated for 20 min at RT. After this time, 1µL of a 40mM rNTP mix (Promega) was added

to each well, except for the “Neg ctrl” well, where no rNTPs were added. The plate was incubated for 1h at 37°C.

In the next steps, the genomic DNA was digested, and mRNA was extracted. From the RNAs-free DNase set (Qiagen), a DNase mix solution was combined in a tube as shown in **Table 20**. 75 µL of solution were added in each well and the plate was incubated at RT for 10 min.

***Table 20**: Dnase I mix solution*

DNase mix solution	Final concentration (1 well)
RDD Buffer	10 µL
DNase I stock	7 units
Nuclease-free H_2O	Up to 62.5 µL

The RNA was extracted with a RNeasy 96 kit (Qiagen) following the manufacturer’s instructions.

Reverse transcriptase PCR

The reverse transcriptase PCR was performed in a 96-well plate, as shown in **Table 19**. A positive control with CMV DNA was added, along with a non-targeting control (NTC) with water instead of RNA. A PCR master mix from QuantiNova Probe RT-PCR Kit (Qiagen) was combined in a tube as described in **Table 21:**

***Table 21**: PCR master mix for QuantiNova Probe RT-PCR kit.*

PCR Master mix	Final concentration (1 well)
2x QuantiNova Probe RTPCR Master Mix	1x
CB_HN_Scribe_fwd_3	500nM
CB_HN_Scribe_rev_3	500nM
CB_HN_Scribe_Probe 3	250nM
Nuclease-free H_2O	Up to 17.8 µL

17.8µL of the PCR master mix was given to each well. Then 0.2µL of QN-Probe RT mix was added to all the wells except for the positive control and the NTC wells. 2µL of RNA template from the *in vitro* RNA transcription assay were added to the respective wells. 2 ng CMV DNA was added to the positive control well and 2µL H_2O to the NTC well. The

plate was centrifuged briefly, and RT-PCR was run in the BioRad CFX Connect with the cycling conditions defined in **Table 22**:

***Table 22**: PCR cycling conditions.*

	Temperature	**Duration**	
Reverse transcription	45°C	10 min	
Initial denaturation	95°C	5 min	
Denaturation	95°C	5 sec	40 cycles
Annealing	60°C	30 sec	

Ct values were obtained by CFX Maestro Software. The ΔCt of each replicate was calculated in Excel as follows:

$$\Delta Ct = Ct - \bar{x}$$

Where $\bar{x}$ is the average of the triplicates Ct values of the "Untreated" wells. The relative quantity (R) of each triplicate was measured with the formula:

$$R = 2^{-\Delta Ct}$$

The mean of the R triplicate values for each tested concentration was calculated. The RNA polymerase II activity was then expressed in percentage by multiplying the mean values by 100. The percentage values of RNA polymerase II activity were plotted as a function of the $\log_{10}$ of the tested concentrations in GraphPad Prism. The dose-response curve was fitted with a nonlinear regression variable-slope (three parameters) model, and an EC_{50} value for each compound was calculated.

3.2.3 Cell Culture

All cell lines were cultured as adherent monolayers in tissue-culture T75 flasks. Each cell line was grown in the specific growth media described in **Table 12**. Cells were maintained in the incubator at 37°C with 5% CO_2 and passaged when they reached 80-90% confluence. To passage them, the old media was removed, and the cells were washed with once with PBS. After washing, 2mL of a solution of 0.05% Trypsin /EDTA was added to the flask, and incubated for 10 min at 37°C. Once cells were all detached, the reaction was stopped by adding 8.5 mL fresh media and cells were thoroughly resuspended. 20µL of the suspension was diluted 1:1 with Trypan Blue and measured in the Cytosmart cell counter. The desired volume of cells was then added to fresh media in a new T75 flask.

For some cell lines, i.e. HEK 293-OATP1B3 and HEK 293-wt, the flask surface was coated with a solution of 0.1 mg/mL Poly-L-lysine. For this, the Poly-L-lysine solution was incubated in the flask for 30 minutes and then washed three times with PBS.

3.2.4 Cytotoxicity assay

The plate was set up as shown in **Table 23**.

In "Blank" wells only media was added, as negative control. In the "100%" and "Background" no treatment was performed. In the "Test compound" columns, different dilutions of a small molecule or ADC were tested. The wells marked with a number and a letter, e.g.1A, 1B, 1C represent the same concentration in triplicates. Depending on the experiment, starting from a final concentration of compound, 1:5 or 1:3 serial dilutions were performed and tested. Cell lines were seeded in a black 96 well plate at a concentration of 2 – 2.5x10^3 cells per well and incubated for 24h at 37°C, 5% CO_2. After 24h incubation, cells were treated accordingly and incubated for 96h at 37°C. Read-out was performed with the Cell proliferation ELISA, BrdU chemiluminescent Kit (Sigma-Aldrich). After 96h incubation, Brdu labelling solution was added at a final concentration of 10µM. Cells were incubated again for 4h at 37°C. No labelling solution was added in the "Background" cells. After incubation, labelling medium was then removed and cells were fixed with FixDenat for 30 min at room temperature. After fixation, cells were incubated with anti-BrdU-POD solution for 90 min. Afterwards, the plate was washed three times with washing buffer and the substrate solution was added to each well. The plate was incubated in a shaking platform for 3 min at room temperature and signal was measured within 10 min in a microplate reader.

***Table 23**: Set up of a cytotoxicity assay plate.*

	1	2	3	4	5	6	7	8	9	10	11	12
		Test compound 1			Test compound 2			Test compound 3				
A	Blank	1A	1B	1C	1A	1B	1C	1A	1B	1C	100%	Background
B	Blank	2A	2B	2C	2A	2B	2C	2A	2B	2C	100%	Background
C	Blank	3A	3B	3C	3A	3B	3C	3A	3B	3C	100%	Background
D	Blank	4A	4B	4C	4A	4B	4C	4A	4B	4C	100%	Background
E	Blank	5A	5B	5C	5A	5B	5C	5A	5B	5C	100%	Background
F	Blank	6A	6B	6C	6A	6B	6C	6A	6B	6C	100%	Background
G	Blank	7A	7B	7C	7A	7B	7C	7A	7B	7C	100%	Background
H	Blank	8A	8B	8C	8A	8B	8C	8A	8B	8C	100%	Background

"Blank" signal was subtracted from all values. In GraphPad Prism 9.0, the signal obtained from the tested treatment was plotted as a function of the treatment concentration, which was subsequently transformed in log(x). Data were normalized using as 100% cell viability the mean of the values obtained in the "100%" wells and as 0% cell viability the mean of the values obtained in the "Background" wells. The dose-response curve was fitted with a nonlinear regression variable-slope (four parameters) model and EC_{50} values for each compound were calculated.

3.2.5 Antibody cloning and expression

Antibody cloning

Site-directed mutagenesis was performed on the pHDP-anti-PSMA HC plasmid (Heidelberg Pharma) to introduce a cysteine into the heavy chain constant region on the S399 residue. The mutagenesis was performed via PCR reaction, assembled as shown in **Table 24**:

***Table 24**: PCR reaction mix for site-directed mutagenesis.*

PCR reaction mix	Final concentration
2x Phusion High-Fidelity PCR Master Mix with HF Buffer	1x
Forward Primer (100µM)	1µM
Plasmid (10-20ng/µL)	1-2 ng
DMSO	1:20
H_2O	up to 50 µL

PCR was conducted with the following program (**Table 25**):

***Table 25**: PCR program conditions for site-directed mutagenesis*

	Temperature	Duration	
Initial denaturation	98°C	30 sec	
Denaturation	98°C	15 sec	29 Cycles
Annealing	55°C	30 sec	
Extension	72°C	4 min	
Final Extension	72°C	10 min	

After program completion, 40 units of DpnI restriction enzyme were added to the sample to digest the parental DNA. The sample was incubated for 3h at 37°C, and afterwards, DpnI was deactivated at 80°C for 30 min. The digested PCR mixture was then transformed

into chemical competent NEB5α bacteria (NEB). 5 µL of PCR mixture was added to 50µL of bacteria, which were incubated on ice for 30 min. Then, bacteria were heat-shocked at 42°C for 30 sec. and incubated again on ice for 5 min. 950 µL of SOC recovery media was added to the bacteria and the culture was transferred to a culture tube. Bacteria were incubated at 37°C for 1h in a shaking platform (200-250 rpm). After 1h, bacteria were centrifuged at 4300 rpm for 10 min, 900 µL of supernatant was removed, and the pellet was re-dissolved and spread on a LB agar selection plate with ampicillin as selection antibiotic. The plate was incubated at 37°C overnight. The next day, six colonies were selected and grown overnight in ampicillin media. DNA was isolated via QIAprep Spin Miniprep Kit (Quiagen) and was sent for sequencing to GATC/Eurofins (Köln). Successful mutagenesis was then amplified with Endofree Plasmid Mega Kit (Quiagen) for subsequent expression.

Antibody expression

Trastuzumab antibodies, T-D265C and T-S399C and anti-PSMA antibodies, anti-PSMA-D265C and anti-PSMA-S399C, were expressed in Expi293F human embryonic kidney cells. The plasmid containing the heavy chain and the plasmid containing the light chain of a specific antibody were mixed to a total of 750 µg DNA in 25 mL OptiMEM medium. In another 25 mL OptiMEM medium, the PEI transfection reagent, a cationic polymer, was added. The DNA solution and the PEI solution were then combined and incubated for 15 min at room temperature. The mixed solution was then added to $1.25x10^9$ Expi293F cells in 425 mL Expi293 expression medium in a 2L shake flask culture. Cells were incubated at 37°C in a humidified atmosphere with 5% CO_2 in an orbital shaker rotating at 125 rpm. After 18 hours, cell media was changed to fresh media, and cells were incubated for 5 additional days. On day 6, cells were harvested using the Sartoclear Dynamics filtration kit and the supernatant containing the antibody was collected. The antibody was purified via Protein A affinity chromatography, using a TOYOSCREEN AfrProtein column in the Äkta Pure protein purification system (Cytiva). The column was equilibrated with PBS pH 7.4 and the supernatant was applied to the column at a flow rate of 5 mL/min. The antibody bound to the protein A resin was then eluted with 0.1 M Glycine pH 3.0 to fractionation tubes containing neutralization buffer, 1 M Tris-HCl pH 9.0. Antibody containing fractions with a threshold of 50 mAU at 280 nM were pooled. Pooled fractions were purified from aggregates and endotoxins by size-exclusion chromatography (SEC) Fast protein liquid chromatography (FPLC) with HiLoad 16/600 Superdex 200 pg column in the Äkta Start (Cytivia). The column was equilibrated with PBS 7.4 and pooled fractions were loaded with a flow rate of 1.6 mL/min. Fractions with a threshold above 50 mAU at 280 nm were pooled

together and concentrated using Amicon ultra centrifugal filters with 50,000 molecular weight cut-off (MWCO). The antibodies were then stored at 4° C.
High molecular weight and low molecular weight species in the antibody sample were analyzed via SEC High performance liquid chromatography (HPLC) as described in **section 3.2.6**. Endotoxin content was analyzed via Endozyme® II Endotoxin Detection Assay (Biomerieux) as described in **section 3.2.7**. An endotoxin content ≥ 5 EU/mg was considered acceptable.

3.2.6 SEC-HPLC

The presence of low molecular weight and high molecular weight antibody species was measured via SEC-HPLC using a Tosoh UP SW 3000 gel filtration column on an Agilent 1260 Infinity II. The column was first equilibrated with SEC-HPLC running buffer, and 40µg of antibody was then loaded onto the column. The instrument protocol was set to run for 8 minutes at a flow rate of 0.350 mL/min, with the antibody being measured at 280 nm. The results were analyzed using the OpenLab software (Agilent). The peaks were integrated and form that, the area percentage was calculated and the peak retention time determined.

3.2.7 Endotoxin assay

Endotoxin content in the antibody sample was detected using the Endozyme® II Endotoxin Detection Assays (Biomerieux). This assay is based on the on recombinant Horseshoe Crab Factor C (rFC). A standard curve for Lipopolysaccharide (LPS) was established, initiating from a concentration of 50 EU/mL and employing 1:3 serial dilutions in PBS, ultimately reaching a concentration of 0.005 EU/mL. Quality control samples with an LPS concentration of 5 EU/mL and 0.5 EU/mL were prepared. Quality control values were deemed acceptable if they fell within the range of 50% to 200% of the true value. Test samples were diluted 1:5 and 1:50 in PBS. Standard curve solutions, quality control solutions, and samples were added in duplicate to a microplate. The Assay reagent was prepared by combining 8 parts of Assay Buffer, 1 part of Enzyme, and 1 part of Substrate. The assay reagent was added to the standard curve wells, quality control wells, and samples wells, and the fluorescence signal was read at time zero in a pre-warmed 37°C plate reader. Reading was performed with an excitation filter set at 380 nm and an emission filter at 440 nm. The plate was then incubated at 37°C for an hour. After incubation, the plate was read again. The Signal obtained at time zero was then subtracted from the signal read after 1h incubation. The obtained values were plotted in GraphPad Prism 9.0 as a function of the LPS standard concentrations. The standard curve was fitted

with a nonlinear regression variable-slope (four parameters) model, and test values were interpolated to obtain the concentration of LPS in the samples. The concentration limit of LPS in the samples was set to 5 EU/mg.

3.2.8 Antibody conjugation

The first step of the conjugation consisted of the reduction of the thiol groups on the engineered cysteine residues of the antibody. First, the antibody's buffer was exchanged with the specific buffer used for the conjugation. The antibody was injected in a Slide-A-Lyzer dialysis cassette with a molecular weight cut-off (MWCO) of 20K and dialyzed in the specific buffer overnight. For conjugations done in PBS 7.4, this step was not necessary. TCEP was employed in the reduction process, dissolved in the specific buffer for the conjugation, along with 1 mM EDTA to achieve a final concentration of 50 mM. After overnight dialysis, the antibody was placed in a falcon tube, and EDTA was added to a final concentration of 1 mM. 40 equivalents (eq.) of TCEP were used for 1 equivalent of antibody. After TCEP addition, the antibody was incubated at 37°C for 3h in a shaking platform. The antibody was then dialyzed for 4h in 5L of the specific buffer used for the conjugation to remove excess of TCEP. After 4h, the buffer was discarded, and fresh buffer was added to continue the dialysis overnight. The following day, mild oxidation was performed to reform the disulfide bonds of the antibody chains. 20 eq. of dehydroascorbic acid (50 mM in DMSO) were given to the antibody, which was incubated for 3h at room temperature on a shaking platform. Afterward, the payload was added with different equivalents depending on the compound: 10 eq. for Ama-N^{N3}-Bromoacetamide (**16**), 15 eq. Ama-W^{N3}-Bromoacetamide (**17**) and 4 eq. for Ama-N-ctrl (**18**) and Ama-W-ctrl (**19**). Antibody and payload were incubated for 1h at room temperature in the dark on a shaking platform. To stop the reaction with the payload, 25 eq. of N-acetyl cysteine (100 mM in H_2O) were added, and the antibody was further incubated for an additional 15 min at room temperature.

When the conjugation was completed, the newly generated Antibody-drug conjugate (ADC) was then purified to remove the excess of the reagents employed. For *in vitro* experiments only, the ADC was purified with a PD-10 desalting column (Cytivia) using PBS 7.4, following the manufacturer's instructions. For *in vivo* experiments, the ADC was purified by SEC FPLC with HiLoad 16/600 Superdex 200 pg column in the Äkta Start (Cytivia). The column was equilibrated with PBS 7.4 and pooled fractions were loaded with a flow rate of 1.6 mL/min. Fractions with a threshold above 50 mAU at 280 nm were pooled together and concentrated by using Amicon ultra centrifugal filters with 50K MWCO. The antibodies were then stored at 4° C.

Quality control analysis of the ADC comprised SDS-Page (**section 3.2.9**), amanitin Western Blot (**section 3.2.10**), SEC-HPLC (**section 3.2.6**), endotoxin detection assay (**section 3.2.7**), free-amanitin competitive ELISA (**section 3.2.11**), and DAR analysis. Drug to antibody-ratio (DAR) analyses, to detect the conjugated species, were performed with the intact protein in LC-MS (TOF-MS) by the Bioanalytical Department of Heidelberg Pharma GmbH.

3.2.9 SDS-PAGE

To verify purity and molecular weight, the antibodies and ADCs were analyzed by SDS-Page. The ADC, naked antibody and a control ADC were analyzed under reducing and non-reducing conditions. In the reduced samples, 1x Roti buffer (containing beta-mercaptoethanol) was added to 15µg of antibody and heated at 95°C for 5 minutes, while in the non-reduced samples, 1x loading buffer was added to 15µg of antibody. Samples were loaded and on a pre-cast 4-20% Mini-protean TGX stain-free gel and run at 200V for 30 min. Stain-free gels are based on a trihalo compound that covalently binds to tryptophan residues, generating fluorescence. The fluorescence was detected by UV excitation at 302 nm with Azure C400 imaging system.

3.2.10 Western Blot

Successful amanitin conjugation to the heavy chain of the antibody was detected with an anti-amanitin Western Blot. Samples were prepared as described for the SDS-Page experiment, but 10 ng of the tested samples were loaded instead of 15 µg. After electrophoresis, semi-dry blotting was performed using a TransBlot Turbo, and proteins were transferred to a polyvinylidene fluoride (PVDF) membrane for 7 min at 25 V. Subsequently the membrane was incubated with Western Blot blocking buffer for 2h at room temperature. Afterward, the membrane was incubated overnight at 4°C with the anti-amanitin polyclonal antibody. The following day, the excess primary antibody was removed with 3x washing of 10 min in TBST buffer, and membranes were incubated with the secondary antibody, anti-rabbit HRP-linked, for 2h at room temperature. The membrane was washed again three times in TBST buffer and a solution of luminol substrate was added. The chemiluminescent signal was detected with an Azure C400 imaging system.

3.2.11 Free-amanitin competitive ELISA

To detect the presence of free unconjugated toxin in the ADC sample, a free-amanitin competitive ELISA was performed.

The assay was performed in a 96-well Nunc-Immuno plate, coated overnight with a concentration of 6.67 µg/mL anti-amanitin serum in PBS. After incubation with the serum, plates were incubated with ELISA blocking buffer (3% BSA in PBS) for 1h t 37°C and then washed three times with ELISA washing buffer (0.05% Tween in PBS).

The ADC samples were diluted to concentrations of 0.5 mg/mL and 0.1 mg/mL, and 240 µL of 100% ethanol was added to 60 µL of each sample. Then, the solutions were incubated at -20°C for 20 min to facilitate protein precipitation. Afterwards, samples were centrifuged for 10 min at 13000 rpm at 4°C and the supernatant was collected to be evaporated in a rotational speed vacuum for 4h at 53°C. After evaporation, the dried toxin was re-dissolved in 60 µL ELISA sample buffer (1% BSA in PBS, 20% EtOH). Meanwhile, a standard curve was generated, starting from a concentration of 8100 nM amanitin, and serially diluting at a 1:3 ratio, ultimately reaching the lowest concentration of 0.4 nM. The standard curve and the test samples were then mixed with a 1:1 ratio to a solution of 1 nM biotin-amanitin-conjugate. 50 µL of the mixed solutions were then added in duplicate to the coated plate and incubated for 1h at 37°C. Afterward, the plate was washed three times with washing buffer and a solution of 1:1000 streptavidin-HRP in 3% BSA/PBS was added to the wells. The plate was incubated again for 1h at 37°C. Finally, the plate was washed three times with washing buffer, and 100 µL of a TMB-working solution was added to obtain a colorimetric signal. The reaction was stopped after 20 minutes by adding 50 µL of 1 M H_2SO_4. The absorbance of the oxidized TMB substrate was detected at 450 nm and the background signal at 570 nm. The background signal was subtracted from the 450 nm signal, and the analysis proceeded using GraphPad Prism 9.0. The standard curve values were plotted as a function of the amanitin concentration and fitted with a nonlinear regression variable-slope (four parameters) model. Test values were interpolated to obtain the concentration of free toxin in the samples. A maximum of 0.1 µM of free amanitin was accepted in the samples.

3.2.12 *In vivo* studies

Animals were purchased at the age of 6 weeks and experiments were performed following an adaptation period of 1-2 weeks. NMRI nude mice were housed in specific pathogen-free (SPF) rooms in individually ventilated cages, with water and food *ad libitum*. Mice were monitored daily, and body weight was recorded twice a week.

The following termination criteria were applied: Net body weight loss > 20% (compared to body weight at group allocation); tumor weight > 10% of net body weight; tumor volume >

1600 mm^3; ulceration of tumors; poor general conditions and general signs of pain. Euthanasia was performed via cervical dislocation or perfusion with hearth incision.
For *in vivo* applications, BCN-PEG_6-OH (**6**) and DBCO-PEG_4-COOH (**7**) were first dissolved in a vehicle solution of 10% DMSO and 10% (2-Hydroxypropyl)-β-cyclodextrin in PBS, at 20 mg/mL and 15 mg/mL, respectively. ADCs and compounds **6**-**7** were all administered as sterile solutions in PBS, pH 7.4 with an application volume of 10 ml/kg, unless otherwise specified.
Animal handling, caring, euthanasia, and necropsy were conducted by the *in vivo* department of Heidelberg Pharma GmbH. Animal experiments were approved by the local ethics committee (G-64/21 and G-157/17, Regierungspräsidium Karlsruhe, Germany).

3.2.13 Cell line-derived xenograft (CDX) mice models

Tumor-bearing mice were employed to test the efficacy of the ADC treatment and to assess its biodistribution. JIMT-1 xenograft NMRI nude female mice were generated by subcutaneous injection in the right flank of $5x10^6$ JIMT-1 cells in 200 µL RPMI without phenol red. 22RV1 xenograft NMRI nude male mice were generated by subcutaneous inoculation of $5x10^6$ 22RV1 cells in 50% Matrigel and 200 µL RPMI without phenol red. Tumor volume was measured twice a week by caliper measurement according to the formula:

$$Tumor\ volume = \frac{W^2 * L}{2}$$

L= length and W= perpendicular width of the tumor, L>W. If unusual growth was observed, the following formula was used:

$$Tumor\ volume = \frac{L * W * D}{6000}\pi$$

D=diameter.
Once the tumor reached a volume of 100-200 mm^3, mice were randomly allocated in their designated experimental groups.

3.2.14 Determination of the maximum tolerated dose

The maximum tolerated dose (MTD) was determined through the administration of escalating ADC or compound doses via a single-dose intravenous application. Each dose was tested on three animals. The animals were monitored for a duration of up to 3 weeks, with body weight measurements recorded twice weekly. N-azido-ADC, BCN-PEG_6-OH (**6**), and DBCO-PEG_4-COOH (**7**) MTDs were determined in tumor-free NMRI nude female

mice. The PSMA-azido-ADC MTD was determined in both tumor-free and 22RV1 xenograft NMRI nude male mice.

3.2.15 Co-administration studies with the ADC and the neutralizing agents

Co-administration studies with N-azido-ADC, BCN-PEG_6-OH (**6**), and DBCO-PEG_4-COOH (**7**) were performed in tumor-free NMRI nude female mice, with three mice per group. While co-treatment studies with PSMA-azido-ADC and compound **7** were performed in 22RV1 CDX NMRI nude male mice, with three mice per group. ADC treatment was administered by intravenous injection at timepoint zero with an application volume of 5 ml/kg. A second treatment with either compound **6** or **7** was administered at a later timepoint by intravenous injection with an application volume of 10 ml/kg. Animals were monitored for 14 days and body weight was recorded twice weekly. If planned, blood was sampled from the lateral tail vein, collected in anticoagulant-treated tubes, and centrifuged for 10 min at 1000 x g to remove cells. The supernatant, plasma, was collected and stored at -80°C until further use.

3.2.16 Efficacy studies in CDX mice

ADC treatment efficacy in tumor, was evaluated in efficacy studies on CDX mice. Ten mice per group were employed to assess the efficacy of N-azido-ADC, PSMA-azido-ADC, and co-administration effect with DBCO-PEG_4-COOH (**7**). If no second treatment with compound **7** was planned, ADCs were administered intravenously with an application volume of 10 ml/kg. If a second treatment was planned, then the application volume used was 5 ml/kg. The second treatment was applied at a later timepoint by intravenous injection with an application volume of 10 ml/kg. Groups were monitored for a maximum of 100 days. Body weight and tumor volume were recorded twice weekly.

3.2.17 Histopathological and Biodistribution studies

In the histopathological and biodistribution studies, three mice were used for each time point of planned tissue collection. For blood and organ sampling, mice were treated with meloxicam, an analgesic, and anesthetized with isoflurane. Blood was drawn from the retrobulbar venous plexus, and plasma was prepared as described in **3.2.15**. While under anesthesia, animals were perfused with a catheter cannula with 10 mL 0.9% NaCl containing Na-Heparin (20 UI/mL) as an anticoagulant. After perfusion, necropsy was performed, and organs/ tumors were collected. For biodistribution studies, tissues were

weighed, snap-frozen, and stored at -80°C in a cryo vial until further use. For histopathological studies, tissues were embedded in 4% formalin and sent to the Fraunhofer-Institut für Toxikologie und Experimentelle Medizin (ITEM) for pathological evaluation.

3.2.18 Organs and tumor preparation for the ELISA assays

Tissues were placed into homogenizing tubes, each containing one bead. A volume of mouse serum three times that of the tissues was added. In cases where the tissue weight was below 100 mg, the serum volume was proportionally increased, reaching up to six times the tissue weight. Samples were homogenized in the Precellys 24 Homogenizer (Bertin Technologies) with two consecutive cycles at 5500 rpm for 15 sec. Lysates were then centrifuged for 10 min at 13000 rpm at 4°C. The supernatant was used for ELISA experiments.

3.2.19 Azido-ADC ELISA

The assay was performed with 96-well streptavidin-coated plates (Thermo Fisher). The plate was first washed three times with washing buffer (0.05% Tween in PBS) and then 100µL per well of a solution of 10 µg/mL Dibenzocyclooctyne-PEG_4-biotin conjugate in 0.05% Tween in PBS were applied. The plate was incubated at 37°C for 1h. After incubation, plate was washed again three times with washing buffer.
Test samples and standard curve samples were prepared in a solution of 0.02% mouse serum in Sample Buffer (Candor Bioscience). Standard curve dilutions were prepared starting from a concentration of 13400 pM N^{N3} ADC in 0.02% serum in Sample buffer. This concentration was serially diluted in the same buffer in a 1:2 ratio to obtain seven additional concentrations: 6700 pM, 3350 pM, 1680 pM, 830 pM, 420 pM, 210 pM and 110 pM of N^{N3} ADC. Three concentrations, 3350 pM, 830 pM and 210 pM were used as quality control samples. A blank sample with just 0.02% Serum in sample buffer was prepared. Tissue samples underwent an initial 1:10 dilution in PBS, followed by a secondary dilution tailored to the ADC treatment dose. Plasma samples were subjected to a second 1:100 dilution in 0.02% serum in Sample Buffer, while organ and tumor samples underwent a second 1:5 dilution in 0.02% serum in Sample Buffer. 50 µL of standard curve, quality control and tissue samples were added in duplicates to the respective wells and the plate was incubated for 1h at 37°C. Meanwhile, a 1:10000 dilution of anti-Human IgG HRP-linked secondary antibody was prepared in Sample Buffer (without serum). After sample incubation plate was washed three times in washing buffer and 50 µL of secondary

antibody were added in each well. The plate was incubated again at 37°C for 1h. Finally, the plate was washed three times with washing buffer, and 100 µL of a TMB-working solution was added to obtain a colorimetric signal. The reaction was stopped after 20 minutes by adding 50 µL of 1 M H_2SO_4. The absorbance of the oxidized TMB substrate was detected at 450 nm and the background signal at 570 nm. The background signal was subtracted from the 450 nm signal, and the analysis proceeded using GraphPad Prism 9.0. The standard curve values were plotted as a function of the N-azido ADC concentration and fitted with a nonlinear regression variable-slope (four parameters) model. Test values were interpolated to obtain the concentration of N^{N3} ADC in the samples. Mean of duplicate values (m) obtained from the interpolation was adjusted to the dilution factor applied (d), organ weight (W), supernatant volume (V) and ADC molecular weight (MW) according to the formula:

$$ADC\ concentration\ \left(\frac{\mu g}{mL}\right) = \frac{m * d * MW * V}{W} 10^{-9}$$

For plasma samples W=1 and V=1.

3.2.20 Total ADC ELISA

To calculate the concentration of Total ADC in the sample, an anti-amanitin ELISA assay, was performed. For this assay, Nunc-immuno 96-well plates were coated with 50 µL/well of 6.67 µg/mL anti-amanitin serum in PBS and incubated overnight. After incubation, anti-amanitin serum solution was discarded and 150 µL/well of Smart Block (Candor Bioscience) were added. Plate was then incubated at 37°C for 1h. Subsequently, plate was washed three times with washing buffer (0.05% Tween in PBS).

Test samples and standard curve samples were prepared in a solution of 0.02% mouse serum in Sample Buffer (Candor Bioscience). Standard curve dilutions were prepared starting from a concentration of 200 pM N^{N3} ADC in 0.02% serum in Sample buffer. This concentration was serially diluted in the same buffer in a 1:2 ratio to obtain seven additional concentrations: 100 pM, 50 pM, 25 pM, 12.5 pM, 6.3 pM, 3.2 pM and 1.6 pM of N^{N3} ADC. Three concentrations, 100 pM, 25 pM and 6.3 pM were used as quality control samples. A blank sample with just 0.02% Serum in sample buffer was prepared. Tissue samples underwent an initial 1:10 dilution in PBS, followed by a secondary dilution tailored to the ADC treatment dose. Plasma samples of the were subjected to a second 1:100 dilution in 0.02% serum in Sample Buffer, while organ and tumor samples underwent a second 1:10 dilution in 0.02% serum in Sample Buffer. In co-administration studies (**3.2.15**), plasma

samples were subjected to a subsequent 1:20 dilution in 0.02% serum in Sample Buffer. Concurrently, plasma samples obtained from the biodistribution study (**3.2.17**) underwent an additional 1:5 dilution in 0.02% serum in Sample Buffer. 50 µL of the standard curve, quality control and tissue samples were added in duplicates to the respective wells and plate was incubated for 1h at 37°C. Meanwhile, a 1:10000 dilution of anti-Human IgG HRP-linked secondary antibody was prepared in Sample Buffer (without serum). After sample incubation the plate was washed three times in washing buffer and 50 µL of secondary antibody were added in each well. The plate was incubated again at 37°C for 1h. Finally, the plate was washed three times with washing buffer, and 100 µL of a TMB-working solution was added to obtain a colorimetric signal. The reaction was stopped after 20 minutes by adding 50 µL of 1 M H_2SO_4. The absorbance of the oxidized TMB substrate was detected at 450 nm and the background signal at 570 nm. The background signal was subtracted from the 450 nm signal, and the analysis proceeded using GraphPad Prism 9.0. The standard curve values were plotted as a function of the Total ADC concentration and fitted with a nonlinear regression variable-slope (four parameters) model. Test values were interpolated to obtain the concentration of the Total ADC in the samples. Mean of duplicate values (m) obtained from the interpolation was adjusted to the dilution factor applied (d), organ weight (W), supernatant volume (V) and ADC molecular weight (MW) according to the formula:

$$ADC\ concentration\ \left(\frac{\mu g}{mL}\right) = \frac{m * d * MW * V}{W} 10^{-9}$$

For plasma samples W=1 and V=1.

3.2.21 Statistical analysis

Statistical analyses were performed in GraphPad Prism 9.0.
RNA polymerase II assay and HEK293-OATP1B3 cytotoxicity assay were analyzed with One-way ANOVA with Turkey multiple comparison test.
ELISA assay results were analyzed with two-way ANOVA using Bonferroni multiple comparison test. In the ELISA assays, a Lower Limit of Quantification (LLQ), i.e. the lowest acceptable detectable concentration, was determined for each plate. The LLQ was calculated from the lowest acceptable concentration obtained in the calibration curve.
Tumor growth inhibition (TGI) in the efficacy studies was calculated with the following formula:

$$TGI\% = \left(1 - \frac{mean\ TV\ treated\ tumors}{mean\ TV\ control\ tumors}\right) * 100$$

TV=tumor volume.

Survival statistical analysis between different treatment groups was calculated via Log-rank test. Data are shown as the mean ± SEM, as indicated for each experiment. Level of significance was considered at values *p<0.05, **p < 0.01 and ***p < 0.001, ****p < 0.0001.

4 Results

4.1 Generation of neutralized amanitin compounds and their *in vitro* bioactivity

Amanitin-based ADCs (ATAC®s) utilize their cytotoxic payload by efficiently inhibiting cellular transcription through binding to RNA polymerase (RNA pol) II. ATAC®s demonstrated promising results in both *in vitro* and *in vivo* studies (Pahl et al. 2019). Although antibody drug-conjugates (ADCs) are engineered to precisely target tumor tissue, there remains a risk of affecting healthy tissues through off-target uptake. Such off-tumor toxicity poses a substantial obstacle in ADC treatment, and thorough research has revealed that the target-independent uptake of the ADC or of the free payload by healthy cells contributes to this challenge (Nguyen, 2023). In a recent study, the Strain-Promoted Azido-Alkyne Cycloaddition (SPAAC) reaction was used as a neutralization strategy to inactivate the anticoagulant activity of Warfarin post-administration in mice (Ursuegui *et al.*, 2017). SPAAC is based on the reaction of an azide moiety and a strained alkyne which generate a stable triazole (Agard et al. 2004).

To assess the *in vivo* applicability of the neutralization strategy developed by Ursuegui et al. for detoxifying post-treatment of amanitin-based ADCs, the chemistry department of Heidelberg Pharma functionalized amanitin with an azide moiety, resulting in the generation of two new azido-amanitin compounds, Ama-N-azido (**2**) and Ama-W-azido (**3**) (**Scheme 1**). These compounds were then subjected to the neutralization strategy by reacting them with various cycloalkynes, known as neutralizing agents, to produce novel neutralized amanitin compounds. Two of the cycloalkynes tested beard also a PEG moiety to increase their hydrophilicity and facilitate *in vivo* administration (Turecek et al. 2016). Bioactivity of these new compounds was subsequently characterized *in vitro*.

4.1.1 Generation of neutralized amanitin compounds

The Azido-amanitin derivatives Ama-N-azido (**2**) and Ama-W-azido (**3**) were reacted with the neutralizing agents BCN-OH (**4**), DBCO-COOH (**5**), BCN-PEG_6-OH (**6**) or DBCO-PEG_4-COOH (**7**) to obtain the neutralized compounds Ama-N-BCN-OH (**8**), Ama-N-DBCO-COOH-a (**9a**), Ama-N-DBCO-COOH-b (**9b**), Ama-N-BCN-PEG_6-OH (**10**), Ama-N-DBCO-PEG_4-COOH-a (**11a**), Ama-N-DBCO-PEG_4-COOH-b (**11b**), Ama-W-BCN-OH (**12**),

Ama-W-DBCO-COOH (**13**), Ama-W-BCN-PEG$_6$-OH (**14**) and Ama-W-DBCO-PEG$_4$-COOH (**15**) as illustrated in **Scheme 1**.

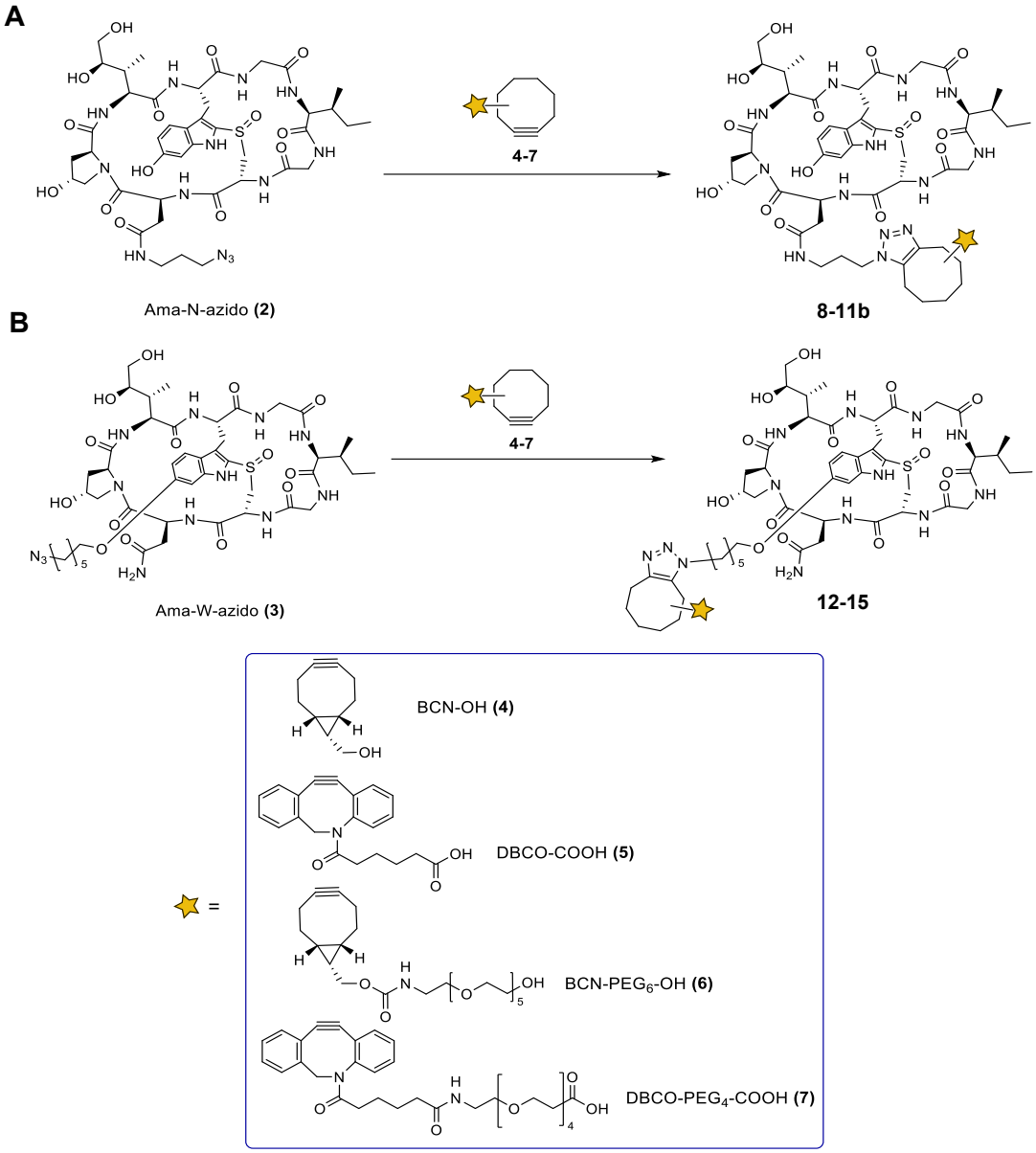

	A (products)	B (products)
BCN-OH (**4**)	Ama-N-BCN-OH (**8**)	Ama-W-BCN-OH (**12**)
DBCO-COOH (**5**)	Ama-N-DBCO-COOH-a/b (**9a-9b**)	Ama-W-DBCO-COOH (**13**)
BCN-PEG$_6$-OH (**6**)	Ama-N-BCN-PEG$_6$-OH (**10**)	Ama-W-BCN-PEG$_6$-OH (**14**)
DBCO-PEG$_4$-COOH (**7**)	Ama-N-DBCO-PEG$_4$-COOH-a/b (**11a-11b**)	Ama-W-DBCO-PEG$_4$-COOH (**15**)

Scheme 1: Synthesis of the amanitin compounds 8-15*. (A) Ama-N-azido (**2**), **4-7**, DMF, until completion. (B) Ama-W-azido (**3**), **4-7**, DMF, until completion.*

Compounds **2** and **3** are derived from α-amanitin, featuring an azide moiety attached to either the asparagine residue (Compound **2**) or the 6-hydroxy group of the tryptophan in the amanitin backbone (Compound **3**). The azide group of **2** and **3** was reacted via SPAAC with the alkyne moiety of the neutralizing agents **4**-**7**, generating a stable 1,2,3-triazole bond. SPAAC reactions with DIBO and BCN derivatives are known to produce regioisomers and diastereoisomers depending on the chirality of the azide.(Dommerholt et al. 2010; Gröst and Berg 2015). However, when compound **2** reacted with the neutralizing agents **5** and **7**, two regioisomers were isolated for each reaction. These products are designated as **9a** and **9b** for the reaction with agent **5**, and **11a** and **11b** for the reaction with agent **7** (**Figure 8**)**.** The bioactivity of the newly generated amanitin compounds **8**-**15** (**Scheme 1**) was evaluated in two complementing assays: an assay that measures cytotoxicity in a cell line that overexpresses the OATP1B3 transporter and an assay that detects RNA polymerase II activity.

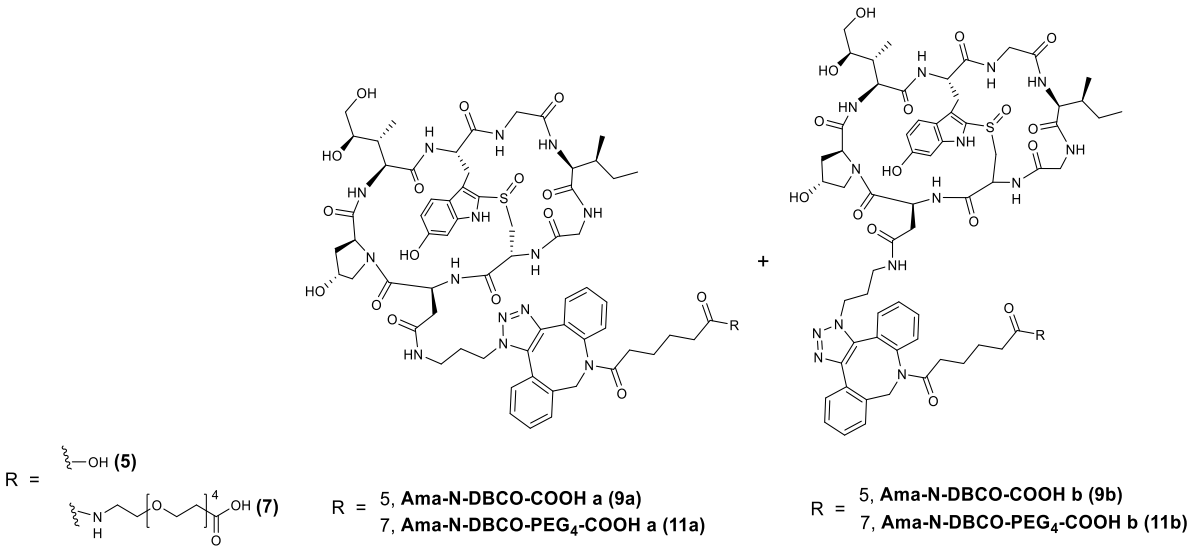

***Figure 8**: **Structure of the regioisomers.** Four regioisomers were obtained upon reaction of Ama-N-azido (**2**) with DBCO-COOH (**5**) or Ama-N-azido (**2**) with DBCO-PEG$_4$-COOH (**7**).*

4.1.2 Cytotoxicity of the neutralized compounds on HEK293-OATP1B3 cells

To characterize the bioactivity of the neutralized compounds **8-15**, their cytotoxicity was analyzed in the HEK293-OATP1B3 cell line. The HEK293-OATP1B3 cell line stably overexpresses the OATP1B3 transporter, which mediates the uptake of amanitin into liver cells (**Figure 9**). This assay was used to evaluate the compounds' affinity for OATP1B3 and their ability to inhibit RNA polymerase II by measuring their cytotoxic effects on the HEK293-OATP1B3 cell line.

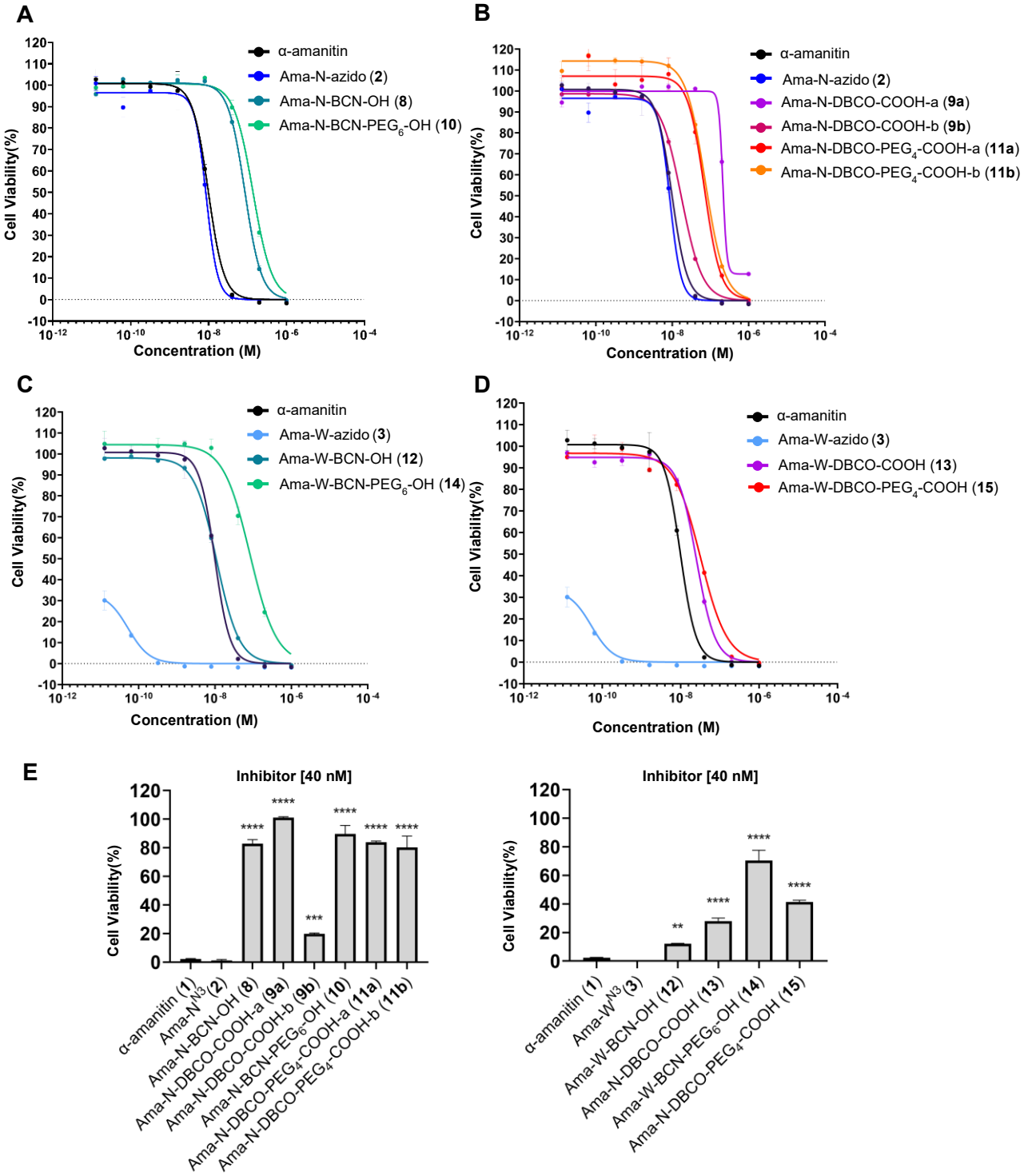

Figure 9: Cytotoxicity on HEK293-OATP1B3 cell line after treatment with the neutralized amanitin derivatives. *Cells were treated with neutralized compounds. .96 h after treatment, cell proliferation was determined by BrdU incorporation assay following manufacturers guidelines. (A) Dose-response curves of α-amanitin (**1**), Ama-N-azido (**2**), Ama-N-BCN-OH (**8**), Ama-N-BCN-PEG6-OH (**9**). (B) Dose-response curves of α-amanitin (**1**), Ama-N-azido (**2**), Ama-N-DBCO-COOH-a (**10a**), Ama-N-DBCO-COOH-b (**10b**), Ama-N-DBCO-PEG4-COOH-a (**11a**), Ama-N-DBCO-PEG4-COOH-b (**11b**).(C) Dose-response curves of α-amanitin (**1**), Ama-W-azido (**3**), Ama-W-BCN-OH (**12**), Ama-W-BCN-PEG6-OH (**13**). (D) Dose-response curves of α-amanitin (**1**), Ama-W-azido (**3**), Ama-W-DBCO-COOH (**14**), Ama-W- DBCO-PEG4-COOH (**15**). (E) Differences in HEK293-OATP1B3 cell viability at 40 nM of the clicked amanitin derivatives. One-way ANOVA Multiple comparison to Ama-N-azido (**2**) or Ama-W-azido (**3**): **p≤0.01; ***p≤0.001; ****p≤0.0001.*

Table 26: EC_{50} values of neutralized amanitin derivatives on HEK293-OATP1B3 cell line. *EC_{50} values calculated from the dose-response curves shown in* ***Figure 9.***

	EC_{50} (nM)		**EC_{50} (nM)**
α-amanitin **(1)**	9.84	α-amanitin **(1)**	9.84
Ama-N-azido **(2)**	8.68	Ama-W-azido **(3)**	0.05
Ama-N-BCN-OH **(8)**	85.1	Ama-W-BCN-OH **(12)**	11.0
Ama-N-DBCO-COOH-a **(9a)**	211	Ama-W-DBCO-COOH **(13)**	25.4
Ama-N-DBCO-COOH-b **(9b)**	17.4	Ama-W-BCN-PEG_6-OH **(14)**	85.4
Ama-N-BCN-PEG_6-OH **(10)**	137.2	Ama-W- DBCO-PEG_4-COOH **(15)**	32.6
Ama-N-DBCO-PEG_4-COOH-a **(11a)**	74.1		
Ama-N-DBCO-PEG_4-COOH-b **(11b)**	69.2		

α-amanitin and Ama-N-azido (**2**) exhibited a similar cytotoxic profile in HEK293-OATP1B3 cells with EC_{50} values of 9.84 nM and 8.68 nM, whereas Ama-W-azido (**3**) showed an even higher cytotoxicity with an EC_{50} value of 0.05 nM (**Figure 9A-C** and **Table 26**). In contrast, the neutralized amanitin compounds **8-15** showed reduced cytotoxicity compared to α-amanitin, compound **2** or compound **3** (**Figure 9A-D** and **Table 26**). The EC_{50} values of compounds **8**, **11a**, and **11b** exhibited a striking deviation of one order of magnitude from the EC_{50} value of compound **2**. Notably, compounds **8** and **10** demonstrated significantly lower cytotoxicity, with their EC_{50} values diverging by two orders of magnitude from that of compound **2**. A considerable reduction in the cytotoxic activity was seen with Ama-W-BCN-OH (**12**), Ama-W-DBCO-COOH (**13**), Ama-W-BCN-PEG_6-OH (**14**) and Ama-W-DBCO-PEG_4-COOH (**15**) compared to the parent compound **3**. Calculated EC_{50} showed differences of three order of magnitude between compounds **12**, **13**, **14** and **15** in comparison to **3** (**Figure 9D-C** and **Table 26**).

To provide a more comprehensive understanding of the achieved results, residual HEK293-OATP1B3 cell viability of the neutralized amanitin compounds **8-15** was compared with α-amanitin, Ama-N-azido (**2**) or Ama-W-azido (**3**) at the concentration of 40 nM (**Figure 9E**). The cell viability percentage at 40 nM acquired from the cytotoxicity experiment in **Figure 9A-D** was plotted for each compound. 40 nM of α-amanitin, compound **2** or **3** were sufficient to achieve complete cell death with no residual cell viability, whereas 40 nM of compounds **8**, **9a**, **10, 11a** and **11b** and **14** led to residual cell viability in the range of 80-100%, confirming their reduced activity.

The neutralized compounds **8-15** were also tested on the HEK293-wild type (wt) cell line, which lack the OATP1B3 expression, to exclude any toxicity related to a transporter-independent uptake (**Figure 10** and **Table 27**). Because of the inherent hydrophilicity of α-amanitin, cellular uptake via passive diffusion is not possible, and *in vitro* cytotoxicity manifests only upon macro-pinocytosis at concentrations in the micromolar range (Pahl et al. 2019). α-amanitin and compound **2** showed poor cytotoxicity, with EC_{50} values of 0.22 µM and 0.27 µM, respectively. A slight cytotoxic effect was also seen with compounds **12** and **14**, with EC_{50} values of 0.82 µM and 0.28 µM.

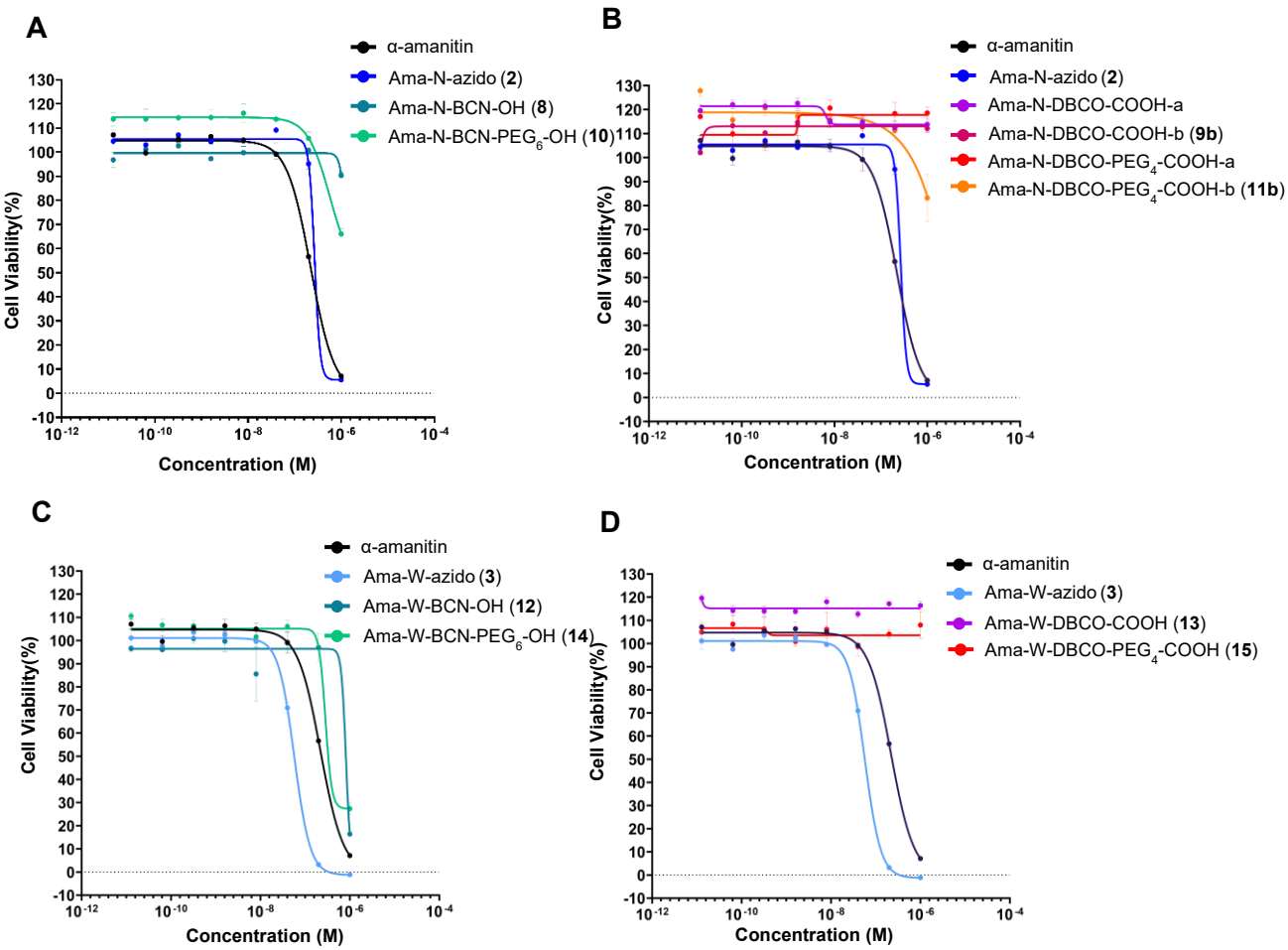

Figure 10: Cytotoxicity on HEK293-wt cell line after treatment with the neutralized compounds*. Cells were treated for 96 h and the read-out was generated by BrdU assay. (A) Dose-response curves of α-amanitin (**1**), Ama-N-azido (**2**), Ama-N-BCN-OH (**8**), Ama-N-BCN-PEG6-OH (**9**). (B) Dose-response curves of α-amanitin (**1**), Ama-N-azido (**2**), Ama-N-DBCO-COOH-a (**10a**), Ama-N-DBCO-COOH-b (**10b**), Ama-N-DBCO-PEG4-COOH-a (**11a**), Ama-N-DBCO-PEG4-COOH-b (**11b**).(C) Dose-response curves of α-amanitin (**1**), Ama-W-azido (**3**), Ama-W-BCN-OH (**12**), Ama-W-BCN-PEG6-OH (**13**). (D) Dose-response curves of α-amanitin (**1**), Ama-W-azido (**3**), Ama-W-DBCO-COOH (**14**), Ama-W- DBCO-PEG4-COOH (**15**).*

Conversely, compound **3** showed slightly higher cytotoxicity with an EC_{50} value of 0.057 µM. The remaining compounds **8**, **9a-b**, **10, 11a-b, 13** and **14** showed no cytotoxicity.

Table 27: EC_{50} values of neutralized amanitin derivatives on HEK293-wt cell line. *EC_{50} values calculated from the dose-response curves shown in* ***Figure 10.*** *n.d.= not determined*

	EC_{50} (µM)		**EC_{50} (µM)**
α-amanitin **(1)**	0.22	α-amanitin **(1)**	0.22
Ama-N-azido **(2)**	0.27	Ama-W-azido **(3)**	0.057
Ama-N-BCN-OH **(8)**	n.d.	Ama-W-BCN-OH **(12)**	0.82
Ama-N-DBCO-COOH-a **(9a)**	n.d.	Ama-W-DBCO-COOH **(13)**	0.28
Ama-N-DBCO-COOH-b **(9b)**	n.d.	Ama-W-BCN-PEG_6-OH **(14)**	n.d.
Ama-N-BCN-PEG_6-OH **(10)**	n.d.	Ama-W- DBCO-PEG_4-COOH **(15)**	n.d.
Ama-N-DBCO-PEG_4-COOH-a **(11a)**	n.d.		
Ama-N-DBCO-PEG_4-COOH-b **(11b)**	n.d.		

The neutralizing agents BCN-OH (**4**), DBCO-COOH (**5**), BCN-PEG_6-OH (**6**), DBCO-PEG_4-COOH (**7**) and DMSO (vehicle control) were tested on HEK293-OATP1B3 cells and in the parental HEK293-wt cells (control cells) to exclude any unspecific toxicity (**Figure 11**). On both cell lines the neutralizing agents **4-7** showed cytotoxicity only at high concentrations, with EC_{50} values of 1 µM or higher (**Table 28**).

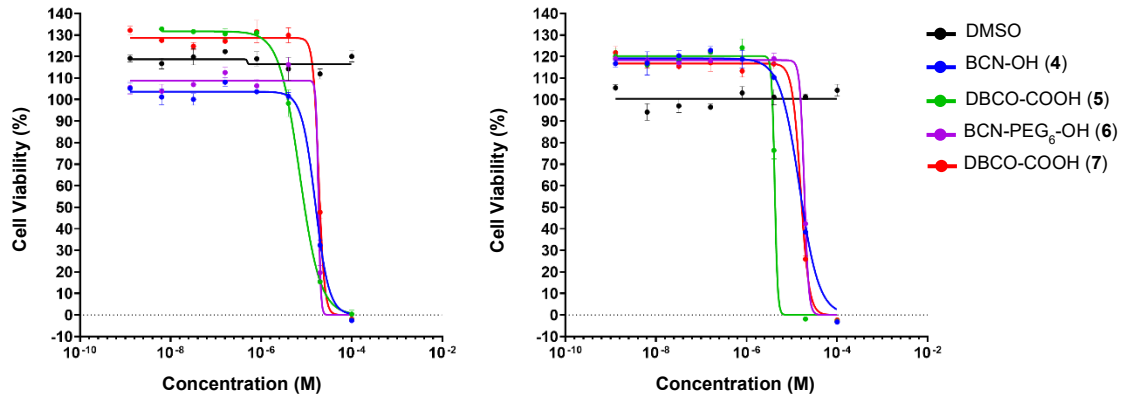

Figure 11: Cytotoxicity of the neutralizing agents 4-7 in HEK293-OATP1B3 and HEK293-wt cells. *HEK293-OATP1B3 (A) or HEK293-wt (B) cells were incubated with the neutralizing agents* ***4-7*** *for 96h. DMSO served as vehicle control. Cell proliferation was determined by BrdU incorporation assay following manufacturers guidelines. Dose-response curves and EC_{50} values were obtained by Prism 9.0 software.*

Table 28: EC_{50} values of neutralizing agents on HEK293-OATP1B3 and HEK293-wt cell lines. *EC_{50} values calculated from the dose-response curves shown in **Figure 11**. n.d.= not determined.*

	HEK293-OATP1B3 EC_{50} (µM)	HEK293-wt EC_{50} (µM)
BCN-OH **(4)**	15.6	14.8
DBCO-COOH **(5)**	7.05	4.29
BCN-PEG_6-OH **(6)**	17.4	18.8
DBCO-PEG_4-COOH **(7)**	18.9	15.6
DMSO	n.d.	n.d.

These results suggested that the SPAAC reaction between BCN-OH (**4**), DBCO-COOH (**5**), BCN-PEG_6-OH (**6**) or DBCO-PEG_4-COOH (**7**) with Ama-N-azido (**2**) or Ama-W-azido (**3**), generated neutralized compounds **8-15** with reduced cytotoxic activity in HEK293-OATP1B3. Structural modifications in the azido-amanitin compounds 2 and 3, resulting from the SPAAC reaction with the neutralizing agents, may inhibit or reduce their uptake by the OATP1B3 transporter. This, combined with reduced inhibition of RNA polymerase II, could explain their lower cytotoxicity.

Amanitin and the azido-amanitin compounds **2** and **3** showed cytotoxicity in the micromolar range in HEK293-wt, while the majority of the neutralized compounds had no cytotoxicity or showed cytotoxicity similar to amanitin. Likewise, the neutralizing agents **4-7** exhibited cytotoxicity in both HEK293-OATP1B3 and HEK293-wt cells only at high concentrations, suggesting non-specific low cytotoxic effects unrelated to the OTAP1B3 transporter.

4.1.3 Impact of the neutralizing reaction on RNA polymerase II activity

The impact of the neutralizing SPAAC reaction on RNA polymerase (RNA pol) II enzyme activity was assessed by comparing RNA pol II inhibition of the neutralized compounds **8-15**, with α-amanitin, Ama-N-azido (**2**) and Ama-W-azido (**3**). Since amatoxins are natural RNA pol II inhibitors, this assay aimed to detect the ability of the newly generated compounds to bind the enzyme, thus inhibiting its function (**Figure 12**). The experimental procedure involved incubating the compounds with the DNA of the Cytomegalovirus (CMV) in a cell nuclear extract containing RNA pol II and all essential components for transcription. After incubation, the resulting mRNA was purified and quantified using reverse-transcriptase PCR. This assay, along with the cytotoxicity results on HEK293-OATP1B3 cells, provides a comprehensive overview of the compounds' activity compared to natural α-amanitin.

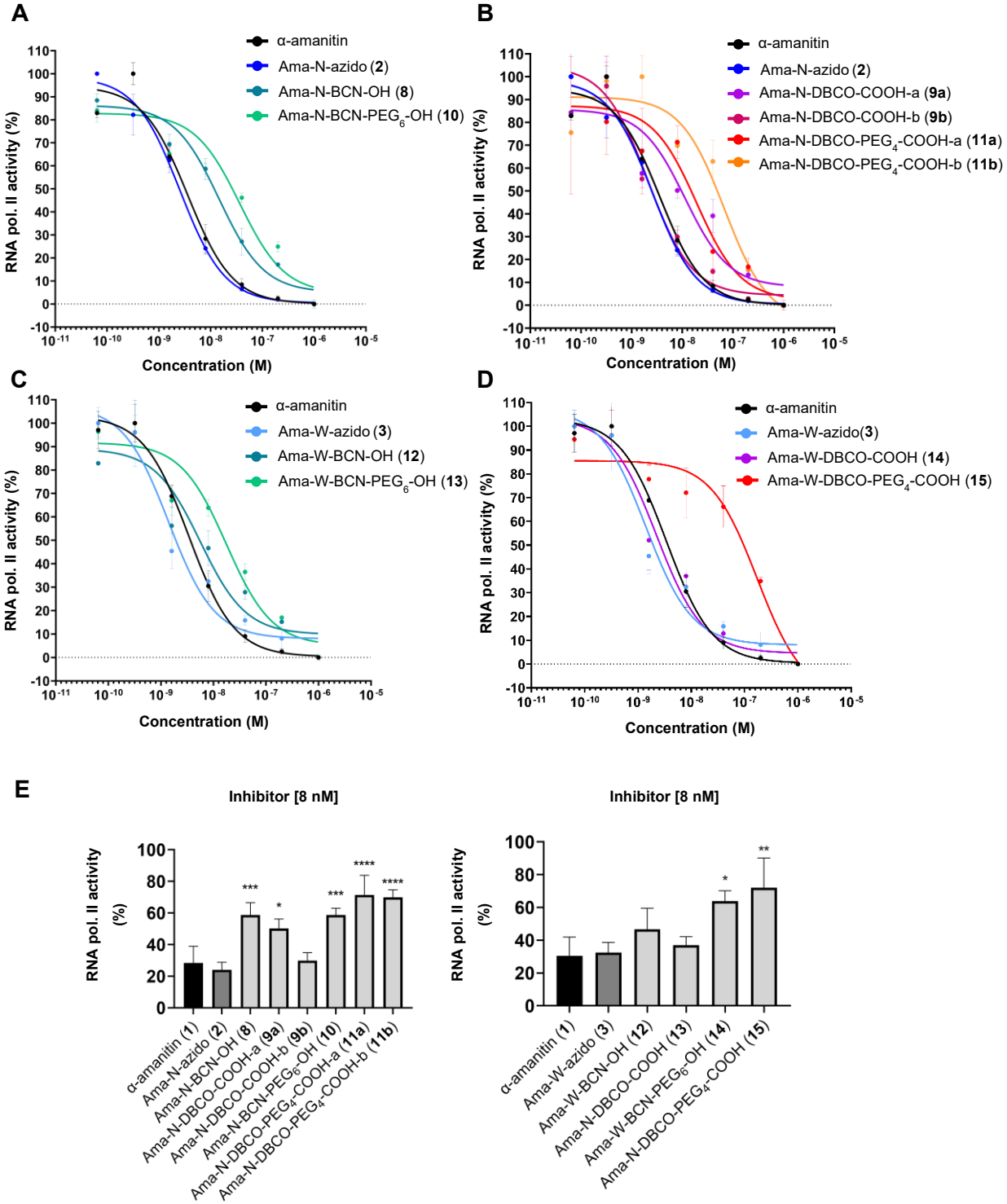

Figure 11: RNA polymerase II activity after treatment with the neutralized amanitin compounds. *Compounds were incubated in a nuclear extract, followed by isolation of the RNA transcript and quantification by RT-qPCR. (A) Dose-response curves of α-amanitin (**1**), Ama-N-azido (**2**), Ama-N-DBCO-COOH-a (**10a**), Ama-N-DBCO-COOH-b (**10b**), Ama-N-DBCO-PEG4-COOH-a (**11a**), Ama-N-DBCO-PEG4-COOH-b (**11b**).(C) Dose-response curves of α-amanitin (**1**), Ama-W-azido (**3**), Ama-W-BCN-OH (**12**), Ama-W-BCN-PEG6-OH (**13**). (D) Dose-response curves of α-amanitin (**1**), Ama-W-azido (**3**), Ama-W-DBCO-COOH (**14**), Ama-W-DBCO-PEG4-COOH (**15**). (E) Differences in RNA pol II activity at 8 nM of the clicked amanitin derivatives. One-way ANOVA Multiple comparison to Ama-N-azido (**2**) or Ama-W-azido (**3**): *p≤0.05; **p≤0.01; ***p≤0.001; ****p≤0.0001.*

Table 29: EC_{50} values of RNA pol II activity dose-response curves. *EC_{50} values were obtained by Prism 9.0 software. Corresponding dose-response curves are shown in* ***Figure 12.***

	EC_{50} (nM)		**EC_{50} (nM)**
α-amanitin **(1)**	3.61	α-amanitin **(1)**	3.61
Ama-N-azido **(2)**	2.55	Ama-W-azido **(3)**	1.40
Ama-N-BCN-OH **(8)**	14.6	Ama-W-BCN-OH **(12)**	5.62
Ama-N-DBCO-COOH-a **(9a)**	11.3	Ama-W-DBCO-COOH **(13)**	2.23
Ama-N-DBCO-COOH-b **(9b)**	2.10	Ama-W-BCN-PEG_6-OH **(14)**	17.6
Ama-N-BCN-PEG_6-OH **(10)**	36.6	Ama-W- DBCO-PEG_4-COOH **(15)**	173
Ama-N-DBCO-PEG_4-COOH-a **(11a)**	19.2		
Ama-N-DBCO-PEG_4-COOH-b **(11b)**	68.2		

As expected, α-amanitin showed a clear, dose-dependent inhibition of RNA pol II activity with EC_{50} = 3.61 nM, (**Figure 12A** and **Table 29**) (Wienland and Faulstich 1991).

Compound **2**, showed an RNA pol II activity profile similar to the one of α-amanitin (EC_{50} = 2.55 nM), while compound **3** displayed an even stronger inhibition (EC_{50} = 1.40 nM, **Table 29**). These results indicate that the introduction of the azide moiety does not affect the ability of the amanitin derivatives to bind to RNA polymerase II and disrupt its function. On the contrary, almost all neutralized amanitin compounds, except compounds **9b**, **12** and **13**, displayed at least a 5-fold higher RNA pol II activity and thereby a reduced RNA pol II inhibition, compared to compound **2** or **3** (**Figure 12A-D** and **Table 29**). Among the compounds derived from Ama-N-azido (**2**), compounds **10**, **11a** and **11b** led to the weakest inhibition of RNA pol II showing a RNA pol II activity 14-fold, 7-fold and 26-fold higher compared to compound **2**, respectively (**Figure 12A-B** and **Table 29**). Interestingly, the regioisomers **9a** and **9b**, as well as **11a** and **11b**, demonstrated distinct levels of inhibition of RNA polymerase II, indicating that isomers may possess varying levels of bioactivity, likely influenced by the conformations they adopt.

Among the compounds resulting from Ama-W-azido (**3**), compounds **14** and **15** displayed the weakest inhibition of RNA pol II (**Figure 12C-D**) showing a 13-fold, and 123-fold higher RNA pol II activity compared to compound **3**, respectively (**Table 29**).

For a more comprehensive view, the RNA pol II activity of the neutralized amanitin compounds **8**-**15** was compared with α-amanitin, Ama-N-azido (**2**), or Ama-W-azido (**3**) at a concentration of 8 nM, slightly above the EC_{50} of amanitin (**Figure 12E**). With compound **2** only approximately 20% residual activity of RNA pol II was observed, while in case of the neutralized compounds **8**, **10, 11a** and **11b** 60% residual activity of the enzyme was

maintained. Similarly, residual RNA pol II activity was 30-40% higher with neutralized compounds **14,** and **15,** than with the parent compound **3**.

In summary, these results indicate that the SPAAC reaction between Ama-N-azido (**2**) or Ama-W-azido (**3**) and either BCN-PEG_6-OH (**6**) or DBCO-PEG_4-COOH (**7**) yielded the most effective neutralized amanitin compounds, exhibiting at least a 5-fold higher EC_{50} compared to compound **2** or **3**. These compounds exhibited a reduced capacity to bind RNA pol II, consequently disrupting the inhibitory function of the toxin.

The SPAAC reaction with the neutralizing agents **4-7** possibly induced structural changes or potential steric hindrance in the neutralized compounds disrupting the binding to RNA pol II. In particular, the neutralized compounds **10**, **11a**, **11b, 14** and **15** showed lower RNA pol II inhibition compared to the azido-amanitin Ama-N-azido (**2**) or Ama-W-azido (**3**). The reduced activity of compounds **10**, **11a**, **11b** and **14**, **15** in comparison with **2** or **3** was also confirmed by a lower cytotoxicity on HEK293-OATP1B3 cells. Interestingly, compound **3** showed a full-blown cytotoxicity with an EC_{50} 200-fold lower than that of α-amanitin, while demonstrating an RNA pol II activity profile similar to α-amanitin. This result might suggest that the introduction of the azide moiety in the tryptophan residue of amanitin increases affinity for the OATP1B3 transporter.

Based on these outcomes, BCN-PEG_6-OH (**6**) or DBCO-PEG_4-COOH (**7**) were selected as optimal neutralizing agents for the detoxification of amanitin-based ADCs post-treatment.

4.2 Generation of new azido-amanitin ADCs and *in vitro* evaluation

Results from the RNA polymerase II activity and HEK293-OATP1B3 cytotoxicity assays demonstrated that the SPAAC reaction between the azido-amanitin derivatives Ama-N-azido (**2**) or Ama-W-azido (**3**) and BCN-PEG_6-OH (**6**) or DBCO-PEG_4-COOH (**7**) generated neutralized compounds with reduced activity. The next phase involved examining the impact of the neutralization strategy with the neutralizing agents **6** and **7** on amatoxin-based ADCs to assess whether treatment activity can be reduced. To evaluate this approach, Ama-N-azido (**2**) and Ama-W-azido (**3**) were conjugated to the anti-HER2 antibody Trastuzumab to create two novel azido-amanitin-based ADCs. Trastuzumab was selected as a model for the conjugation due to its extensive *in vitro* and *in vivo* characterization and its well-documented use in the treatment of HER2-positive breast cancer with two FDA-approved ADCs Trastuzumab emtansine and Trastuzumab Deruxtecan (Barok et al. 2014; André et al. 2023).

Prior to *in vivo* studies, the cytotoxic activity of the new azido-amanitin-based ADCs was tested on HER2-positive and HER2-negative breast cancer cell lines *in vitro*.

4.2.1 Thiol-bromoacetamide conjugation to a Trastuzumab-based THIOMAB™

Although the thiol-maleimide conjugation has been used by the majority of ADCs (Walsh et al. 2021) approved by the FDA, and in clinical trials, it turned out that the structure of Ama-N-azido (**2**) and Ama-W-azido (**3**) was not suitable for this type of conjugation. It has been shown that a 1,3 Dipolar Cycloaddition reaction can occur between the maleimide and the azide moiety, leading to polymerization of the compound (Sinclair et al. 2009) (**Figure 13**). Therefore, instead of a maleimide moiety, a bromoacetyl group was chosen to facilitate conjugation to the engineered unpaired cysteine side chains of the THIOMAB™. The antibody T-D265C, a Trastuzumab-based antibody with engineered cysteines on both aspartate residues in position 265 (according to EU numbering) (Edelman et al. 1969) of the heavy chains, was used to perform the site-specific conjugation.

Compounds **2** and **3** were equipped with a cathepsin B cleavable linker, on the hydroxytryptophan residue in Ama-N-azido-Bromoacetamide (**16**) and on the first asparagine residue in Ama-W-azido-Bromoacetamide (**17**). Additionally, a terminal bromoacetamide group was included for the conjugation (**Figure 14A**). The cleavable linker consisted of a valine-alanine (Val-Ala) dipeptide and a p-aminobenzyl (PAB) self-immolating spacer. The reaction of a bromoacetamide derivative to a thiol group at a slightly alkaline pH leads to the formation of a thioether bond via nucleophilic substitution (**Figure 14B**)(Hermanson, 2013).

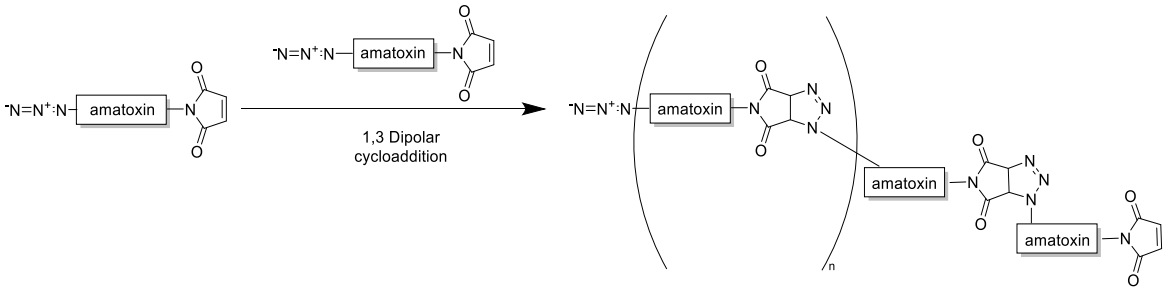

Figure 13: 1,3-Dipolar Cycloaddition of an azido-amanitin derivative functionalized with maleimide. *The cycloaddition reaction between the azide moiety and the maleimide group led to the polymerization of the compound.*

However, the conjugation is not 100% specific due to possible side reactions with the imidazolyl side chain of histidines, the primary ε-amine group of lysines and the thioether of methionines. This necessitates a strict control of the pH during conjugation to avoid the formation of such undesired by-products (Hermanson 2013b). The key benefit of this

conjugation method lies in the formation of a thioether bond, which has demonstrated greater stability in plasma and does not undergo retro-Michael reaction, the so-called maleimide exchange to other plasma thiols, e.g. human serum albumin (Alley et al. 2008). This stability prevents the deconjugation of the ADC in blood circulation, which would otherwise lead to the loss of payload and a reduction in efficacy, as well as off-site toxicity due to binding to serum albumin (Szijj et al. 2018).

The first conjugation was performed with 4 equivalents of Ama-N-azido-Bromoacetamide (**16**) at different conditions and various buffers (**Table 30**). To confirm the success of the conjugation, the ratio of the payload conjugated to the antibody, also referred to as drug-to-antibody-ratio (DAR) was measured by Liquid chromatography-mass spectrometry (LC-MS). This first round of conjugation resulted in either a low or heterogeneous DAR. Conjugations in PBS at pH=7.4 with 1 to 3h of incubation with the reactive payload, led to DARs below 1 and to up to 80% of unconjugated antibody heavy chain (HC), which carries the engineered cysteine position and should be the target of the conjugation.

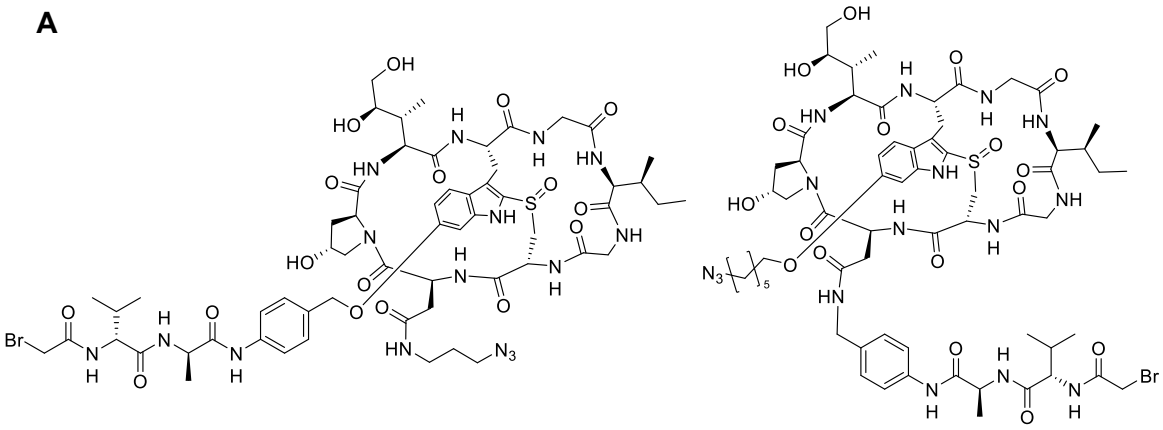

Figure 12: Structures of Ama-N-azido-bromoacetamide (16), Ama-W-azido-bromoacetamide (17) and linker: *(A) Structure of compound **16**, bearing a Val-Ala cleavable linker on the hydroxytryptophan residue and compound **17** bearing a Val-Ala cleavable linker on the asparagine residue. Both compounds (**16**, **17**) are functionalized with a terminal bromoacetamide for conjugation to the antibody´s thiol group. (B) Illustration of the thiol-bromoacetamide conjugation and linker composition.*

Also, conjugation in either Borate, NaPi/NaCl or Tris/NaCl buffer caused low DARs with high percentage of unconjugated species. Therefore, those buffers were excluded from further conjugation optimization.

Table 30: Conjugation test of Ama-N-azido-bromoacetamide (16) to T-D265C. *Conditions for conjugation of compound* ***16*** *to T-D265C. 4 eq. of the compound were incubated for 1h at RT with T-D265C unless otherwise specified.*

Buffer	pH	Unconjugated HC (%)	Av. DAR
PBS, 1mM EDTA	7.4	40	0.75
PBS, 1mM EDTA 3h incubation*	7.4	80	0.35
20 mM Boric acid, 1mM EDTA	8	55	0.67
20 mM TRIS, 0.15 M NaCl, 1mM EDTA	8.5	54	0.77
20 mM NaPi, 0.15 M NaCl, 1mM EDTA	8	64	0.57
50 mM Boric acid, 1mM EDTA	8	60	0.62
50 mM TRIS, 0.15 M NaCl, 1mM EDTA	8.5	66	1.04

The position of the engineered cysteine on the antibody can play a huge role in the reactivity of the thiol group and in the stability of the conjugate (Junutula et al. 2008a; Ohri et al. 2018). Therefore, to improve the thiol-bromoacetyl conjugation to Trastuzumab, engineered cysteines at positions A118, A327, S239 and S399 of the Trastuzumab heavy chain were evaluated for conjugation efficiency. Conjugation was performed with 4 eq. of Ama-N-azido-Bromoacetamide (**16**) in PBS buffer pH=7.4 (**Table 31**). Conjugation to Trastuzumab bearing the S399C substitution (T-S399C) led to the highest and most homogeneous DAR result with only 33% of unconjugated HC, so this antibody was chosen for further optimizations.

Next, the equivalents of compound **16** were increased from 4 to 10 and PBS buffer was adjusted to a pH of 8 right before incubation with the payload. This adjustment aimed to enhance the availability of thiolate anions for the subsequent reaction with bromoacetamide and to avoid side reactions with histidines and lysins at more alkaline pHs (Wall et al. 2012).

Table 31: Conjugation of Ama-N-azido-Bromoacetamide (16) to different engineered cysteines in Trastuzumab. *Conjugations were performed for 1h at RT in PBS pH=7.4, 1 mM EDTA with 4 eq. of compound **16**.*

Cysteine substitution on Trastuzumab	Unconjugated HC (%)	Av. DAR
HC-A118C	87	0.11
HC-A327C	64	0.52
HC-S239C	69	0.45
HC-S399C	33	1.02

The resulting ADC, N-azido-ADC showed a DAR of 2 (**Figure 15A**), whereas the conjugation of Ama-W-azido-Bromoacetamide (**17**) to T-S399C under the same conditions resulted in a DAR of only 1.47. A further increase of the equivalents of compound **17** from 10 to 15 finally led to a W-azido-ADC with a DAR of 2.06 (**Figure 15A**).

The non-reduced SDS-PAGE revealed two closely situated bands at approximately 150 kDa for both N-azido-ADC and W-azido-ADC, falling within the same range as the unbound T-S399C and the Ctrl-ADC, confirming the accurate structure and purity of the samples.

In the reduced SDS-PAGE, all samples exhibited a single band at around 25 kDa, corresponding to the light chains of the antibody, and a more intense band at approximately 50 kDa, representing the heavy chains of the antibody. A slight upward shift of the 50 kDa bands was observed in the conjugated antibodies compared to the unbound T-S399C, indicating the presence of the conjugated payload. In the non-reduced anti-amanitin Western Blot (WB), a signal at 150 kDa was detected, indicating amanitin conjugation to the antibody in samples N-azido-ADC, W-azido-ADC, and Ctrl-ADC.

Furthermore, conjugation of amanitin to the heavy chain was confirmed in the reduced anti-amanitin WB. (**Figure 15B**). These quality analysis results confirmed the correct conjugation of the amanitin derivatives to the T-S399C antibody.

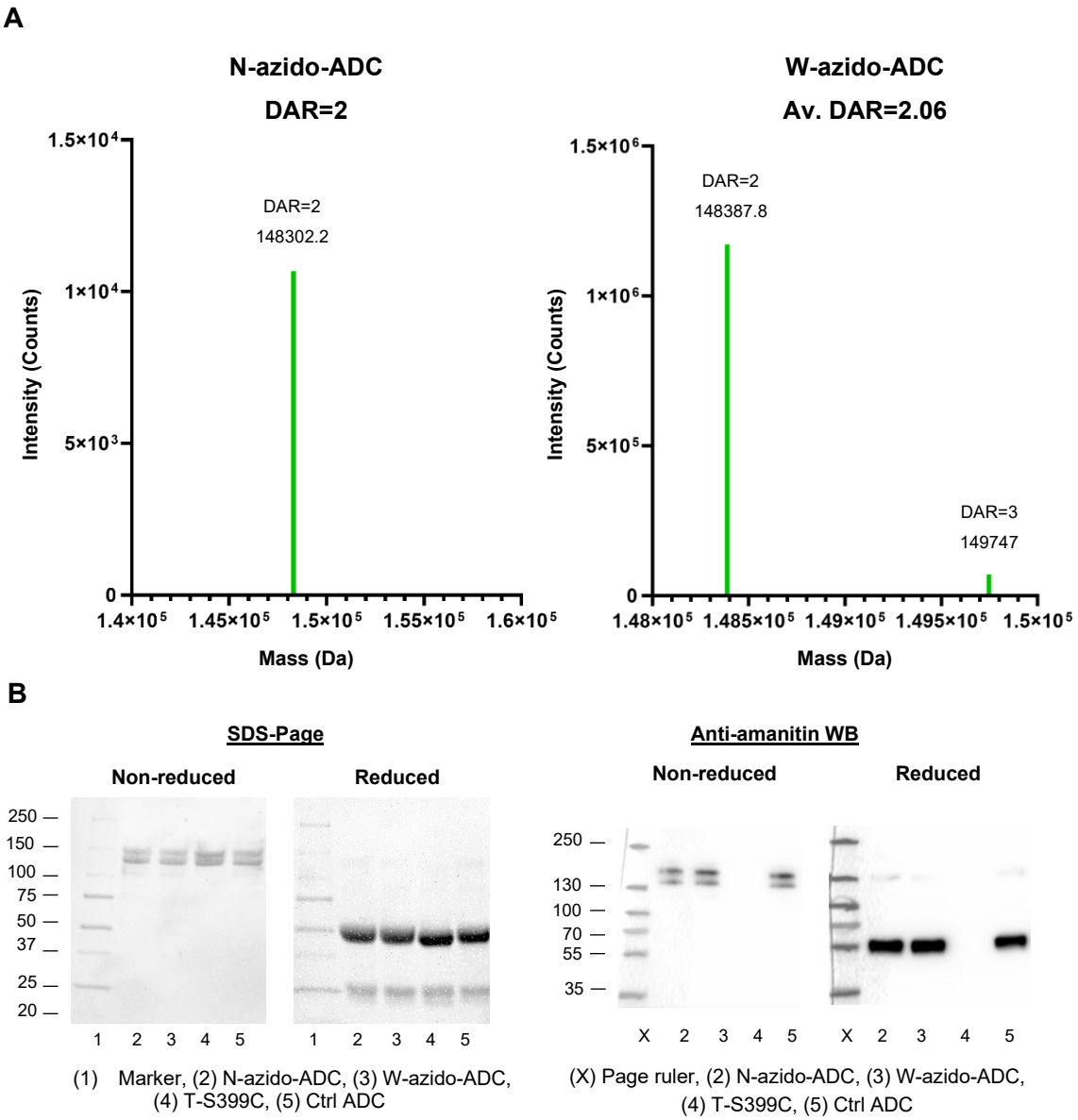

***Figure 13: Conjugation of Ama-N-azido-Bromoacetamide (16) and Ama-W-azido-Bromoacetamide (17) to T-S399C**. (A) DAR profiles of N-azido-ADC, resulting from the conjugation of 10 eq. of compound **16** to T-S399C (left) and of W-azido-ADC, resulting from the conjugation of 15 eq. of compound **17** to T-S399C (right). (B) Non-reduced and reduced SDS-Page (left) and anti-amanitin Western blot (right) of N-azido-ADC, W-azido-ADC, T-S399C and Ctrl-ADC.*

4.2.2 Cytotoxicity of N-azido-ADC and W-azido-ADC on HER2-positive and HER2-negative cell lines

To assess whether the newly synthetized ADCs were still able to induce potent cell killing similar to Trastuzumab ADCs based on unmodified Amanitin, the cytotoxicity of N-azido-ADC and W-azido-ADC was tested in breast adenocarcinoma HER2-positive SKBR-3, JIMT-1 cell lines and on the HER2-negative MDA-MB-231 cell line. Notably, SKBR-3 cells displays higher HER2 expression than JIMT-1 cells (Maddox et al. 2022). The JIMT-1 cell

line shows resistance to anti-HER2 antibody treatment due to low HER2 expression and masking of the trastuzumab binding site by glycoproteins (McCluskey et al. 2013; Mercogliano et al. 2017).

To compare the treatment efficacy of the azido Amanitin ADCs N-azido-ADC and W-azido-ADC, two control ADCs with unmodified Amanitin Ama-N-ctrl (**18**) and Ama-W-ctrl (**19**) were generated (**Figure 16**). Compound **18** features a Val-Ala cleavable linker on the hydroxytryptophan residue of amanitin similar to Ama-N-azido-Bromoacetamide (**16**) but lacks the azide moiety on the asparagine residue. Compound **19** has a Val-Ala cleavable linker on the asparagine residue of amanitin similar to Ama-W-azido-Bromoacetamide (**17**), but no azide moiety on the hydroxytryptophane residue. Both compounds **18** and **19** were equipped with a maleimide moiety on the linker, facilitating thiol-maleimide conjugation to T-S399C. Given that thiol-maleimide conjugation is the standard method for amatoxin-derived antibody-drug conjugates (ATAC®s), this type of conjugation was employed in the control ADCs.

Compounds **18** and **19** were conjugated to T-S399C to produce N-ADC-ctrl and W-ADC-ctrl, both with an average DAR of 2.

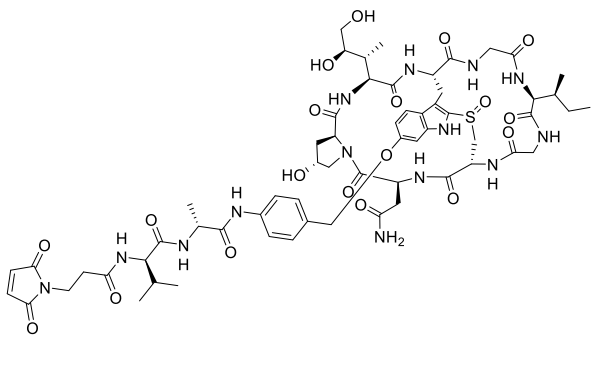

Ama-N-ctrl (18)

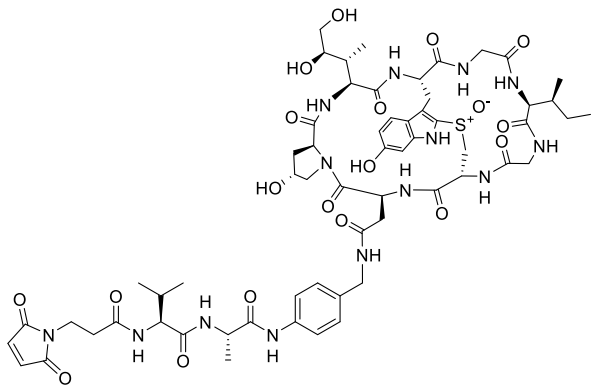

Ama-W-ctrl (19)

Figure 14: Structures of Ama-N-ctrl (18), Ama-W-ctrl (19): *Structure of compound **18**, bearing a Val-Ala cleavable linker on the hydroxytryptophan residue and compound **19** bearing a Val-Ala cleavable linker on the asparagine residue, both bearing a terminal maleimide moiety.*

Cytotoxicity of the N-azido-ADC, W-azido-ADC and the corresponding control ADCs, N-ADC-ctrl and W-ADC-ctrl was then tested in HER-positive SKBR-3, JIMT-1 and HER2-negative MDA-MB-231 cell lines (**Figure 17** and**Table 32**).

N-azido-ADC demonstrated high efficacy in HER2-positive SKBR-3 and JIMT-1 cells. The cytotoxic profile of N-azido-ADC resembled the one obtained with the control ADC, N-ADC-ctrl. While W-azido-ADC showed only partial cytotoxicity in SKBR-3 cells, it

demonstrated no cytotoxic effect in JIMT-1 cells (**Table 32**), W-ADC-ctrl displayed cytotoxic activity against both SKBR-3 and JIMT-1 cell lines. No cytotoxicity was seen in the HER2-negative cell line MDA-MB-231, confirming a specific, target-related cytotoxicity for all four ADCs.

Taken together, the cytotoxicity assay revealed the efficacy of the N-azido-ADC in both HER2-positive cell lines with EC_{50} values in the picomolar range, whereas W-azido-ADC showed only partial cytotoxicity in SKBR-3 cells. Therefore, N-azido-ADC was selected for further *in vitro* and *in vivo* evaluations.

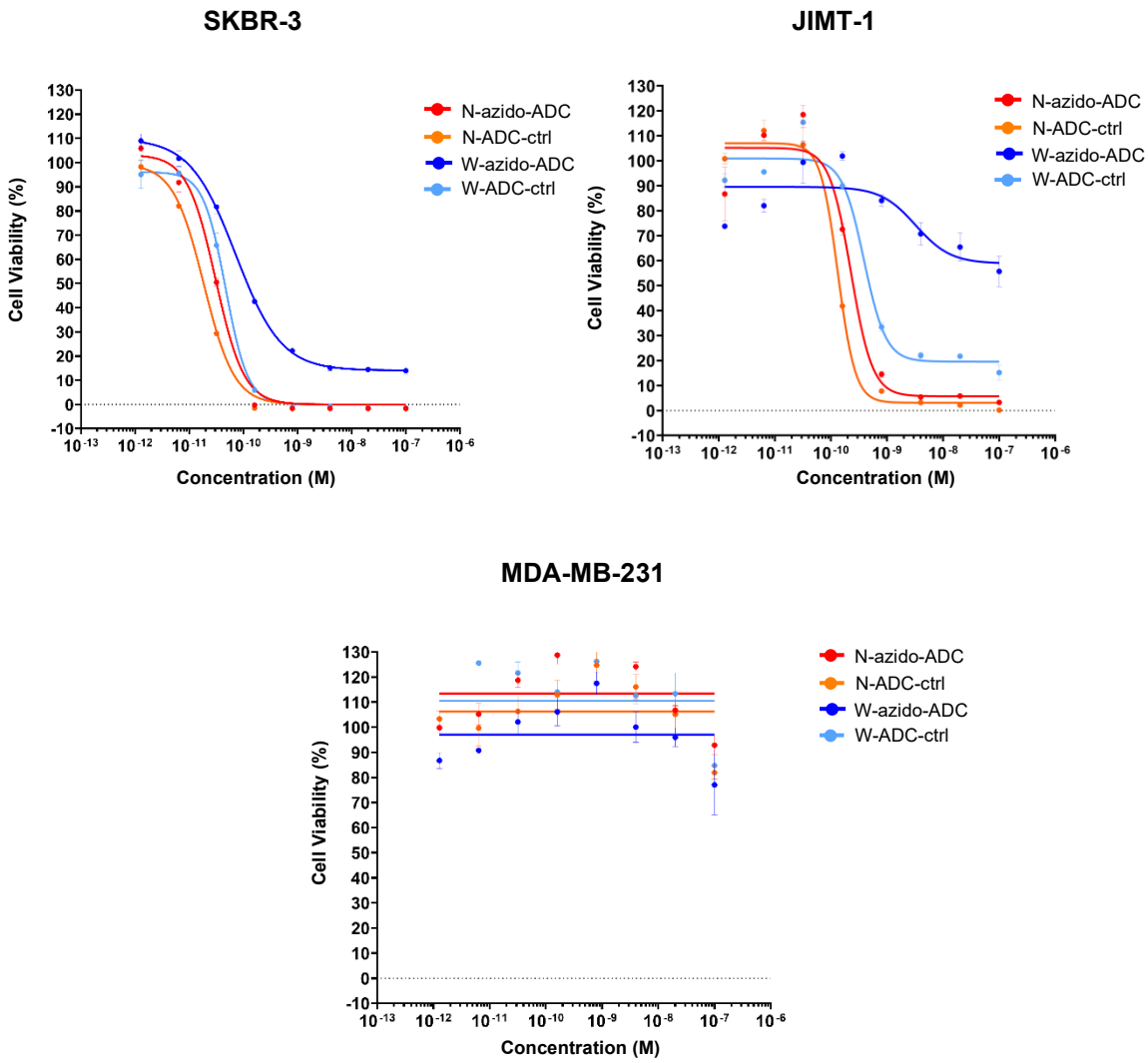

Figure 15: Cytotoxicity of anti-HER2 ADCs on HER2-positive and negative cell lines. *Dose-response curves of anti-HER2 ADCs on SKBR-3, JIMT-1, and MDA-MB-231 cell lines. Cells were treated with different concentrations of the ADCs or α-amanitin (**1**) for 96 h. Cell proliferation was determined by BrdU incorporation assay following manufacturers guidelines. Dose-response curves and EC_{50} values were obtained by Prism 9.0 software.*

Table 32*: EC_{50} values for the treatment of HER2 positive and negative cell lines with anti-HER2 ADCs.** *EC_{50} values were calculated from the dose-response curves shown in* ***Figure 17*.*

Cell line	N-azido-ADC (EC_{50} pM)	W-azido-ADC (EC_{50} pM)	N-ADC-ctrl (EC_{50} pM)	W-ADC-ctrl (EC_{50} pM)
SKBR-3	30.7	72.0	18.5	46.9
JIMT-1	227	-	133	388
MDA-MB-231	-	-	-	-

4.3 *In vitro* evaluation of the neutralization strategy for the azido-ADC treatment

The SPAAC reaction between Ama-N-azido (**2**) and the neutralizing compounds BCN-PEG_6-OH (**6**) or DBCO-PEG_4-COOH (**7**) led to the neutralized amanitin compounds Ama-N-BCN-PEG_6-OH (**10**), Ama-N-DBCO-PEG_4-COOH-a (**11a**) Ama-N-DBCO-PEG_4-COOH-b (**11b**), which displayed lower *in vitro* bioactivity compared to α-amanitin and compound **2** (section **4.1.2** and **4.1.3**). The T-S399C ADC based on Compound **2** (N-azido-ADC) proved to be effective against HER2-positive cell lines (section **0**). To assess the feasibility of applying the neutralization strategy to N-azido-ADC and reducing its cytotoxic activity *in vitro*, HER2-positive JIMT-1 cells were treated with N-azido-ADC followed by an additional treatment of BCN-PEG_6-OH (**6**) or DBCO-PEG_4-COOH (**7**). To investigate the time dependency of the neutralization effect, the neutralizing agents **6-7** were administered at different time points following N-azido-ADC treatment. Additionally, escalating concentrations of both the neutralizing agents and the N-azido-ADC were examined to comprehensively evaluate the maximum potential of the neutralization strategy in mitigating ADC treatment cytotoxicity.

4.3.1 Impact of BCN-PEG_6-OH (6) and DBCO-PEG_4-COOH (7) on N-azido-ADC treatment of JIMT-1 HER2-positive cells

To evaluate the impact of both neutralizing agents **6** and **7** on the N-azido-ADC treatment activity, JIMT-1 cells were initially treated with a cytotoxic dose (1 nM) of N-azido-ADC. Subsequently, at 1, 6, 12, 24, and 48 hours post-treatment, increasing concentrations ranging from 10^{-5} to 10^{-10} M of compounds **6** and **7** were added to the cells. (**Figure 18A-B**). The selection of the 1 nM dose of N-azido-ADC was based on the previous cytotoxicity results in JIMT-1 cells, where cell viability was notably low (~10%) at this concentration (**Figure 17**).

The results showed that concentrations higher than 1μM of compounds **6** and **7** were able to counteract N-azido-ADC treatment cytotoxic effect, retaining 100% cell viability. Specifically, supplementary treatment with 2 μM of Compound **7** within 12 hours post-N-azido-ADC treatment preserved 100% cell viability (**Figure 18B**), whereas concentrations greater than 2 μM of compound **6** were required to inhibit treatment-induced cytotoxicity within the same timeframe (**Figure 18A**). Moreover, the capacity of neutralizing agents to disrupt N-azido-ADC treatment appeared to be time-dependent. In particular, compound **7**'s neutralization effect was more dependent on the timing of application. Treatment with compound **7** after 24 or 48 hours could only partially reduce N-azido-ADC cytotoxicity, retaining a cell viability percentage of 80% and 50% at the respective timepoints (**Figure 18B**). On the contrary, for compound **6**, treatment 48 hours post-N-azido-ADC treatment still resulted in 80% of cell viability (**Figure 18A**).

To further verify if higher concentrations of ADC could be neutralized, the assay was performed with increasing concentrations of N-azido-ADC and a fixed concentration of the neutralizing agents **6** and **7**. JIMT-1 cells were first treated with concentrations of N-azido-ADC ranging from 10^{-7} to 10^{-12} M, followed by administration of 2μM of BCN-PEG_6-OH (**6**) or DBCO-PEG_4-COOH (**7**) or DMSO (control) 1 hour later (**Figure 18C**). Compound **6** only partially reduced the cytotoxicity of the N-azido-ADC treatment, as evidenced by a rightward shift of the dose-response curve compared to the control dose-response curve with N-azido-ADC and DMSO. On the contrary, compound **7** completely neutralized the cytotoxicity of the N-azido-ADC treatment, resulting in no dose-response curve.

To confirm the specificity of the SPAAC reaction between N-azido-ADC and the neutralizing agents, a parallel study was conducted with the N-ADC-ctrl, which lacks the azide moiety and, therefore, the reactive group for the SPAAC reaction. JIMT-1 cells were treated first with concentrations of N-ADC-ctrl ranging from 10^{-7} to 10^{-12} M, and 1h after with 2μM of either BCN-PEG_6-OH (**6**) or DBCO-PEG_4-COOH (**7**) or DMSO (**Figure 18D**). As expected, there was no variation in the cytotoxicity, following administration of the neutralizing agents **6-7**.

This result suggested that the azide group on N-azido-ADC is crucial for the SPAAC reaction with the neutralizing agents **6** and **7**, resulting in the formation of an N-azido-ADC-neutralized, with reduced or negligible cytotoxic activity on JIMT-1 cells. The findings indicate that an excess of both BCN-PEG_6-OH (**6**) and DBCO-PEG_4-COOH (**7**) were able to affect the activity of N-azido-ADC *in vitro* in a time-dependent manner. In particular, complete elimination of N-azido-ADC cytotoxicity with the neutralizing agents **6** and **7** was possible within 12 hours post-ADC treatment. Higher concentrations of N-azido-ADC could be partially neutralized with compound **6** or completely neutralized with compound **7**, leading to reduced cell cytotoxicity in JIMT-1 cells. The next step was to analyze how the

administration of the neutralizing agents could affect the efficacy of the N-azido-ADC *in vivo*.

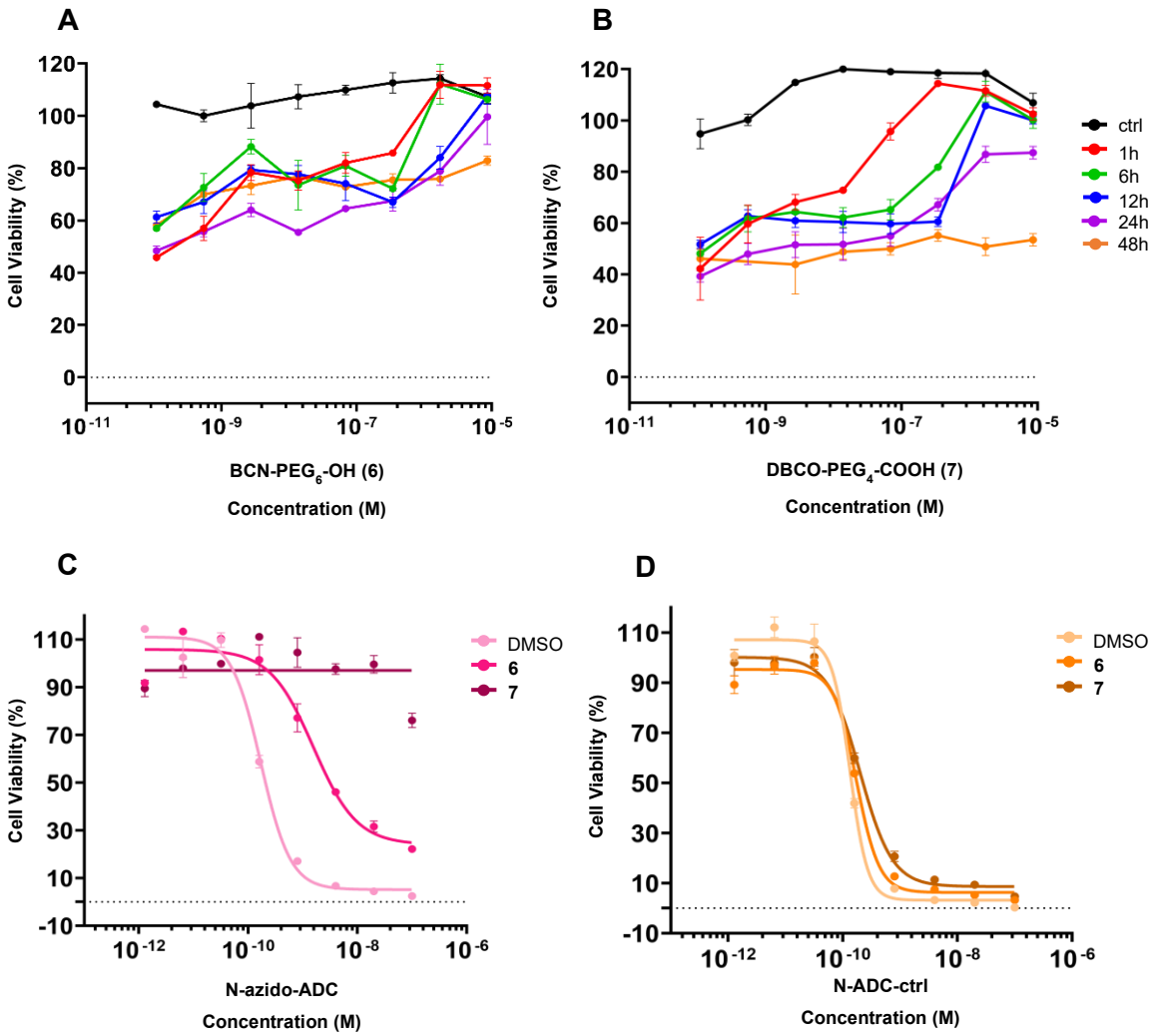

Figure 16: Neutralization of N-azido-ADC treatment after click reaction with BCN-PEG$_6$-OH (6) or DBCO-PEG$_4$-acid (7) in HER2-positive JIMT-1 cells. *(A-B) JIMT-1 cells were treated with 1 nM N-azido-ADC, and at 1h, 6h, 12h, 24h, or 48h, different concentrations of BCN-PEG$_6$-OH (**6**) or DBCO-PEG$_4$-COOH (**7**) were administered. In the ctrl, cells were treated with BCN-PEG$_6$-OH (A) or DBCO-PEG$_4$-COOH (B) alone. (C-D) JIMT-1 cells were treated with different concentrations of N-azido-ADC (C) or N-ADC-ctrl (D) and after 1h with 2 µM of BCN-PEG$_6$-OH (6) or DBCO-PEG$_4$-COOH (7). Cell proliferation was determined by BrdU incorporation assay following manufacturers guidelines. Dose-response curves and EC$_{50}$ values were obtained by Prism 9.0 software.*

4.4 Development of an N-azido-ADC ELISA to detect N-azido-ADC in tissue

Before progressing to the *in vivo* phase of the study, an azido-ADC ELISA was developed to detect active N-azido-ADC and distinguish it from the inactive N-azido-ADC-neutralized compound generated by the reaction between N-azido-ADC and the neutralizing agents. This assay was developed to measure the concentration of non-reacted N-azido-ADC in plasma or tissues and to analyze the efficacy of the Strain-Promoted Azido-Alkyne Cycloaddition (SPAAC) reaction with the neutralizing agents **6** and **7**. The concentration of N-azido-ADC was compared to the Total ADC concentration in the sample, which was measured using the company's established anti-ADC ELISA. This comparison was done to evaluate the extent of ADC neutralization by the treatment with the neutralizing agents.

4.4.1 Establishment of a new azido-ADC ELISA

In the tissue sample, the ADC species present after treatment with N-azido-ADC and the neutralizing agents **6-7** include both the non-reacted azido-ADC and the SPAAC-reacted azido-ADC-neutralized that has been neutralized (**Figure 19A**). The newly developed azido-ADC ELISA involved using a biotin derivative bearing a DBCO moiety on a streptavidin-coated plate to capture the azido-ADCs (**Figure 19B**). The principle of the assay was based on the high specificity of the SPAAC reaction between the free azide moiety of the amanitin payload and the strained alkyne group of the DBCO on the biotin derivative. With this approach, the N-azido-ADC-neutralized in the sample is washed away during the washing steps of the ELISA, leaving only the non-reacted N-azido-ADC bound to the biotin. Then, the concentration of bound N-azido-ADC is detected with an anti-human antibody linked to the horse-radish peroxidase (HRP) via a colorimetric reaction.
Regarding the detection of the Total ADC concentration, an established anti-ADC ELISA assay based on a polyclonal anti-Amanitin antibody for capturing the ADC in the sample was used (**Figure 19C**). This way, it was possible to quantify the non-reacted N-azido-ADC and, through quantification of the Total ADC and to obtain an estimation of how much N-azido-ADC was neutralized. Before analyzing the experimental samples, the azido-ADC ELISA was tested for its specificity in recognizing the non-reacted N-azido-ADC. To confirm the specific detection of the non-reacted N-azido-ADC, two neutralized-ADCs, N-azido-ADC-BCN and N-azido-ADC-DBCO, generated *in vitro* by SPAAC reaction with BCN-PEG_6-OH (**6**) and DBCO-PEG_4-COOH (**7**), were tested. Additionally, a control ADC (ctrl ADC) lacking an azide moiety on the payload and another ADC bearing an azide moiety on a different residue (W-azido-ADC) were included.

The same samples were analyzed in the anti-ADC ELISA to determine if both azido-ADCs and neutralized-ADCs were detected by the anti-amanitin serum coating.
A known concentration of the different ADCs (150 µg/mL) was spiked in serum or plasma and diluted 1:1000 in the sample buffer. In each experiment, a lower limit of quantification (LLQ), which represents the lowest detectable concentration of the ADC, was determined from the standard curve (**section 3.2.19**).

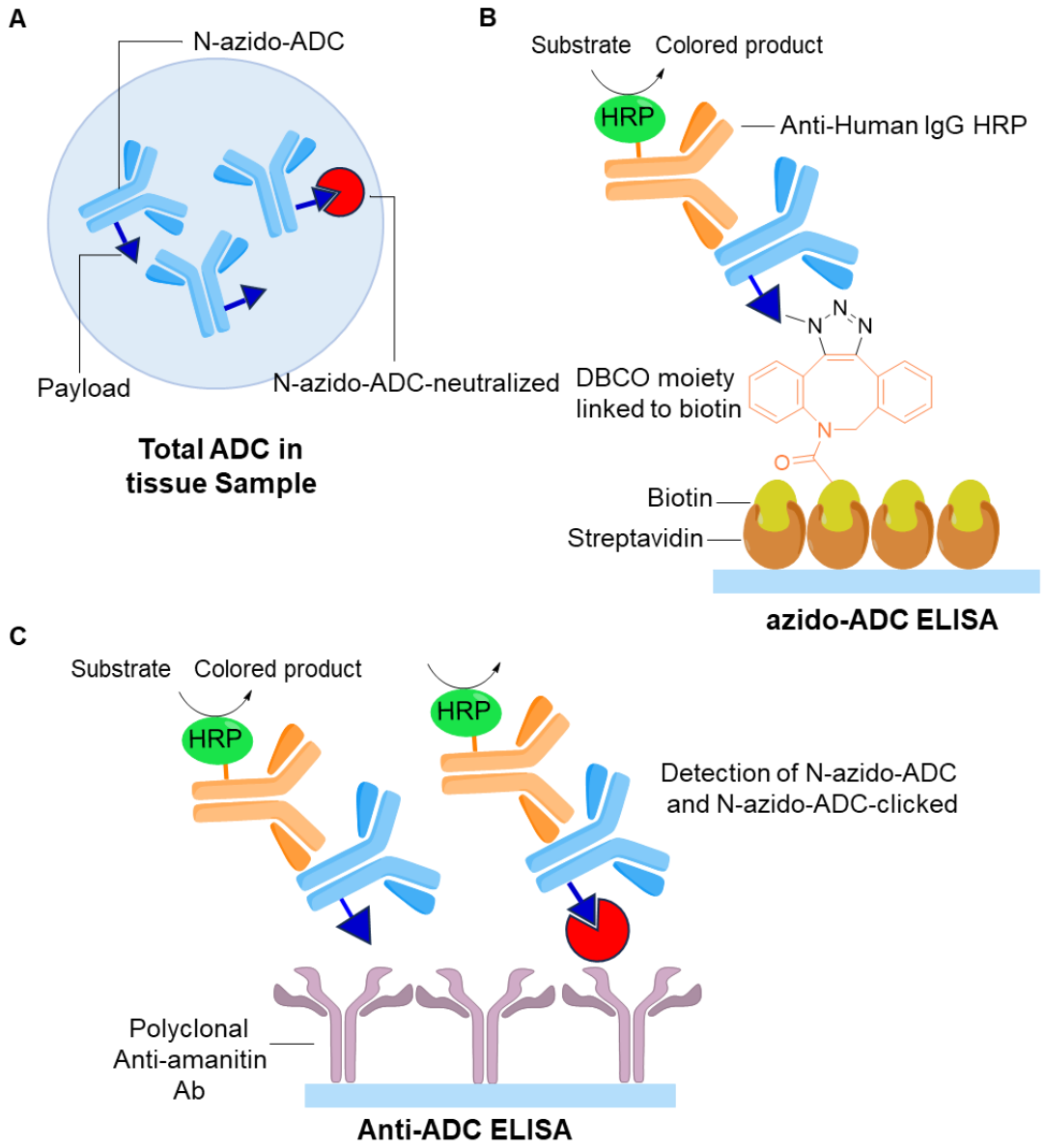

Figure 17: Illustration of the azido-ADC ELISA and anti-ADC ELISA. *(A) illustration of the expected ADC species in a tissue sample: the N-azido-ADC and the SPAAC- N-azido-ADC-neutralized. (B) illustration of a sandwich ELISA assay developed to detect N-azido-ADC by click reaction with a DBCO-linked biotin. More information on the protocol can be found in Methods section 3.2.19. (C) Illustration of an anti-ADC ELISA which detects amanitin- ADCs with the anti-amanitin polyclonal serum coating. More information on the protocol can be found in Methods section 3.2.20.*

The accuracy of the values calculated in the two ELISAs was assessed based on the recovery rate in percent. The Recovery rate represents the ratio between the observed value and the expected value and excludes the effect of complex matrixes (e.g. serum, tissues) on the measurements. The Recovery rate was calculated as follows:

$$Recovery\ rate\ (\%) = \frac{[Observed\ value]}{[Theorethical\ value]} * 100$$

A Recovery rate between 80% and 120% was set as an acceptable range, meaning that for a true value of 150 µg/mL only concentration values between 120 and 180 µg/mL determined by ELISA were acceptable.

In the azido-ADC ELISA, N-azido-ADC but also W-azido-ADC were detected in both matrices, plasma and serum, with a higher absorbance than N-azido-ADC-BCN, N-azido-ADC-DBCO and ctrl ADC (**Figure 20A**). The calculated concentration of N-azido-ADC and W-azido-ADC in plasma and serum showed an acceptable Recovery rate. N-azido-ADC-BCN, N-azido-ADC-DBCO, and ctrl ADC values were below the LLQ (**Figure 20C**). These results confirmed that N-azido-ADC could be detected with the azido-ADC ELISA when the azide moiety on the payload was free. In the case of the neutralized N-azido-ADC (N-azido-ADC-BCN and N-azido-ADC-DBCO) the absorbance values decreased to a similar range as observed for the control ADC.

In the anti-ADC ELISA, all ADC species were detected with similar absorbance in both matrices (**Figure 20B**). and all values showed an acceptable Recovery rate (**Figure 20D**). These findings suggested that both azido-ADCs and neutralized-ADCs could be detected with acceptable accuracy.

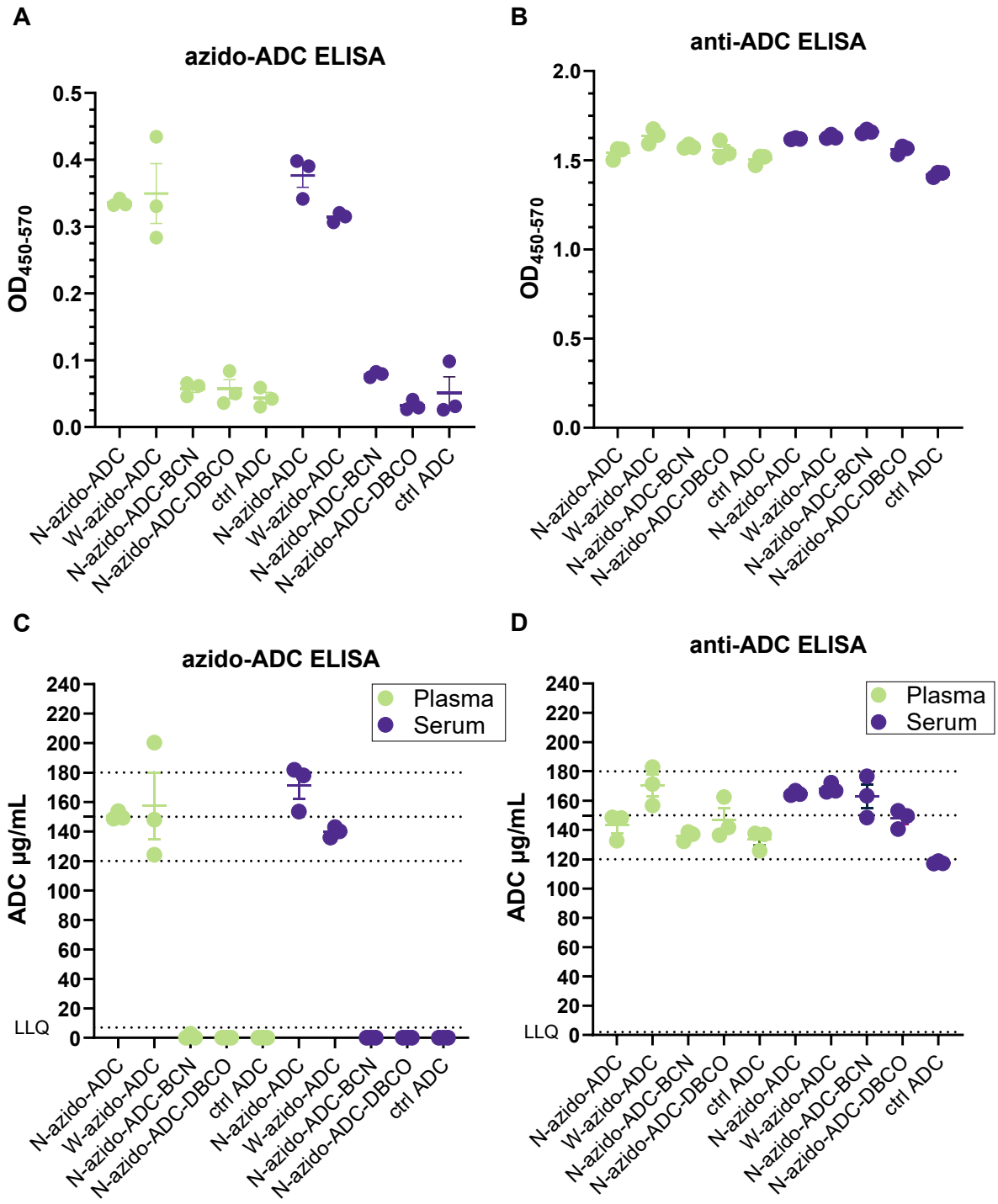

Figure 18: Specificity of the azido-ADC ELISA compared to anti-ADC ELISA. *150 µg/mL of different ADCs were spiked in either serum or plasma and were diluted 1:1000 in sample buffer to be measured in the azido-ADC ELISA or 1:10000 in sample buffer to be measured in anti-ADC ELISA. All samples were analyzed in triplicates. Absorbance values of raw data obtained with the azido-ADC ELISA (A) and anti-ADC ELISA (B). Calculated concentrations for the different ADC species detected with azido-ADC ELISA (C) and anti-ADC ELISA (D). Values between 120 and 180 µg/mL were accepted. LLQ= lowest limit of quantification.*

4.5 The neutralizing effect of BCN-PEG$_6$-OH (6) and DBCO-PEG$_4$-COOH (7) on the tolerability of N-azido-ADC *in vivo*

The previous results demonstrating a reduction in N-azido-ADC cytotoxicity on JIMT-1 cells, after administration of BCN-PEG$_6$-OH (**6**) or DBCO-PEG$_4$-COOH (**7**), proved that neutralizing agents could affect *in vitro* activity of the ADC (**section 4.3**). To assess the impact of the neutralization strategy on N-azido-ADC tolerability *in vivo*, the Maximum Tolerated Dose (MTD), i.e. the highest tolerable dose without side effects, of N-azido-ADC in mice was determined. Subsequently, a lethal dose of N-azido-ADC was administered, followed by the application of the neutralizing agents **6** or **7**, to evaluate if tolerability could be increased. Moreover, to understand the efficiency and the time-course of the Strain-Promoted Azido-Alkyne Cycloaddition (SPAAC) reaction, the concentration of the non-reacted N-azido-ADC and the neutralized N-azido-ADC species in plasma were analyzed at different time points.

4.5.1 Analysis of the maximum tolerated dose of N-azido-ADC

Before being able to assess the potential of neutralizing agents **6** and **7** to rescue mice from a lethal dose of N-azido-ADC, the maximum tolerated dose (MTD) of N-azido-ADC in female NMRI nude mice was determined (**Figure 21A**).

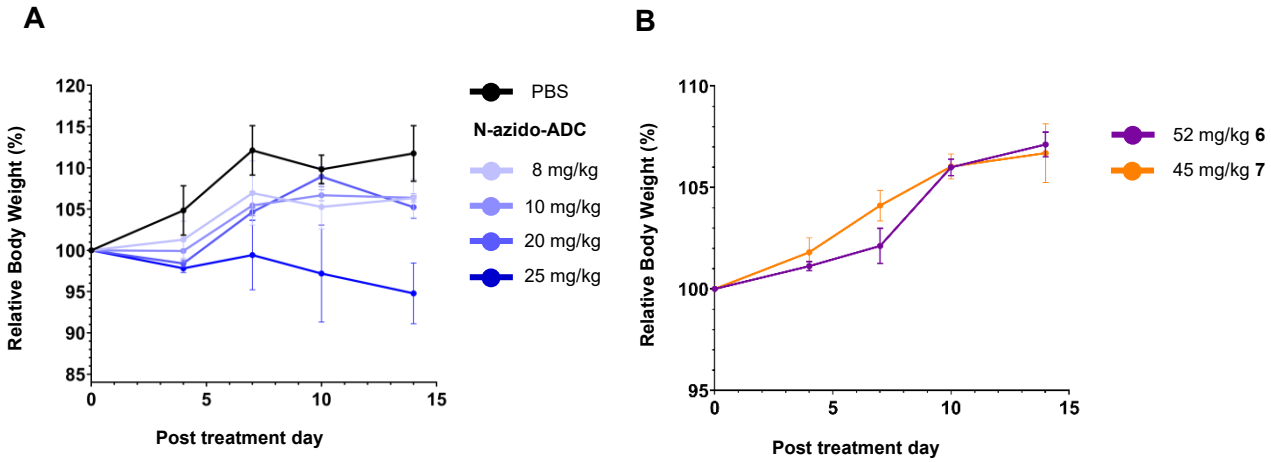

Figure 19: Maximum Tolerated Dose (MTD) study of N-azido-ADC and tolerability of BCN-PEG$_6$-OH (6) DBCO-PEG$_4$-COOH (7) in NMRI nude mice at doses used for neutralization. *(A) MTD was evaluated by injecting i.v. different doses of N-azido-ADC. Body weight was measured twice weekly for 14 days. Each data point represents the mean ± SEM of n=3. (B) Tolerability of i.v. injected BCN-PEG$_6$-OH (**6**) 52 mg/kg and DBCO-PEG$_4$-COOH (**7**) at 45 mg/kg. Body weight was measured twice weekly for 14 days. Each data point represents the mean ± SEM of n=3.*

Escalating doses of N-azido-ADC starting from 8 mg/kg were applied to female NMRI nude mice (n=3). 8, 10, and 20 mg/kg of N-azido-ADC did not alter body weight to a significant extent and were well tolerated. 25 mg/kg N-azido-ADC was also well tolerated, although a relative body weight loss to 95% was detected at day 14 (end of the study). Since higher doses were not tolerated, the MTD was determined to be 25 mg/kg. The tolerability of the neutralizing agents BCN-PEG_6-OH (**6**) and DBCO-PEG_4-COOH (**7**) alone was also tested in female NMRI nude mice (**Figure 21B**). According to Ursuegui et al (Ursuegui et al. 2017), compound **6** was dosed at 52 mg/kg whereas compound **7** was dosed at only 45 mg/kg since it showed a higher neutralizing capacity in the *in vitro* studies (**section 4.3**). Both compounds were found to be well tolerated.

4.5.2 Tolerability of N-azido-ADC after administration of the neutralizing compounds

To determine if the neutralizing agents could effectively increase tolerability, mice were treated with compound **6** or **7**, following a lethal dose of N-azido-ADC of 1.2 times the MTD (30 mg/kg). Female NMRI nude mice were treated with 30 mg/kg N-azido-ADC, and one hour later, either vehicle, compound **6** at 52 mg/kg or compound **7** 45 mg/kg, was intravenously injected (**Figure 22A**). Thus, to 1 molar equivalent of N-azido-ADC an excess of ~500 equivalents for compound **6** and ~400 equivalents for compound **7** were administered.

Mice treated with either compound **6** or compound **7** survived throughout the subsequent 14 days with an increase in relative body weight above 100%. In contrast, in the group receiving N-azido-ADC along with the vehicle, only one mouse survived to the end of the study, while the rest had to be sacrificed for reaching the humane endpoint criteria (**Figure 22B**).

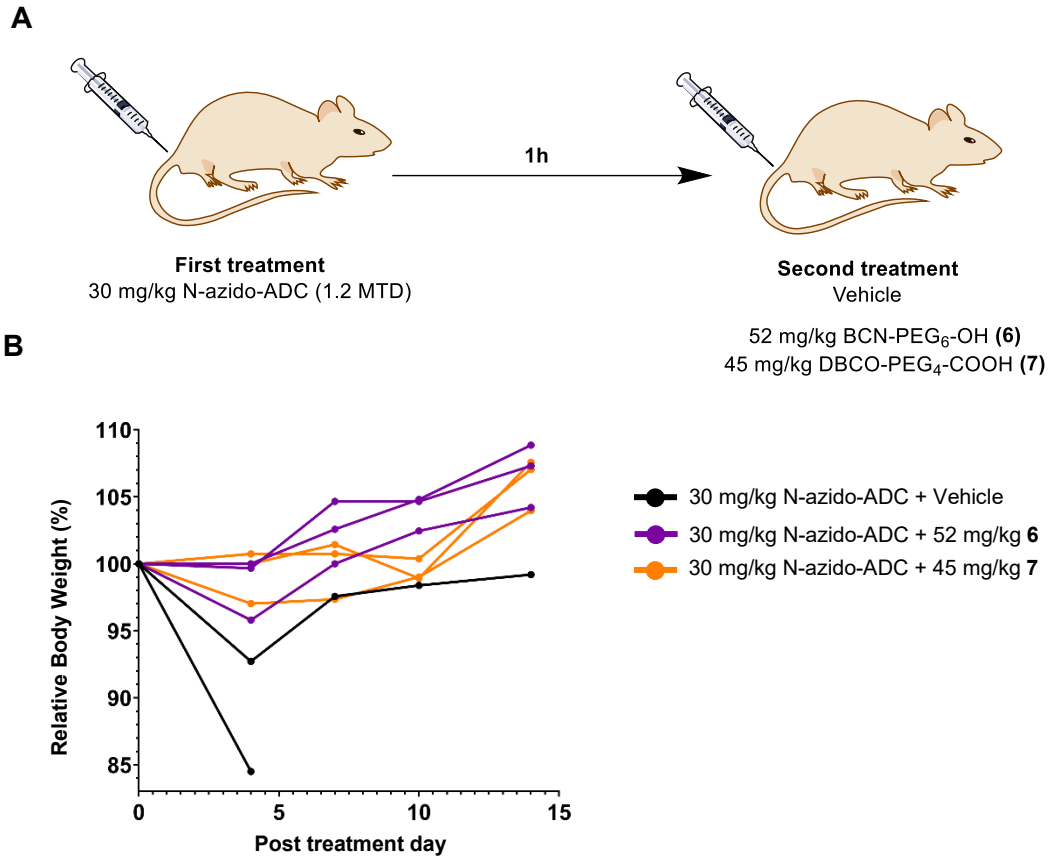

Figure 20: Rescue of a lethal N-azido-ADC dose after click reaction with BCN-PEG$_6$-OH (6) or DBCO-PEG$_4$-COOH (7) in NMRI nude female mice. *(A)Set up of the experiment: NMRI nude female mice (n=9) were injected i.v. with 30 mg/kg N-azido-ADC (1.2 MTD) and 1h after with either vehicle (n=3), 52 mg/kg BCN-PEG$_6$-OH (**6**) (n=3) or 45 mg/kg DBCO-PEG$_4$-COOH (**7**) (n=3). (B) Single curve plot of the relative body weight %, Each line represents an animal. Body weight was measured twice weekly for 14 days.*

4.5.3 Evaluation of N-azido-ADC in plasma and comparison of Strain-promoted azido-alkyne Cycloaddition (SPAAC) efficiency with BCN-PEG$_6$-OH (6) or DBCO-PEG$_4$-COOH (7)

To further elucidate the efficiency of the SPAAC reaction *in vivo* involving the neutralizing agents **6** and **7** and the N-azido-ADC, the concentrations of N-azido-ADC and Total ADC in plasma were analyzed. Mice were administered 30 mg/kg (1.2 MTD) of N-azido-ADC, followed by treatment with either vehicle, 52 mg/kg of compound **6**, or 45 mg/kg of compound **7** one hour later. Subsequently, plasma samples were collected at 15, 30, and 45 minutes after the second treatment. The sample were then analyzed in parallel in both azido-ADC ELISA and anti-ADC ELISA, described in **section 4.4** (**Figure 23**).

In the group treated with 30 mg/kg (1.2 MTD) N-azido-ADC and vehicle, the N-azido-ADC concentration measured by N-azido-ADC ELISA was ~ 350 µg/ml, which remained constant for all the timepoints (**Figure 23A**). Similarly, the concentration of the Total ADC

measured in the same treatment group was ~ 400 µg/ml and remained constant for the three different timepoints (**Figure 23B**). This outcome was anticipated due to the absence of any neutralizing agent within this group, alongside consistent ADC concentration across ELISAs. This finding further validates the precision of the azido-ADC ELISA method.

In the group treated with 30 mg/kg (1.2 MTD) N-azido-ADC + 52 mg/kg BCN-PEG_6-OH (**6**), the N-azido-ADC concentration measured at 15 minutes in the anti-ADC ELISA was 200 µg/ml and remained constant at 30 and 60 min (**Figure 23A**). The same group measured in the anti-ADC ELISA gave a double ADC concentration of ~400 µg/ml at 15, 30 and 60 minutes (**Figure 23B**). This finding suggests that within 15 minutes post-administration of compound **6**, approximately half of the circulating N-azido-ADC had already reacted with the compound, resulting in N-azido-ADC-neutralized, which cannot be detected by the azido-ADC ELISA.

In the group treated with 30 mg/kg (1.2 MTD) N-azido-ADC + 45 mg/kg DBCO-PEG_4-COOH (**7**), the N-azido-ADC concentration was only approximately 50 µg/ml at all timepoints (**Figure 23A**). The same samples were measured in the anti-ADC ELISA to detect the total ADC concentration (**Figure 23B**). The measured concentrations of ~400 µg/ml exhibited non-significant variations among the groups at the different timepoints.

To better compare the efficiency of the SPAAC reaction with the neutralizing agents **6** and **7**, the N-azido-ADC-neutralized % was calculated by combining the data obtained from the azido-ADC ELISA and anti-ADC ELISA. The N-azido-ADC-neutralized % was calculated as one minus the ratio of N-azido-ADC to Total ADC converted in percentage as:

$$N-\mathrm{ADC}-\mathrm{neutralized}\ \% = \left(1 - \frac{[N-azido-\mathrm{ADC}]}{[Total\ ADC]}\right) * 100$$

The calculated N-ADC neutralized % of the treated groups is summarized in **Table 33**. 15 minutes after the administration of BCN-PEG_6-OH (**6**), the percentage of neutralized N-azido-ADC- was 48% and remained stable within 60 minutes. The administration of DBCO-PEG_4-COOH (**7**) led to 90% N-azido-ADC neutralization within the first 15 minutes post-treatment and remaining constant at ~ 92% at 60 minutes.

These results suggested that a large proportion of N-azido-ADC is neutralized within the first 15 minutes after administration of the neutralizing agents **6** and **7**. Moreover, compound **7** showed higher efficiency in reacting with N-azido-ADC, leading to 90% N-azido-ADC-neutralized in the first 15 minutes. Therefore, DBCO-PEG_4-COOH (**7**) was chosen as neutralizing compounds for the further *in vivo* characterization.

Table 33: Percentage of N-azido-ADC-neutralized % calculated from the data obtained in the ELISA analysis. *Data in the table indicate the average percentage calculated from n=3 ± SEM.*

Time after second treatment (min)	N-azido-ADC-neutralized (%) with compound 6	N-azido-ADC-neutralized (%) with compound 7
15	48 ± 2	90 ± 2
30	50 ± 2	90 ± 2
60	44 ± 6	92 ± 1

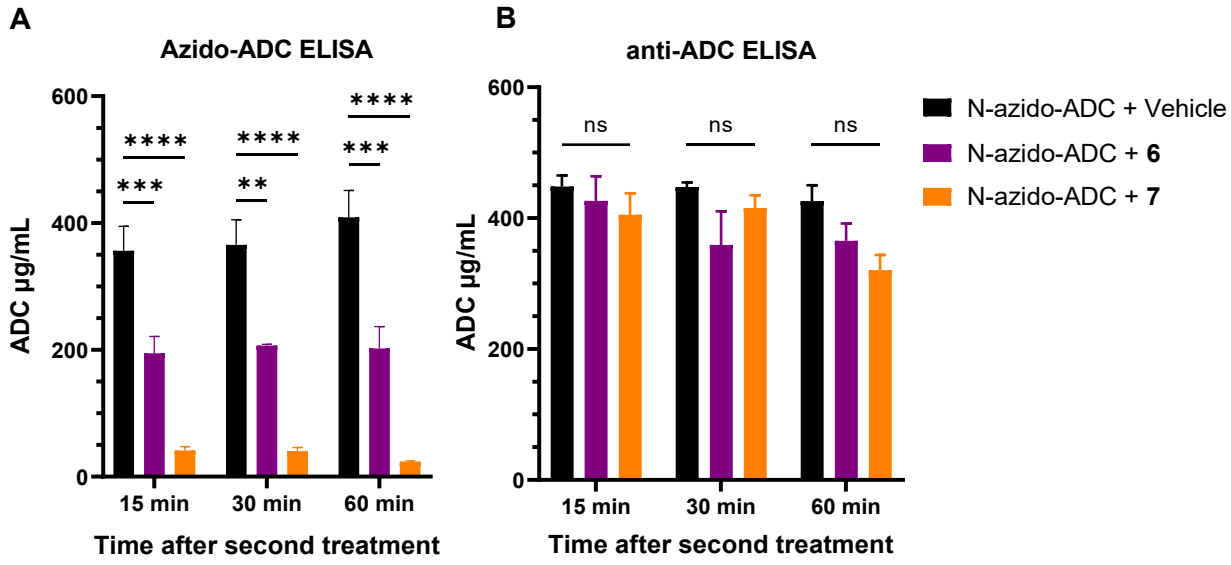

Figure 21: Efficiency of the in vivo SPAAC reaction of BCN-PEG$_6$-OH (6) and DBCO-PEG$_4$-COOH (7) with N-azido-ADC. *Female NMRI nude mice (n=9) were treated with 30 mg/kg N-azido-ADC i.v. (1.2 MTD) and 1h later with either vehicle (n=3), 52 mg/kg BCN-PEG6-OH (**6**) (n=3) or 45 mg/kg DBCO-PEG4-acid (**7**) (n=3). Plasma samples were collected 15, 30 and 60 minutes after the second treatment. Plasma samples were analyzed in parallel in the azido-ADC ELISA (A) and in the anti-ADC ELISA (B). Two-way ANOVA with Tukey's multiple comparison test: ns>0.05, *p≤0.05.*

4.6 The influence of DBCO-PEG$_4$-COOH (7) administration at different timepoints on N-azido-ADC tolerability

In the previous study, administration of BCN-PEG$_6$-OH (**6**) or DBCO-PEG$_4$-COOH (**7**) one hour after treatment with a lethal dose of N-azido-ADC rescued mice from ADC toxicity, improving the survival rate. The findings obtained with the ELISA assays suggested that DBCO-PEG$_4$-COOH (**7**) exhibited higher and faster reactivity with N-azido-ADC, achieving a 90% neutralization rate in circulation. Because of its faster kinetic and higher efficiency, compound **7** was chosen for the following studies.

Biodistribution studies revealed that the targeted accumulation of ADC in solid tumors following treatment may extend over several days, with notable uptake typically observed 24 hours or more post-treatment (Alley et al. 2008; Jacobson et al. 2017). To effectively employ the SPAAC click reaction strategy to neutralize the toxicity of the ADC treatment but to ensure a maximum ADC effect on the tumor, DBCO-PEG_4-COOH (**7**) should be administered at the latest possible timepoint.

4.6.1 Effects of administration of DBCO-PEG_4-COOH (7) at different timepoints on the tolerability of a lethal dose of N-azido-ADC

To assess the most effective administration time for DBCO-PEG_4-COOH (**7**) in neutralizing N-azido-ADC toxicity, compound **7** was administered at different timepoints after treatment with a lethal dose of N-azido-ADC. Female NMRI nude mice were treated with 30 mg/kg (1.2 MTD) of N-azido-ADC and after 6, 12, 15 and 24 hours with 45 mg/kg compound **7** (**Table 34**). The study was conducted for 14 days, and the mouse weight was measured twice weekly.

In the control group 1, where DBCO-PEG_4-COOH (**7**) alone was administered, all mice survived and showed an increase in Relative Body Weight (RBW) to 110-120 %. As expected, in group 2, treatment with 30 mg/kg (1.2 MTD) N-azido-ADC and the vehicle led to poor survival, confirming that 30 mg/kg (1.2 MTD) N-azido-ADC was lethal for the mice (**Figure 24A**). Remarkably, signs of treatment-related toxicity emerged within six days following the administration of the ADC treatment, necessitating the sacrifice of mice due to deteriorating general conditions or significant loss of body weight, and in the most severe instances, resulted in mortality. In group 3 and 4, administering compound **7** 6 hours and 12 hours after N-azido-ADC treatment improved treatment tolerability, resulting in a 100% survival rate among the mice and an increase in RBW (**Figure 24B**). On the contrary, In the case of group 5 and 6, where compound **7** was administered 15 and 24 hours after the lethal dose of N-azido-ADC, only two out of three mice survived, indicating that the administration of the neutralizing agent at later timepoint was not increasing treatment tolerability (**Figure 24C**).

The administration of DBCO-PEG_4-COOH (**7**) at different timepoints after a lethal dose of N-azido-ADC demonstrated varying effects on treatment tolerability and survival rates in NMRI nude female mice. Notably, when compound **7** was applied 6 hours and 12 hours after N-azido-ADC treatment (groups 3 & 4), increased tolerability was observed, with all mice surviving and displaying favorable relative body weight. However, delaying the administration of compound **7** to 15 hours or 24 hours resulted in reduced survival and signs of toxicity appeared within six days after treatment with N-azido-ADC.

Table 34: Tolerability of N-azido-ADC after administration DBCO-PEG$_4$-COOH (7) at different timepoints. *Overview of the treatment groups and animal survival outcome of the rescue study with N-azido-ADC and DBCO-PEG$_4$-COOH (**7**). n=3 NMRI nude female mice were used for each group.*

Group	1st treatment	2nd treatment	Survival
1	PBS	t=24h **DBCO-PEG$_4$-COOH (7)**	3/3 mice on day 14
2	30 mg/kg (1.2 MTD) **N-azido-ADC**	t=24h Vehicle	0/3 mice on day 5 (2 mice were FD[1] on day 2, 1 mouse was sacrificed on day 5 due to BWL[2])
3	30 mg/kg (1.2 MTD) **N-azido-ADC**	t=6h 45 mg/kg **DBCO-PEG$_4$-COOH (7)**	3/3 mice on day 14
4	30 mg/kg (1.2 MTD) **N-azido-ADC**	t=12h 45 mg/kg **DBCO-PEG$_4$-COOH (7)**	3/3 mice on day 14
5	30 mg/kg (1.2 MTD) **N-azido-ADC**	t=15h 45 mg/kg **DBCO-PEG$_4$-COOH (7)**	2/3 mice on day 14 (1 mouse sacrificed on day 2 due to PGC[3])
6	30 mg/kg (1.2 MTD) **N-azido-ADC**	t=24h 45 mg/kg **DBCO-PEG$_4$-COOH (7)**	2/3 mice on day 14 (1 mouse sacrificed on day 2 due to PGC[3])

[1] FD = found dead; [2] BWL=Body weigh loss; [3] PGC=Poor general conditions

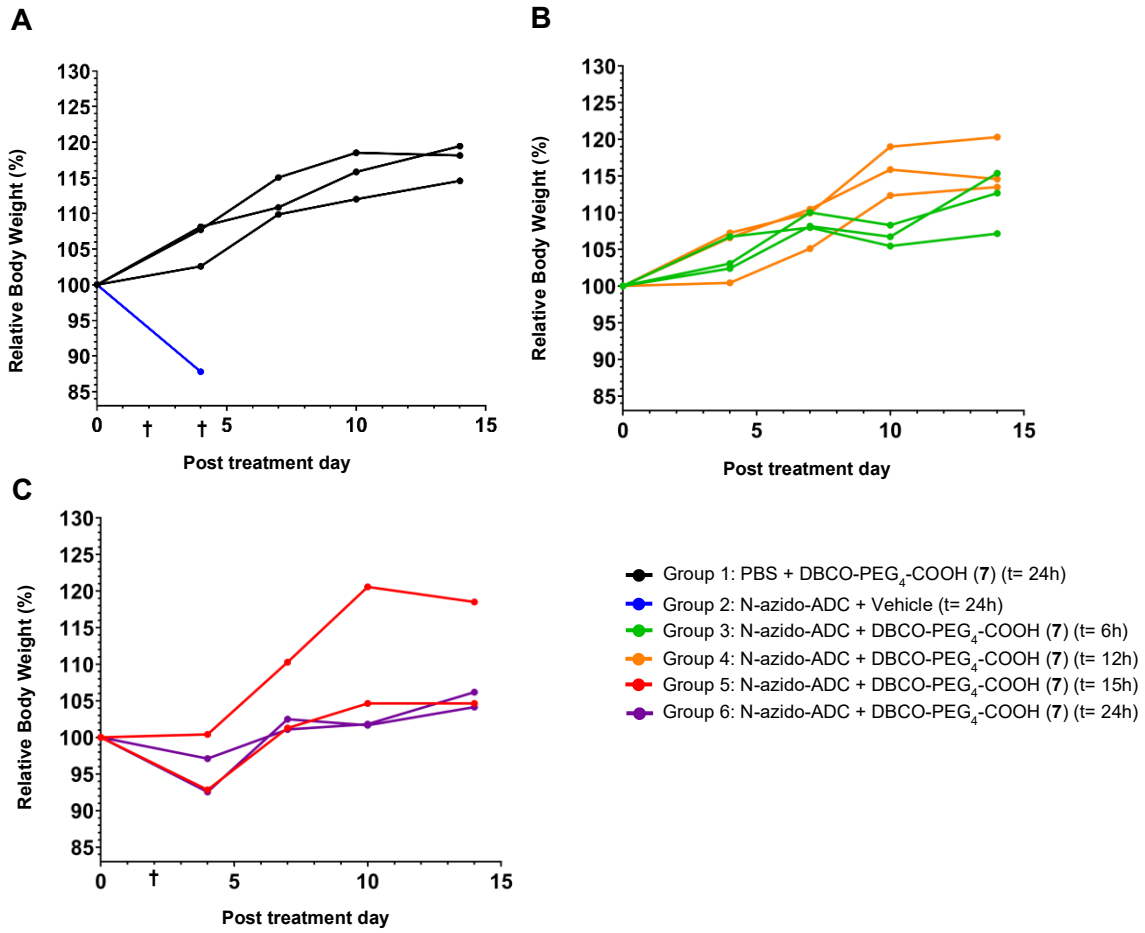

Figure 22: Body weight curves of individual animals upon a lethal dose of N-azido-ADC with DBCO-PEG$_4$-COOH (7) administered at different timepoints. *Each line represents a single animal. Body weight was measured twice weekly for 14 days. Treatment groups are described in Table 1. (A) Single curve plot of Groups 1 and 2 (B) Single curve plot of Groups 3 and 4 (C) Single curve plot of Groups 5 and 6. The cross indicates when a mouse was sacrificed or found dead.*

4.7 Histopathological analysis of liver and kidney tissues following N-azido-ADC treatment and administration of DBCO-PEG$_4$-COOH (7)

The liver and kidneys play pivotal roles in metabolizing and clearing both small molecules and large molecules such as antibody-drug conjugates (ADCs), making them susceptible to off-target toxicity. This vulnerability is not limited to the free payload alone, since the ADC itself can also contribute to off-target toxicity (Nguyen, 2023). Typical signs of amatoxin liver intoxication in human include massive centrilobular hepatic necrosis, vacuolar degeneration of hepatocytes and inflammatory cells infiltration (Pond et al. 1986). Amatoxin-induced kidney lesions include tubule basophilia, tubule necrosis, hyperplasia, and tubule dilation (Fineschi et al. 1996). Depending on the severity grade, tubule dilation

and tubule basophilia can also manifest as “spontaneous” lesions and are usually unrelated to treatment (Chirukandath and Vasanthi 2014).

To better understand how the application of the neutralizing agent DBCO-PEG$_4$-COOH (**7**) could counteract toxic ADC and payload activity and reduce drug-induced tissue lesions, histopathological analysis was performed on liver and kidney tissues. Tissue analysis was conducted on day 6 post-N-azido-ADC treatment to identify acute toxicity indicators and on day 14 post-treatment to examine signs of recovery.

4.7.1 The Impact of DBCO-PEG$_4$-COOH (7) administration following N-azido-ADC treatment on liver and kidneys

In the case of N-azido-ADC, doses exceeding the MTD in mice revealed initial signs of acute toxicity emerging within the first 6 days after treatment, resulting in poor general condition and mortality (**section 4.5.2**). To evaluate alterations in liver and kidney tissues, female NMRI nude mice were treated with N-azido-ADC at the MTD of 25 mg/kg and subsequent DBCO-PEG$_4$-COOH (**7**) administration at 45 mg/kg. The dose of N-azido-ADC was selected, considering that higher doses might significantly compromise mouse survival, thereby influencing the subsequent organ harvest. DBCO-PEG$_4$-COOH (**7**) was administered 6 hours and 20 hours after treatment with N-azido-ADC. The selection of the 6-hour timepoint was based on the finding that an application of compound **7** 6 hours after a lethal dose of N-azido-ADC increased tolerability and contributed to the survival of the mice. The application of compound **7** 15 or 24 hours after a lethal dose of N-azido-ADC, did not improve ADC tolerability, but given the lower dose of N-azido-ADC in this experiment, the 20 hours timepoint was selected to assess the impact of a later application on the liver and kidneys (**section 4.6**). Two control groups, with a total of three mice per group, were treated with PBS and 6 hours later with either vehicle (group 1) or compound **7** (group 2). Liver and kidney tissues were harvested 6 days after the first injection. Vehicle and compound **7** did not affect survival in mice, as three out of three animals survived in both groups. Groups are summarized in **Table 35**. Treatment groups 3, 4, and 5 were divided into two subgroups each for tissue collection at day 6 and day 14, with three animals allocated to each respective subgroup.

Unexpectedly, animals in groups 3 had to be sacrificed due to poor general conditions or were found dead. Among the animals, signs of acute treatment-related toxicity arose within 6 days after treatment with the N-azido-ADC. While one mouse was sacrificed on day 9 due to body weight loss, indicating a late stage of treatment-related toxicity. Similarly, in group 5, where compound **7** was applied 20 hours after ADC treatment, two mice had to

be sacrificed on day 2 due to poor general conditions. These findings suggest potential variability in animal tolerance to the MTD dose.

***Table 35**: **Impact of DBCO-PEG$_4$-COOH (7) on liver and kidneys following N-azido-ADC administration.** Overview of the treated groups and mice survival.*

Group	1st treatment	2nd treatment	Survival
1	PBS	t=6h Vehicle	3/3 mice on day 6
2	PBS	t=6h 45 mg/kg **DBCO-PEG$_4$-COOH (7)**	3/3 mice on day 6
3	25 mg/kg (MTD) **N-azido-ADC**	t=6h Vehicle	1/3 mice on day 6 and 1/3 mice on day 14 (1 mouse FD[1] on day 2, 1 mouse sacrificed on day 2, 1 mouse sacrificed on day 5 due to PGC[3] and 1 mouse sacrificed on day 9 due to BWL[2])
4	25 mg/kg (MTD) **N-azido-ADC**	t=6h 45 mg/kg **DBCO-PEG$_4$-COOH (7)**	2/3 mice on day 6 and 3/3 mice on day 14 (1 mouse was sacrificed as control)
5	25 mg/kg (MTD) **N-azido-ADC**	t=20h 45 mg/kg **DBCO-PEG$_4$-COOH (7)**	3/3 mice on day 6 and 1/3 mice on day 14 (2 mice sacrificed on day 2 due to PGC[3])

[1] *FD = found dead;* [2] *BWL=Body weight loss;* [3] *PGC=Poor general conditions*

Liver and kidney tissues of prematurely sacrificed animals were collected and compared to the initially planned timepoints at day 6 and 14. No tissues were collected from the animal found dead in group 3, as harvesting samples postmortem could compromise the integrity of the histopathological analysis.
Liver and kidney samples were sent to the Fraunhofer Institute for Toxicology and Experimental Medicine (ITEM) in Hannover, where they were finally analyzed.

4.7.2 Histopathological findings in liver tissue

The data in this section are based on the report *Internal Fraunhofer ITEM Study No. 05N23526 - non-GLP study* by veterinary pathologist Dirk Schaudien on 18 October 2023. The main findings are summarized in **Table 36**.

***Table 36**: Main pathological findings in the liver tissue at day 6 and 14 after co-treatment with N-azido-ADC and DBCO-PEG$_4$-COOH (7).*

Group	Pathological findings for liver
	Day 6
1	A1- no significant histopathological lesions
	A2- very slight multifocal mixed inflammatory cell infiltration
	A3- no significant histopathological lesions
2	A4- no significant histopathological lesions
	A5- very slight multifocal mixed inflammatory cell infiltration
	A6- very slight multifocal mixed inflammatory cell infiltration
3	A7- slight multifocal midzonal mitosis, very slight multifocal single cell necrosis, slight multifocal mixed inflammatory cell infiltration
	A9[1]- severe midzonal to diffuse necrosis, very slight multifocal mixed inflammatory cell infiltration
4	A13[4]- no significant histopathological lesions
	A14- no significant histopathological lesions
	A15- no significant histopathological lesions
5	A19- very slight multifocal single cell-necrosis, very slight multifocal midzonal mitosis
	A20- very slight multifocal single-cell necrosis, very slight multifocal mixed inflammatory cell infiltration
	A21- very slight multifocal mixed inflammatory cell infiltration
Group	**Pathological findings for liver**
	Day 14
3	A10[3]- slight multifocal mixed inflammatory cell infiltration, slight diffuse hepatocellular basophilia, very slight multifocal single-cell necrosis.
	A11[2]- severe midzonal to diffuse necrosis, slight diffuse hepatocellular basophilia, slight multifocal vacuolation, slight multifocal mixed inflammatory cell infiltration.
	A12- very slight multifocal mixed inflammatory cell infiltration, very slight multifocal single cell necrosis
4	A16- no significant histopathological lesions
	A17- very slight multifocal mixed inflammatory cell infiltration
	A18- no significant histopathological lesions
5	A22[1] - severe midzonal to diffuse necrosis
	A23[1] - severe midzonal to diffuse necrosis
	A24- no significant histopathological lesions

[1]sacrificed on day 2 due to PGC ; [2]sacrificed on day 5 due to PGC; [3] sacrificed on day 9 due to PGC; [4]sacrificed on day 2 as control per sponsor's request

Control groups 1 and 2, alongside specific animals in treatment groups 3 and 5, displayed a common background lesion characterized by very slight multifocal mixed inflammatory cell infiltration in their liver tissues. In group 3 and 5, signs of treatment-related acute toxicity were seen in liver samples from animals sacrificed due to poor general conditions within 5 days after N-azido-ADC treatment. These signs included severe midzonal to diffuse necrosis. Notably, in one animal, A11 (group 3), additional indicators such as hepatocellular basophilia and multifocal vacuolation characteristic of necrotic processes, were observed. The animal A10 (group 3), sacrificed 9 days post-ADC treatment due to poor general conditions, also exhibited single-cell necrosis and hepatocellular basophilia. However, the absence of severe necrosis suggested potential signs of late toxicity. Single-cell necrosis was also observed in animal A7 from group 3, which was sacrificed at the planned 6-day timepoint. This was accompanied by midzonal mitosis, indicating hepatic regeneration, which likely plays a role in repairing liver damage induced by the ADC treatment. A comparable outcome was seen in animal A19 and A20 from group 5. This result suggested that administration of DBCO-PEG_4-COOH (**7**) 20 hours after N-azido-ADC might be too late to revert treatment-related toxicity in some animals.
Interestingly, liver samples from animals in group 4, treated with compound **7** 6 hours after ADC administration, showed no significant histopathological lesions on days 6 and 14. This result suggested that administration of compound **7** 6 hours after ADC treatment neutralizes treatment-related toxicities.
Overall, diffuse liver necrosis appeared to be the main pathological cause of treatment-related toxicity. Administration of DBCO-PEG_4-COOH (**7**) at 6 hours post ADC treatment (group 4) completely counteracted treatment-related pathological lesions at day 6 and day 14. On the contrary, the application of compound **7** at 20-hour timepoint (group 5) was not able to completely counteract treatment toxicity but resulted in a reduction of severe toxicological lesions.

4.7.3 Histopathological findings in kidney tissues

The data in this section are based on the report *Internal Fraunhofer ITEM Study No. 05N23526 - non-GLP study* by veterinary pathologist Dirk Schaudien on 18 October 2023. Main findings are summarized in **Table 37**.
In control groups 1 and 2, common background kidney lesions, including tubule basophilia and mixed inflammatory cell infiltration, were detected. These lesions were also observed in some animals in treated groups 3, 4, and 5. Kidney samples from animals sacrificed due to poor general conditions on day 2 showed no severe pathological lesions.

Table 37: *Main pathological findings in the kidneys at day 6 and 14 after co-treatment with N-azido-ADC and DBCO-PEG$_4$-COOH (7).*

Group	Pathological findings for kidneys Day 6
1	A1- no significant histopathological lesions A2- very slight multifocal tubule basophilia, very slight multifocal mixed inflammatory cell infiltration. A3- very slight multifocal tubule basophilia, very slight multifocal mixed inflammatory cell infiltration.
2	A4- no significant histopathological lesions A5- no significant histopathological lesions A6- no significant histopathological lesions
3	A7- no significant histopathological lesions A9[1]- very slight multifocal mixed inflammatory cell infiltration
4	A13[4]- no significant histopathological lesions A14- no significant histopathological lesions A15- no significant histopathological lesions
5	A19- no significant histopathological lesions A20- no significant histopathological lesions A21- no significant histopathological lesions
Group	**Pathological findings for kidneys Day 14**
3	A10[3]- moderate multifocal tubule basophilia, slight multifocal Bowman's capsule hyperplasia, slight multifocal tubule necrosis, slight multifocal tubule dilation, very slight multifocal mixed inflammatory cell infiltration A11[2]- moderate multifocal tubule and glomerular necrosis, moderate multifocal tubule vacuolation A12- moderate multifocal tubule basophilia, slight multifocal Bowman's capsule hyperplasia, slight multifocal tubule necrosis, slight multifocal tubule dilatation, very slight multifocal mixed inflammatory cell infiltration
4	A16- very slight multifocal tubule basophilia A17- very slight multifocal tubule basophilia A18- no significant histopathological lesions
5	A22[1] - no significant histopathological lesions A23[1] - no significant histopathological lesions A24- very slight multifocal tubule basophilia

[1]*sacrificed on day 2 due to PGC ;* [2]*sacrificed on day 5 due to PGC;* [3] *sacrificed on day 9 due to PGC;*
[4]*sacrificed on day 2 as control per sponsor's request*

However, animals A11 and A10 (group 3), sacrificed on days 5 and 9, respectively, exhibited signs of tubule and glomerular necrosis, suggesting potential toxicity development at a later stage. Additionally, animal A10 displayed signs of hyperplasia, indicative of tissue regeneration and tubule dilation. Similar findings were seen on day 14 in the kidney sample of animal A12 in group 3. These results suggested that kidney toxicity developed later compared to liver toxicity and, in some cases, was accompanied by tissue repair. No histopathological changes were observed in kidney samples from animals in groups 4 and 5 on day 6 and day 14, as well as in animal A7 in group 3 sacrificed on day 6.

In general, the kidneys exhibited lesser involvement in the early stages of toxicity induced by the ADC treatment. However, in the tissues of animals sacrificed after 6 days, manifestations of prolonged toxicity, e.g. necrosis and tissue regeneration were more evident. interestingly, signs of prolonged toxicity after 14 days were not present in groups treated with DBCO-PEG$_4$-COOH (**7**).

4.8 The impact of DBCO-PEG$_4$-COOH (7) administration on N-azido-ADC tumor efficacy

In vivo, the administration of DBCO-PEG$_4$-COOH (**7**) within 12 hours post-application of a lethal dose of N-azido-ADC led to increased tolerability and improved mice survival (**section 4.6.1**). The application of compound **7** has also been proven to reduce toxic side effects substantially in the liver and kidneys (**section 4.7**).

The primary cause of Antibody-drug conjugate (ADC) toxicity in healthy tissues arises from the fact that only 0.1% of the injected ADC is estimated to reach the targeted tumor population, while the rest is uptaken by healthy tissues, such as the liver and kidneys (Poli et al. 2013; Wada et al. 2014; Nguyen 2023). Nevertheless, the extended exposure of the tumor to the ADC, facilitated by its prolonged half-life compared to small molecules, represents an advantage in enhancing tumor efficacy (Colombo and Rich 2022; Gerber et al. 2023). To assess if early neutralization of the ADC by application of compound **7** could affect tumor response and improve treatment-related tolerability, two efficacy studies were conducted in JIMT-1 cell line-derived xenograft (CDX) mice. Initially, the efficacy of N-azido-ADC was evaluated at various concentrations without application of the neutralizing agent. Subsequently, a second efficacy study was conducted, including a second treatment with DBCO-PEG$_4$-COOH (**7**) to investigate its potential impact on the tumor response. Moreover, two ELISA assays were performed to understand the biodistribution of N-azido-ADC and the total ADC, comprised of N-azido-ADC and N-azido-ADC-

neutralized in tumors, kidney, liver, and plasma samples. Samples were taken at 24 hours and 7 days after application of compound **7** to detect early and late N-azido-ADC uptake in the different tissues.

4.8.1 N-azido-ADC efficacy in JIMT-1 CDX model

To evaluate the therapeutic efficacy of N-azido-ADC, JIMT-1 CDX in female NMRI nude mice were treated with doses of 2.5 mg/kg (1/10 MTD), 5 mg/kg (1/5 MTD) and 10 mg/kg (2/5 MTD). Mice were treated with an intravenous single dose of N-azido-ADC, and the study was conducted over a period of 95 days. Tumor growth was reduced at all three doses, with complete tumor remission from day 15 post-treatment until the end of the study (**Figure 25A**).

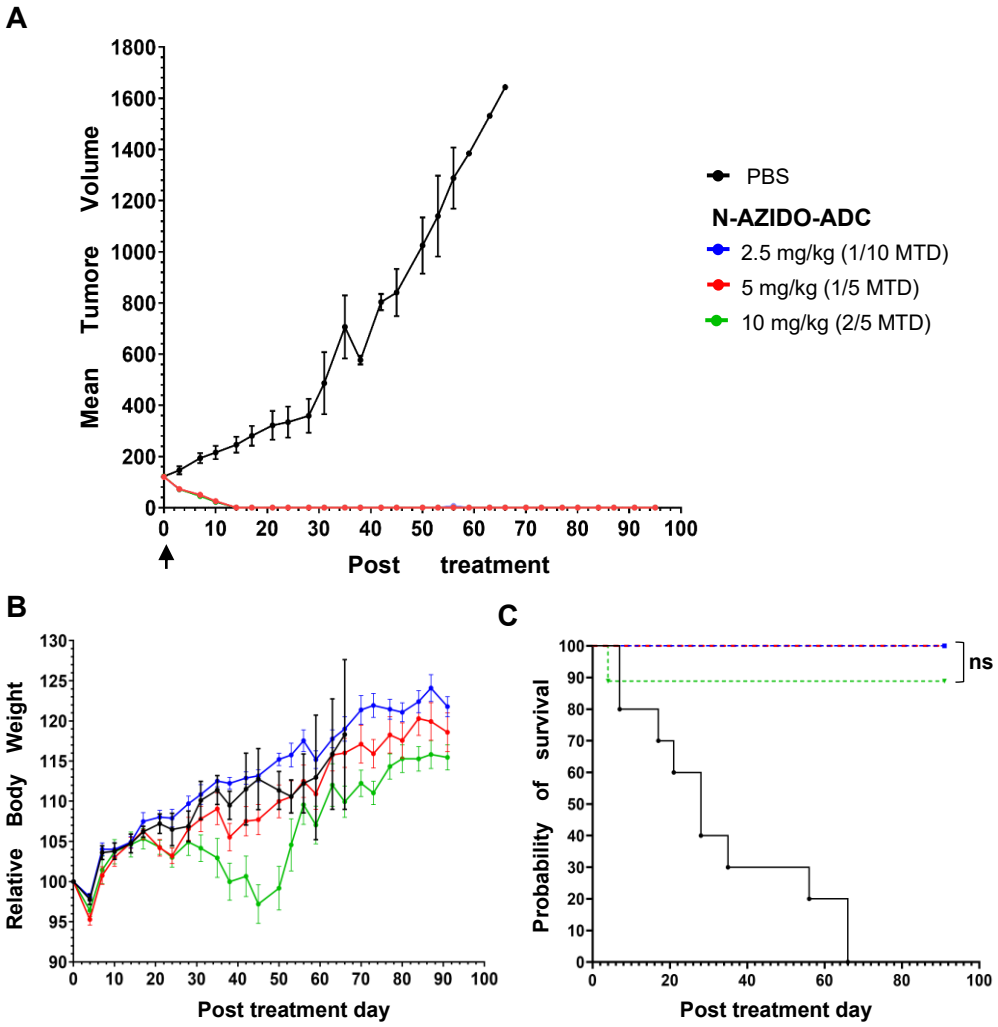

Figure 23: Efficacy study of N-azido-ADC in JIMT-1 CDX in NMRI nude mice*. (A) Mean tumor volume (mm^3) of mice treated with i.v. single doses of N-azido-ADC. (B) Relative body weight of each group. Tumor volume and body weight were monitored twice a week for 95 days. Error bars represent SEM of n=10. (C) Kaplan-Meier survival plots of each group.*

Differences in the relative body weight (RBW) were observed after day 30 post-treatment (**Figure 25B**). Mice treated with 2.5 mg/kg N-azido-ADC and 5 mg/kg N-azido-ADC showed constant weight gain up to 120% and 117% RBW at day 95, respectively. Mice treated with the highest dose of 10 mg/kg displayed body weight drop between days 30 and 45 with an average of 95% RBW at day 45. However, they regained weight to 112% RBW at day 95. Survival of treated groups greatly outperformed the PBS control group, where mice did not survive until the end of the study (**Figure 25C**). No differences in the probability of survival were seen among the three treatment groups. One mouse was found dead at day 4 in the treatment group with the highest dosage of 10 mg/kg, probably due to treatment-related toxicity. Overall, N-azido-ADC showed high efficacy against JIMT-1 CDX tumors with complete tumor remission already at the lowest dose of 2.5 mg/kg (1/10 MTD), and improved survival compared to the control group. The highest dose of 10 mg/kg (2/5 MTD) was slightly less tolerated, with a lower increase in body weight compared to the other dosages.

4.8.2 Impact of DBCO-PEG$_4$-COOH (7) administration on the tumor efficacy of N-azido-ADC in JIMT-1 CDX model

To assess the impact of DBCO-PEG$_4$-COOH (**7**) administration on the efficacy and tolerability of N-azido-ADC, an efficacy study in a JIMT-1 CDX model in female NMRI nude mice with 10 mg/kg N-azido-ADC and additional administration of compound **7** was performed. 10 mg/kg N-azido-ADC caused mortality in one mouse and lower body weight compared to doses of 5 mg/kg and 2.5 mg/kg N-azido-ADC (**section 4.8.1**). Consequently, the objective was to assess whether the additional treatment with compound **7** post-N-azido-ADC administration could maintain tumor response while improving treatment tolerability, avoid mortality and mitigate loss of body weight. Two control groups were treated with PBS and 6 hours later with vehicle or 45 mg/kg compound **7** to determine any side effects of the substances on the animals (**Table 38**).

Table 38: Impact of DBCO-PEG$_4$-COOH (7) on tumor response. *Study groups of the efficacy study with N-azido-ADC and additional treatment with DBCO-PEG$_4$-COOH (**7**) in JIMT-1CDX mice.*

Group	1st treatment	2nd treatment
1	PBS	t=6h, Vehicle
2	PBS	t=6h, 45 mg/kg **DBCO-PEG$_4$-COOH (7)**
3	10 mg/kg (2/5 MTD) **N-azido-ADC**	t=6h, Vehicle
4	10 mg/kg (2/5 MTD) **N-azido-ADC**	t=6h, 45 mg/kg **DBCO-PEG$_4$-COOH (7)**
5	10 mg/kg (2/5MTD) **N-azido-ADC**	t=20h, 45 mg/kg **DBCO-PEG$_4$-COOH (7)**

In treatment group 3, a single dose of N-azido-ADC was administered as the first treatment and 6 hours later the vehicle (10% DMSO + 10% (2-Hydroxypropyl)-β-cyclodextrin in PBS) was applied. In groups 4 and 5, 45 mg/kg of compound **7** was administered 6 and 20 hours after single-dose treatment with N-azido-ADC. The 6-hour and 20-hour timepoints were selected based on the histopathological study (**section 4.7**), to examine the effect of an early and a late application of compound **7**. The study was conducted for 75 days, and tumor volume was measured twice weekly.

The application of DBCO-PEG_4-COOH (**7**) post-N-azido-ADC treatment negatively affected tumor response in group 5 and in group 4 (**Figure 26A**). Only group 3 (10 mg/kg N-azido-ADC and vehicle) showed full tumor remission until day 75. Treatment group 4 (compound **7** 6 hours after N-azido-ADC) showed a decrease in tumor growth until day 20, followed by constant regrowth, reaching a mean tumor average of 400 mm^2 at the end of the study. Treatment group 5 (compound **7** 20 hours after N-azido-ADC) showed tumor remission until day 35, followed by a slight regrowth to a mean tumor average of 100 mm^2 at the end of the study. However, the differences in average tumor volumes at day 75 between group 3 and 5 were statistically not significant, whereas the increase in tumor growth in group 4 was considered a significant variation (**Figure 27**). Tumor growth inhibition (TGI) in group 5 was maintained above 90%, as in group 3, while in group 4 the TGI decreased to 72 % (**Table 39**). The spider plot in **Figure 26B** shows the tumor volume of each mouse from group 3, 4 and 5. In group 3 all mice showed tumor volume equal to zero, while group 4 and 5 showed variations in tumor growth, with the majority of the animals displaying tumor regrowth 20 days after N-azido ADC and compound **7** treatment. The probability of survival of the control groups 1 and 2 at the end of the study was 20% and 0% respectively, while for group 3 and 5 90% and for group 4 70% was reached (**Figure 26D**), showing a significant improvement of the survival in the treated groups compared to the control groups. No statical differences in the probability of survival were seen among group 3 and groups 4 and 5. RBW of treated groups 3, 4 and 5 did not show variations in comparison to the PBS group 1. Group 2 showed higher increase in RBW, probably due to high tumor growth (**Figure 26C**).

Overall, application of 45 mg/kg DBCO-PEG_4-COOH (**7**) 20 hours after single-dose administration of 10 mg/kg N-azido-ADC was able to partially retain tumor treatment efficacy, with the exceptions of some mice exhibiting tumor regrowth. On the contrary, application of compound **7**, 6 hours post- N-azido-ADC treatment failed to maintain tumor remission and a consistent increase in tumor growth after 20 days was detected.

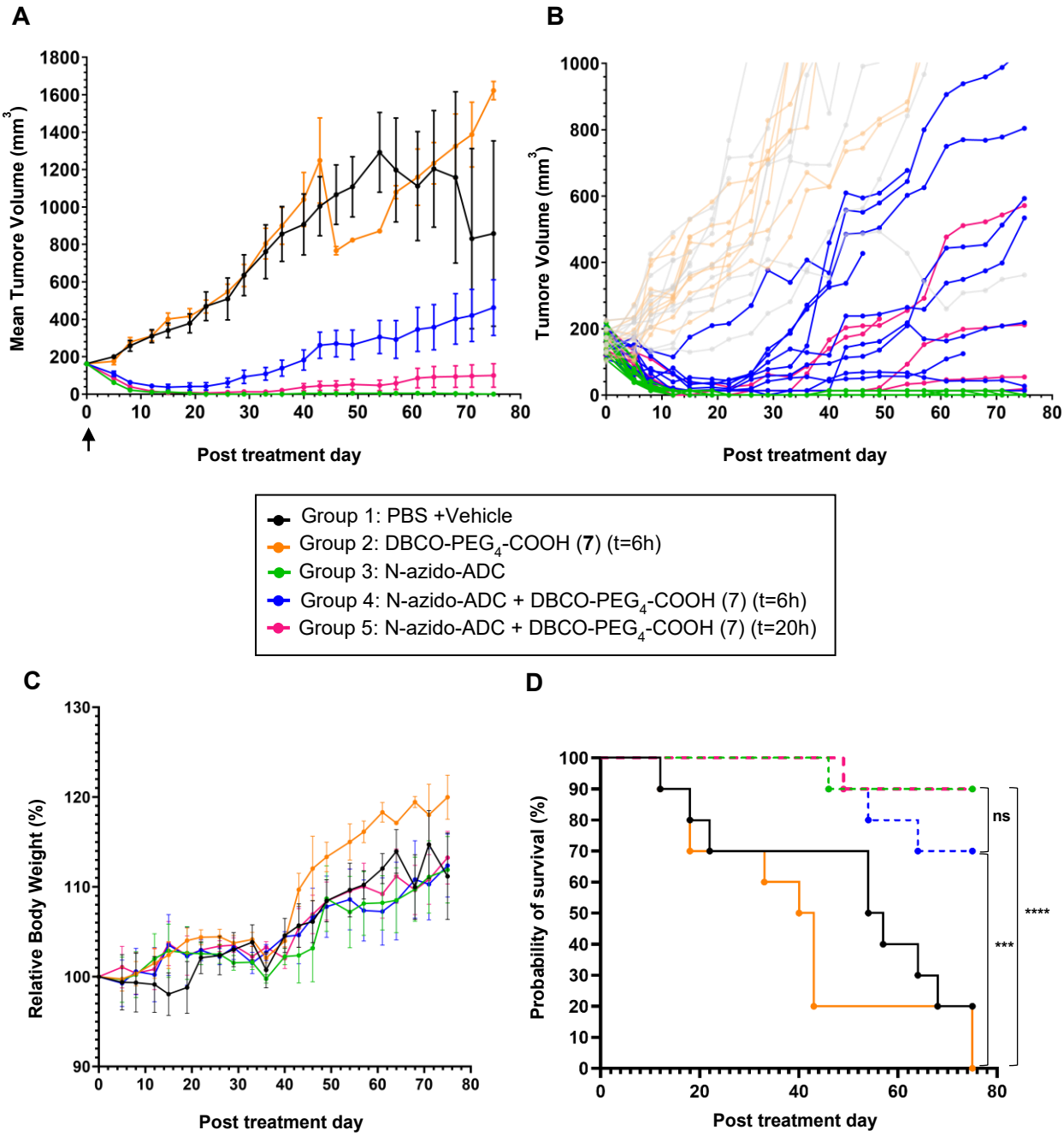

Figure 24: Efficacy study with N-azido-ADC and DBCO-PEG$_4$-COOH (7) co-treatment in JIMT-1 CDX NMRI nude mice. *(A) Mean tumor volume (mm^3) of groups described in Table 1. Error bars represent SEM of n=10 (B) Spider plot of groups 3, 4 and 5 single curves of tumor volume (mm^3): Each curve is representative of an animal. Single curves of animals in group 1 and 2 are in the background. (C) Relative body weight % of each group. Tumor volume and body weight were monitored twice a week for 75 days. Error bars represent SEM of n=10. (D) Kaplan-Meier survival plots of each group. Group 3 and 5 vs. Group 4 (ns, p>0.05), Group 4 vs. Group 2 (***p<0.001) and Group 5 vs. Group 2 (****p<0.0001).*

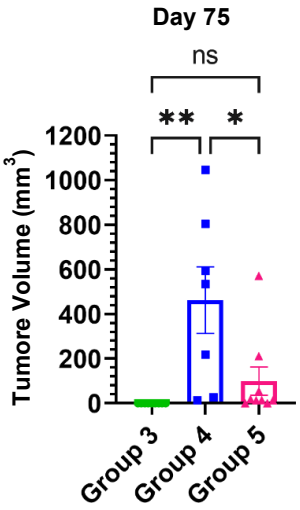

Figure 25: Tumor volume difference among treatment groups of the co-treatment efficacy study shown in Figure 24. *Box plots comparing tumor volumes at the end of the study (day 75). Ordinary One-way ANOVA: *p<0.05, **p<0.01.*

Table 39: Percentage of Tumor Growth Inhibition

Group	Tumor Growth Inhibition TGI (%)
3	98
4	72
5	92

4.8.3 Biodistribution of N-azido-ADC and total ADC in JIMT-1 CDX female NMRI nude mice

Previously, the Strain-Promoted Azido-Alkyne cycloaddition (SPAAC) reaction efficiency of DBCO-PEG_4-COOH (**7**) and BCN-PEG_6-OH (**6**) with N-azido-ADC was assessed *in vivo* quantifying the plasma concentration of N-azido-ADC with the azido-ADC ELISA and the Total ADC, comprised of unreacted N-azido-ADC and N-azido-ADC-neutralized in the anti-ADC ELISA (**section 4.5.3**). In this study, the SPAAC reaction efficiency and the biodistribution of the unreacted N-azido-ADC and the N-azido-ADC-neutralized were quantified *in vivo* in tumor, kidneys, liver, and plasma. The study design was identical to the efficacy study with N-azido-ADC and compound **7** (**section 4.8.2, Table 38**). Tissues were collected 24 hours and seven days after treatment with either vehicle or compound **7** and were analyzed with the azido-ADC ELISA and the anti-ADC ELISA. Results are shown in **Figure 28**. In group 3, treated with 10 mg/kg N-azido-ADC and the vehicle, the

concentration of N-azido-ADC and Total ADC measured with the two ELISAs was non significantly different. This result was expected because no compound **7** was administered, preventing N-azido-ADC from reacting with the neutralizing agent. Consequently, this confirmed the reliability of the azido-ADC ELISA (**Figure 28A**). 24 hours post-application of compound **7**, N-azido-ADC concentration in tumor was 10-12 µg/g, 10 times higher compared to the concentration in the liver (1-2 µg/g) and two times higher than in the kidneys (5 µg/g). However, most of the ADC was still in circulation in plasma at 24 hours. At the 7-day timepoint, tumor samples from group 3 exhibited a similar N-azido-ADC concentration of approximately 10 µg/mL as observed in the 24-hour samples. Likewise, liver samples maintained a consistently low N-azido-ADC concentration of approximately 1 µg/g. In contrast, both kidney and plasma ADC concentrations experienced a notable decrease on day seven, with only half of ADC in plasma compared to the 24-hours timepoint.

ELISA analysis of samples from group 4 treated with 45 mg/kg compound **7** 6 hours after N-azido-ADC treatment, showed significantly different concentrations of N-azido-ADC in comparison to Total ADC in the tumor and plasma samples at both, 24 hours and 7 days after collection (**Figure 28B**). Concentration of non-reacted N-azido-ADC at 24 hours in tumors fell below the lower limit of quantification (LLQ), while total ADC concentration was approximately 12 µg/mL. In plasma samples, at 24-hour timepoint, no N-azido-ADC was detected, while Total ADC was 90 µg/mL. Similarly, at the 7-day timepoint, neither tumor nor plasma samples showed any presence of N-azido-ADC, while the total ADC concentration decreased by half to around 5 µg/mL in tumors and approximately 45 µg/mL in plasma compared to the 24-hour timepoint. Examination of liver samples revealed no significant differences between N-azido-ADC and Total ADC concentrations at both timepoints. Notably, in kidneys, there was a tendency for Total ADC levels to be slightly elevated compared to N-azido-ADC at both timepoints, although the difference did not reach statistical significance.

ELISA analysis of samples from group 5, treated with compound **7** 20 hours after N-azido-ADC treatment, showed similar differences in concentration between N-azido-ADC and Total ADC as seen for group 4 (**Figure 28C**). At the 24-hour timepoint, total ADC concentration was at 12 µg/g in tumor samples and 100 µg/mL in plasma samples, whereas N-azido-ADC concentration in tumor was undetectable and in plasma sample only at 2 µg/mL. Similarly, at the 7-day timepoint Total ADC concentration was higher than N-azido-ADC concentration in both tumor and plasma with 5 µg/g and 45 µg/mL, respectively. Again, no significant differences between Total ADC and N-azido-ADC were detected in the liver. While total ADC levels in the kidneys exhibited a five-fold increase in comparison to N-azido-ADC, this variance did not reach statistical significance.

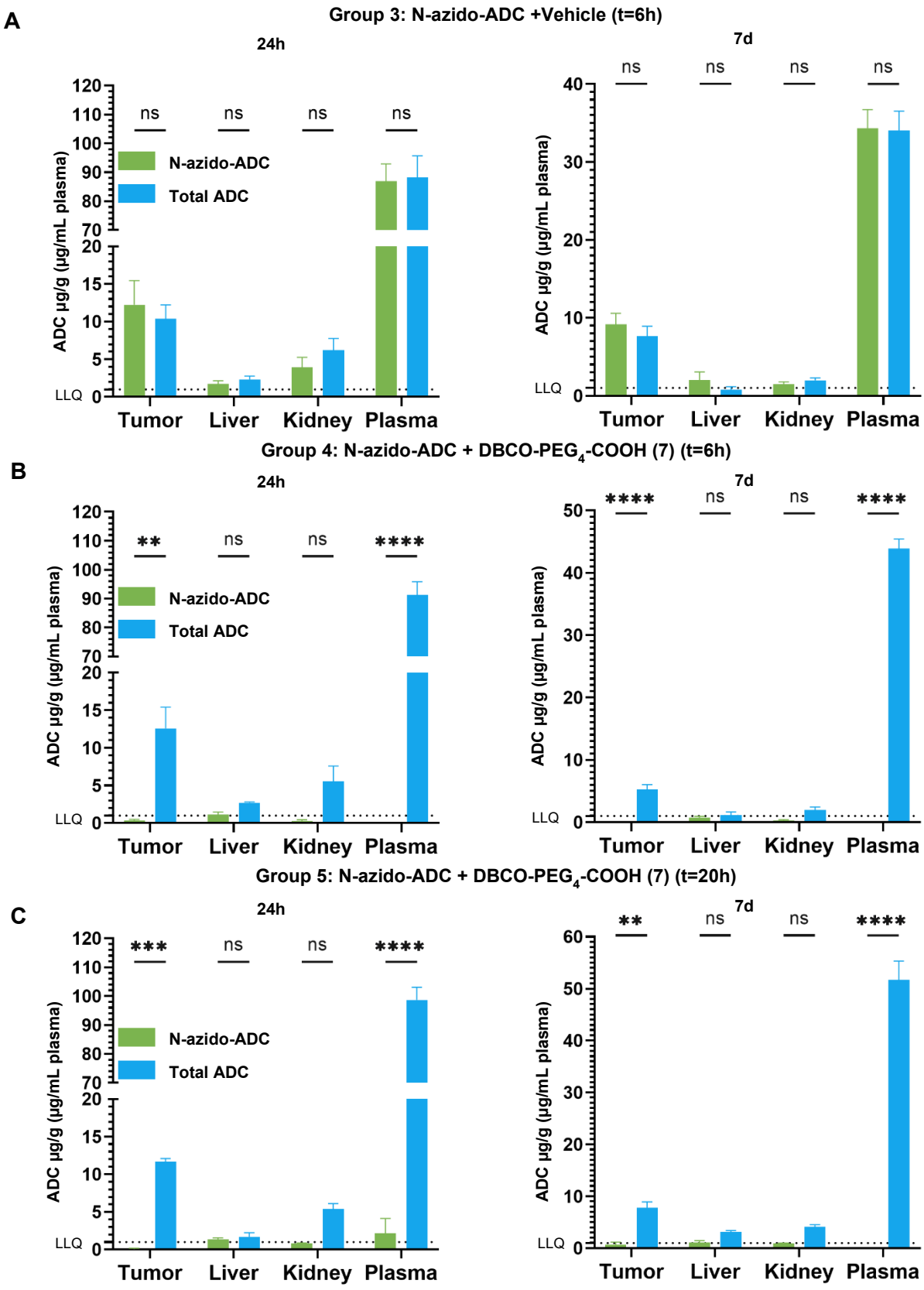

***Figure 26**: **Biodistribution of N-azido-ADC and total -ADC upon co-treatment with compound 7 in a JIMT-1 CDX in NMRI nude mice.** Mice were treated as described in **Table 38** (section 4.8.2). Tumor, liver, kidney, and plasma were collected 24h and 7 days after treatment with either Vehicle or DBCO-PEG$_4$-COOH (**7**). N-azido-ADC in the samples was measured with azido-ADC ELISA, while total ADC was measured with anti-ADC ELISA. Error bars represent n=3 ± SEM. Two-way ANOVA with Tukey's multiple comparison test: ns>0.05, *p≤0.05, **p≤0.01, ***p≤0.001, ****p≤0.0001*

The N-azido-ADC-neutralized (%) was calculated based on the data obtained in the azido-ADC ELISA and the anti-ADC ELISA as described in the formula in **section 4.5.3** (**Table 40**). The percentage of N-azido-ADC neutralized in both plasma and tumor in both groups ranged between 90% and 100%, suggesting that most of the administered N-azido-ADC promptly reacted with compound **7** in plasma and subsequently accumulated in the tumor. Interestingly, the liver exhibited the lowest percentage of N-azido-ADC neutralization, particularly evident in group 5, where compound **7** was administered 20 hours post-ADC administration. At the 24-hour timepoint in group 5, only 22% of N-azido-ADC was neutralized in the liver, implying that a significant portion of the N-azido-ADC was initially distributed and accumulated in the liver following administration. Conversely, in the kidney samples of group 4, the majority of the uptaken ADC was N-azido-ADC-neutralized, indicating a preferential distribution of the compound in renal tissue. In the kidney samples of group 5, N-azido-ADC-neutralized % was lower compared to group 4, ~80% at the 24-hour and 7-day timepoints.

***Table 40*:Percentage of N-azido-ADC-neutralized-in different tissues as determined by ELISA in Figure 28**. *Data in the table indicate the average percentage calculated from n=3 ± SEM.*

	N-azido-ADC-neutralized (%) Group 4		**N-azido-ADC-neutralized (%) Group 5**	
Tissue	**24h**	**7d**	**24h**	**7d**
Tumor	97±2	100	99±1	90±5
Liver	57±11	48±5	22±3	63±4
Kidney	96±2	88±6	81±2	76±3
Plasma	100	100	98±2	100

In both tumor and plasma samples from groups 4 and 5, the concentration of N-azido-ADC significantly decreased compared to the Total ADC levels 24 hours and 7 days post-application of DBCO-PEG_4-COOH (**7**), with over 90% of N-azido-ADC being neutralized. This indicated that administering compound **7** 6 and 20 hours after N-azido-ADC treatment resulted in the formation of nonactive, N-azido-ADC-neutralized, incapable of eliminating tumor cells effectively. This finding potentially suggested why the tumor response in JIMT CDX was adversely impacted by the addition of compound **7**. Conversely, it was evident that N-azido-ADC had a tendency to accumulate preferentially in the liver. Moreover, the kidneys exhibited a higher uptake of N-azido-ADC neutralized compared to its active form in both groups 4 and 5.

4.9 Application of the neutralization strategy in a difficult-to-treat prostatic tumor model

The studies performed so far proved the ability of DBCO-PEG_4-COOH (**7**) administration in improving N-azido-ADC tolerability. However, administration of compound **7** in JIMT-1 Cell-derived xenograft (CDX) mice affected tumor response, increasing tumor regrowth, especially when the neutralizing agent was administered 6 hours after ADC treatment.

As demonstrated in **section 4.8.1**, the JIMT-1 CDX tumor exhibited considerable sensitivity to N-azido-ADC. A single dose of 2.5 mg/kg N-azido-ADC alone (1/10 MTD) led to complete tumor remission until day 95. Due to its high sensitivity to N-azido-ADC treatment, JIMT-1 might not be a suitable tumor model for the application of the SPAAC neutralization strategy since a high tumor efficacy is reached already with tolerable doses of N-azido-ADC. To assess the potential benefits of the neutralization strategy with compound **7**, this approach was applied to the 22RV1 xenograft model (CDX), a difficult-to-treat model of prostate cancer. 22RV1 is an androgen-dependent human prostate carcinoma cell line derived from a xenograft propagated in mice after castration-induced regression (Sramkoski et al. 1999). This tumor is characterized by moderate and heterogeneous expression of the Prostate-Specific Membrane Antigen (PSMA), with approximately 30-50% of cells expressing PSMA (Gorges et al. 2016). Furthermore, studies have demonstrated that a subpopulation within the 22RV1 cell line possesses stem-like characteristics and expresses multi-drug resistance proteins, posing challenges in controlling tumor growth through treatments (Liu et al. 2010; Kushwaha et al. 2022).

In this study, a high concentration of an anti-PSMA ADC bearing the Ama-N-azido-bromoacetamide (**16**) compound was administered to 22RV1 CDX male NMRI nude mice. To reduce potential side effects associated to the high treatment concentrations, compound **7** was aimed to be administered at the latest possible timepoint after the ADC treatment. Initially, a novel anti-PSMA ADC carrying compound **16** was produced, and characterized *in vitro* alongside a standard anti-PSMA ATAC®. Subsequently, the Maximum Tolerated Dose (MTD) for both conjugates was determined in 22RV1 CDX tumor-bearing mice. Various doses exceeding the MTD were then co-administered with compound **7** at different timepoints to evaluate the latest possible application before signs of toxicity occur. Based on the outcome, an efficacy study in 22RV1 CDX male NMRI nude mice was conducted.

4.9.1 Generation and characterization of PSMA-azido-ADC and PSMA-ADC

As previously described in **section 4.2.1**, the conjugation of compound Ama-N-azido-Bromoacetamide (**16**) was optimized for an anti-PSMA antibody (Wolf *et al.*, 2010; Hechler and Pahl, 2023) with an engineered cysteine at position S399 of the Fc portion of the antibody.

For the required mutation, the S399 residue of the constant heavy chain (HC) sequence of the anti-PSMA antibody was mutated into a cysteine. The site-directed mutagenesis was performed with the pHDP-anti-PSMA-HC plasmid, which contains the sequence of the variable HC and constant HC region of the anti-PSMA antibody, resulting in the pHDP-anti-PSMA-S399C-HC plasmid (**Figure 29**).

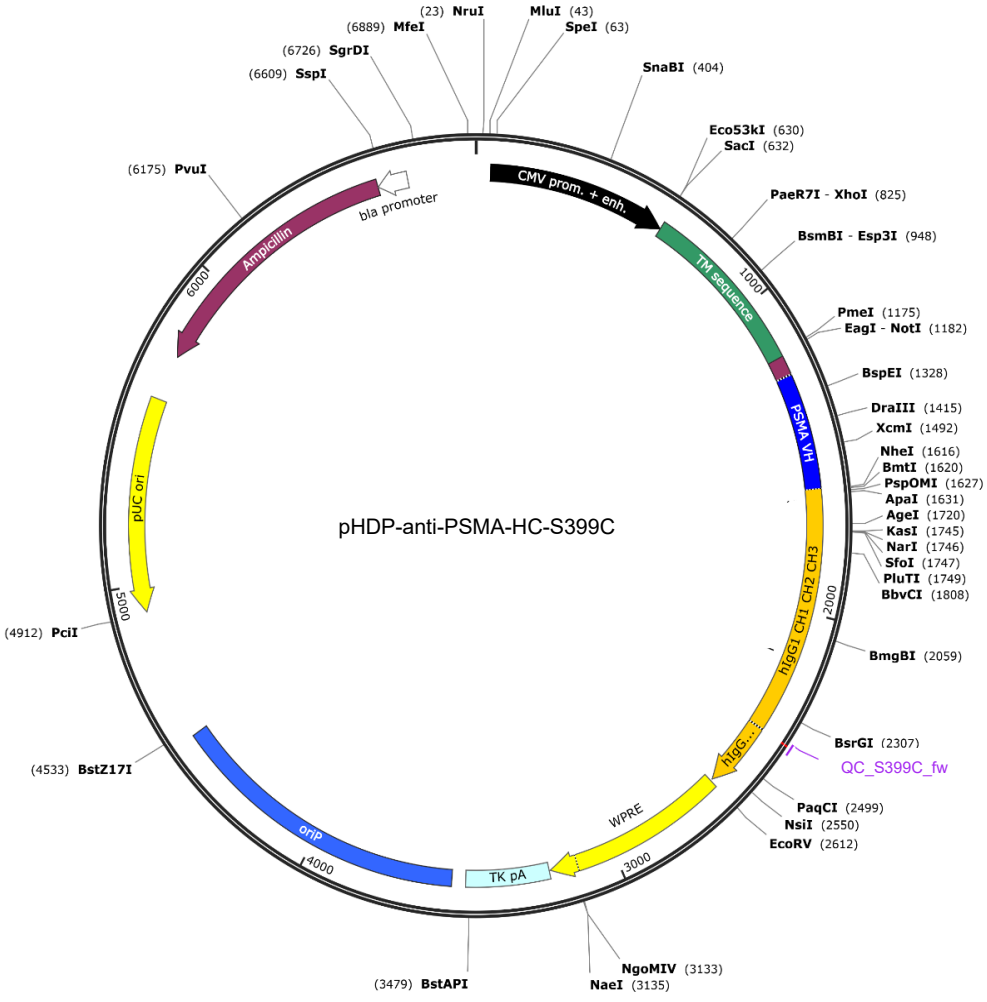

Figure 27: Site-directed Mutagenesis of the serine residue 399 to cysteine in the pHDP-anti-PSMA-HC-S399C plasmid. *Replacement of the S399 residue on the heavy chain sequence of the anti-PSMA antibody using the QC_S399C_fw primer. Antibody cloning and expression is described in Method section 3.2.5.*

Successful site-direct mutagenesis was confirmed via sequencing by Eurofins. The plasmid comprises an ampicillin-resistant cassette for selection, the pUC ori for replication in chemo-competent *E.coli* bacteria,(Jeffrey and Joachim 1991) Epstein-Barr virus-derived oriP for plasmid replication in mammalian cells (Black and Vos 2002), the Cytomegalovirus (CMV) promoter and enhancer for transient expression of the transgene (Boshart et al. 1985), a transmembrane domain (TM) for secretion of the protein outside of the cell, the variable HC and constant HC region of the antibody, a woodchuck hepatitis virus post-transcriptional regulatory element (WPRE) sequence to increase transgene expression (Zufferey et al. 1999), and a thymidine kinase poly A from herpes simplex virus (Tk pA) to stabilize the mRNA of the protein by addition of a long chain of adenine nucleotides (Wang et al. 2022).

The newly generated anti-PSMA antibody anti-PSMA-S399C was expressed in mammalian cells and purified with Fast protein liquid chromatography (FPLC) for the subsequent conjugation to compound **16**. Bromoacetamide conjugation was performed as described in **section 4.2.1**. In brief, anti-PSMA-S399C was conjugated in PBS pH=8 with 10 equivalents (eq.) of compound **16** for one hour at room temperature, resulting in the PSMA-azido-ADC. Simultaneously, an anti-PSMA ADC featuring a standard amanitin-derivative, Ama-N-ctrl (**18**), was generated for comparison. The Ama-N-ctrl (**18**) payload which shares a similar structure with compound **16** but lacks the azide moiety on the first amino acid of amanitin, was conjugated via maleimide-thiol conjugation to an anti-PSMA antibody comprising HDP's standard mutation for the generation of ATACs via maleimide conjugation (D265C mutation). 4 eq. of Compound **18** were conjugated to anti-PSMA-D265C in PBS pH=7.4 resulting in the PSMA-ADC.

Drug-to-antibody ratio (DAR) of both conjugates was analyzed by LC-MS showing an average DAR of 1.84 for PSMA-azido-ADC and 1.92 for PSMA-ADC (**Figure 30**). In addition, standard quality analysis of both ADCs was performed (**Method section 3.2.9, 3.2.10, 3.2.11**). Cytotoxicity of PSMA-azido-ADC and PSMA-ADC was tested in PSMA-positive and negative cell lines.

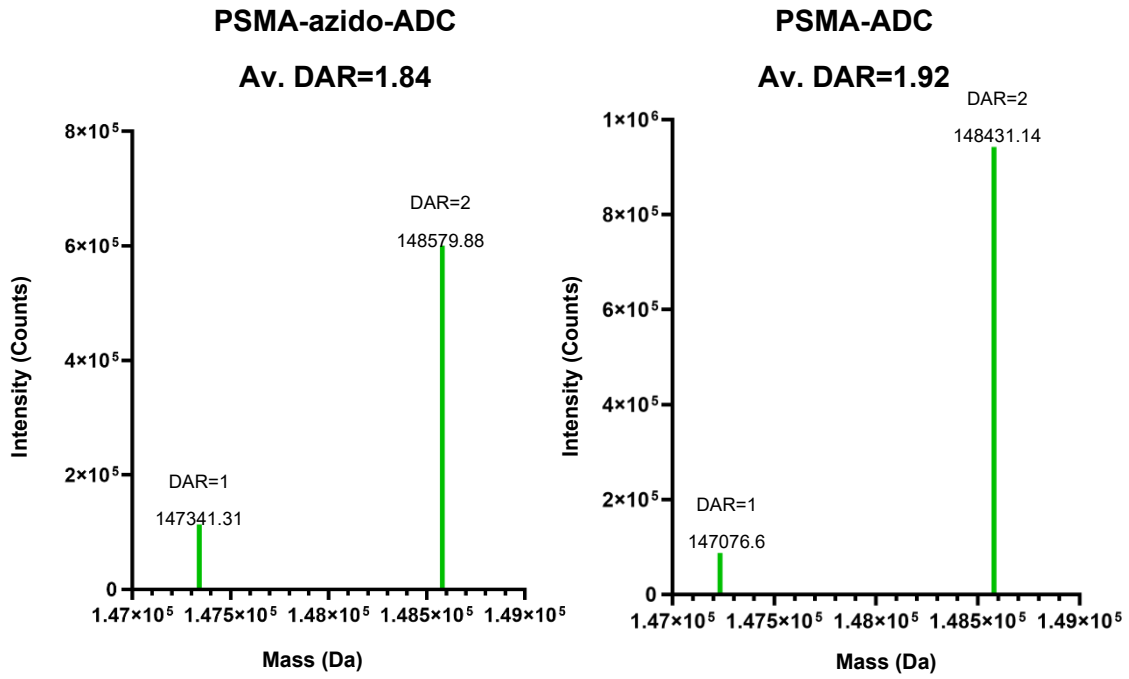

Figure 28: DAR analysis of PSMA-azido-ADC and PSMA-ADC. *(A) DAR profile of PSMA-azido-ADC (left), resulting from the conjugation of compound **16** to anti-PSMA-S399C, and PSMA-ADC (right), resulting from the conjugation of compound **18** to anti-PSMA-D265C.*

4.9.2 Cytotoxicity of PSMA-azido-ADC and PSMA-ADC on PSMA-positive and -negative cell lines

The cytotoxicity of the newly generated PSMA-azido-ADC and PSMA-ADC was tested *in vitro* in LNCaP, 22RV1 and PC3 cells (**Figure 31**). The LNCap cell line has a high expression of PSMA, 22RV1 a moderate expression and PC3 is considered PSMA-negative (Gorges et al. 2016). PSMA-azido-ADC showed higher cytotoxicity compared to PSMA-ADC in both LNCaP and 22RV1 cell lines, while no cytotoxicity was observed in PC3 cells (**Table 41**). Furthermore, both ADCs achieved complete cytotoxicity in LNCaP cells; whereas in 22RV1 cells a residual cell viability between 30% and 40% remained even at high concentrations.

Overall, PSMA-azido-ADC and PSMA-ADC showed a target specific cytotoxic profile with EC_{50} values in the low nanomolar to picomolar range in PSMA-positive cell lines.

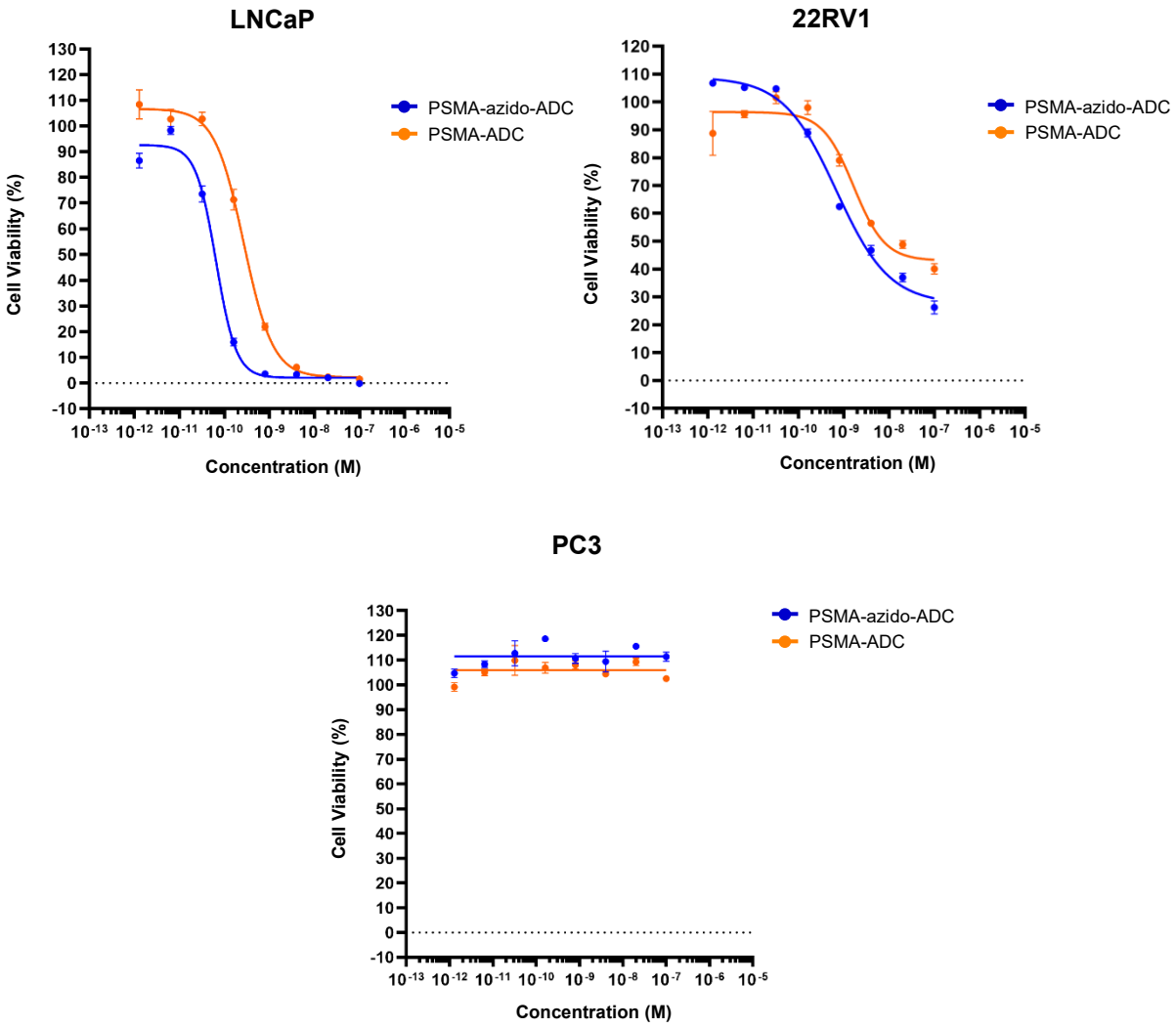

Figure 29: Cytotoxicity of anti-PSMA ADCs on PSMA positive and negative cell lines. *Dose-response curves of anti-PSMA ADCs on LNCaP, 22RV1, and PC3 cell lines. Cells were treated with different concentrations of the ADCs for 96 h.*

Table 41: EC_{50} values of anti-PSMA ADCs' on PSMA positive and negative cell lines. *EC_{50} values were calculated from the dose-response curves shown in* ***Figure 31****.*

Cell line	PSMA-azido-ADC (EC_{50} pM)	PSMA-ADC (EC_{50} pM)
LNCaP	65	268
22RV1	683	1648
PC3	-	-

4.9.3 Maximum Tolerated Dose (MTD) of PSMA-azido-ADC and PSMA-ADC in tumor-bearing mice

The Maximum Tolerated Dose (MTD) of PSMA-azido-ADC and PSMA-ADC was determined in 22RV1 tumor-bearing mice. Three mice per group were treated with an intravenous single dose of the respective ADC. Doses of 10, 20, and 25 mg/kg of PSMA-azido-ADC (**Figure 32A**) and 6, 10, and 15 mg/kg of PSMA-ADC (**Figure 32B**) were examined. The MTD for PSMA-azido-ADC was determined to be 25 mg/kg, and although some mice exhibited body weight oscillations at this dose, no weight loss exceeded 20%. PSMA-ADC showed a lower tolerability, with an MTD of 15 mg/kg. Once again, mice lost weight during the initial 4 days of the study but gradually regained weight until the study end.

Overall, PSMA-azido-ADC was better tolerated than PSMA-ADC.

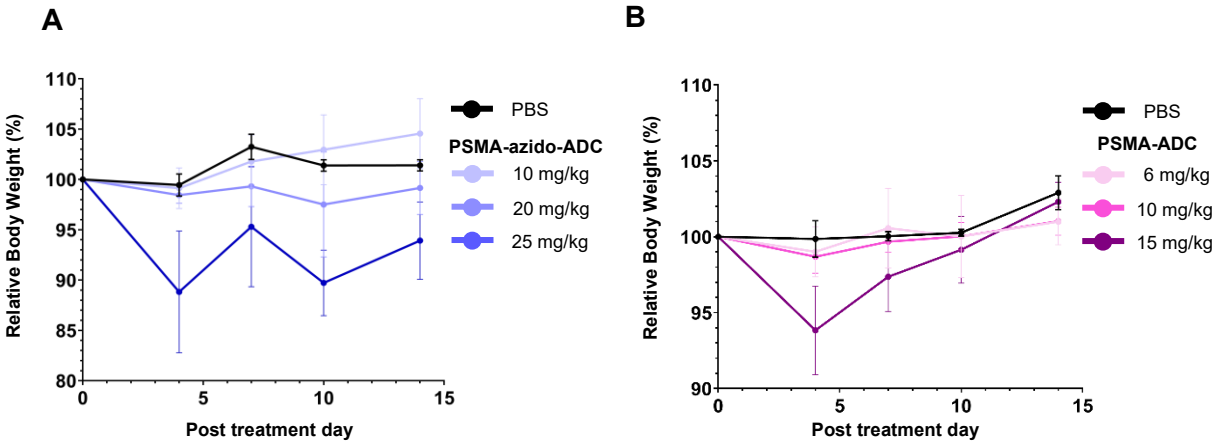

***Figure 30**: **Maximum Tolerated Dose (MTD) study of PSMA-azido-ADC and PSMA-ADC in 22RV1 CDX bearing male NMRI nude mice.** (A) Relative Body Weight upon i.v. injection of different doses of PSMA-azido-ADC. (B) Relative Body Weight upon i.v. injection of different doses of PSMA-ADC. Body weight was measured twice every week for 14 days. Each data point represents the mean ± SEM of n=3*

4.9.4 Lethal doses of PSMA-azido-ADC and additional DBCO-PEG$_4$-COOH (7) treatment in 22RV1 CDX in male NMRI nude mice

To establish an appropriate dose of PSMA-azido-ADC for the efficacy study, various lethal doses exceeding the MTD were evaluated in combination with DBCO-PEG$_4$-COOH (**7**) in 22RV1 tumor-bearing male NMRI nude mice. Compound **7** was administered at different time points after PSMA-azido-ADC application to determine the latest applicable timepoint to sustain tolerability and ensure mouse survival. Three mice per group were first treated with an intravenous single dose of PSMA-azido-ADC and at a second timepoint they

received a second intravenous single dose treatment with 45 mg/kg DBCO-PEG$_4$-COOH (**7**) as described in **Table 42**. Tumor volume and body weight were monitored twice a week for 24 days to assess efficacy and tolerability.

Table 42: Co-administration pilot study with PSMA-azido-ADC and DBCO-PEG$_4$-COOH (7) in 22RV1 CDX male NMRI nude mice.

Group	1st treatment	Timepoint of DBCO-PEG4-COOH (45 mg/kg) application after 1st treatment
1	PBS	t=10h
2	38 mg/kg (1.5 MTD) PSMA-azido-ADC	t=15h
3	50 mg/kg (2 MTD) PSMA-azido-ADC	t=10h
4	38 mg/kg (1.5 MTD) PSMA-azido-ADC	t=20h
5	42 mg/kg (1.7 MTD) PSMA-azido-ADC	t=15h

Mean tumor volume and comparison of tumor volumes at day 24 is shown in **Figure 33A**. Administration of 38 mg/kg (1.5 MTD) PSMA-azido-ADC followed by compound **7** after 15 hours (Group 2) resulted in early tumor regrowth. In contrast, when compound **7** was applied 20 hours after the 38 mg/kg PSMA-azido-ADC, the tumor volume remained stable until day 10, followed by a subsequent increase in tumor growth (Group 4). Tumor volume of mice in Group 4 at day 24 was significantly lower compared to tumor volume of animals in Group 2. Both groups showed good tolerability as all mice in both groups survived until the end of the study (**Figure 33C**).

Treatment with 50 mg/kg (2 MTD) PSMA-azido-ADC and compound **7** 10 hours later (Group 3) led to stable mean tumor volume until day 10 before regrowth started (**Figure 33A**). However, no significant enhancements in tumor response compared to the PBS group were observed, as the tumor volume at day 24 was similar. Furthermore, only one mouse survived until the end of the study. The 2 MTD dose was likely excessively high, as treatment-related toxicity typically occur within the initial 5-6 days post-treatment, and two out of three animals had to be sacrificed within this timeframe because of poor general conditions. (**Figure 33C**).

A dose of 42 mg/kg (1.7 MTD) PSMA-azido-ADC and compound **7** 15 hours later (Group 5) showed tumor regrowth only to 500 mm^3 at day 24, significantly lower than the tumor volume measured for Group 1, 2 and 3 (**Figure 33A**). However, only two out of three mice in Group 5 survived, suggesting that the dose of 42 mg/kg (1.7 MTD) PSMA-azido-ADC was still too high and not well-tolerated (**Figure 33C**). The Relative Body Weight (RBW %)

for the groups exhibited an initial decline until day 4 before all mice subsequently recovered and consistently gained weight until the end of the study (**Figure 33B**).

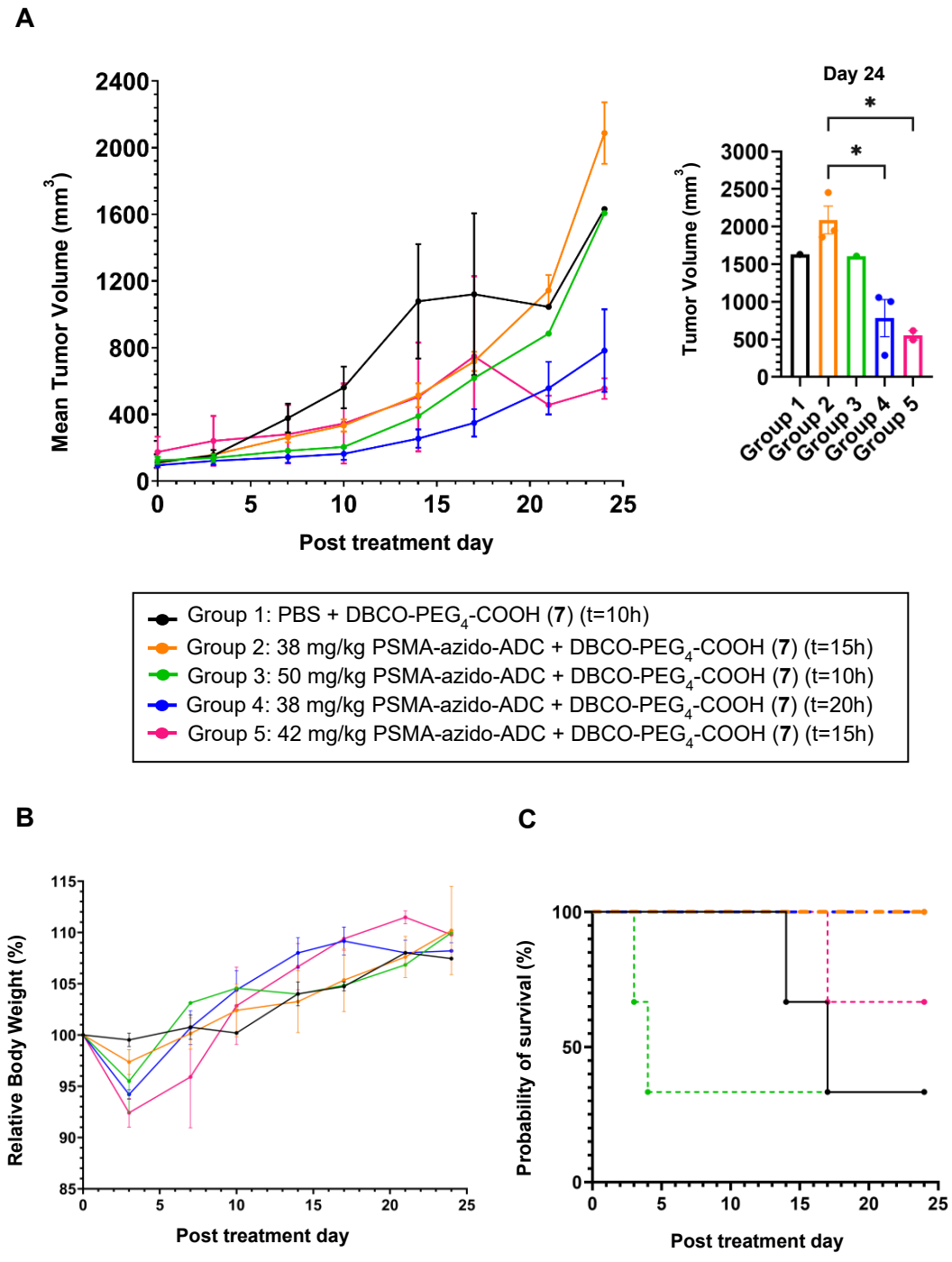

***Figure 31: Treatment with PSMA-azido-ADC and additional administration of DBCO-PEG$_4$-COOH (7) in 22RV1 CDX model**. Mice were treated i.v. with a single dose of PSMA-azido-ADC and later, DBCO-PEG4-COOH (**7**) was applied at different timepoints. (A) Mean tumor volume (mm^3) of mice (left) and tumor volume (mm^3) comparison among groups at day 24 (right). (B) Relative body weight of each group. Tumor volume and body weight were monitored twice a week for 24 days. Error bars represent SEM of n=3. (C) Probability of survival (%) of each group.*

Overall, Application of 38 mg/kg (1.5 MTD) PSMA-azido-ADC and administration of DBCO-PEG$_4$-COOH (**7**) 20 hours later, appeared to be well tolerated and led to a delay in tumor growth. Thus, this dose was selected for the efficacy study in the 22RV1 CDX model in comparison with the standard treatment with PSMA-ADC.

4.9.5 Efficacy study of PSMA-azido-ADC with additional DBCO-PEG$_4$-COOH (7) treatment in 22RV1 CDX male NMRI nude mice

After establishment of the optimal dose of PSMA-azido-ADC and the best timepoint of DBCO-PEG$_4$-COOH (**7**) application in tumor-bearing mice, the treatment regimen was tested in an efficacy study in 22RV1 CDX model. The tumor response to this co-treatment was compared with an HDP standard PSMA-ADC (**Table 43**). The dose of the standard PSMA-ADC was 7.5 mg/kg (1/2 MTD) since doses above the MTD are not employed in standard treatments for ethical reasons.

Table 43: Efficacy study with co-administration of PSMA-azido-ADC and DBCO-PEG$_4$-COOH (7) in 22RV1 CDX model.

Group	1st treatment	2nd treatment t=20h	Schedule
1	PBS	45 mg/kg DBCO-PEG$_4$-COOH (**7**)	Multiple doses (3x)
2	38 mg/kg (1.5 MTD) PSMA-azido-ADC	45 mg/kg DBCO-PEG$_4$-COOH (**7**)	Single dose
3	38 mg/kg (1.5 MTD) PSMA-azido-ADC	45 mg/kg DBCO-PEG$_4$-COOH (**7**)	Multiple doses (3x 1 week apart)
4	7.5 mg/kg (1/2 MTD) PSMA-ADC	Vehicle	Single dose
5	7.5 mg/kg (1/2 MTD) PSMA-ADC	Vehicle	Multiple doses (3x 1 week apart)

Based on the findings from **section 4.8.2**, where tumor regrowth was observed within 10 days after a single-dose treatment, two groups with multiple-dose treatment (once every week for three weeks) were included in addition to the single-dose treatment groups. Tumor volume and body weight were monitored weekly to assess efficacy and tolerability.

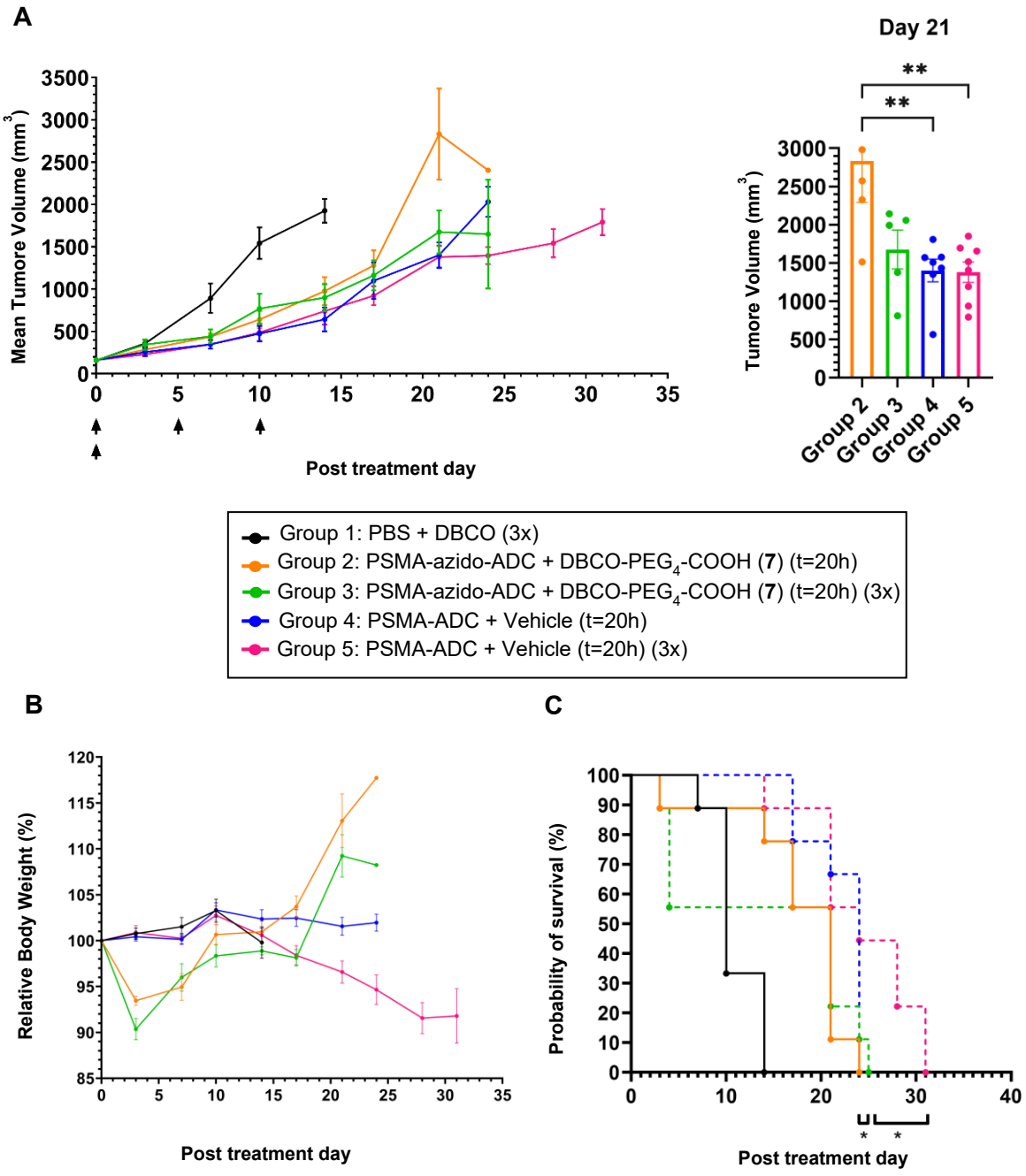

***Figure 32: Efficacy study with PSMA-azido-ADC and additional DBCO-PEG$_4$-COOH (7) treatment in JIMT-1 CDX NMRI nude mice**. (A) Mean tumor volume (mm^3) of groups described in **Table 43** (left) and tumor volume (mm^3) comparison among groups at day 21 (right). Error bars represent SEM of n=9. (B) Relative body weight % of each group. Tumor volume and body weight were monitored twice a week for 31 days. Error bars represent SEM of n=9. (D) Kaplan-Meier survival plots of each group. Group 3 vs. Group 5 (*p<0.05), Group 2 vs. Group 4 (*p<0.05).*

In general, none of the treated groups demonstrated tumor growth inhibition; instead, the tumors remained stable for the initial week before gradually regrowing. Single-dose treatment with PSMA-azido-ADC and compound **7**, group 2, resulted in faster tumor regrowth compared to the multiple-dose treatment with PSMA-azido-ADC, group 3. This

was evident on day 21, where the average tumor volume of group 2 was approximately double that of group 3 (**Figure 34A**). The administration of PSMA-azido-ADC at a dosage of 38 mg/kg appeared to be toxic, even when administered alongside compound **7**. This toxicity manifested in a significant decrease in Relative Body Weight (RBW) observed in groups 2 and 3 within 5 days post-treatment. Interestingly, group 2 showed increased RBW after 20 days, this is probably due to an increase in tumor volume (**Figure 34B**). No significant differences were seen in the probability of survival of the two groups 2 and 3, although both outperformed the PBS control group (**Figure 34C**).

A notable variation in the average tumor volume was evident between the single-dose group 2 (single-dose PSMA-azido-ADC) and both the standard treatment groups 4 (single-dose PSMA-ADC) and 5 (multiple-dose PSMA-ADC) by day 21. No differences in tumor volume were seen between groups 4 and 5 (**Figure 34A**). The PSMA-ADC treatment did not show treatment-related toxicity in both groups 4 and 5 as well, as no decrease in RBW was detected in the first 5 days post-treatment. However, group 5 showed a decline in RBW after 15 days, probably due to tumor progression and poor general conditions of the animals (**Figure 34B**). Significant differences were seen in the probability of survival between the single-dose group 2 and 4 and the multiple-dose treatment groups 3 and 5 (**Figure 34C**).

Taken together, these findings indicated that combining a high dose of 38 mg/kg of PSMA-azido-ADC with DBCO-PEG_4-COOH (**7**) did not enhance tumor efficacy compared to the standard treatment of 7.5 mg/kg of PSMA-ADC. Additionally, the multiple-dose regimen involving PSMA-azido-ADC and compound **7** exhibited comparable tumor efficacy to both single-dose and multiple-dose treatments with PSMA-ADC. However, it is noteworthy that the PSMA-ADC treatment groups 4 and 5 outperformed the PSMA-azido-ADC single-dose and multiple-dose in terms of tumor efficacy. As it has been shown in the efficacy study on JIMT-1 CDX mice and the biodistribution study (**section 4.8.2 and 4.8.3**), it is likely that the administration of compound **7** caused an increase of neutralized nonactive ADC in circulation resulting in decreased activity against tumor cells.

5 Discussion

To date, 15 antibody-drug conjugate (ADC) therapies against different types of cancers have been approved (Maecker et al. 2023). Gemtuzumab ozogamicin (Mylotarg©) paved the way as the first approved ADC on the market in 2000 against acute myeloid leukemia (AML), setting a precedent for the development of subsequent ADC therapies. This therapy with Trastuzumab Deruxtecan (Enhertu®) as a pioneering example of successful ADC therapy. Trastuzumab Deruxtecan has revolutionized the treatment landscape for HER2-positive breast and gastric tumors, offering enhanced tumor efficacy and improved patient survival compared to conventional treatment options. However, despite its remarkable success, more than 50% of patients experienced grade 3 or higher adverse events associated with the treatment during clinical trials (André et al. 2023). These adverse events are caused by intrinsic payload toxicity through off-site uptake into healthy tissues. (Johns and Campbell 2022). Over the years, meticulous optimization of the components of an ADC, including the antibody, linker, and payload, has been conducted to develop ADC therapies with reduced side effects. Despite these efforts, off-target uptake remains a significant issue and further optimizations are necessary to ensure treatments that are free of any potential side effects (Nguyen 2023).

One notable toxic payload is Amanitin, an octapeptide amatoxin derived from the mushroom *Amanita phalloides*, also referred as the “Death Cap” mushroom, responsible for the majority of deaths from mushroom poisoning worldwide (Pahl et al. 2019). The unique mode of action of amanitin is the inhibition of RNA polymerase II. Through non-covalent binding, amanitin disrupts the activity of RNA polymerase II during the mRNA elongation phase (Liu et al. 2018). This interaction immobilizes the trigger loop, which is a vital structural element responsible for folding the active site of the enzyme during RNA chain elongation catalysis and subsequent translocation to the next DNA template position (Brueckner and Cramer 2008; Liu et al. 2018; Pahl et al. 2019). Amanitin's distinct mechanism of action as an RNA polymerase II inhibitor, coupled with its favorable chemical properties as highly hydrophilic molecule, positions this mushroom toxin as a promising payload candidate capable of overcoming the limitations of microtubule inhibitors and DNA-damaging payloads, which mainly rely on active cell division for their effectiveness.

However, amanitin is also a specific substrate of OATP1B3, an organic anion transporter polypeptide found in the liver, responsible for the metabolism of various drugs and xenobiotics (Letschert et al. 2006). OATP1B3 is expressed in human hepatocytes and transports the free toxin upon ingestion of the mushroom, causing the inhibition of mRNA

transcription in hepatocytes and cell death (Garcia et al. 2015). Histopathological findings in liver biopsy of patients who suffered amatoxin intoxication revealed the presence of massive centrilobular hepatic necrosis, vacuolar degeneration of hepatocytes and infiltration of immune inflammatory cells. If left untreated, these pathological symptoms typically progress to liver failure. Nephrotoxicity also commonly occurs in cases of amatoxin poisoning, manifesting as acute tubular necrosis that can progress to renal failure (Pond et al. 1986; Fineschi et al. 1996).

To harness the unique mechanism of action of amanitin while minimizing its toxic side effects on the liver and kidneys, Heidelberg Pharma has developed Amanitin-based Antibody-Drug Conjugates (ATAC®s). ATAC®s have shown promising results in both *in vitro* and *in vivo* studies. Their high potency allows lower doses to be administered, mitigating systemic toxicity, and improving tolerability. Additionally, the linker technology ensures the controlled release of amanitin in tumor cells only, maximizing its therapeutic effect while minimizing adverse consequences on healthy tissues (Pahl et al. 2019). Moreover, it has been shown that the mutation of two leucin amino acids to alanine (LALA) mutation of the Fc domain of ATAC®s prevents unspecific uptake in the liver by the Fcγ receptors (FcγR), improving tolerability in mice (Orlik et al. 2024). However, ADCs can be non-specifically taken up not only by FcγR but also by C-type lectin receptors (CLRs) causing off-target toxicity in healthy tissues (Nguyen 2023). Since the liver is one of the main organs involved in the metabolism of ADCs and the first to be exposed to treatment administration, it is vital to protect it from possible treatment-related toxicity (Boone et al. 2023). While no premature cleavage of the free amanitin toxin has been detected *in vivo*, escalating doses of an anti-CD37 ATAC® in monkeys have shown a transient, mild increase in biochemical liver-damage parameters such as lactate dehydrogenase and aspartate transaminase (Voss et al. 2021). Although the liver damage was transient, a strategy to completely avoid liver toxicity could further enhance the tolerability of ATAC®s and significantly increase their therapeutic index.

One approach to reducing the side effects of a treatment, employed by Ursuegui et al., is the “neutralization strategy”. This strategy was used to down-regulate the post-treatment activity of the anticoagulant drug warfarin in mice. The neutralization strategy is based on a bioorthogonal reaction, the Strained-Promoted Azido-Alkyne Cycloaddition (SPAAC) (Ursuegui et al. 2017). The SPAAC reaction employs strained alkyne compounds as neutralizing agents, which interact with an azide group incorporated into the drug molecule, to form a biological inactive 1,2,3-triazole (Mbua et al. 2011). The reaction between an azide moiety and a strained alkyne is specific, fast, stable and compatible with living organisms and has been tested in different animal models, e.g. mouse or zebrafish for imaging purposes (Mitry et al. 2023).

This study aimed to develop a neutralization strategy, building on the work of Ursuegui et al., to improve the tolerability and increase the therapeutic index of ATAC® treatment. The primary goal was to identify a switch-off mechanism to detoxify the ADC *in vivo* while preserving its efficacy against tumor cells. To achieve this, a stepwise approach was implemented, including the following milestones:

1. Amanitin was functionalized with an azide moiety, resulting in the generation of the azido-amanitin compounds Ama-N-azido (**2**) and Ama-W-azido (**3**). To examine the efficacy of the neutralization strategy *in vitro*, both compounds, were reacted with different neutralizing agents (**4-7**) and the activity of the neutralized compounds was assessed.
2. The new azido-amanitin compounds were conjugated via THIOMAB™ bromoacetamide conjugation to generate azido-amanitin ADCs (Junutula et al. 2008b; Hermanson 2013b) and the effect of the neutralization strategy on the azido-amanitin ADC treatment was tested in cells.
3. The ability of the neutralizing agents in improving azido-amanitin ADC tolerability was evaluated *in vivo*.
4. To demonstrate that the SPAAC reaction could serve as a detoxification method without compromising tumor efficacy, the impact of the administration of the neutralizing agents on tumor response towards ATAC® treatment was examined.

5.1 *In vitro* activity of the azido-amanitin compounds after SPAAC reaction with the neutralizing agents

The SPAAC reaction requires an azide and a strained alkyne to generate a 1,2,3-triazole via 1,3-dipolar cycloaddition (Mbua et al. 2011). Ursuegui et al. introduced the azide moiety on the phenyl moiety of warfarin retaining its anticoagulant activity. The activity of this new azidowarfarin (WN_3) could then be reduced via SPAAC reaction with BCN-PEG_6-OH (Ursuegui et al. 2017). To achieve a similar modification with α-amanitin, the hydroxyl group of the 6-hydroxytryptophan residue and the amide group of the asparagine (Asn) residue were identified as promising sites for introducing an azide moiety. Modifications on these side chains have been demonstrated to preserve the activity of α-amanitin (Pahl et al. 2019). This led to the generation of the azido-amanitin compounds Ama-N-azido (**2**), with the azide moiety on the amide group of asparagine (Asn) and Ama-W-azido (**3**), with the azide moiety on the hydroxyl group of 6-hydroxy-tryptophan. These two compounds were reacted with different neutralizing agents **4-7** resulting in the neutralized compounds **8-15**.

The impact of amanitin derivatives on RNA polymerase II activity was detected in an RNA polymerase II assay, where compounds were incubated in a Hela nuclear extract containing RNA polymerase II. The percentage of RNA polymerase II activity was determined by comparing the quantified transcribed RNA in the treated group to that in the untreated group, which represents 100% RNA polymerase activity (**Figure 12**). The bioactivity of the amanitin derivatives was also analyzed using a cytotoxicity assay in HEK293-OATP1B3 cells, a cell line overexpressing the OATP1B3 transporter (**Figure 9**). This assay enabled the determination of the uptake of the amanitin derivatives through OATP1B3 and their consequent cytotoxic activity in the HE293-OATP1B3 cell line.

The level of RNA polymerase inhibition by compound **2** was comparable to that of α-amanitin. Additionally, compound **2** exhibited a similar cytotoxicity profile in HEK293-OATP1B3 cells, indicating that the introduction of the azide moiety on the carboxamide side chain of an Asn residue did not interfere with its binding to RNA polymerase II or the OATP1B3 transporter. Compound **3** demonstrated full cytotoxicity in the HEK293-OATP1B3 cell line with an EC_{50} value 200-fold lower than that of α-amanitin, but a similar RNA polymerase II activity as α-amanitin. This suggested that the introduction of the azide moiety on the hydroxyl group of 6-hydroxy-tryptophan may enhance the uptake via the OATP1B3 transporter. Indeed, when compound **3** was reacted with one of the neutralizing agents **4**-**7**, a notable decrease in cytotoxicity was observed in the HEK293-OATP1B3 cell line. Thus, the formation of the 1,2,3-triazole via reaction with the neutralizing agents likely reduced the uptake via the transporter.

The SPAAC reaction between compound **3** and the neutralizing agents BCN-PEG_6-OH (**6**) and DBCO-PEG_4-COOH (**7**) resulted in a 30-40% increase in RNA polymerase II activity, indicating less potent inhibition, compared to treatment with compound **3** alone. Additionally, this reaction led to reduced cytotoxicity in the HEK293-OATP1B3 cell line. Conversely, the SPAAC reaction involving either BCN-OH (**4**) and DBCO-COOH (**5**) with compound **3**, which produced compounds **12** and **13** respectively, did not result in an increase in RNA polymerase II activity. However, the cytotoxicity observed in HEK293-OATP1B3 cells was significantly reduced when treated with either of the two neutralized compounds compared to the treatment with compound **3** alone, suggesting inhibited uptake through the OATP1B3 transporter but retained inhibition of RNA polymerase II. The reaction between compound **2** and the neutralizing agents BCN-OH (**4**), DBCO-COOH (**5**), BCN-PEG_6-OH (**6**) and DBCO-PEG_4-COOH (**7**), generated neutralized compounds that showed increased RNA polymerase II activity and decreased cytotoxicity in HEK293-OATP1B3 cells, confirming promising neutralizing activity. In particular, the reaction with neutralizing agents **6** and **7**, which generated compounds **10**, **11a**, and **11b**, showed the best results in maintaining RNA polymerase II activity compared to compound **2**.

Interestingly, the reaction between compound **2** and compound **5** or compound **7** resulted in the formation of two pairs of isomers: **9a** and **9b**, and **11a** and **11b**, each exhibiting distinct *in vitro* activity. BCN and dibenzocyclooctyne (DBCO) derived agents are prone to generate isomers upon reaction with chiral azides (Gröst and Berg 2015; Dommerholt et al. 2016). Stereoisomers often exhibit distinct activities in both *in vitro* and in *vivo*, as demonstrated by the infamous Thalidomide (Contergan®). Thalidomide comprises a racemic mixture of two enantiomers, with one enantiomer demonstrating the desired sedative effects while the other an unwanted teratogenic effect (Kesserwani 2021). Not only stereoisomers, but also constitutional isomers, as generated by the SPAAC reaction in this study, can show differences in biological activity (Bajaj et al. 2023). In particular, the isomer **9b** did not show a significant improvement in RNA polymerase II activity and cytotoxicity in HEK293-OATP1B3 was only slightly increased compared to compound **2**. While the isomer **9a** demonstrated a significant increase in RNA polymerase activity compared to compound **2**. While the isomers **11a** and **11b** exhibited no differences in cytotoxicity towards HEK293-OATP1B3 cells, **11b** demonstrated a significantly higher increase in RNA polymerase II activity compared to **11a**. Further studies are necessary to predict the formation of these different isomers *in vivo*.

The reaction of the azido-amanitin compounds **2** and **3** with the neutralizing agents seems to induce structural modifications and/or a steric hindrance to disrupt the binding of Amanitin to RNA polymerase II and to reduce the uptake via OATP1B3 (Trehan et al. 2002). A definitive conclusion regarding the reason for the reduced uptake via OATP1B3 transporter is challenging since the specific amanitin residues interacting with the transporter remain unknown. Nevertheless, the decreased cytotoxicity of the neutralized compounds on the HEK293-OATP1B3 cell line seems to be primarily attributed to the reduced inhibition of RNA polymerase II, although inhibition of OATP1B3 transport cannot be excluded, as shown for compound **3**.

The binding to RNA polymerase II and the transport via OATP1B3 may be influenced by several factors, including the position of the azide, the neutralizing agent, and the spatial conformation adopted by the compound. Since no premature release of the free amanitin payload was observed with ATAC®s treatment, measuring RNA polymerase activity is crucial for selecting the appropriate neutralizing agents for the neutralization strategy. So far, BCN-PEG_6-OH (**6**) and DBCO-PEG_4-COOH (**7**) have shown a greater improvement in RNA polymerase II activity compared to both azido-Amanitin derivatives **2** and **3**. Therefore, these agents were selected among other neutralizing agents for further experiments.

5.2 *In vitro* characterization of Azido-amanitin ADCs on target-positive cell lines

One of the commonly employed techniques for conjugating drugs with monoclonal antibodies (mAbs) exploits chemical reactions with cysteine residues. Not only the native cysteines in the amino acid sequence of the antibody can be used, but new cysteine residues can be substituted to specific residues through site-directed mutagenesis. This technology, named THIOMAB™, has led to the generation of ADCs with a more homogeneous Drug-to-antibody-ratio (DAR), with improved tolerability and increased therapeutic index, as seen in the Phase I clinical trial of an anti-MUC16 ADC (Junutula, *et al.*, 2008; Liu *et al.*, 2016).To enable the payload to bind to the thiol groups of cysteines, it can be functionalized with maleimide, which reacts with the thiol group generating a thiosuccinimide bond via Michael addition (Yao et al. 2016). ATAC®s employ a THIOMAB™ thiol-maleimide conjugation to conjugate the amanitin payload via cleavable or non-cleavable linker to an antibody with two engineered cysteines on the Aspartate (Asp) 265 residues (EU numbering) (Edelman et al. 1969) of the crystallizable fragment (Fc). This ensures the generation of ADCs with homogenous DAR and excellent plasma stability (Pahl et al. 2019). However, making the thiol-maleimide conjugation was unsuitable for the azido-amanitin compounds since the maleimide moiety in the linker reacted in a 1,3-dipolar cycloaddition with the azide on the amanitin in solution, resulting in the formation of payload-linker polymers. (Dommerholt et al. 2016; Zhu et al. 2016a).

Bromoacetyl conjugation is another type of conjugation which employs a bromoacetyl moiety on the linker and the thiol group of a cysteine. The reaction is conducted at alkaline pH of ~8.2, to allow the thiolate anion to react with the bromoacetyl moiety. Performing the conjugation at a slightly alkaline pH ensures chemo-selectivity for the sulfhydryl groups of cysteines on the antibody and avoids side reactions with the imidazolyl side chain nitrogen of histidines, the primary ε-amine group of lysines and the N-terminal α-amines (Schelté et al. 2000; Hermanson 2013b). The advantage of this conjugation is high plasma stability, due to the formation of a thioether bond between the thiol and the linker (Alley et al. 2008). To perform the bromoacetyl conjugation in this study, a cleavable linker with a bromoacetyl moiety was introduced in the azido-amanitin compounds **2** and **3**, generating the compounds Ama-N-azido-Bromoacetamide (**16**) and Ama-N-azido-Bromoacetamide (**17**), respectively.

In this study, the neutralization strategy was evaluated with Trastuzumab as model antibody due to its extensive characterization in both *in vitro* and *in vivo* settings. Additionally, Trastuzumab is used in HER2-positive tumor therapy as a monoclonal

antibody (mAb) and in the ADC form as Trastuzumab emtansine and Trastuzumab deruxtecan (McKeage and Perry 2002; Chen et al. 2016; Hurvitz et al. 2023).

The careful selection of the appropriate residue for substitution with a cysteine to facilitate the THIOMAB™ conjugation also plays a crucial role for thiol reactivity, ensuring generation of ADCs with a homogeneous DAR (Junutula et al. 2008a). The substitution of serine 399 (Edelman et al. 1969) in the heavy chain of Trastuzumab with a cysteine residue (T-S399C) improved the conjugation outcome compared to the D265C substitution (standard ATAC® position). Additionally, adjustment of the buffer to pH 8 and optimization of the payload equivalents facilitated the generation of two azido-amanitin ADCs, N-azido-ADC (with compound **16**) and W-azido-ADC (with compound **17**), each with an average DAR of 2. Applying the same protocol to the conjugation of compound **16** to an anti-PSMA antibody with S399C substitution on the heavy chain of the antibody led to the generation of the N-azido-PSMA ADC with an average DAR of 1.84.

The Trastuzumab azido-ADCs N-azido-ADC and W-azido-ADC showed high cytotoxicity in the HER2-positive cell line SKBR-3, with EC_{50} values in the picomolar range, similar to the non-azido control ADCs. However, W-azido-ADC did not show cytotoxicity in HER2-positive JIMT-1 cell line in contrast to N-azido-ADC. Recent studies with Trastuzumab emtansine have revealed a correlation between increased expression of the multidrug-resistant protein (MDR) MRP1 in the JIMT-1 cell line and enhanced resistance to the payload (Endo et al. 2018, 2019). MRP1 belongs to the ATP-binding binding cassette subfamily C (ABCC) and is an efflux transporter expressed in the organs involved in drug metabolism such as liver and kidney. It has been shown that OATP transporters and MRPs share common drug substrates (Nigam and Granados 2023). Considering that W-azido-ADC employs compound **3** as payload and given that compound **3** exhibited considerable increased cytotoxicity in the HEK293-OATP1B3 cell line due to an increased uptake via the transporter, it could be that MRPs could also transport compound **3** or its metabolite out of the cells, leading to the reduced cytotoxicity.

Enhanced cytotoxicity of the anti-PSMA PSMA-azido-ADC was observed in PSMA-positive cells, LNCap and 22RV1 cells, compared to the control PSMA-ADC. This improvement is likely due to the hydrophobic polyethylene chain linking the azide moiety to the amanitin payload, which increases the overall hydrophobicity and enhances its ability to permeate the lysosomal lipid bilayer (Lloyd 2000).

SPAAC reaction in cells has been mainly utilized for cell surface modification, typically involving an initial step enabling the attachment of bio-orthogonal reactive moieties to the cell surface, followed by a subsequent reaction with complementary modified biomolecules (Wang and Hu 2023). In this study, the SPAAC reaction was used as a tool to reduce the

treatment activity of the azido-ADC in target-positive cells upon reaction with one of the two neutralizing agents BCN-PEG_6-OH (**6**) and DBCO-PEG_4-COOH (**7**).

First, the SPAAC reaction was applied *in vitro* in the HER2-positive cell line JIMT-1 to test as a proof-of-concept if the neutralization strategy could be applied with N-azido-ADC. The treatment with increasing concentrations (from 10^{-10} M to 10^{-5} M) of BCN-PEG_6-OH (**6**) and DBCO-PEG_4-COOH (**7**) after a cytotoxic concentration (1nM) of N-Azido ADC showed indeed a reduced cytotoxicity of N-azido-ADC. The residual cell viability remained 100% when a high concentration (2 µM) of the neutralizing agents **6** and **7** was applied within 12 hours after the treatment with N-azido-ADC (**Figure 18A-B**). However, treatment with an excess of neutralizing agents at later timepoints (24 and 48 hours) could not completely neutralize N-azido-ADC treatment as 100% cell viability was not retained. These findings suggest that, the neutralizing agents are not able to completely neutralize the ADC treatment when applied after 12 hours, since portion of the ADC has already been internalized and metabolized (Fu et al. 2022). Nevertheless, administering the neutralizing agents 12 hours after the N-azido-ADC treatment can still mitigate cytotoxicity compared to the effects observed with the N-azido-ADC alone.

The ability of the neutralizing agents to reduce N-azido-ADC activity, was also confirmed by treatment with an excess of BCN-PEG_6-OH (**6**) and DBCO-PEG_4-COOH (**7**) (2µM) one hour after treatment with increasing concentrations of N-azido-ADC. In particular, the treatment with compound **7** completely abolished the cytotoxicity of N-azido-ADC, demonstrating a promising use of the neutralization strategy with this neutralizing agent *in vivo* (**Figure 18C-D**).

5.3 Impact of the neutralization on ADC tolerability

Off-target toxicity represents a notable challenge in the development of Antibody-Drug Conjugates (ADCs), impacting their overall tolerability and safety profile. Despite the targeted nature of ADCs, unintended interactions with healthy tissues can lead to adverse effects. Balancing efficacy with tolerability is essential to ensure the clinical success of ADCs, emphasizing the importance of constant optimization (Nguyen 2023). Various strategies have been developed over the years to enhance the tolerability of ADC treatments. Among these, the precise selection of specific antigens that are (over)expressed exclusively in tumor cells, with minimal expression in healthy tissues, plays a crucial role in mitigating off-tumor uptake of the ADC in healthy tissues (Esapa et al. 2023).

In general, all components of an ADC need careful consideration to achieve an ADC with a broad therapeutic index. Besides the binding properties to its target, the structure of the antibody plays a crucial role in influencing the tolerability of an ADC therapy. For instance, Fc silencing, achieved through the substitution of specific residues on the Fc domain of the antibody to inhibit binding to FcγR, can abolish the effector function of the antibody (McDonagh et al. 2008; Zhu et al. 2016b). The linker is also important to avoid premature release of the payload (Alley et al. 2008). Site-specific conjugation, using engineered cysteines (THIOMAB^{TM}) has also helped to achieve homogeneous ADCs to increase the therapeutic index, to reduce aggregation and to avoid a fast clearance from circulation (Junutula et al. 2008b; Mckertish and Kayser 2021; Anami et al. 2022). Nevertheless, off-target toxicity is mostly driven by the intrinsic toxicity of the payload, leading to dose-limiting toxicities (Johns and Campbell 2022; Nguyen 2023).

To date, several therapies have received FDA approval to mitigate side effects associated with ADC payloads. For instance, granulocyte colony-stimulating factors (e.g., Neupogen, Neulasta, Lonquex) and granulocyte-macrophage colony-stimulating factors (e.g., Leukine) are used to combat neutropenia, while erythropoietin (e.g., Epogen) is employed to address anemia (Kolesar 2002; Shi et al. 2006). These treatments exemplify supportive care measures developed to manage the hematological toxicities often observed with ADC therapies. However, they only address the side effects post-treatment, rather than preventing these adverse reactions from occurring in the first place. To date, not many drug-antidote strategies have been developed to address drug safety issues during treatment. One example of drug-antidote currently used in the clinical practice involves administering modified γ-cyclodextrin (Sugammadex) to capture the muscle relaxants rocuronium during general anesthesia (Kovac 2009).

In this study, the neutralization of the payload directly *in vivo* by neutralizing agents using the SPAAC reaction, improved the tolerability of N-azido-ADC treatment and reduced treatment-related toxicities in liver and kidneys. Mice treated with a lethal dose (1.2 times MTD) of N-azido-ADC who 1 hour after received an excess of the neutralizing agents DBCO-PEG$_4$-COOH (**7**) or BCN-PEG$_6$-OH (**6**) survived for 15 days without toxic side effects. This suggests that the SPAAC reaction between the neutralizing agents and the N-azido-ADC can occur not only *in vitro*, but also *in vivo*, generating a neutralized N-azido-ADC with lower toxicity. Thus, the neutralization strategy enables the administration of higher doses of ADC. In fact, the neutralizing agent DBCO-PEG$_4$-COOH (**7**) showed the highest reaction efficiency with N-azido-ADC (**Figure 23**) since within 15 minutes after administration of a 400-fold excess of DBCO-PEG4-COOH (**7**) 90% of N-Azido-ADC were reacted. On the contrary, administration of approximately a 500-fold excess of BCN-PEG$_6$-OH (**6**) led to the conversion of only 48% of N-azido-ADC to neutralized N-azido-ADC after

15 minutes, most likely due to the fast kidney clearance of this compound (Gerber et al. 2023).

In fact, Ursuegui et al. showed that ~ 90% of compound **6,** was found in urine of mice within 1 hour after application (Ursuegui et al. 2017). Compound **6** is equipped with a short neutral oligoethyleneglycol (OEG) chain which makes the small molecule hydrophilic (Warther et al. 2021). Compound **7** is also hydrophilic due to its polar acidic moiety, which carries a permanent charge at neutral pH and should though undergo renal clearance, similar to compound **6**. However, the renal clearance of compound **7** might be delayed due to a potential interaction between strained alkynes and plasma proteins. Warther et al. demonstrated that plasma proteins, such as albumin, can influence the kinetics of the SPAAC reaction. Specifically, they found that the SPAAC reaction between an azide and a strained alkyne, which typically exhibits low second-order rate kinetics in methanol and aqueous buffer, displayed up to 40-fold faster kinetics in plasma. Additionally, they investigated the binding of BCN derivatives to plasma proteins, revealing that only 26% of BCN-PEG_6-OH binds to albumin (Warther et al. 2021). With regards to DBCO, van den Bosch et al. hypothesized that the binding of serum proteins to a DBCO-Lu177 labeled probe could enhance its blood retention, thus extending the timeframe for the SPAAC reaction (van den Bosch et al. 2013). The addition of two phenyl rings in DBCO-PEG_4-COOH (**7**) compared to BCN probably enhances its binding to albumin, thereby delaying renal clearance and increasing its availability for the SPAAC reaction with the N-azido-ADC (Zhang et al. 2018; López-Yerena et al. 2020). A more comprehensive analysis of the pharmacokinetics of strained alkyne compounds could offer valuable insights into the *in vivo* kinetics of the SPAAC reaction and biodistribution across various tissues.

Ursuegui et al. also investigated the effectiveness of delayed application of BCN-PEG_6-OH in neutralizing the activity of azido-warfarin. They demonstrated that an application of BCN-PEG_6-OH 10 or 30 minutes after the administration of azido-warfarin effectively deactivated its anticoagulant activity to the same extent as when administered after 5 minutes (Ursuegui et al. 2017). Indeed, an administration of compound **7** within 12 hours after the administration of a lethal dose of N-azido-ADC led to the survival of all animals and effectively increased tolerability of the ADC treatment (**Figure 24**). This result demonstrated that the toxic effects of the ADC treatment could be neutralized at later time points, thereby preventing the onset of treatment-related toxicities.

The histopathological evaluation of liver and kidneys of mice treated with a lethal dose of N-azido-ADC resembled the amanitin toxicity lesions reported in the literature. In fact, mice sacrificed at day two and at day five post N-azido-ADC administration showed signs of severe midzonal to diffuse necrosis, indicating that the liver was the main organ of treatment-related toxicity in the first days of exposure to the treatment. No signs of kidney

toxicity were seen in these animals. In contrast, mice sacrificed approximately six days or more after N-azido-ADC treatment alone showed liver toxicity and additional signs of nephrotoxicity, such as moderate tubule necrosis and tubule vacuolation, indicating that the kidneys suffer in a later stage of exposure. Interestingly, the application of 45 mg/kg of compound **7** 6 hours after the N-azido-ADC treatment resulted in no significant histopathological lesions in both liver and kidney. In case of the administration of compound **7** 20 hours post-N-azido-ADC treatment on the other hand, 2 out of 6 mice showed poor general conditions and needed to be prematurely sacrificed at day two. The liver of these two mice showed severe midzonal to diffuse liver necrosis, indicating treatment-related liver damage. The residual mice of the same treatment group sacrificed at day six post-treatment showed multifocal cell necrosis, indicating a possible onset of liver damage. No histopathological lesions were observed in the kidneys of both groups treated with compound **7**, indicating that the reaction with the neutralizing agent was neutralizing the payload before it could cause damage in the kidneys.

High-perfused organs with leaky vasculatures, such as the liver, are more exposed to IgG and ADC than other tissues. Moreover, the presence of the Kupffer cells and the expression of C-type lectin receptors on the hepatocytes facilitates ADC uptake and degradation in these liver cells, eventually leading to liver damage (Eipel et al. 2010; Mahalingaiah et al. 2019).

These findings suggest that administering compound **7** 20 hours after a toxic dose of N-azido-ADC treatment may be too late to mitigate ADC-driven toxicity, since this delay seems to result in an increased uptake of N-azido-ADC in the liver before the application of the neutralizing agent. However, administering compound **7** 6 hours after N-azido-ADC treatment can effectively abolish treatment-related toxic lesions, indicating that the liver's exposure to the ADC is still low enough to prevent severe damage caused by the release of the payload in hepatocytes. These results align with previous findings, demonstrating that administering compound **7** within 6 hours and 12 hours of a lethal dose of N-azido-ADC significantly enhances tolerability. However, administration 15 hours post-dose proved insufficient to improve tolerability.

In summary, these findings emphasize the critical role of timing the administration of the neutralizing agent to enhance tolerability and mitigate toxicity.

5.4 Preserving tumor efficacy while enhancing tolerability through the neutralization strategy

Tumor efficacy, as well as tolerability of an ADC therapy, is highly influenced by the pharmacokinetic (PK) and pharmacodynamic (PD) profile of the ADC itself (Hedrich et al. 2018). The PK includes the absorption, distribution, metabolism, and elimination (ADME) of an ADC and retains several aspects of the unconjugated antibody: slow clearance, long half-life, low volume of distribution and proteolysis-mediated catabolism in liver, kidneys, skin and muscles (Lin et al. 2013). The PD refers to the biological effects resulting from the interaction between drugs and biological systems. In the context of ADCs, PD is influenced by the interaction between the target antigen and the antibody, as well as by the mode of action of the payload, and is interconnected with the PK (Yeung et al. 2024). The most commonly reported parameters in ADC PK/PD studies include the area under the plasma drug concentration-time curve (AUC), which measures drug exposure in circulation, and the peak concentration in plasma (C_{max}) (Deslandes 2014). These two parameters can influence the therapeutic window of an ADC therapy. The therapeutic window, delineates the range of drug exposures that elicit a therapeutic response without inducing significant toxic effects (Yeung et al. 2024). It appears that the AUC of an ADC therapy plays an important role in maintaining the tumor response, while the C_{max} may correlate with the toxic effects and tolerability of the therapy. Although this correlation has not been completely proven for all ADCs and both, C_{max} and AUC can play a role in treatment-related toxicity.

In past clinical trials, some strategies have been used to retain tumor efficacy while increasing tolerability of the ADC treatment. One example was the fractionated dosing with Gemtuzumab Ozogamicin. Fractionated dosing can widen the therapeutic window by increasing tolerability and retaining tumor efficacy. Administering an intravenous dose of 3 mg/m^2 of Gemtuzumab Ozogamicin on day 1, 4, and 7, as opposed to a biweekly intravenous dose of 9 mg/m^2, may mitigate hepatic adverse events and early mortality, while maintaining comparable ADC exposure (AUC), and efficacy. From exposure-response analysis, it appeared that hepatic toxicities seen with Gemtuzumab Ozogamicin were caused by the high C_{max} at the 9 mg/m^2 dosage, which was lowered with the fractioned 3 mg/m^2 administration, while maintaining a similar AUC (Liao et al. 2021).

In this study, a neutralization strategy was evaluated to assess its effectiveness in neutralizing amanitin-based ADC activity *in vivo*. The goal was to enhance tolerability while maintaining tumor exposure to ensure the efficacy of the treatment. The administration of 45 mg/kg DBCO-PEG$_4$-COOH (**7**) after intravenous application of 10 mg/kg (2/5 MTD) N-

azido-ADC in JIMT-1 cell-derived xenograft (CDX) NMRI nude mice negatively affected tumor efficacy of the ADC, causing tumor regrowth in some animals (**Figure 26**). The impact of the neutralization on tumor response was examined at two different application timepoints. When given 6 hours after N-azido-ADC treatment, compound **7** reduced the tumor growth inhibition (TGI) from 98% to 72%, whereas the administration 20 hours post-N-azido-ADC treatment maintained a TGI of 92%. Nonetheless, even in the latter case, tumor regrowth occurred in four out of ten mice, indicating variable effects on tumor response among the animals. This variability may stem from differences in tumor uptake and pharmacokinetics, as well as from other variations, e.g., tumor growth rate or antigen expression (Daublain et al. 2017). These findings provide initial insights into how neutralization of the amanitin payload by reaction with compound **7** could affect the PK/PD profile of the N-azido ADC treatment and, consequently, tumor efficacy.

A biodistribution analysis of tissues collected 24 hours and 7 days after the neutralization at 6 hours or 20 hours post-ADC administration indeed showed that the neutralization strategy reduced the bioavailability of the active N-azido-ADC in favor of the inactive N-azido-ADC-neutralized (**Figure 28** and **Table 40**). The ratio of N-azido-ADC concentration to Total ADC in tumor and plasma was significantly reduced already 24 hours after administration of compound **7** at both timepoints. After 7 days, a halving of tumor and plasma concentrations of Total ADC was observed. However, the concentration of N-azido-ADC remained lower compared to Total ADC. Within 24 hours over 90% of the ADC in circulation is inactivated to N-azido-ADC-neutralized. Since the neutralized payload is almost inactive and has reduced activity, it fails to exert its killing function upon reaching the tumor, thereby enabling tumor regrowth. These results highlight the significance of ADC exposure and the PD of N-azido-ADC, in tumor efficacy. In fact, administration of compound **7** at 20 hours after N-azido-ADC treatment allowed longer exposure of the N-azido-ADC to the tumor, partially retaining tumor efficacy.

These findings indicate a correlation between the area under the curve (AUC) and tolerability. Administering compound **7** at 6 hours after a lethal dose of N-azido-ADC significantly increased survival, likely by reducing the AUC of active N-azido-ADC in favor of its inactive neutralized form. The PD of N-azido-ADC is also affected, as the amanitin payload becomes less active upon the addition of compound **7**. This modification results in diminished efficacy against tumor cells, leading to a decrease in tumor response. However, it simultaneously reduces the off-target toxic effects caused by unspecific uptake of ADC in healthy tissues. Consequently, while the tolerability of N-azido-ADC improves due to the reaction with compound **7**, the tumor response is negatively impacted.

Interestingly, liver tissues exhibited a lower percentage of N-azido-ADC-neutralized compared to other tissues at both the 24-hour and 7-day time points. This can be attributed

to the liver sinusoidal endothelial cells, which express Fcγ receptors and C-type lectin scavenger receptors, playing a significant role in the uptake and clearance of immunoglobulins from the blood (James et al. 2022). It is likely that due to the presence of these receptors, N-azido-ADC may early accumulate in the liver and undergo metabolism within the first hours before the administration of compound **7**. On the contrary, the kidneys of the groups treated with compound **7** showed a higher concentration of N-azido-ADC-neutralized compared to N-azido-ADC. ADCs are nonspecifically metabolized not only by the liver, but also by the kidneys (Mahmood 2021). Since for the neutralization agent BCN-PEG_4-OH (**6**) the preferential route for clearance was through the kidneys, it is possible that also DBCO-PEG_4-COOH (**7**) redirects the clearance to this organ (Ursuegui et al. 2017).

Exposure of the ADC to the tumor (AUC) and PD plays a crucial role in tumor efficacy, as seen by a reduction in tumor response upon the reaction of N-azido-ADC with compound **7**. The gold standard in ADC therapy would be to maximize tumor exposure, so to treat with high doses of ADC, while avoiding toxicities, which means the broader the therapeutic window the better (Gerber et al. 2023). However, with some specific tumors, e.g. with heterogeneous tumors or poorly vascularized tumors, the minimum efficacious dose (MED) might not be reached and concentrations higher than the maximum tolerated dose (MTD) might be necessary to obtain a tumor response (Chakraborty and Rahman 2012). For example, the 22RV1 xenograft tumor exhibits moderate and heterogeneous expression of the Prostate-Specific Membrane Antigen (PSMA), with approximately 30-50% of cells expressing PSMA and it is considered a difficult-to-treat tumor model due to the rapid tumor growth rate and for the presence of cancer stem cells which may be responsible for cancer resistance (Sramkoski et al. 1999; Phi et al. 2018). Different studies that aimed to treat 22RV1 tumor model failed to obtain tumor eradication, but usually were able to stabilize tumor growth for few days before it started re-growing (Reddy et al. 2019; Bidkar et al. 2023). A treatment approach that uses higher concentrations of ADC would increase exposure to the tumor, increasing accumulation, promoting binding and retention to the target on tumor cells (Nessler et al. 2021).

In this study, the neutralization strategy aimed at allowing the administration of doses exceeding the MTD to maximize tumor exposure and accumulation before neutralizing the treatment at a later time point. The goal was to achieve greater tumor efficacy compared to the treatment with a standard PSMA-ADC (**Figure 34**). Unfortunately, a single intravenous dose 1.5 times higher than the MTD of PSMA-azido-ADC, followed by neutralization with compound **7** 20 hours later, did not enhance tumor efficacy in the 22RV1 CDX model. The tumor volume remained stable until day 3 and started increasing thereafter. The same dosing regimen was administered once a week for three weeks,

resulting also only in a short delay in tumor growth. Interestingly, the tumor response with PSMA-azido-ADC and compound **7** was comparable to 7.5 mg/kg (1/2 MTD) of PSMA-ADC, without exhibiting significant improvement in tumor efficacy. However, mice treated with the PSMA-ADC once a week for three weeks showed best results with delayed tumor response and improved probability of survival. This result may be due to the neutralization of the 1.5 MTD dose of PSMA-azido-ADC with compound **7**, 20 hours post-administration, significantly decreasing the availability of active PSMA-azido-ADC in circulation. This reduction leads to a greater decrease in tumor response compared to the ½ MTD dose of PSMA-ADC. Additionally, some mice treated with the 1.5 MTD dose of PSMA-azido-ADC could not tolerate the high dosage and had to be sacrificed within the first four days, highlighting variability in response to the therapy among the animals.

The efficacy studies in JIMT-1 and 22RV1 CDX models highlighted the significance of ADC exposure, the AUC, in both tumor and healthy tissues. It appears that neutralization of the payload with compound **7** could lead to a reduction in available active PSMA-azido-ADC, consequently diminishing tumor efficacy. Furthermore, the timing of application of compound **7** emerges as a crucial factor, as some mice succumbed within the two days following PSMA-azido-ADC administration, likely due to treatment-related toxicity. Although animal tolerability varied, the 20-hour timepoint for compound **7** application seems suboptimal for safety considerations. An earlier timepoint might have increased anti-tumor efficacy and simultaneously survival of the mice.

5.5 Future directions

This study highlights the potential of using Strained-Promoted Azido Alkyne Cycloaddition (SPAAC) as a neutralization strategy to improve the tolerability of amanitin-based ADCs (ATAC®s). While promising advancements were achieved in improving ATAC® tolerability, further optimization is necessary to maintain the tumor response of the ATAC® treatment. The timing of DBCO-PEG_4-COOH (**7**) administration plays a crucial role in enhancing tolerability and preserving tumor efficacy. This is because the pharmacokinetic and pharmacodynamic (PK/PD) profile of N-azido-ADC is significantly influenced by the introduction of compound **7**. When compound **7** is administered and reacts with N-azido-ADC, it generates an inactive N-azido-ADC-neutralized species reducing the exposure (AUC) of the active N-azido-ADC to the tumor. The decline in N-azido-ADC concentration in circulation diminishes tumor efficacy, as it reduces the amount of active amanitin payload reaching the tumor. Optimizing the timing of compound **7** administration could

yield more promising results, potentially enhancing the balance between retaining treatment efficacy and increasing tolerability.

Another intriguing strategy would involve the administration of the azido-ADC subcutaneously and the neutralizing agent intravenously. Usually ADCs are administered intravenously, enabling 100% bioavailability, with a high maximum concentration (C_{max}) concentration in circulation in the first minutes after application. On the contrary, the subcutaneous route leads to 50-80 % of ADC bioavailability, due to slow absorption rate governed by their size and lower C_{max} in circulation compared with an equivalent intravenous administration (Davis et al. 2024). Decker et. al showed that the subcutaneous application of the anti-PSMA-Ama1 ATAC® in monkeys increased the half-life, decreased the C_{max} and improved tolerability increasing MTD from 5 mg/kg to 7.5 mg/kg. Moreover, Decker et al. confirmed the importance of the AUC in tumor response for ATAC®s, as the same dose of anti-PSMA-Ama1 applied intravenously and subcutaneously retained a similar AUC and a similar effect on tumor response (Decker et al. 2023). Subcutaneous administration of the ADC could lower the C_{max}, reducing the initial onset of toxicity while maintaining ADC exposure. Subsequently, the neutralizing agent could be administered as supplementary treatment in case animals exhibit symptoms of treatment-related toxicity (Decker et al. 2023; Davis et al. 2024).

Another approach could involve using a different bioorthogonal reaction with faster kinetics for the neutralization of the amanitin payload, such as the inverse electron-demand Diels-Alder (IEDDA) reaction. IEDDA relies on the reaction between a tetrazine and a cyclooctene with kinetics between 10^2 and 10^6 M^{-1} s^{-1}, while the SPAAC reaction kinetic ranges from 1.2×10^{-4} and to 2.4×10^{-4} M^{-1} s^{-1}(Handula et al. 2021). The IEDDA reaction was used to develop a prodrug strategy wherein a diabody was conjugated to an MMAE molecule linked to a cyclooctene. Upon binding of the diabody to a non-internalized tumor target, a tetrazine activator was administered, reacting with MMAE to release the payload in the tumor microenvironment. This approach demonstrated robust tumor efficacy coupled with favorable tolerability (Rossin et al. 2018). Activating amanitin directly at the tumor site, as demonstrated by Rossin et al., could offer a promising approach to mitigate off-target toxicity and enhance the therapeutic index. However, considering the hydrophilic nature of amanitin, which does not allow for passive diffusion, activating the payload before internalization at the tumor site presents a challenge that needs careful consideration and innovative solutions. A possible solution could be to generate a prodrug amanitin linked to cyclooctene that is released upon reaction with a tetrazine activator derivatized to alkyl chains or PEGylated esters. The alkyl-chain or ester groups would increase amanitin lipophilicity potentially promoting *in situ* passive diffusion to the targeted cancer cell (Rautio et al. 2008; N'Da 2014).

Meyer et al. devised a pretargeting strategy wherein an antibody bearing a cyclooctene moiety was first administered *in vivo* to pre-target tumor cells. Subsequently, a radioligand with a tetrazine moiety was introduced to undergo an IEDDA reaction with the mAb and allow directed accumulation of the radioligand in the tumor. To prevent premature reaction with the radioligand in circulation due to the long half-life of mAbs, Meyer et al. "masked" the cyclooctene reacting moiety on the circulating mAb using a tetrazine-dextran polymer compound. This tetrazine conjugate reacted with the cyclooctene on the circulating mAb, rendering it unavailable for subsequent reaction with the tetrazine-radioligand in plasma (Meyer et al. 2018). An innovative approach could involve splitting the amanitin structure into two inactive components, one incorporating a tetrazine moiety and the other a strained cyclooctene. The cyclooctene-bearing component could be conjugated to the mAb, targeting the antibody to cancer cells. Subsequently, the azide-bearing component could be administered at a later timepoint. The bioorthogonal reaction between these two components would result in the *in situ* formation of active amanitin, potentially enhancing tumor specificity and minimizing off-target effects.

The FDA has approved various therapies to manage side effects associated with chemotherapy-related toxicity. These treatments aim to reverse conditions like neutropenia or address anemia, which are common adverse effects also observed in ADC therapies. (Kolesar 2002; Shi et al. 2006). The neutralization strategy developed in this study holds promise as an antidote to neutralize ADC treatment activity upon the onset of treatment-related toxicities. This approach could potentially prevent the escalation of adverse events in patients undergoing ADC therapy. Further research is needed to optimize and validate this strategy in pre-clinical settings. Additionally, exploring the possibility of integrating real-time monitoring techniques to detect early signs of toxicity and prompt administration of neutralizing agents could enhance its efficacy and applicability.

6 Abstract

Off-target toxicity poses a significant challenge in the development and clinical application of antibody-drug conjugates (ADCs), often leading to severe adverse effects due to non-specific uptake by healthy tissues. This is evident even in FDA-approved ADCs, which have shown substantial off-target toxicity in clinical settings. For instance, Trastuzumab emtansine (Kadcyla®) and Brentuximab vedotin (Adcetris®) both have reported adverse effects stemming from their cytotoxic payloads affecting non-cancerous cells.

Heidelberg Pharma has developed ATAC®s (Amanitin-based Antibody-Drug Conjugates) utilizing amanitin, a potent RNA polymerase II inhibitor, as the cytotoxic payload. Despite their high specificity and promising *in vitro* and *in vivo* results, unspecific liver toxicity caused by the non-specific uptake of ATAC®s remains a concern. This underscores the need for further optimization to mitigate off-tumor toxicity and enhance the therapeutic index of ATAC®s, thereby ensuring safer and more effective cancer treatments.

In this thesis, the Strain-Promoted Azido-Alkyne Cycloaddition (SPAAC) reaction was explored as a neutralization strategy to improve the tolerability of ATAC®s. The goal was to neutralize the activity of ATAC®s post-administration, thereby reducing off-target effects while maintaining efficacy against tumor cells. Azido-amanitin derivatives were synthesized and their activity was evaluated upon reaction with different strained alkyne compounds, known as neutralizing agents. The SPAAC reaction with a PEG-cycloalkyne successfully reduced the *in vitro* activity of azido-amanitin and decreased cytotoxicity in target-positive cells when used to neutralize azido-amanitin ADCs. The corresponding azido-amanitin ADCs were then evaluated *in vivo* to determine if the neutralization strategy could improve the tolerability of the ADC treatment. In tumor-free mice, the tolerability of these conjugates improved, even with delayed administration of the neutralizing agents, resulting in reduced toxic lesions in the liver and kidneys and improved survival. To assess whether tumor efficacy could be retained after applying the neutralization strategy, efficacy studies were conducted in tumor-bearing mice using the azido-amanitin ADCs along with additional treatment with the neutralizing agents. These studies demonstrated that the azido-amanitin ADCs induced a tumor response comparable to the standard ATAC® treatment. However, the administration of the neutralizing agents adversely affected the tumor response, with variability observed among mice in the same treatment group. Notably, the earlier the neutralizing agent was administered, the more significantly the tumor response was affected, highlighting the critical importance of sustained ADC exposure to the tumor.

The results demonstrate that the SPAAC reaction can serve as an effective detoxification method, significantly improving the tolerability of ATAC®s. However, the timing of neutralization was found to be crucial, as it significantly influenced the balance between increasing tolerability and maintaining an anti-tumor response. Further optimization of the treatment schedule and SPAAC reaction conditions is necessary to ensure that the therapeutic efficacy of ATAC®s is not compromised. The SPAAC-based neutralization strategy developed in this work provides one option for reducing unwanted adverse effects of ADC-treatment potentially enhancing the clinical application of ATAC®s, providing a safer and more effective therapeutic option for cancer patients.

7 Zusammenfassung

Die Off-Target-Toxizität stellt eine bedeutende Herausforderung bei der Entwicklung und klinischen Anwendung von Antikörper-Wirkstoff-Konjugaten (ADCs) dar und führt oft zu schweren Nebenwirkungen aufgrund der nicht spezifischen Aufnahme durch gesunde Gewebe. Dies ist selbst bei von der FDA zugelassenen ADCs offensichtlich, die in klinischen Studien erhebliche Off-Target-Toxizität gezeigt haben. Zum Beispiel wurden für Trastuzumab Emtansin (Kadcyla®) und Brentuximab Vedotin (Adcetris®) Nebenwirkungen berichtet, die aus den zytotoxischen Wirkstoffen resultieren und nicht-krebsartige Zellen betreffen.

Heidelberg Pharma hat ATAC®s (Amanitin-basierte Antikörper-Wirkstoff-Konjugate) entwickelt, die Amanitin, einen potenten RNA-Polymerase-II-Inhibitor, als zytotoxischen Wirkstoff nutzen. Trotz ihrer hohen Spezifität und vielversprechenden *in vitro* und *in vivo* Ergebnisse bleibt die unspezifische Lebertoxizität durch die nicht spezifische Aufnahme von ATAC®s ein Problem. Dies unterstreicht die Notwendigkeit weiterer Optimierungen, um die Off-Tumor-Toxizität zu verringern und den therapeutischen Index von ATAC®s zu verbessern, um sicherere und effektivere Krebstherapien zu gewährleisten.

In dieser Arbeit wurde die spannungsvermittelte Azid-Alkin-Cycloaddition (SPAAC) als Neutralisierungsstrategie untersucht, um die Verträglichkeit von ATAC®s zu verbessern. Ziel war es, die Aktivität von ATAC®s nach der Verabreichung zu neutralisieren, um Off-Target-Effekte zu reduzieren, während die Wirksamkeit gegen Tumorzellen erhalten bleibt. Azido-Amanitin-Derivate wurden synthetisiert und ihre Aktivität nach der Reaktion mit verschiedenen gespannten Alkinverbindungen, die als Neutralisierungsmittel bekannt sind, bewertet. Die SPAAC-Reaktion mit einem PEG-Cycloalkin reduzierte erfolgreich die *in vitro* Aktivität von Azido-Amanitin und verringerte die Zytotoxizität in target-positiven Zellen, wenn sie zur Neutralisierung von Azido-Amanitin ADCs verwendet wurde. Die entsprechenden Azido-Amanitin-Konjugate wurden daraufhin *in vivo* bewertet, um festzustellen, ob die Neutralisierungsstrategie die Verträglichkeit der ADC-Behandlung verbessern könnte. Bei tumorfreien Mäusen verbesserte sich die Verträglichkeit dieser Konjugate, selbst bei verzögerter Verabreichung der Neutralisierungsmittel, was zu reduzierten toxischen Läsionen in Leber und Nieren und verbesserter Überlebensrate führte.

Um zu beurteilen, ob die Tumorwirksamkeit auch bei Anwendung der Neutralisierungsstrategie erhalten bleibt, wurden Wirksamkeitsstudien an tumortragenden Mäusen mit den Azido-Amanitin-Konjugaten zusammen mit nachträglicher Behandlung mit den Neutralisierungsmitteln durchgeführt. Diese Studien zeigten, dass die Azido-

Amanitin-Konjugate eine tumorsupprimierende Reaktion ähnlich der Standard-ATAC®-Behandlung auslösten. Jedoch beeinträchtigte die Verabreichung der Neutralisierungsmittel die Tumorreaktion negativ, wobei Variabilität unter den Mäusen in derselben Behandlungsgruppe beobachtet wurde. Bemerkenswert war, dass je früher das Neutralisierungsmittel verabreicht wurde, desto stärker die Tumorreaktion beeinträchtigt wurde, was die kritische Bedeutung einer kontinuierlichen ADC-Exposition des Tumors hervorhebt.

Die Ergebnisse zeigen, dass die SPAAC-Reaktion als effektive Entgiftungsmethode dienen kann und die Verträglichkeit von ATAC®s erheblich verbessert. Allerdings erwies sich die zeitliche Abfolge der Neutralisierung als entscheidend, da diese das Gleichgewicht zwischen erhöhter Verträglichkeit und Aufrechterhaltung der Anti-Tumor-Wirkung signifikant beeinflusste. Weitere Optimierungen des Behandlungsplans und der SPAAC-Reaktionsbedingungen sind notwendig, um sicherzustellen, dass die therapeutische Wirksamkeit von ATAC®s nicht zu stark beeinträchtigt wird. Die in dieser Arbeit entwickelte SPAAC-basierte Neutralisierungsstrategie bietet eine Option zur Reduzierung unerwünschter Nebenwirkungen der ADC-Behandlung und könnte die klinische Anwendung von ATAC®s verbessern, was eine sicherere und möglicherweise effektivere therapeutische Option für Krebspatienten darstellt.

8 Abbreviations

Ab	Antibody
ABCC	ATP-binding cassette sub-family C
ACN	Acetonitrile
ADC	Antibody-drug conjugate
ADCC	Antibody-dependent cellular toxicity
ADCP	Antibody-dependent cellular phagocytosis
ADME	Absorption, distribution, metabolism, elimination
Ala (A)	Alanine
Asn (N)	Asparagine
Asp (D)	Aspartic acid
ATAC®	Amanitin-based antibody-drug conjugates
AUC	Area under the curve
Av. DAR	Average Drug-to-antibody ratio
BCN	Bicyclo[6.1.0]non-4-yne
BW	Body weight
CAR	Chimeric antigen receptor
CDC	Complement-dependent cytotoxicity
CDR	Complementarity-determining region
CDX	Cell line-derived xenograft
Cit	Citrulline
CLR	C-type lectin receptor
C_{max}	Maximum plasma concentration
CMV	Cytomegalovirus
Ct	Cycle threshold
CuAAC	Copper(I)-catalyzed cycloaddition
Cys (C)	Cysteine
DAR	Drug-to-antibody ratio
DBCO	Dibenzocyclooctyne
DMF	Dimethylformamide
DMSO	Dimethyl sulfoxide
DNA	Deoxyribonucleic acid
dNTP	Deoxyribonucleoside triphoshpate
EC50	Half maximal effective concentration
EDTA	Ethylenediaminetetraacetic acid
ELISA	Enzyme-linked immunosorbent assay
Eq.	Equivalents
Fab	Fragment antigen-binding
Fc	Fragment crystallizable
FcR	Fc receptor
FcRn	Fc neonatal receptor
FcγR	Fcγ receptor
FD	Found dead
FDA	Food and Drug administration

FPLC	Fast protein liquid chromatography
GCO	Global Cancer Observatory
GSH	Gluthation
GTEx	Gene-Tissue expression
HC	Heavy chain
HDP	Heidelberg Pharma
HER2	Human epidermal growth factor 2
HPLC	High performance liquid chromatography
HRP	Horse radish peroxydase
HSC	Hematopoietic stem cells
i.v.	Intravenous
IC50	Half maximal inhibitory concentration
IEDDA	Electron Demand Diels-Alder
IgG	Immunoglobulin G
LC-MS	Liquid chromatography-mass spectrometry
LLQ	Lower limit of quantification
LPS	Lipopolysaccharide
Lys	Lysine
mAb	Monoclonal antibody
MC	Maleimidocaproyl
MED	Minimum efficacious dose
MRP	Multidrug resistant protein
MR	Mannose receptor
MTD	Maximum Tolerated Dose
NHS	N-hydroxysuccinimide
NK	Natural killer
OATP1B3	Organic Anion-transporting Polypeptide 1B3
PAB	4-Aminobenzoic acid
PBD	Pyrrolobenzodiazepine
PBS	Phosphate-buffered saline
PD	Pharmacodynamic
PEG	Polyethylene glycol
PGC	Poor general conditions
PK	Pharmacokinetic
PVDF	Polyvinylidene fluoride
rFC	Horseshoe Crab Factor C
RNA	Ribonucleic acid
RNA pol	RNA polymerase
rNTP	Ribonucleoside triphosphate
RPC	Reverse Phase Chromatography
RT	Room temperature
RT PCR	Reverse trasncriptase PCR
SEC	Size-exclusion chromatography
Ser (S)	Serine
SPAAC	Strain-Promoted Azide-Alkyne Cycloaddition
SPF	specific-pathogen free
TCEP	Tris(2-chlorehyl)phosphat

TCGA	The Cancer Genome Atlas
TCO	Transcyclooctene
TFA	Trifluoroacetic acid
TGI	Tumor Growth Inhibition
TI	Therapeutic Index
Tk pA	thymidine kinase poly A
TM	Transmembrane domain
TOF MS	Time-of-flight mass spectometry
Val (V)	Valine
WB	Western Blot
WN_3	Azidowarfarin
WPR	Woodchuck hepatitis virus post-transcriptional regulatory element

9 Bibliography

Agard NJ, Prescher JA, Bertozzi CR (2004) A Strain-Promoted [3 + 2] Azide−Alkyne Cycloaddition for Covalent Modification of Biomolecules in Living Systems. J Am Chem Soc 126:15046–15047. https://doi.org/10.1021/ja044996f

Akaiwa M, Dugal-Tessier J, Mendelsohn BA (2020) Antibody–Drug Conjugate Payloads; Study of Auristatin Derivatives. Chem Pharm Bull (Tokyo) 68:201–211. https://doi.org/10.1248/cpb.c19-00853

Akilesh S, Christianson GJ, Roopenian DC, Shaw AS (2007) Neonatal FcR Expression in Bone Marrow-Derived Cells Functions to Protect Serum IgG from Catabolism1. J Immunol 179:4580–4588. https://doi.org/10.4049/jimmunol.179.7.4580

Alley SC, Benjamin DR, Jeffrey SC, et al (2008) Contribution of Linker Stability to the Activities of Anticancer Immunoconjugates. Bioconjug Chem 19:759–765. https://doi.org/10.1021/bc7004329

Alt M, Stecca C, Tobin S, et al (2020) Enfortumab Vedotin in urothelial cancer. Ther Adv Urol 12:1756287220980192. https://doi.org/10.1177/1756287220980192

Altun İ, Sonkaya A (2018) The Most Common Side Effects Experienced by Patients Were Receiving First Cycle of Chemotherapy. Iran J Public Health 47:1218–1219

Anami Y, Otani Y, Xiong W, et al (2022) Homogeneity of antibody-drug conjugates critically impacts the therapeutic efficacy in brain tumors. Cell Rep 39:110839. https://doi.org/10.1016/j.celrep.2022.110839

André F, Hee Park Y, Kim S-B, et al (2023) Trastuzumab deruxtecan versus treatment of physician's choice in patients with HER2-positive metastatic breast cancer (DESTINY-Breast02): a randomised, open-label, multicentre, phase 3 trial. The Lancet 401:1773–1785. https://doi.org/10.1016/S0140-6736(23)00725-0

Arruebo M, Vilaboa N, Sáez-Gutierrez B, et al (2011) Assessment of the Evolution of Cancer Treatment Therapies. Cancers 3:3279–3330. https://doi.org/10.3390/cancers3033279

Azar I, Alkassis S, Fukui J, et al (2021) Spotlight on Trastuzumab Deruxtecan (DS-8201,T-DXd) for HER2 Mutation Positive Non-Small Cell Lung Cancer. Lung Cancer Targets Ther 12:103–114. https://doi.org/10.2147/LCTT.S307324

Bajaj K, Andres SA, Hofsommer DT, et al (2023) Physical structure of constitutional isomers influences antiproliferation activity of thiosemicarbazone-alkylthiocarbamate copper complexes. J Inorg Biochem 246:112288. https://doi.org/10.1016/j.jinorgbio.2023.112288

Bargh JD, Isidro-Llobet A, Parker JS, Spring DR (2019) Cleavable linkers in antibody–drug conjugates. Chem Soc Rev 48:4361–4374. https://doi.org/10.1039/C8CS00676H

Barok M, Joensuu H, Isola J (2014) Trastuzumab emtansine: mechanisms of action and drug resistance. Breast Cancer Res 16:209. https://doi.org/10.1186/bcr3621

Battigelli A, Almeida B, Shukla A (2022) Recent Advances in Bioorthogonal Click Chemistry for Biomedical Applications. Bioconjug Chem 33:263–271. https://doi.org/10.1021/acs.bioconjchem.1c00564

Beck A, Goetsch L, Dumontet C, Corvaïa N (2017) Strategies and challenges for the next generation of antibody-drug conjugates. Nat Rev Drug Discov 16:315–337. https://doi.org/10.1038/nrd.2016.268

Bertozzi CR, Meldal M, Sharpless KB (2022) The Nobel Prize in Chemistry 2022

Bhakta S, Erickson H, Junutula JR, et al (2016) Cysteine engineered antibodies and conjugates

Bidkar AP, Wang S, Bobba KN, et al (2023) Treatment of Prostate Cancer with CD46-targeted 225Ac Alpha Particle Radioimmunotherapy. Clin Cancer Res 29:1916–1928. https://doi.org/10.1158/1078-0432.CCR-22-3291

Black J, Vos J-M (2002) Establishment of an oriP/EBNA1-based episomal vector transcribing human genomic β-globin in cultured murine fibroblasts. Gene Ther 9:1447–1454. https://doi.org/10.1038/sj.gt.3301808

Boone AC, Adetunji SA, Kohnken R, Koyama K (2023) Select Toxicologic Pathology Case Studies of the Hepatobiliary System. Toxicol Pathol 51:465–469. https://doi.org/10.1177/01926233231224464

Boshart M, Weber F, Jahn G, et al (1985) A very strong enhancer is located upstream of an immediate early gene of human cytomegalovirus. Cell 41:521–530. https://doi.org/10.1016/S0092-8674(85)80025-8

Boune S, Hu P, Epstein AL, Khawli LA (2020) Principles of N-Linked Glycosylation Variations of IgG-Based Therapeutics: Pharmacokinetic and Functional Considerations. Antibodies 9:22. https://doi.org/10.3390/antib9020022

Bower JE (2014) Cancer-related fatigue: Mechanisms, risk factors, and treatments. Nat Rev Clin Oncol 11:597–609. https://doi.org/10.1038/nrclinonc.2014.127

Bray F, Laversanne M, Sung H, et al (2022) Global cancer statistics 2022: GLOBOCAN estimates of incidence and mortality worldwide for 36 cancers in 185 countries. CA Cancer J Clin n/a: https://doi.org/10.3322/caac.21834

Bray F, Laversanne M, Weiderpass E, Soerjomataram I (2021) The ever-increasing importance of cancer as a leading cause of premature death worldwide. Cancer 127:3029–3030. https://doi.org/10.1002/cncr.33587

Brueckner F, Cramer P (2008) Structural basis of transcription inhibition by α-amanitin and implications for RNA polymerase II translocation. Nat Struct Mol Biol 15:811–818. https://doi.org/10.1038/nsmb.1458

Chakraborty S, Rahman T (2012) The difficulties in cancer treatment. ecancermedicalscience 6:ed16. https://doi.org/10.3332/ecancer.2012.ed16

Chen L, Wang L, Shion H, et al (2016) In-depth structural characterization of Kadcyla® (ado-trastuzumab emtansine) and its biosimilar candidate. mAbs 8:1210–1223. https://doi.org/10.1080/19420862.2016.1204502

Cheung-Ong K, Giaever G, Nislow C (2013) DNA-Damaging Agents in Cancer Chemotherapy: Serendipity and Chemical Biology. Chem Biol 20:648–659. https://doi.org/10.1016/j.chembiol.2013.04.007

Chio TI, Bane SL (2020) Click Chemistry Conjugations. Methods Mol Biol Clifton NJ 2078:83–97. https://doi.org/10.1007/978-1-4939-9929-3_6

Chirukandath G, Vasanthi M (2014) Atlas of Toxicological Pathology. Springer

Chumsae C, Gaza-Bulseco G, Liu H (2009) Identification and Localization of Unpaired Cysteine Residues in Monoclonal Antibodies by Fluorescence Labeling and Mass Spectrometry. Anal Chem 81:6449–6457. https://doi.org/10.1021/ac900815z

Colombo R, Rich JR (2022) The therapeutic window of antibody drug conjugates: A dogma in need of revision. Cancer Cell 40:1255–1263. https://doi.org/10.1016/j.ccell.2022.09.016

Costa A, Scholer-Dahirel A, Mechta-Grigoriou F (2014) The role of reactive oxygen species and metabolism on cancer cells and their microenvironment. Semin Cancer Biol 25:23–32. https://doi.org/10.1016/j.semcancer.2013.12.007

Damelin M, Zhong W, Myers J, Sapra P (2015) Evolving Strategies for Target Selection for Antibody-Drug Conjugates. Pharm Res 32:3494–3507. https://doi.org/10.1007/s11095-015-1624-3

Daublain P, Feng K-I, Altman MD, et al (2017) Analyzing the Potential Root Causes of Variability of Pharmacokinetics in Preclinical Species. Mol Pharm 14:1634–1645. https://doi.org/10.1021/acs.molpharmaceut.6b01118

Davis JD, Bravo Padros M, Conrado DJ, et al (2024) Subcutaneous Administration of Monoclonal Antibodies: Pharmacology, Delivery, Immunogenicity, and Learnings From Applications to Clinical Development. Clin Pharmacol Ther 115:422–439. https://doi.org/10.1002/cpt.3150

Decker K, Vranic M, Schmitt M, et al (2023) Abstract 1523: Subcutaneous dosing of amatoxin-based ADCs increases the therapeutic index. Cancer Res 83:1523. https://doi.org/10.1158/1538-7445.AM2023-1523

Deslandes A (2014) Comparative clinical pharmacokinetics of antibody-drug conjugates in first-in-human Phase 1 studies. mAbs 6:859–870. https://doi.org/10.4161/mabs.28965

DeVita VT Jr, Chu E (2008) A History of Cancer Chemotherapy. Cancer Res 68:8643–8653. https://doi.org/10.1158/0008-5472.CAN-07-6611

Dondelinger M, Filée P, Sauvage E, Quinting B, Muyldermans S, Galleni M, Vandevenne MS. Understanding the Significance and Implications of Antibody Numbering and Antigen-Binding Surface/Residue Definition. Front Immunol. 2018 Oct 16;9:2278. doi: 10.3389/fimmu.2018.02278. PMID: 30386328; PMCID: PMC6198058.

Dokter W, Ubink R, van der Lee M, et al (2014) Preclinical Profile of the HER2-Targeting ADC SYD983/SYD985: Introduction of a New Duocarmycin-Based Linker-Drug

Platform. Mol Cancer Ther 13:2618–2629. https://doi.org/10.1158/1535-7163.MCT-14-0040-T

Dommerholt J, Rutjes FPJT, van Delft FL (2016) Strain-Promoted 1,3-Dipolar Cycloaddition of Cycloalkynes and Organic Azides. Top Curr Chem Cham 374:16. https://doi.org/10.1007/s41061-016-0016-4

Dommerholt J, Schmidt S, Temming R, et al (2010) Readily Accessible Bicyclononynes for Bioorthogonal Labeling and Three-Dimensional Imaging of Living Cells. Angew Chem Int Ed Engl 49:9422–9425. https://doi.org/10.1002/anie.201003761

Donaghy H (2016) Effects of antibody, drug and linker on the preclinical and clinical toxicities of antibody-drug conjugates. mAbs 8:659–671. https://doi.org/10.1080/19420862.2016.1156829

Ducry L, Stump B (2010) Antibody−Drug Conjugates: Linking Cytotoxic Payloads to Monoclonal Antibodies. Bioconjug Chem 21:5–13. https://doi.org/10.1021/bc9002019

Edelman GM, Cunningham BA, Gall WE, et al (1969) THE COVALENT STRUCTURE OF AN ENTIRE γG IMMUNOGLOBULIN MOLECULE*. Proc Natl Acad Sci U S A 63:78–85

Ehrlich P (1907) Chemotherapeutische trypanosomen-studien. Berl Klin Wochenschr 233–309

Eipel C, Abshagen K, Vollmar B (2010) Regulation of hepatic blood flow: The hepatic arterial buffer response revisited. World J Gastroenterol WJG 16:6046–6057. https://doi.org/10.3748/wjg.v16.i48.6046

Ellestad GA, Ding W (1994) Calicheamicin. In: Neidle S, Waring M (eds) Molecular Aspects of Anticancer Drug-DNA Interactions: Volume 2. Macmillan Education UK, London, pp 130–161

Endo Y, Lyon S, Shen Y, et al (2019) Cell proliferation and invasion are regulated differently by EGFR and MRP1 in T-DM1-resistant breast cancer cells. Sci Rep 9:16383. https://doi.org/10.1038/s41598-019-52797-z

Endo Y, Shen Y, Youssef LA, et al (2018) T-DM1-resistant cells gain high invasive activity via EGFR and integrin cooperated pathways. mAbs 10:1003–1017. https://doi.org/10.1080/19420862.2018.1503904

Esapa B, Jiang J, Cheung A, et al (2023) Target Antigen Attributes and Their Contributions to Clinically Approved Antibody-Drug Conjugates (ADCs) in Haematopoietic and Solid Cancers. Cancers 15:1845. https://doi.org/10.3390/cancers15061845

Estrela JM, Ortega A, Obrador E (2006) Glutathione in Cancer Biology and Therapy. Crit Rev Clin Lab Sci 43:143–181. https://doi.org/10.1080/10408360500523878

Fineschi V, Di Paolo M, Centini F (1996) Histological Criteria for Diagnosis of Amanita Phalloides Poisoning. J Forensic Sci 41:429–432. https://doi.org/10.1520/JFS13929J

Fontaine SD, Reid R, Robinson L, et al (2015) Long-Term Stabilization of Maleimide–Thiol Conjugates. Bioconjug Chem 26:145–152. https://doi.org/10.1021/bc5005262

Fu Z, Li S, Han S, et al (2022) Antibody drug conjugate: the “biological missile” for targeted cancer therapy. Signal Transduct Target Ther 7:1–25. https://doi.org/10.1038/s41392-022-00947-7

Garcia J, Costa VM, Carvalho A, et al (2015) Amanita phalloides poisoning: Mechanisms of toxicity and treatment. Food Chem Toxicol 86:41–55. https://doi.org/10.1016/j.fct.2015.09.008

Gerber H-P, Gangwar S, Betts A (2023) Therapeutic index improvement of antibody-drug conjugates. mAbs 15:2230618. https://doi.org/10.1080/19420862.2023.2230618

Gondi CS, Rao JS (2013) Cathepsin B as a Cancer Target. Expert Opin Ther Targets 17:281–291. https://doi.org/10.1517/14728222.2013.740461

Gorges TM, Riethdorf S, von Ahsen O, et al (2016) Heterogeneous PSMA expression on circulating tumor cells - a potential basis for stratification and monitoring of PSMA-directed therapies in prostate cancer. Oncotarget 7:34930–34941. https://doi.org/10.18632/oncotarget.9004

Gorovits B, Krinos-Fiorotti C (2013) Proposed mechanism of off-target toxicity for antibody–drug conjugates driven by mannose receptor uptake. Cancer Immunol Immunother 62:217–223. https://doi.org/10.1007/s00262-012-1369-3

Gregson SJ, Masterson LA, Wei B, et al (2017) Pyrrolobenzodiazepine Dimer Antibody–Drug Conjugates: Synthesis and Evaluation of Noncleavable Drug-Linkers. J Med Chem 60:9490–9507. https://doi.org/10.1021/acs.jmedchem.7b00736

Gröst C, Berg T (2015) PYRROC: the first functionalized cycloalkyne that facilitates isomer-free generation of organic molecules by SPAAC. Org Biomol Chem 13:3866–3870. https://doi.org/10.1039/C5OB00212E

Hafeez U, Parakh S, Gan HK, Scott AM (2020) Antibody–Drug Conjugates for Cancer Therapy. Molecules 25:4764. https://doi.org/10.3390/molecules25204764

Hallam TJ, Wold E, Wahl A, Smider VV (2015) Antibody Conjugates with Unnatural Amino Acids. Mol Pharm 12:1848–1862. https://doi.org/10.1021/acs.molpharmaceut.5b00082

Hamblett KJ, Senter PD, Chace DF, et al (2004) Effects of Drug Loading on the Antitumor Activity of a Monoclonal Antibody Drug Conjugate. Clin Cancer Res 10:7063–7070. https://doi.org/10.1158/1078-0432.CCR-04-0789

Hanahan D, Weinberg RA (2000) The Hallmarks of Cancer. Cell 100:57–70. https://doi.org/10.1016/S0092-8674(00)81683-9

Handula M, Chen K-T, Seimbille Y (2021) IEDDA: An Attractive Bioorthogonal Reaction for Biomedical Applications. Molecules 26:4640. https://doi.org/10.3390/molecules26154640

Hang HC, Yu C, Kato DL, Bertozzi CR (2003) A metabolic labeling approach toward proteomic analysis of mucin-type O-linked glycosylation. Proc Natl Acad Sci U S A 100:14846–14851. https://doi.org/10.1073/pnas.2335201100

Hechler T, Pahl A (2023) Humanized Antibodies Against PSMA

Hedrich WD, Fandy TE, Ashour HM, et al (2018) Antibody–Drug Conjugates: Pharmacokinetic/Pharmacodynamic Modeling, Preclinical Characterization, Clinical Studies, and Lessons Learned. Clin Pharmacokinet 57:687–703. https://doi.org/10.1007/s40262-017-0619-0

Heidelberg Pharma AG (2024) Heidelberg Pharma announces progress into Cohort 6 with its proprietary ATAC candidate HDP-101 in Phase I/IIa multiple myeloma study [Press release]. https://heidelberg-pharma.com/en/press-investors/announcements/press-releases-and-ad-hoc-announcements/heidelberg-pharma-announces-progress-into-cohort-6-with-its-proprietary-atac-candidate-hdp-101-in-phase-i-iia-multiple-myeloma-study. Accessed 25 Mar 2024

Hermanson GT (2013a) Chapter 2 - Functional Targets for Bioconjugation. In: Hermanson GT (ed) Bioconjugate Techniques (Third Edition). Academic Press, Boston, pp 127–228

Hermanson GT (2013b) Chapter 3 - The Reactions of Bioconjugation. In: Hermanson GT (ed) Bioconjugate Techniques (Third Edition). Academic Press, Boston, pp 229–258

Hurvitz SA, Hegg R, Chung W-P, et al (2023) Trastuzumab deruxtecan versus trastuzumab emtansine in patients with HER2-positive metastatic breast cancer: updated results from DESTINY-Breast03, a randomised, open-label, phase 3 trial. The Lancet 401:105–117. https://doi.org/10.1016/S0140-6736(22)02420-5

Jackson DY (2016) Processes for Constructing Homogeneous Antibody Drug Conjugates. Org Process Res Dev 20:852–866. https://doi.org/10.1021/acs.oprd.6b00067

Jacobson O, Li Q, Chen H, et al (2017) PET-Guided Evaluation and Optimization of Internalized Antibody–Drug Conjugates Targeting Erythropoietin-Producing Hepatoma A2 Receptor. J Nucl Med 58:1838–1844. https://doi.org/10.2967/jnumed.117.192245

James BH, Papakyriacou P, Gardener MJ, et al (2022) The Contribution of Liver Sinusoidal Endothelial Cells to Clearance of Therapeutic Antibody. Front Physiol 12:753833. https://doi.org/10.3389/fphys.2021.753833

Jeffrey V, Joachim M (1991) New pUC-derived cloning vectors with different selectable markers and DNA replication origins. Gene 100:189–194. https://doi.org/10.1016/0378-1119(91)90365-I

Johns AC, Campbell MT (2022) Toxicities from Antibody-Drug Conjugates. Cancer J 28:469–478

Johnson ZL, Chen J (2017) Structural Basis of Substrate Recognition by the Multidrug Resistance Protein MRP1. Cell 168:1075-1085.e9. https://doi.org/10.1016/j.cell.2017.01.041

Junutula JR, Bhakta S, Raab H, et al (2008a) Rapid identification of reactive cysteine residues for site-specific labeling of antibody-Fabs. J Immunol Methods 332:41–52. https://doi.org/10.1016/j.jim.2007.12.011

Junutula JR, Raab H, Clark S, et al (2008b) Site-specific conjugation of a cytotoxic drug to an antibody improves the therapeutic index. Nat Biotechnol 26:925–932. https://doi.org/10.1038/nbt.1480

Kenry, Liu B (2019) Bio-orthogonal Click Chemistry for *In Vivo* Bioimaging. Trends Chem 1:763–778. https://doi.org/10.1016/j.trechm.2019.08.003

Kesserwani H (2021) Death and Rebirth of the Thalidomide Molecule: A Case of Thalidomide-Induced Sensory Neuropathy. Cureus 13:e13140. https://doi.org/10.7759/cureus.13140

Klein C, Brinkmann U, Reichert JM, Kontermann RE (2024) The present and future of bispecific antibodies for cancer therapy. Nat Rev Drug Discov 1–19. https://doi.org/10.1038/s41573-024-00896-6

Kolb HC, Finn MG, Sharpless KB (2001) Click Chemistry: Diverse Chemical Function from a Few Good Reactions. Angew Chem Int Ed 40:2004–2021. https://doi.org/10.1002/1521-3773(20010601)40:11<2004::AID-ANIE2004>3.0.CO;2-5

Kolesar JM (2002) Novel approaches to anemia associated with cancer and chemotherapy. Am J Health Syst Pharm 59:S8–S11. https://doi.org/10.1093/ajhp/59.suppl_4.S8

Kondo N, Takahashi A, Ono K, Ohnishi T (2010) DNA Damage Induced by Alkylating Agents and Repair Pathways. J Nucleic Acids 2010:543531. https://doi.org/10.4061/2010/543531

Koniev O, Wagner A (2015) Developments and recent advancements in the field of endogenous amino acid selective bond forming reactions for bioconjugation. Chem Soc Rev 44:5495–5551. https://doi.org/10.1039/C5CS00048C

Kovac AL (2009) Sugammadex: the first selective binding reversal agent for neuromuscular block. J Clin Anesth 21:444–453. https://doi.org/10.1016/j.jclinane.2009.05.002

Kushwaha PP, Verma S, Kumar S, Gupta S (2022) Role of prostate cancer stem-like cells in the development of antiandrogen resistance. Cancer Drug Resist 5:459–471. https://doi.org/10.20517/cdr.2022.07

Laplagne C, Domagala M, Le Naour A, et al (2019) Latest Advances in Targeting the Tumor Microenvironment for Tumor Suppression. Int J Mol Sci 20:4719. https://doi.org/10.3390/ijms20194719

Latvala S, Jacobsen B, Otteneder MB, et al (2017) Distribution of FcRn Across Species and Tissues. J Histochem Cytochem 65:321–333. https://doi.org/10.1369/0022155417705095

Lee A (2021) Loncastuximab Tesirine: First Approval. Drugs 81:1229–1233. https://doi.org/10.1007/s40265-021-01550-w

Lefranc MP, Lefranc G. IMGT ® Nomenclature of Engineered IGHG Variants Involved in Antibody Effector Properties and Formats. Antibodies (Basel). 2022 Oct 18;11(4):65. doi: 10.3390/antib11040065. PMID: 36278618; PMCID: PMC9624366.

Letschert K, Faulstich H, Keller D, Keppler D (2006) Molecular Characterization and Inhibition of Amanitin Uptake into Human Hepatocytes. Toxicol Sci 91:140–149. https://doi.org/10.1093/toxsci/kfj141

Levengood MR, Zhang X, Hunter JH, et al (2017) Orthogonal Cysteine Protection Enables Homogeneous Multi-Drug Antibody–Drug Conjugates. Angew Chem Int Ed 56:733–737. https://doi.org/10.1002/anie.201608292

Liao MZ, Lu D, Kågedal M, et al (2021) Model-Informed Therapeutic Dose Optimization Strategies for Antibody–Drug Conjugates in Oncology: What Can We Learn From US Food and Drug Administration–Approved Antibody–Drug Conjugates? Clin Pharmacol Ther 110:1216–1230. https://doi.org/10.1002/cpt.2278

Lim WA, June CH (2017) The Principles of Engineering Immune Cells to Treat Cancer. Cell 168:724–740. https://doi.org/10.1016/j.cell.2017.01.016

Lin K, Tibbitts J, Shen B-Q (2013) Pharmacokinetics and ADME Characterizations of Antibody–Drug Conjugates. In: Ducry L (ed) Antibody-Drug Conjugates. Humana Press, Totowa, NJ, pp 117–131

Liu JF, Moore KN, Birrer MJ, et al (2016) Phase I study of safety and pharmacokinetics of the anti-MUC16 antibody–drug conjugate DMUC5754A in patients with platinum-resistant ovarian cancer or unresectable pancreatic cancer. Ann Oncol 27:2124–2130. https://doi.org/10.1093/annonc/mdw401

Liu S, Verma A, Kettenberger H, et al (2021) Effect of variable domain charge on in vitro and in vivo disposition of monoclonal antibodies. mAbs 13:1993769. https://doi.org/10.1080/19420862.2021.1993769

Liu T, Xu F, Du X, et al (2010) Establishment and characterization of multi-drug resistant, prostate carcinoma-initiating stem-like cells from human prostate cancer cell lines 22RV1. Mol Cell Biochem 340:265–273. https://doi.org/10.1007/s11010-010-0426-5

Liu X, Farnung L, Wigge C, Cramer P (2018) Cryo-EM structure of a mammalian RNA polymerase II elongation complex inhibited by α-amanitin. J Biol Chem 293:7189–7194. https://doi.org/10.1074/jbc.RA118.002545

Liu Y, Zhang X, Han C, et al (2015) TP53 loss creates therapeutic vulnerability in colorectal cancer. Nature 520:697–701. https://doi.org/10.1038/nature14418

Lloyd JB (2000) Lysosome membrane permeability: implications for drug delivery. Adv Drug Deliv Rev 41:189–200. https://doi.org/10.1016/S0169-409X(99)00065-4

Lo M, Kim HS, Tong RK, et al (2017) Effector-attenuating Substitutions That Maintain Antibody Stability and Reduce Toxicity in Mice *. J Biol Chem 292:3900–3908. https://doi.org/10.1074/jbc.M116.767749

Lonsdale J, Thomas J, Salvatore M, et al (2013) The Genotype-Tissue Expression (GTEx) project. Nat Genet 45:580–585. https://doi.org/10.1038/ng.2653

López de Sá A, Díaz-Tejeiro C, Poyatos-Racionero E, et al (2023) Considerations for the design of antibody drug conjugates (ADCs) for clinical development: lessons learned. J Hematol OncolJ Hematol Oncol 16:1–13. https://doi.org/10.1186/s13045-023-01519-0

López-Yerena A, Perez M, Vallverdú-Queralt A, Escribano-Ferrer E (2020) Insights into the Binding of Dietary Phenolic Compounds to Human Serum Albumin and Food-Drug Interactions. Pharmaceutics 12:1123. https://doi.org/10.3390/pharmaceutics12111123

Lu J, Jiang F, Lu A, Zhang G (2016) Linkers Having a Crucial Role in Antibody–Drug Conjugates. Int J Mol Sci 17:561. https://doi.org/10.3390/ijms17040561

Luqmani YA (2005) Mechanisms of drug resistance in cancer chemotherapy. Med Princ Pract Int J Kuwait Univ Health Sci Cent 14 Suppl 1:35–48. https://doi.org/10.1159/000086183

Lutz C, Simon W, Werner-Simon S, et al (2020) Total Synthesis of α- and β-Amanitin. Angew Chem Int Ed 59:11390–11393. https://doi.org/10.1002/anie.201914935

Lyon RP, Bovee TD, Doronina SO, et al (2015) Reducing hydrophobicity of homogeneous antibody-drug conjugates improves pharmacokinetics and therapeutic index. Nat Biotechnol 33:733–735. https://doi.org/10.1038/nbt.3212

Maddox AL, Brehove MS, Eliato KR, et al (2022) Molecular Assessment of HER2 to Identify Signatures Associated with Therapy Response in HER2-Positive Breast Cancer. Cancers 14:2795. https://doi.org/10.3390/cancers14112795

Maecker H, Jonnalagadda V, Bhakta S, et al (2023) Exploration of the antibody–drug conjugate clinical landscape. mAbs 15:2229101. https://doi.org/10.1080/19420862.2023.2229101

Mahalingaiah PK, Ciurlionis R, Durbin KR, et al (2019) Potential mechanisms of target-independent uptake and toxicity of antibody-drug conjugates. Pharmacol Ther 200:110–125. https://doi.org/10.1016/j.pharmthera.2019.04.008

Mahmood I (2021) Clinical Pharmacology of Antibody-Drug Conjugates. Antibodies 10:20. https://doi.org/10.3390/antib10020020

Mbua NE, Guo J, Wolfert MA, et al (2011) Strain-promoted alkyne-azide cycloadditions (SPAAC) reveal new features of glycoconjugate biosynthesis. Chembiochem Eur J Chem Biol 12:1912–1921. https://doi.org/10.1002/cbic.201100117

McCluskey AJ, Olive AJ, Starnbach MN, Collier RJ (2013) Targeting HER2-positive cancer cells with receptor-redirected anthrax protective antigen. Mol Oncol 7:440–451. https://doi.org/10.1016/j.molonc.2012.12.003

McDonagh CF, Kim KM, Turcott E, et al (2008) Engineered anti-CD70 antibody-drug conjugate with increased therapeutic index. Mol Cancer Ther 7:2913–2923. https://doi.org/10.1158/1535-7163.MCT-08-0295

McDonald GB, Freston JW, Boyer JL, DeLeve LD (2019) Liver complications following treatment of hematologic malignancy with ANTI-CD22-calicheamicin (inotuzumab ozogamicin). Hepatol Baltim Md 69:831–844. https://doi.org/10.1002/hep.30222

McKeage K, Perry CM (2002) Trastuzumab. Drugs 62:209–243. https://doi.org/10.2165/00003495-200262010-00008

Mckertish CM, Kayser V (2021) Advances and Limitations of Antibody Drug Conjugates for Cancer. Biomedicines 9:872. https://doi.org/10.3390/biomedicines9080872

Mercogliano MF, De Martino M, Venturutti L, et al (2017) TNFα-Induced Mucin 4 Expression Elicits Trastuzumab Resistance in HER2-Positive Breast Cancer. Clin Cancer Res 23:636–648. https://doi.org/10.1158/1078-0432.CCR-16-0970

Meyer J-P, Tully KM, Jackson J, et al (2018) Bioorthogonal Masking of Circulating Antibody–TCO Groups Using Tetrazine-Functionalized Dextran Polymers. Bioconjug Chem 29:538. https://doi.org/10.1021/acs.bioconjchem.8b00028

Mitry MMA, Greco F, Osborn HMI (2023) In Vivo Applications of Bioorthogonal Reactions: Chemistry and Targeting Mechanisms. Chem – Eur J 29:e202203942. https://doi.org/10.1002/chem.202203942

Morè S, Offidani M, Corvatta L, et al (2023) Belantamab Mafodotin: From Clinical Trials Data to Real-Life Experiences. Cancers 15:. https://doi.org/10.3390/cancers15112948

Nadkarni DV (2020) Conjugations to Endogenous Cysteine Residues. In: Tumey LN (ed) Antibody-Drug Conjugates: Methods and Protocols. Springer US, New York, NY, pp 37–49

Natsume A, Niwa R, Satoh M (2009) Improving effector functions of antibodies for cancer treatment: Enhancing ADCC and CDC. Drug Des Devel Ther 3:7–16

N'Da DD (2014) Prodrug Strategies for Enhancing the Percutaneous Absorption of Drugs. Molecules 19:20780–20807. https://doi.org/10.3390/molecules191220780

Nessler I, Menezes B, Thurber GM (2021) Key Metrics to Expanding the Pipeline of Successful Antibody Drug Conjugates. Trends Pharmacol Sci 42:803–812. https://doi.org/10.1016/j.tips.2021.07.005

Nguyen TD (2023) Mechanisms of ADC Toxicity and Strategies to Increase ADC Tolerability. Cancers 15:713. https://doi.org/10.3390/cancers15030713

Nigam SK, Granados JC (2023) OAT, OATP, and MRP Drug Transporters and the Remote Sensing and Signaling Theory. Annu Rev Pharmacol Toxicol 63:637–660. https://doi.org/10.1146/annurev-pharmtox-030322-084058

Ohri R, Bhakta S, Fourie-O'Donohue A, et al (2018) High-Throughput Cysteine Scanning To Identify Stable Antibody Conjugation Sites for Maleimide- and Disulfide-Based Linkers. Bioconjug Chem 29:473–485. https://doi.org/10.1021/acs.bioconjchem.7b00791

Orlik C, Decker K, Vranic M, et al (2024) Abstract 7183: Liver toxicity of amanitin-based antibody drug conjugates (ATACs) is caused by unspecific uptake of the ATAC into liver cells. Cancer Res 84:7183. https://doi.org/10.1158/1538-7445.AM2024-7183

Oroudjev E, Lopus M, Wilson L, et al (2010) Maytansinoid-Antibody Conjugates Induce Mitotic Arrest by Suppressing Microtubule Dynamic Instability. Mol Cancer Ther 9:2700–2713. https://doi.org/10.1158/1535-7163.MCT-10-0645

Pahl A, Lutz C, Hechler T (2019) Amatoxins as RNA Polymerase II Inhibiting Antibody–Drug Conjugate (ADC) Payloads. In: Thurston DE, Jackson PJM (eds) Cytotoxic Payloads for Antibody – Drug Conjugates. The Royal Society of Chemistry, pp 398–426

Pegram MD, Hamilton EP, Tan AR, et al (2021) First-in-Human, Phase 1 Dose-Escalation Study of Biparatopic Anti-HER2 Antibody–Drug Conjugate MEDI4276 in Patients with HER2-positive Advanced Breast or Gastric Cancer. Mol Cancer Ther 20:1442–1453. https://doi.org/10.1158/1535-7163.MCT-20-0014

Phi LTH, Sari IN, Yang Y-G, et al (2018) Cancer Stem Cells (CSCs) in Drug Resistance and their Therapeutic Implications in Cancer Treatment. Stem Cells Int 2018:5416923. https://doi.org/10.1155/2018/5416923

Poli GL, Bianchi C, Virotta G, et al (2013) Radretumab Radioimmunotherapy in Patients with Brain Metastasis: A 124I-L19SIP Dosimetric PET Study. Cancer Immunol Res 1:134–143. https://doi.org/10.1158/2326-6066.CIR-13-0007

Pond SM, Olson KR, Woo OF, et al (1986) Amatoxin Poisoning in Northern California, 1982-1983. West J Med 145:204–209

Powles T, Rosenberg JE, Sonpavde GP, et al (2021) Enfortumab Vedotin in Previously Treated Advanced Urothelial Carcinoma. N Engl J Med 384:1125–1135. https://doi.org/10.1056/NEJMoa2035807

Rao C, Rangan VS, Deshpande S (2015) Challenges in antibody–drug conjugate discovery: a bioconjugation and analytical perspective. Bioanalysis 7:1561–1564. https://doi.org/10.4155/bio.15.81

Rautio J, Laine K, Gynther M, Savolainen J (2008) Prodrug Approaches for CNS Delivery. AAPS J 10:92–102. https://doi.org/10.1208/s12248-008-9009-8

Reddy V, Iskander A, Hwang C, et al (2019) Castration-resistant prostate cancer: Androgen receptor inactivation induces telomere DNA damage, and damage response inhibition leads to cell death. PLoS ONE 14:e0211090. https://doi.org/10.1371/journal.pone.0211090

Riley RS, June CH, Langer R, Mitchell MJ (2019) Delivery technologies for cancer immunotherapy. Nat Rev Drug Discov 18:175–196. https://doi.org/10.1038/s41573-018-0006-z

Rossin R, Läppchen T, Bosch SM van den, et al (2013) Diels–Alder Reaction for Tumor Pretargeting: In Vivo Chemistry Can Boost Tumor Radiation Dose Compared with Directly Labeled Antibody. J Nucl Med 54:1989–1995. https://doi.org/10.2967/jnumed.113.123745

Rossin R, Versteegen RM, Wu J, et al (2018) Chemically triggered drug release from an antibody-drug conjugate leads to potent antitumour activity in mice. Nat Commun 9:1484. https://doi.org/10.1038/s41467-018-03880-y

Rostovtsev VV, Green LG, Fokin VV, Sharpless KB (2002) A Stepwise Huisgen Cycloaddition Process: Copper(I)-Catalyzed Regioselective “Ligation” of Azides and Terminal Alkynes. Angew Chem Int Ed 41:2596–2599. https://doi.org/10.1002/1521-3773(20020715)41:14<2596::AID-ANIE2596>3.0.CO;2-4

Satomaa T, Pynnönen H, Vilkman A, et al (2018) Hydrophilic Auristatin Glycoside Payload Enables Improved Antibody-Drug Conjugate Efficacy and Biocompatibility. Antibodies 7:15. https://doi.org/10.3390/antib7020015

Saxon E, Bertozzi CR (2001) Chemical and biological strategies for engineering cell surface glycosylation. Annu Rev Cell Dev Biol 17:1–23. https://doi.org/10.1146/annurev.cellbio.17.1.1

Schelté Philippe, Boeckler C, Frisch B, Schuber F (2000) Differential Reactivity of Maleimide and Bromoacetyl Functions with Thiols: Application to the Preparation of Liposomal Diepitope Constructs. Bioconjug Chem 11:118–123. https://doi.org/10.1021/bc990122k

Shahrokhinia A, Biswas P, Reuther JF (2021) Orthogonal synthesis and modification of polymer materials. J Polym Sci 59:1748–1786. https://doi.org/10.1002/pol.20210345

Shen B-Q, Xu K, Liu L, et al (2012) Conjugation site modulates the in vivo stability and therapeutic activity of antibody-drug conjugates. Nat Biotechnol 30:184–189. https://doi.org/10.1038/nbt.2108

Sheyi R, de la Torre BG, Albericio F (2022) Linkers: An Assurance for Controlled Delivery of Antibody-Drug Conjugate. Pharmaceutics 14:396. https://doi.org/10.3390/pharmaceutics14020396

Shi Y, Liu CH, Roberts AI, et al (2006) Granulocyte-macrophage colony-stimulating factor (GM-CSF) and T-cell responses: what we do and don't know. Cell Res 16:126–133. https://doi.org/10.1038/sj.cr.7310017

Sinclair AJ, Amo V del, Philp D (2009) Structure–reactivity relationships in a recognition mediated [3+2] dipolar cycloaddition reaction. Org Biomol Chem 7:3308–3318. https://doi.org/10.1039/B908072D

Sletten EM, Bertozzi CR (2011) From Mechanism to Mouse: A Tale of Two Bioorthogonal Reactions. Acc Chem Res 44:666–676. https://doi.org/10.1021/ar200148z

Sodani K, Patel A, Kathawala RJ, Chen Z-S (2012) Multidrug resistance associated proteins in multidrug resistance. Chin J Cancer 31:58–72. https://doi.org/10.5732/cjc.011.10329

Sramkoski RM, Pretlow TG, Giaconia JM, et al (1999) A new human prostate carcinoma cell line, 22Rv1. Vitro Cell Dev Biol - Anim 35:403–409. https://doi.org/10.1007/s11626-999-0115-4

Staudacher AH, Brown MP (2017) Antibody drug conjugates and bystander killing: is antigen-dependent internalisation required? Br J Cancer 117:1736–1742. https://doi.org/10.1038/bjc.2017.367

Stirpe F, Fiume L (1967) Effect of alpha-amanitin on ribonucleic acid synthesis and on ribonucleic acid polymerase in mouse liver. Biochem J 103:67-68P

Strebhardt K, Ullrich A (2008) Paul Ehrlich's magic bullet concept: 100 years of progress. Nat Rev Cancer 8:473–480. https://doi.org/10.1038/nrc2394

Sun X, Ponte JF, Yoder NC, et al (2017) Effects of Drug–Antibody Ratio on Pharmacokinetics, Biodistribution, Efficacy, and Tolerability of Antibody–Maytansinoid Conjugates. Bioconjug Chem 28:1371–1381. https://doi.org/10.1021/acs.bioconjchem.7b00062

Sysa-Shah P, Xu Y, Guo X, et al (2012) Cardiac-Specific Over-Expression of Epidermal Growth Factor Receptor 2 (ErbB2) Induces Pro-Survival Pathways and Hypertrophic Cardiomyopathy in Mice. PLOS ONE 7:e42805. https://doi.org/10.1371/journal.pone.0042805

Szijj PA, Bahou C, Chudasama V (2018) Minireview: Addressing the retro-Michael instability of maleimide bioconjugates. Drug Discov Today Technol 30:27–34. https://doi.org/10.1016/j.ddtec.2018.07.002

Szijj PA, Gray MA, Ribi MK, et al (2023) Chemical generation of checkpoint inhibitory T cell engagers for the treatment of cancer. Nat Chem 15:1636–1647. https://doi.org/10.1038/s41557-023-01280-4

Takahashi I, Takahashi K-I, Ichimura M, et al (1988) DUOCARMYCIN A, A NEW ANTITUMOR ANTIBIOTIC FROM STREPTOMYCES. J Antibiot (Tokyo) 41:1915–1917. https://doi.org/10.7164/antibiotics.41.1915

Tamargo J, Le Heuzey J-Y, Mabo P (2015) Narrow therapeutic index drugs: a clinical pharmacological consideration to flecainide. Eur J Clin Pharmacol 71:549–567. https://doi.org/10.1007/s00228-015-1832-0

Tarcsa E, Guffroy MR, Falahatpisheh H, et al (2020) Antibody-drug conjugates as targeted therapies: Are we there yet? A critical review of the current clinical landscape. Drug Discov Today Technol 37:13–22. https://doi.org/10.1016/j.ddtec.2020.07.002

Tornøe CW, Christensen C, Meldal M (2002) Peptidotriazoles on Solid Phase: [1,2,3]-Triazoles by Regiospecific Copper(I)-Catalyzed 1,3-Dipolar Cycloadditions of Terminal Alkynes to Azides. J Org Chem 67:3057–3064. https://doi.org/10.1021/jo011148j

Trehan I, Morandi F, Blaszczak LC, Shoichet BK (2002) Using Steric Hindrance to Design New Inhibitors of Class C β-Lactamases. Chem Biol 9:971–980. https://doi.org/10.1016/S1074-5521(02)00211-9

Turecek PL, Bossard MJ, Schoetens F, Ivens IA (2016) PEGylation of Biopharmaceuticals: A Review of Chemistry and Nonclinical Safety Information of Approved Drugs. J Pharm Sci 105:460–475. https://doi.org/10.1016/j.xphs.2015.11.015

Uppal H, Doudement E, Mahapatra K, et al (2015) Potential Mechanisms for Thrombocytopenia Development with Trastuzumab Emtansine (T-DM1). Clin Cancer Res 21:123–133. https://doi.org/10.1158/1078-0432.CCR-14-2093

Ursuegui S, Recher M, Krężel W, Wagner A (2017) An in vivo strategy to counteract post-administration anticoagulant activity of azido-Warfarin. Nat Commun 8:15242. https://doi.org/10.1038/ncomms15242

van den Bosch SM, Rossin R, Renart Verkerk P, et al (2013) Evaluation of strained alkynes for Cu-free click reaction in live mice. Nucl Med Biol 40:415–423. https://doi.org/10.1016/j.nucmedbio.2012.12.006

van der Velden VHJ, te Marvelde JG, Hoogeveen PG, et al (2001) Targeting of the CD33-calicheamicin immunoconjugate Mylotarg (CMA-676) in acute myeloid leukemia: in vivo and in vitro saturation and internalization by leukemic and normal myeloid cells. Blood 97:3197–3204. https://doi.org/10.1182/blood.V97.10.3197

Vetter J (2023) Amanitins: The Most Poisonous Molecules of the Fungal World. Molecules 28:5932. https://doi.org/10.3390/molecules28155932

Vo KT, Montgomery ME, Mitchell ST, et al (2017) Amanita phalloides Mushroom Poisonings — Northern California, December 2016. Morb Mortal Wkly Rep 66:549–553. https://doi.org/10.15585/mmwr.mm6621a1

Voss S, Palfi A, Mueller C, et al (2021) Abstract 915: Preclinical evaluation of anti-CD37 antibody-targeted amanitin conjugates (ATAC) in B-cell malignancies. Cancer Res 81:915. https://doi.org/10.1158/1538-7445.AM2021-915

Wada R, Erickson HK, Lewis Phillips GD, et al (2014) Mechanistic pharmacokinetic/pharmacodynamic modeling of in vivo tumor uptake, catabolism, and tumor response of trastuzumab maytansinoid conjugates. Cancer Chemother Pharmacol 74:969–980. https://doi.org/10.1007/s00280-014-2561-2

Wall S, Oh J-Y, Diers A, Landar A (2012) Oxidative Modification of Proteins: An Emerging Mechanism of Cell Signaling. Front Physiol 3:

Walsh SJ, Bargh JD, Dannheim FM, et al (2021) Site-selective modification strategies in antibody–drug conjugates. Chem Soc Rev 50:1305–1353. https://doi.org/10.1039/D0CS00310G

Wang L-X, Tong X, Li C, et al (2019) Glycoengineering of Antibodies for Modulating Functions. Annu Rev Biochem 88:433–459. https://doi.org/10.1146/annurev-biochem-062917-012911

Wang X, Du Q, Zhang W, et al (2022) Enhanced Transgene Expression by Optimization of Poly A in Transfected CHO Cells. Front Bioeng Biotechnol 10:

Wang Y, Hu Q (2023) Bio-Orthogonal Chemistry in Cell Engineering. Adv NanoBiomed Res 3:2200128. https://doi.org/10.1002/anbr.202200128

Wang Z, Li H, Gou L, et al (2023) Antibody–drug conjugates: Recent advances in payloads. Acta Pharm Sin B 13:4025–4059. https://doi.org/10.1016/j.apsb.2023.06.015

Warther D, Dursun E, Recher M, et al (2021) Plasma induced acceleration and selectivity in strain-promoted azide–alkyne cycloadditions. Org Biomol Chem 19:5063–5067. https://doi.org/10.1039/D1OB00529D

Weinstein JN, Collisson EA, Mills GB, et al (2013) The Cancer Genome Atlas Pan-Cancer Analysis Project. Nat Genet 45:1113–1120. https://doi.org/10.1038/ng.2764

Wieland T (1986) Peptides of Poisonous Amanita Mushrooms. In: Peptides of Poisonous Amanita Mushrooms. Springer-Verlag New York Inc.

Wieland T (1983) The toxic peptides from Amanita mushrooms. Int J Pept Protein Res 22:257–276. https://doi.org/10.1111/j.1399-3011.1983.tb02093.x

Wienland T, Faulstich H (1991) Fifty years of amanitin. Experientia 47:1186–1193. https://doi.org/10.1007/BF01918382

Wijdeven MA, van Geel R, Hoogenboom JH, et al (2022) Enzymatic glycan remodeling–metal free click (GlycoConnect™) provides homogenous antibody-drug conjugates with improved stability and therapeutic index without sequence engineering. mAbs 14:2078466. https://doi.org/10.1080/19420862.2022.2078466

Wittig G, Krebs A (1961) Zur Existenz niedergliedriger Cycloalkine, I. Chem Ber 94:3260–3275. https://doi.org/10.1002/cber.19610941213

Wolf P, Freudenberg N, Bühler P, et al (2010) Three conformational antibodies specific for different PSMA epitopes are promising diagnostic and therapeutic tools for prostate cancer. The Prostate 70:562–569. https://doi.org/10.1002/pros.21090

Wolska-Washer A, Robak T (2019) Safety and Tolerability of Antibody-Drug Conjugates in Cancer. Drug Saf 42:295–314. https://doi.org/10.1007/s40264-018-0775-7

Yao H, Jiang F, Lu A, Zhang G (2016) Methods to Design and Synthesize Antibody-Drug Conjugates (ADCs). Int J Mol Sci 17:194. https://doi.org/10.3390/ijms17020194

Yeung CHT, Verstegen RHJ, Greenberg R, Lewis TR (2024) Pharmacokinetic and pharmacodynamic principles: unique considerations for optimal design of neonatal clinical trials. Front Pediatr 11:. https://doi.org/10.3389/fped.2023.1345969

Zahavi D, Weiner L (2020) Monoclonal Antibodies in Cancer Therapy. Antibodies 9:34. https://doi.org/10.3390/antib9030034

Zhang Y, Wu S, Qin Y, et al (2018) Interaction of phenolic acids and their derivatives with human serum albumin: Structure–affinity relationships and effects on antioxidant activity. Food Chem 240:1072–1080. https://doi.org/10.1016/j.foodchem.2017.07.100

Zhao H, Atkinson J, Gulesserian S, et al (2018) Modulation of Macropinocytosis-Mediated Internalization Decreases Ocular Toxicity of Antibody–Drug Conjugates. Cancer Res 78:2115–2126. https://doi.org/10.1158/0008-5472.CAN-17-3202

Zhu H-Z, Wang G, Wei H-L, et al (2016a) Click synthesis of hydrogels by metal-free 1,3-dipolar cycloaddition reaction between maleimide and azide functionalized polymers. Macromol Res 24:793–799. https://doi.org/10.1007/s13233-016-4120-7

Zhu X-W, Wang Y, Wei Y-H, et al (2016b) Comprehensive Assessment of the Association between FCGRs polymorphisms and the risk of systemic lupus erythematosus:

Evidence from a Meta-Analysis. Sci Rep 6:31617. https://doi.org/10.1038/srep31617

Zhu Y, Liu K, Wang K, Zhu H (2023) Treatment-related adverse events of antibody–drug conjugates in clinical trials: A systematic review and meta-analysis. Cancer 129:283–295. https://doi.org/10.1002/cncr.34507

Zufferey R, Donello JE, Trono D, Hope TJ (1999) Woodchuck Hepatitis Virus Posttranscriptional Regulatory Element Enhances Expression of Transgenes Delivered by Retroviral Vectors. J Virol 73:2886–2892